

Swansea University E-Theses

Characterisation of materials with hyperelastic microstructures through computational homogenisation and optimisation methods.

Speirs, Derek C. D

How to cite:

Speirs, Derek C. D (2007) *Characterisation of materials with hyperelastic microstructures through computational homogenisation and optimisation methods..* thesis, Swansea University.
<http://cronfa.swan.ac.uk/Record/cronfa42354>

Use policy:

This item is brought to you by Swansea University. Any person downloading material is agreeing to abide by the terms of the repository licence: copies of full text items may be used or reproduced in any format or medium, without prior permission for personal research or study, educational or non-commercial purposes only. The copyright for any work remains with the original author unless otherwise specified. The full-text must not be sold in any format or medium without the formal permission of the copyright holder. Permission for multiple reproductions should be obtained from the original author.

Authors are personally responsible for adhering to copyright and publisher restrictions when uploading content to the repository.

Please link to the metadata record in the Swansea University repository, Cronfa (link given in the citation reference above.)

<http://www.swansea.ac.uk/library/researchsupport/ris-support/>



CIVIL AND COMPUTATIONAL ENGINEERING CENTRE
PRIFYSGOL ABERTAWE
SWANSEA UNIVERSITY



Characterisation of Materials with Hyperelastic Microstructures through Computational Homogenisation and Optimisation Methods

DEREK C. D. SPEIRS

*Submitted to Swansea University in partial
fulfillment of the requirements for the degree of PhD.*

September 2007

ProQuest Number: 10798062

All rights reserved

INFORMATION TO ALL USERS

The quality of this reproduction is dependent upon the quality of the copy submitted.

In the unlikely event that the author did not send a complete manuscript and there are missing pages, these will be noted. Also, if material had to be removed, a note will indicate the deletion.



ProQuest 10798062

Published by ProQuest LLC (2018). Copyright of the Dissertation is held by the Author.

All rights reserved.

This work is protected against unauthorized copying under Title 17, United States Code
Microform Edition © ProQuest LLC.

ProQuest LLC.
789 East Eisenhower Parkway
P.O. Box 1346
Ann Arbor, MI 48106 – 1346

To Fatma, Evan and my parents.

Summary

The constitutive modelling of microheterogeneous materials is a subject of considerable practical and theoretical interest. Among many approaches *computational homogenisation* is particularly powerful and versatile. This is based on the numerical estimation of the mechanical response of a volume element representing the material's microstructure.

This thesis is concerned with computational homogenisation and its particular use in characterising materials with hyperelastic microstructures through an optimisation based methodology.

Details of a finite element implementation of the computational homogenisation procedure are presented. These are derived from a variational treatment of the homogenisation problem. Examples of the application of the method to hyperelastic microstructures are reported.

Next a procedure to provide a convenient characterisation of the behaviour of composite material is considered. This consists of adopting a conventional explicit model to approximate the macroscopic mechanical behaviour. Parameters of the model are chosen by established optimisation methods so that the macro model best fits the calculated homogenised response of a model of the microstructure.

The optimisation based methodology is applied to the problem of modelling the constitutive behaviour of artery walls.

“A wise man proportions his beliefs to the evidence.”

Hume

Contents

Table of Contents	i
Acknowledgments	vi
1 Introduction	1
1.1 Heterogeneous materials	1
1.2 Outline	7
2 Elements of Continuum Mechanics	10
2.1 Introduction	10
2.2 The Continuum concept	11
2.3 Kinematics	11
2.3.1 Configurations and motions	11
2.3.2 Material and spatial descriptions	13
2.3.3 Differentiating kinematic field variables	14
2.3.4 The deformation gradient	15
2.3.5 Rate of deformation and velocity gradients	16
2.3.6 Changes in volume and area	18
2.3.7 Polar decomposition of the deformation gradient	21
2.3.8 Strain Tensors	24
2.4 Forces and Stresses	27
2.4.1 Distributed Forces	27
2.4.2 The Cauchy Stress Tensor	30
2.4.3 The First Piola-Kirchhoff Stress Tensor	30
2.4.4 Other Stress Tensors	31
2.5 Conservation Principles	31
2.5.1 Conservation of Mass	32
2.5.2 Balance of Linear Momentum	33
2.5.3 Balance of Angular Momentum	35
2.5.4 Balance of mechanical energy	36
2.5.5 Principle of Virtual Work	37
2.6 Constitutive Laws	39
2.6.1 Fundamental principles of constitutive theory	40
2.6.2 Special classes of constitutive law	43
2.6.3 Material symmetry	46
2.6.4 Some examples of Hyperelastic Material Models	50
2.7 The Quasi-Static Initial Boundary Value Problem	52

2.7.1	Conventional boundary conditions	53
2.7.2	The Mechanical Quasi-static I.B.V.P. - Spatial Description . .	54
2.7.3	The Mechanical Quasi-static IBVP - Material Description . .	55
3	Review of the finite element method	57
3.1	Spatial Discretisation	58
3.1.1	Parametric Finite Elements	58
3.1.2	Shape Functions	60
3.1.3	Interpolation - Isoparametric Formulation	61
3.1.4	Deformation Gradient and Strains	61
3.1.5	Integration	63
3.1.6	Voigt Notation	64
3.2	Temporal Discretisation	66
3.3	Linearisation	68
3.3.1	Newton-Raphson Method	68
3.3.2	Linearisation of Virtual Work	69
3.3.3	Spatial Discretisation of Virtual Work	72
3.4	Overall Algorithm	75
4	Computational homogenisation	78
4.1	Introduction	78
4.2	The representative volume element	79
4.3	Definition of averaged quantities	79
4.4	Split between homogeneous deformation and fluctuations	81
4.5	Equilibrium of the RVE	82
4.6	Constraints	82
4.6.1	Prescribed average deformation gradient	82
4.6.2	Admissible fluctuations under the minimal constraint	83
4.6.3	Admissible fluctuations under general kinematic constraints . .	84
4.6.4	The Hill-Mandel principle	85
4.7	The RVE equilibrium problem	87
4.8	The homogenised constitutive functional	87
4.9	Homogenisation with elastic and hyperelastic micro-constituents . .	88
4.10	Some specific kinematic constraints	89
4.10.1	The minimal constraint: uniform traction on boundary	89
4.10.2	The periodic boundary condition	92
4.10.3	The linear boundary condition	97
4.10.4	The Taylor condition	98
4.11	Observations on the symmetry of homogenised constitutive models . .	99
4.11.1	Symmetry of the RVE	99
4.12	Finite element discretisation of the homogenisation procedure	106
4.12.1	Uniform traction constraint: discretisation	107
4.12.2	Periodic boundary condition: discretisation	112
4.12.3	Linear boundary condition: discretisation	116
4.12.4	Taylor condition: discretisation	117
4.13	Implementation of the computational homogenisation procedure . . .	117

5	Application of computational homogenisation	121
5.1	Introduction	121
5.2	Soft matrix with stiff inclusions	122
5.2.1	Problem definition	122
5.2.2	Results	123
5.3	Test of isotropy	125
5.3.1	Problem details	126
5.3.2	Results	127
5.4	Comparison of RVEs with varying void and inclusion ratios	128
5.4.1	Problem details	128
5.4.2	Results	130
5.5	Comparison of RVEs with varying densities of holes	135
5.5.1	Problem details	135
5.5.2	Results	135
5.6	Comparison of regular and irregular void distributions	138
5.6.1	Problem details	138
5.6.2	Results	139
5.7	Conclusion	142
6	Characterisation of homogenised properties by optimisation	143
6.1	Introduction	143
6.2	Optimisation of material parameters	144
6.2.1	Choice of the canonical form of the macro model	145
6.2.2	Choice of objective function	145
6.2.3	Optimisation procedure	146
6.2.4	Sensitivity analysis	146
6.3	Application to composites of Ogden materials	147
6.3.1	Finite element model of RVE	147
6.3.2	Homogenised data sets	148
6.3.3	Macroscopic models and objective functions	149
6.3.4	Optimisation procedure	151
6.3.5	Results	152
6.3.6	Sensitivity analysis	162
6.3.7	Macroscopic boundary value problem	164
6.3.8	Conclusions	167
7	Computational homogenisation for modelling of arterial walls	169
7.1	Introduction	169
7.2	Structure and histology of the arterial wall	170
7.2.1	Structure and histology	170
7.2.2	Characteristic passive mechanical behaviour of arteries	174
7.3	Macroscopic constitutive models for arterial tissue	175
7.3.1	Arterial wall constitutive model by Zulliger <i>et al.</i>	176
7.3.2	Arterial wall constitutive model by Holzapfel <i>et al.</i>	177
7.4	FE model of microstructure	177
7.5	Objective functions	180
7.6	Optimisation results	182

7.7	Macro boundary value problem – inflation and extension of artery . .	185
7.8	Conclusion	189
8	Conclusion	190
	References	193

Acknowledgments

I would like to thank Prof. D. Perić and Dr. E. A. de Souza Neto for their invaluable guidance and encouragement.

I am very grateful also to have been supported financially by the Engineering and Physical Sciences Research Council and through the James Callaghan scholarship awarded by the University of Wales Swansea.

I am indebted also to Deniz Somer and Dr W. Dettmer who allowed me to use their program.

Further thanks are due to Maziar, Mayur, Sadok, Mauro, Arturo, Javier, Hong Wen and all my other friends and colleagues in the PhD room who have been good companions during my time of study.

Finally to my family in Scotland who have supported me all my life and to my wife Fatma and son Evan I offer the most heartfelt thanks of all.

Chapter 1

Introduction

1.1 Heterogeneous materials

This thesis is concerned with heterogeneous materials or more precisely micro-heterogeneous materials. That is to say materials for which it is possible to identify distinct *macro* and *micro* scales. The macro scale is the scale at which most useful physical measurements are made. Viewed at this resolution such materials appear uniform. At the micro scale however a heterogeneous structure becomes apparent. This microstructure is characterised by lengths much smaller than the macro scale but still large enough to lie within the domain of continuum mechanics. In some materials it is useful to consider even finer scales at which the constituent materials of the microstructure appear heterogeneous.

Heterogeneous materials are common and play important roles both in engineering and natural processes. Both man-made and naturally occurring examples abound.

Microstructural detail is seen in most if not all materials of biological origin. Timber and plant tissue for instance exhibit a cellular structure as illustrated in figure 1.1(a). A less regular microscopic structural arrangement is generally seen in coral, sponge and bone (figure 1.1(c)). The soft tissues of humans and other animals have particularly complex microstructures involving numerous constituents and substructures. The mechanical properties of such materials are of great interest for medical applications. Artery wall tissue is considered in some detail in chapter 7 of this thesis.

Among man-made substances also are a great many whose mechanical properties depend on micro-heterogenities. Metallic alloys for instance have a polycrystalline

microstructure. Metal foams have also been created with a porous structure. Figure 1.1(d) shows the microstructure of a titanium foam created for orthopedic applications. More common and longer established examples of inhomogeneous engineering materials are found in the construction industry. These include concrete and brick. Manufactured composites comprise another large class of heterogeneous materials. Polymers for instance are commonly reinforced with glass, carbon or aramid fibres. Carbon, rubber and ceramics are other examples of matrix materials reinforced variously with fibres, whiskers and particles of many materials. In recent years highly engineered materials have emerged whose microstructure is carefully controlled. One example, illustrated in figure 1.1(b), is a polymer sheet perforated by laser micro-drilling that has been developed for biomedical tissue engineering applications.

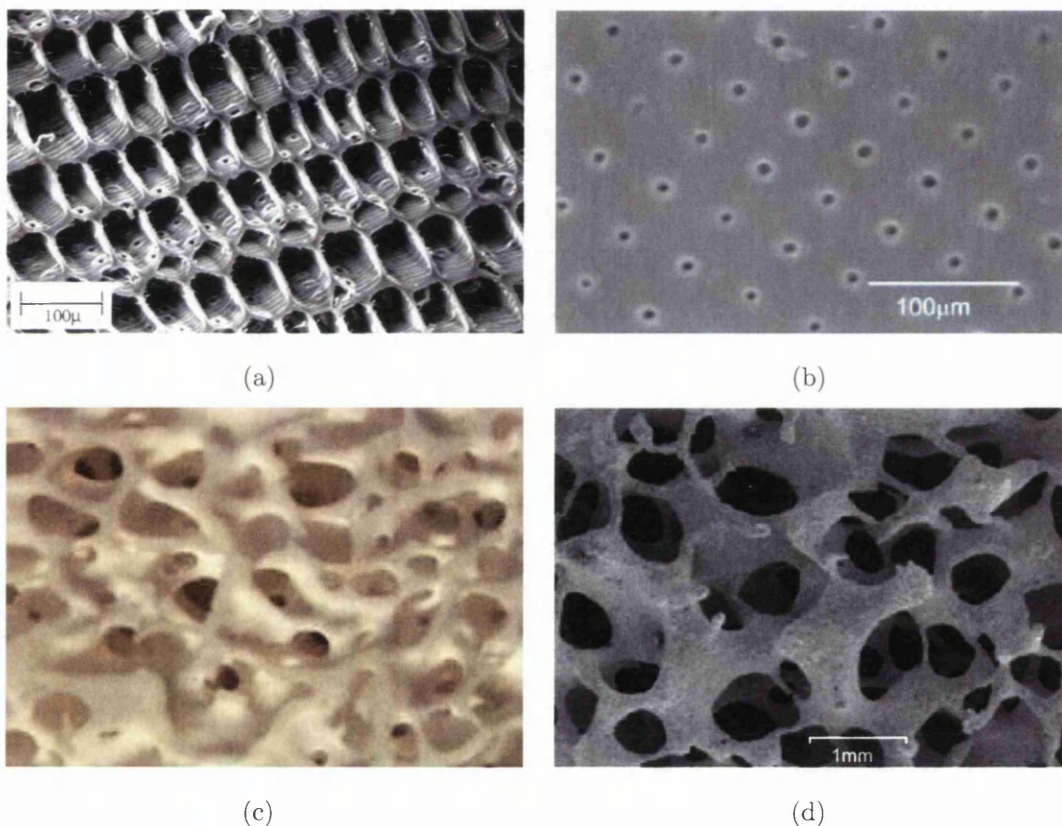


Figure 1.1: Images of natural and artificial microstructures: (a) norway spruce; (b) laser drilled sheet of polycaprolactone (PCT); (c) cancellous bone; (d) titanium foam.

Approaches to modelling heterogeneous materials

There are then a wide variety of heterogeneous materials in existence. Many of these find application in engineering where it is valuable to be able to predict their me-

chanical response. In principle one could model the entire microstructure as a single body over the macroscopic domain. However the size and complexity of the problem would in almost all cases be intractable analytically and make computational solutions prohibitively expensive. In any case generally speaking the microscopic fluctuations in stress and displacement are not ultimately of interest. Rather it is the stresses and strains measured at the macroscopic level with relatively coarse precision that is required. Thus a constitutive model relating macroscopic deformation and stress is usually sought. The simplest way to do this is to adopt a purely phenomenological strategy whereby an explicit macro model is proposed with parameters chosen to best fit experimental results. The unsatisfactory aspect of this approach is that it ignores any available microstructural information making it impossible to link known changes in the microstructural form and composition to the overall mechanical response. In order to overcome this shortcoming a number of modelling strategies have been put forward. Broadly speaking these can be divided into analytical and computational approaches.

The simplest of the analytical strategies is the rule of mixtures. This assumes that the overall moduli of composites of linear elastic materials are given by the average of the corresponding microscopic values of each constituent phase weighted by the respective volume fractions. The generalisation to non linear materials sets the macroscopic stress equal to the weighted average of the microscopic stresses assuming the strain in each phase is uniformly equal to the macroscopic strain. The rule of mixtures does not generally provide a very accurate estimate of composite material behaviour as it takes no account of interactions between different phases in the aggregate.

A more sophisticated line of analytical micro-mechanical investigation originates in the important work of Eshelby [23–25]. Eshelby considered an infinite linear elastic continuum containing a single linear elastic inclusion of ellipsoidal shape and obtained the dependency of the stress and strain fields on their far field values. The result allows overall properties of composites with dilute concentrations of particulate inclusions to be estimated. This approach, sometimes known as the effective medium approach, has been enhanced by many authors (e.g. [6, 22, 42, 57, 80, 82]) to address other inclusion geometries and types of constituent materials as well as finite deformations.

The self consistent method originated by Hershey [46] and Kröner [88, 89] and elaborated by Budiansky [9], Hill [48–50] and others is a variation of the effective

medium approach. The basic idea is to assign known material properties to the inclusion and the as yet unknown effective macroscopic properties to the surrounding infinite matrix. The requirement of so called self-consistency – the equality of the inclusion strain with the overall average strain – results in an implicit formula for the overall effective moduli. An extension of the method is the self consistent embedded cell model [1,21] whereby a structured cell rather than a simple inclusion is embedded in the effective medium. The procedure is generally not purely analytical and typically involves a finite element solution to a boundary value problem.

The application of variational principles (minimisation of energy) has extended the analytical approach to more complicated multiphase composites. The work of Hashin and Shtrikman [43,44] is of particular importance in this area. They obtained upper and lower bounds on the values of overall elastic moduli for materials with phases of arbitrary geometry. In particular cases the bounds are close enough to each other to provide a good estimate of effective properties. An extension of the variational approach to nonlinear constituent materials by Talbot and Willis [108,110,124] has been used to establish bounds on the effective energy functions of composites reinforced with elastoplastic fibres [109]. Further bounds and estimates have been derived by Ponte Castañeda [115–117] and Suquet [105,106] among many others.

Another analytical approach to modelling inhomogeneous materials is provided by asymptotic expansion homogenisation. This theory is based around the separation of macro and micro scales. A local position variable $\mathbf{y} = \mathbf{x}/\epsilon$ is defined in terms of the macroscopic position \mathbf{x} and a scale parameter $\epsilon = l/L$ representing the ratio between a characteristic macroscopic length L and the characteristic microscopic length l . The dependence of field variables on \mathbf{y} is generally assumed to be periodic making the approach applicable to repetitive microstructures. Results are derived through an asymptotic expansion of the field variables about \mathbf{x} with respect to the parameter ϵ . Accounts of the theory and its application may be found in [5,19,29,32,33,51,67,90,118] for example.

As outlined above considerable effort has been directed toward analytical modelling of heterogeneous materials. A comprehensive introduction to the field may be found in the text by Nemat-Nasser and Hori [83]. However the purely analytical approach is generally limited to simple microstructural geometries and materials. Most results require quite strong and restrictive assumptions such as small deformations, linear elasticity or ellipsoidal geometry or they provide only approximate bounds.

In order to address materials with more complicated heterogeneities computational homogenisation methods have been developed.

Central to computational homogenisation (as well as many analytical methods) is the concept of the representative volume element (RVE). The RVE is a microscopically scaled continuum domain containing a distribution of materials that is considered to be representative of the microstructure of the heterogeneous material. Essentially it is a sample of the microstructure large enough to be considered typical but much smaller than the macroscopic body of material. Computational homogenisation has two essential steps – localisation (or macro-to-micro transition) and homogenisation proper (or micro-to-macro transition). Localisation consists of determining the microscopic fields over the RVE from given macroscopic values. Most commonly a deformation driven approach is used. In this case the macroscopic deformation or strain is the given input from which constraints on the RVE are derived. This allows a boundary value problem to be formulated and solved computationally thus providing the microscopic deformation and stress. The homogenisation step consists of calculating overall macroscopic variables from the micro fields. This is almost always a matter of computing the volume average. Thus the output of deformation driven homogenisation is the average micro stress which is adopted as the overall homogenised macroscopic stress.

Numerical solutions of the RVE problem have been obtained by several methods. The most common is the standard finite element method (FEM). Alternatives include the Veronoi cell finite element method [35, 79], which is a specialization of the FEM designed to deal with non-uniform microstructures, and Fourier transform methods proposed for periodic microstructures [72, 81].

The most direct application of computational homogenisation is the fully coupled multiscale method. In this approach a macroscopic boundary value problem is solved using a numerical algorithm such as the finite element method just as for a homogeneous material except that the response of the macro material is provided by a computational homogenisation procedure rather than by a conventional model. In other words the homogenised behaviour of the RVE directly provides the required constitutive relation for the macro continuum. In practice for a standard finite element formulation this means solving a micro level boundary value problem at each Gauss point. The multi scale methodology has only been developed relatively recently with notable contributions by Ladeveze *et al.* [64, 65], Smit *et al.* [100], Miehe

et al. [73–78], Terada and Kikuchi [113], Kouznetsova *et al.* [60], Terada *et al.* [114], Reese [95], Ibrahimbegović and D. Marković [56], Matsui *et al.* [58], Goktepe and Miehe [37], Li and E [69] amongst others.

Coupled multi-scale computations require the solution of nested boundary value problems and are therefore intrinsically computationally expensive. This drawback has been addressed through the use of parallelisation [26, 28, 66] and by selective use [34] of the procedure.

A further enhancement of the coupled multi-scale method is the use of second order homogenisation. In most computational homogenisation procedures the RVE response is governed by the macro deformation gradient alone – that is the first gradient of displacement. As a consequence the absolute size of the RVE and its constituents have no influence on the overall response in contrast to empirical observations. In response to this shortcoming second order homogenisation has been developed by Kouznetsova and others [27, 59, 61–63] whereby the first and second gradient of the macro displacement govern the boundary conditions of the RVE.

Computational homogenisation has also been used to model heterogeneous materials without the direct coupling of micro and macro levels involved in the multi-scale method. One method is to compile an extensive database of RVE responses across a range macroscopic deformations [8, 94, 112]. The homogenised response to an arbitrary deformation, as required to solve a macro level problem, may subsequently be obtained by interpolation between discrete points in the database.

Another approach is to assume a form of macroscopic constitutive relation and use the homogenised response of the RVE to certain test loadings to obtain effective material parameters. In the simplest case the RVE constituents are linear elastic and a single loading is sufficient to determine the effective shear and bulk moduli if isotropy is assumed. Zohdi and Wriggers [128] used this approach to obtain a range of overall moduli for a statistical sample of randomised RVEs. Some authors have applied simple load histories such as incremental uniaxial stretching or shear tests to an RVE in order to obtain homogenised stress strain curves [11, 87, 101, 125]. In some cases overall moduli such as elastic moduli and yield stresses are readily obtained from the results [3]. Testing an elasto-plastic RVE under a more comprehensive range of deformations has been used to calculate effective yield surfaces for the composite [92, 97].

If the RVE consists of more complex constituents such as highly non-linear hy-

perelastic materials, then its homogenised response may still be approximated by an explicit macroscopic constitutive relation. However a suitable macroscopic model will generally be more complicated. In such cases it is not usually possible to determine effective material parameters adequately from a small number of RVE loadings. Instead they may be obtained by an optimisation procedure fitting the macro model to the homogenised response across an extensive range of macro deformations. This is the methodology applied in the present work. A similar approach has been adopted by Van der Sluis et al [122]. They considered a 2-D microcell consisting of a viscoplastic matrix with a void and fitted a viscoplastic model of the same form as the matrix model to the averaged response. The six macro model parameters were derived from a uniaxial tensile test with a single load history using certain simplifying assumptions. However the method used to obtain these parameters was specific to the form of the model and avoided simultaneous optimisation of all the parameters over a wider data set. More recently Reese et al. [96] have fitted an orthotropic hyperelastic model to the results from a finite element model of a sample of fibre reinforced rubber membrane. Their RVE (they do not use the terminology of homogenisation) is however relatively large and does not exploit the periodicity of the fibre configuration. Moreover optimisation of macro parameters is performed using a hybrid of linear least squares estimation on the linear parameters and trial and error on the nonlinear parameters.

In conclusion the modeling of micro-heterogeneous materials has been approached in many ways and is a well established but evolving field of research. Computational strategies in particular are attracting growing interest. The concept of using optimisation techniques to fit a macroscopic model to homogenised data, as discussed in the preceding paragraph, is central to this thesis. Chapter 6 discusses the methodology in more detail.

1.2 Outline

The work of this thesis has been directed toward two main goals – firstly to develop and examine a computational strategy for homogenisation valid for large deformations and secondly to use this strategy in conjunction with optimisation methods to find explicit constitutive models to characterise heterogeneous materials. This latter procedure has been applied to the modelling of arterial tissue.

Chapter 2

Continuum mechanics provides the basic theory which underlies all of the approaches to mechanical modelling discussed in this introductory chapter and throughout the thesis. The fundamentals of the subject are reviewed in Chapter 2. The focus is on the mechanics of non linear solid materials undergoing finite deformations.

Chapter 3

The use of the finite element method in solving boundary value problems in continuum mechanics is discussed in chapter 3. This well established procedure is essential to the work of this thesis as it provides the basis of the computational homogenisation strategy employed in subsequent chapters.

Chapter 4

Chapter 4 is concerned with homogenisation itself. This is the procedure by which the average constitutive response of a representative volume element (RVE) typifying the material's microstructure is derived. The variational formulation of the problem is described followed by details of its computational implementation by means of the finite element method.

Chapter 5

Some numerical examples using computational homogenisation are presented in chapter 5. These include comparisons of different boundary conditions used to calculate the homogenised response and some simple studies of the effect of RVE morphology.

Chapter 6

In chapter 6 an optimisation based procedure to characterise the large strain behaviour of heterogeneous materials with a hyperelastic microstructure is considered. This modelling approach consists of fitting the parameters of an explicit macroscopic model to the homogenised constitutive response of an RVE. An application of the method to a composite with rubber-like microconstituents is reported.

Chapter 7

The procedure described in chapter 6 is applied in chapter 7 to the modelling of the tissue in artery walls. Two constitutive models from the literature are fitted to the homogenised response of a representative volume element made up of the protein elastin reinforced with fibers of collagen. Results are compared in the solution of a simple macro scale boundary value problem.

Chapter 8

Chapter 8 concludes the thesis with a brief review of the work undertaken and some comments on its outcomes. Suggestions are offered for future research into the modelling of heterogeneous materials.

Chapter 2

Elements of Continuum Mechanics

2.1 Introduction

This chapter presents a concise review of the theory of continuum mechanics that forms the basis of the rest of the work in this thesis. The main aspects of the theory may be identified as:

Kinematics: This is the mathematical description of the motion and deformation of a body and develops the essential concept of strain.

Forces and Stresses: This topic provides a description of the forces acting on elements within the body.

Conservation and Balance Principles: These provide expressions of the fundamental physical laws as applied to a continuum.

Constitutive Laws: These laws relate the deformation of a continuum body to the forces acting it and are specific to the type of material it is made of.

Subsequent sections of the chapter consider these items in turn prefaced by a brief discussion of the underlying concept of the continuum itself. The principal aim is to arrive at a formulation of the basic problem of determining stresses and displacements of a body subject to given initial and boundary conditions. Only purely mechanical processes are addressed without consideration of thermodynamics. The emphasis is on the quasistatic deformation of solids.

The material that follows has become standard theory and may be found in many texts. In particular the books by Holzapfel [52], Bonet and Wood [7] and de Souza

Neto, Perić and Owen [17] have guided the present presentation of the subject. Other sources include Gurtin [40], Green and Adkins [39], Spencer [103], Ogden [85] and Chadwick [12]. Truesdell [120] offers an axiomatic approach to the subject with much greater rigour than has been attempted here.

2.2 The Continuum concept

Underlying the continuum approach to mechanics is the notion that physical bodies can be considered as continuous (or piecewise continuous) distributions of matter with all its associated properties such as mass and energy. This is inconsistent with the fundamentals of modern physics in which atomic and subatomic particles feature in a more discretised quantum view of nature. However as long as the bodies under consideration are sufficiently large compared with their discontinuous microstructures, continuum theory has proved in practice to be highly effective in describing and predicting mechanical behaviour. The justification is empirical. All continuum models are therefore in this sense phenomenological. However this does not preclude taking account of microstructures which though much smaller than the overall dimensions of the body are still large enough compared with the atomic scale to be amenable to the continuum approach. Indeed in later chapters such continuum microstructures are the focus of attention.

2.3 Kinematics

Kinematics allows one to characterise the motion of material bodies in a quantitative and mathematical way. It provides measures of deformation and relations between them that are valid regardless of the specific materials which constitute the body.

2.3.1 Configurations and motions

We consider a general continuum *body*, \mathcal{B} , occupying an open region Ω_0 within three dimensional Euclidean space, \mathbb{E}^3 , at time t_0 . Let P denote an arbitrary particle¹ in \mathcal{B} which lies at *reference* or *material* position \mathbf{X} relative to some origin \mathcal{O} . At some

¹The term particle is used here to indicate an infinitesimal part of the continuum and is not meant imply any discretisation of the body.

other time t the particle has moved to its *spatial* or *current* position \mathbf{x} as illustrated in Figure 2.1. Although other formulations are possible we shall usually refer both \mathbf{X} and \mathbf{x} to the same fixed Cartesian basis $(\mathbf{e}_1, \mathbf{e}_2, \mathbf{e}_3)$ with origin \mathcal{O} . The mapping which relates the reference and spatial positions of each particle in the body is termed the *configuration* of \mathcal{B} at time t and is denoted:

$$\phi : \Omega_0 \rightarrow \mathbb{E}^3 \quad (2.1)$$

so that

$$\mathbf{x} = \phi(\mathbf{X}) . \quad (2.2)$$

The deformed body now occupies the region $\Omega = \phi(\Omega_0)$. We assume that the mapping ϕ is invertible thereby ruling out the interpenetration of matter from different parts of the body.

In general the configuration of the body will change with time. The continuous sequence of configurations undergone by \mathcal{B} is known as the *motion* of the body. Denoting the motion by χ and time domain by $T \in \mathbb{R}$, we can write,

$$\chi : \Omega_0 \times T \rightarrow \mathbb{E}^3 \quad (2.3)$$

with

$$\mathbf{x} = \chi(\mathbf{X}, t) . \quad (2.4)$$

For any given time χ is a bijection between Ω_0 and the current spatial domain $\Omega(t)$ so that the inverse relation $\mathbf{X} = \chi^{-1}(\mathbf{x}, t)$ is always well defined.

We have emphasised the functional relationship between \mathbf{x} , \mathbf{X} and t by using χ to indicate the mapping. In subsequent expressions however we shall frequently write $\mathbf{x}(\mathbf{X}, t)$ for $\chi(\mathbf{X}, t)$ and $\mathbf{X}(\mathbf{x}, t)$ in place of $\chi^{-1}(\mathbf{x}, t)$.

We conclude this section by defining the displacement as

$$\mathbf{U}(\mathbf{X}, t) \equiv \mathbf{x}(\mathbf{X}, t) - \mathbf{X} \quad (2.5)$$

or equivalently

$$\mathbf{u}(\mathbf{x}, t) \equiv \mathbf{x} - \mathbf{X}(\mathbf{x}, t) . \quad (2.6)$$

Clearly $\mathbf{U}(\mathbf{X}, t) = \mathbf{u}(\mathbf{x}, t)$ for all \mathbf{X} , \mathbf{x} such that $\mathbf{x} = \chi(\mathbf{X}, t)$. We use a capital \mathbf{U} to express the displacement field as a function of reference position and a lower case \mathbf{u} when spatial position is the argument. The use of capitals to represent referential fields and lower case letters for variables with a spatial dependence is a convention which for the most part will be observed in this chapter. The important distinction between spatial and material fields is discussed in the next section.

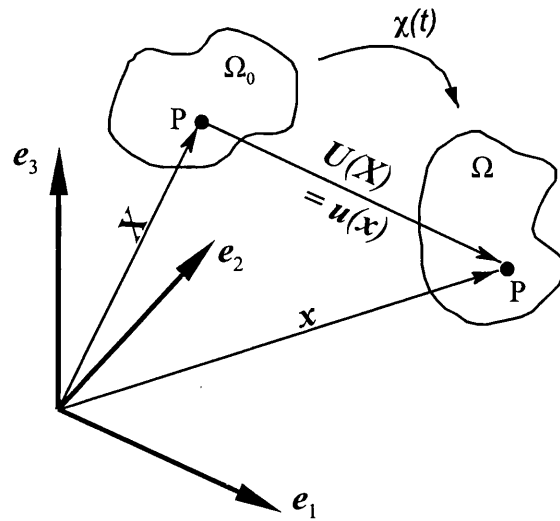


Figure 2.1: General motion of a deformable body.

2.3.2 Material and spatial descriptions

The *material* or *Lagrangian* description of motion is a representation of the kinematics of deformation with reference to the material configuration. In this view the field variables are expressed as functions of reference position \mathbf{X} (and time). Such a field with $T \times \Omega_0$ as its domain is termed a *material* or *Lagrangian field*. Conceptually the Lagrangian approach is to follow a material particle through the motion and observe variables from this point of view.

Alternatively the motion of a body may be characterised in relation to its spatial configuration. This is known as the *spatial* or *Eulerian* description. In this representation *spatial* or *Eulerian* fields are used whereby quantities are viewed as functions of spatial position \mathbf{x} and time t . The Eulerian description can be thought of as focusing on a fixed point in space and observing the motion as particles of the body move through it.

Formally we may write

$$\begin{aligned} F(\mathbf{X}, t) & \text{ is a material field,} & \text{and} \\ f(\mathbf{x}, t) & \text{ is a spatial field,} \end{aligned}$$

where F and f are generic fields that may take on scalar, vector or tensor values.

Some caution needs to be observed in applying the adjectives material and spatial because some quantities that are naturally associated with the spatial description may be expressed as a material field and vice versa. An example of this is density with

respect to deformed volume, ρ . This is the mass per unit of deformed volume and may be expressed as a spatial field $\rho(\mathbf{x}, t)$ or a material field $P(\mathbf{X}, t) = \rho(\chi^{-1}(\mathbf{X}, t), t)$. However the material field must not be confused with the density with respect to material volume. This is a distinct field and represents the mass per unit volume of an element of the undeformed body. This second material density has a spatial description ρ_0 but in general $\rho_0(\mathbf{x}, t) \neq \rho(\mathbf{x}, t)$.

2.3.3 Differentiating kinematic field variables

Spatial and material gradients

Two types of gradients are defined in kinematics - the *material gradient* and the *spatial gradient*.

As the name suggests the material gradient represents differentiation with respect to material position \mathbf{X} and is denoted by ∇_0 or *Grad* (note the capital “G”) or by $\partial(\bullet)/\partial\mathbf{X}$. For a generic material field, $F(\mathbf{X}, t)$ we may write

$$\nabla_0 F(\mathbf{X}, t) = \text{Grad} F(\mathbf{X}, t) = \frac{\partial F(\mathbf{X}, t)}{\partial \mathbf{X}} .$$

The spatial gradient by contrast is obtained by differentiation with respect to spatial position \mathbf{x} and is variously denoted by ∇ , *grad* (with lower case “g”) and $\partial(\bullet)/\partial\mathbf{x}$. For the generic spatial field f we write

$$\nabla f(\mathbf{x}, t) = \text{Grad} f(\mathbf{x}, t) = \frac{\partial f(\mathbf{x}, t)}{\partial \mathbf{x}} .$$

Temporal derivatives: material and spatial

Kinematic fields may be differentiated with respect to time in one of two ways. The first of these is to take the partial time derivative holding the reference position constant. This is termed the *material* or *total time derivative*. Alternatively one may differentiate with respect to time with spatial position held constant and this results in the *spatial* or *local time derivative*.

The material derivative is denoted $D(\bullet)/Dt$ or by a superposed dot. Application to a generic material field F is simple:

$$\dot{F}(\mathbf{X}, t) = \frac{DF(\mathbf{X}, t)}{Dt} = \left(\frac{\partial F(\mathbf{X}, t)}{\partial t} \right)_{\mathbf{X} \text{ const}} .$$

An important example is the velocity field. This is the material derivative of the spatial position $\mathbf{x}(\mathbf{X}, t)$ given by

$$\mathbf{V}(\mathbf{X}, t) = \dot{\mathbf{x}}(\mathbf{X}, t) \tag{2.7}$$

or in its Eulerian description,

$$\mathbf{v}(\mathbf{x}, t) = \mathbf{V}(\boldsymbol{\chi}(\mathbf{X}, t), t) . \quad (2.8)$$

Evaluating the material derivative of a spatial field f requires a little more care:

$$\begin{aligned} \dot{f}(\mathbf{x}, t) &= \left(\frac{\partial f(\mathbf{x}(\mathbf{X}, t), t)}{\partial t} \right)_{\mathbf{X}=\boldsymbol{\chi}^{-1}(\mathbf{x}, t) \text{ const}} \\ &= \left(\frac{\partial f(\mathbf{x}, t)}{\partial t} \right)_{\mathbf{x} \text{ const}} + \left(\frac{\partial f(\mathbf{x}, t)}{\partial \mathbf{x}} \right)_{t \text{ const}} \frac{\partial \mathbf{x}}{\partial t} \end{aligned}$$

where we have employed the chain rule to obtain the last equality. We recognise the spatial gradient, $\nabla f = \partial f / \partial \mathbf{x}$, and velocity, $\mathbf{v} = \partial \mathbf{x} / \partial t$, in this last expression and rewrite it as:

$$\dot{f}(\mathbf{x}, t) = \frac{\partial f(\mathbf{x}, t)}{\partial t} + \nabla f(\mathbf{x}, t) \cdot \mathbf{v}(\mathbf{x}, t) . \quad (2.9)$$

Equation (2.9) above makes it obvious that in general the material derivative of a spatial field is not equal to its spatial derivative, i.e.

$$\dot{f}(\mathbf{x}, t) \neq \frac{\partial f(\mathbf{x}, t)}{\partial t} .$$

2.3.4 The deformation gradient

Of fundamental importance in characterising the deformation of bodies is the *deformation gradient*. This is the material gradient of the current position given symbolically by,

$$\mathbf{F}(\mathbf{X}, t) = \nabla_0 \mathbf{x}(\mathbf{X}, t) = \frac{\partial \mathbf{x}}{\partial \mathbf{X}} , \quad (2.10)$$

or in component notation referred to Cartesian axes,

$$F_{aB} = \frac{\partial x_a}{\partial X_B} . \quad (2.11)$$

\mathbf{F} maps infinitesimal line elements $d\mathbf{X}$ in the reference configuration to the corresponding line elements in the current configuration:

$$\mathbf{F}d\mathbf{X} = d\mathbf{x} ,$$

as illustrated in Figure 2.2. In general the deformation gradient varies throughout the body but its evaluation at some material point can be thought of as a linearisation of the deformed coordinates with respect to the original position vector in a small neighbourhood about the point.

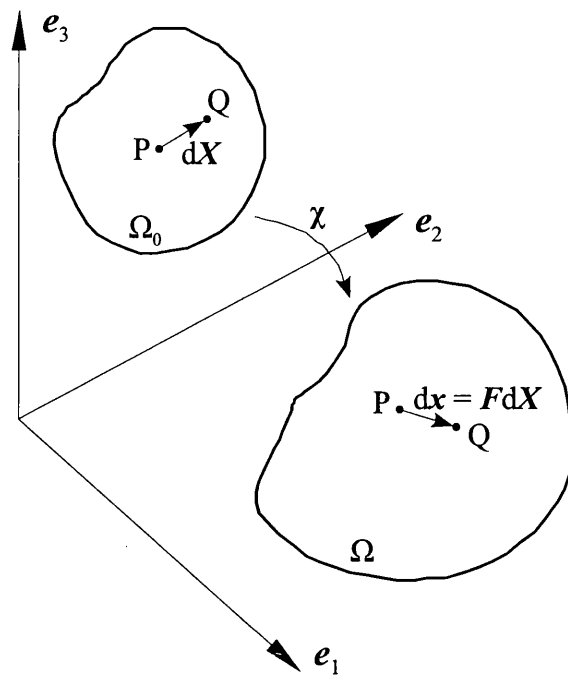


Figure 2.2: Deformation of infinitesimal position vector.

It is often convenient to express \mathbf{F} in terms of the displacement field. In the material description we obtain:

$$\mathbf{F}(\mathbf{X}, t) = \frac{\partial (\mathbf{X} + \mathbf{U}(\mathbf{X}, t))}{\partial \mathbf{X}} = \mathbf{I} + \nabla_0 \mathbf{U}(\mathbf{X}, t), \quad (2.12)$$

where \mathbf{I} is the identity tensor. In the spatial description we have

$$\mathbf{F}^{-1}(\mathbf{x}, t) = \frac{\partial \mathbf{X}}{\partial \mathbf{x}} = \frac{\partial (\mathbf{x} - \mathbf{u}(\mathbf{x}, t))}{\partial \mathbf{x}} = \mathbf{I} - \nabla \mathbf{u}(\mathbf{x}, t),$$

so that

$$\mathbf{F}(\mathbf{x}, t) = (\mathbf{I} - \nabla \mathbf{u}(\mathbf{x}, t))^{-1}. \quad (2.13)$$

2.3.5 Rate of deformation and velocity gradients

It is sometimes useful in kinematics to consider the gradients, both material and spatial, of the velocity field $\mathbf{V}(\mathbf{X}, t) = \mathbf{v}(\chi(\mathbf{X}, t), t) = \mathbf{v}(\mathbf{x}, t)$.

The *material velocity gradient* is obtained by taking the material gradient of the velocity field i.e. $\nabla_0 \mathbf{V}(\mathbf{X}, t)$. By interchanging the order of temporal and positional

differentiation this may be expressed in terms of the deformation gradient thus:

$$\begin{aligned}
 \nabla_0 \mathbf{V}(\mathbf{X}, t) &= \frac{\partial \mathbf{V}(\mathbf{X}, t)}{\partial \mathbf{X}} \\
 &= \frac{\partial}{\partial \mathbf{X}} \left(\frac{\partial \mathbf{x}(\mathbf{X}, t)}{\partial t} \right) \\
 &= \frac{\partial}{\partial t} \left(\frac{\partial \mathbf{x}(\mathbf{X}, t)}{\partial \mathbf{X}} \right) \\
 &= \dot{\mathbf{F}}(\mathbf{X}, t)
 \end{aligned} \tag{2.14}$$

The spatial gradient of the velocity field defines the *spatial velocity gradient* and is denoted by \mathbf{l} so that,

$$\mathbf{l}(\mathbf{x}, t) = \nabla \mathbf{v}(\mathbf{x}, t) = \frac{\partial \mathbf{v}(\mathbf{x}, t)}{\partial \mathbf{x}} . \tag{2.15}$$

We may relate the spatial velocity gradient to the deformation gradient by considering the material time derivative of \mathbf{F} thus:

$$\begin{aligned}
 \dot{\mathbf{F}} &= \frac{\partial}{\partial t} \left(\frac{\partial \mathbf{x}(\mathbf{X}, t)}{\partial \mathbf{X}} \right) \\
 &= \frac{\partial}{\partial \mathbf{X}} \left(\frac{\partial \mathbf{x}(\mathbf{X}, t)}{\partial t} \right) \\
 &= \frac{\partial}{\partial \mathbf{x}} \left(\frac{\partial \mathbf{x}(\chi^{-1}(\mathbf{X}, t), t)}{\partial t} \right) \frac{\partial \mathbf{x}}{\partial \mathbf{X}} \\
 &= \frac{\partial \mathbf{v}(\mathbf{x}, t)}{\partial \mathbf{x}} \frac{\partial \mathbf{x}}{\partial \mathbf{X}} \\
 &= \mathbf{l} \mathbf{F} .
 \end{aligned} \tag{2.16}$$

Solving for \mathbf{l} yields,

$$\mathbf{l} = \nabla \mathbf{v} = \dot{\mathbf{F}} \mathbf{F}^{-1} . \tag{2.17}$$

The spatial velocity gradient may be decomposed into symmetric and antisymmetric parts to give two further tensor fields. The symmetric part, known as the *rate of deformation tensor* and denoted by \mathbf{d} , is constructed as follows:

$$\mathbf{d} = \frac{1}{2} (\mathbf{l} + \mathbf{l}^T) . \tag{2.18}$$

Its antisymmetric counterpart is called the *spin tensor* and is denoted by \mathbf{w} with the following definition:

$$\mathbf{w} = \frac{1}{2} (\mathbf{l} - \mathbf{l}^T) . \tag{2.19}$$

Clearly by construction the following relations hold:

$$\mathbf{d} = \mathbf{d}^T \tag{2.20}$$

$$\mathbf{w} = -\mathbf{w}^T \tag{2.21}$$

$$\mathbf{l} = \mathbf{d} + \mathbf{w} . \tag{2.22}$$

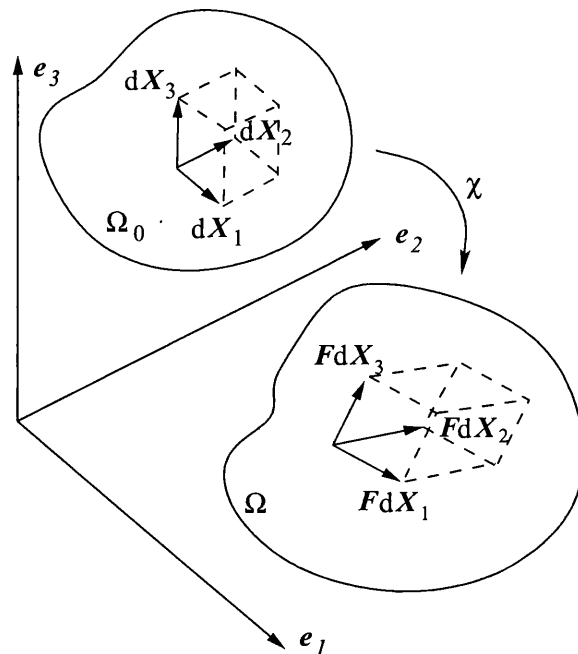


Figure 2.3: Deformation of an infinitesimal volume element.

2.3.6 Changes in volume and area

Problems in continuum mechanics frequently require us to integrate quantities with respect to volume and to area. This can be done in either the reference or the deformed configurations and it is invaluable to be able to switch between the two formulations. To this end we examine the relationship between differential volume and area elements in the Lagrangian and Eulerian descriptions.

Volume

Consider an infinitesimal volume element at some point \mathbf{X} in the reference configuration having edge vectors $d\mathbf{X}_1$, $d\mathbf{X}_2$ and $d\mathbf{X}_3$ aligned with the Cartesian axes. At some time t the motion χ deforms the element into a parallelepiped at $\mathbf{x} = \chi(\mathbf{X}, t)$ with edge vectors $d\mathbf{x}_1 = \mathbf{F}d\mathbf{X}_1$, $d\mathbf{x}_2 = \mathbf{F}d\mathbf{X}_2$ and $d\mathbf{x}_3 = \mathbf{F}d\mathbf{X}_3$. Figure 2.3 illustrates the transformation.

In the reference configuration the volume of the element, dV , is given by the scalar triple product of the edge vectors so that:

$$dV = d\mathbf{X}_1 \cdot (d\mathbf{X}_2 \times d\mathbf{X}_3) .$$

Written in terms of Cartesian components this expression becomes:

$$dV = \varepsilon_{IJK} [d\mathbf{X}_1]_I [d\mathbf{X}_2]_J [d\mathbf{X}_3]_K .$$

Since $d\mathbf{X}_1$, $d\mathbf{X}_2$ and $d\mathbf{X}_3$ align with the orthogonal Cartesian axes this simplifies to

$$dV = dX_1 dX_2 dX_3 , \quad (2.23)$$

where $dX_I = |d\mathbf{X}_I|$ for $I = 1, 2, 3$.

The volume of the deformed parallelepiped, dv , may also be obtained from the scalar triple product of its edge vectors $\mathbf{F}d\mathbf{X}_1$, $\mathbf{F}d\mathbf{X}_2$ and $\mathbf{F}d\mathbf{X}_3$ so that:

$$\begin{aligned} dv &= \mathbf{F}d\mathbf{X}_1 \cdot (\mathbf{F}d\mathbf{X}_2 \times \mathbf{F}d\mathbf{X}_3) \\ &= \varepsilon_{pqr} F_{pI} [d\mathbf{X}_1]_I F_{qJ} [d\mathbf{X}_2]_J F_{rK} [d\mathbf{X}_3]_K . \end{aligned} \quad (2.24)$$

Now since each $d\mathbf{X}_a$ ($a = 1, 2, 3$) is parallel to the corresponding basis vector \mathbf{e}_a we may write,

$$[d\mathbf{X}_1]_I = \delta_{1I} dX_1 ; \quad [d\mathbf{X}_2]_J = \delta_{2J} dX_2 ; \quad [d\mathbf{X}_3]_K = \delta_{3K} dX_3 ;$$

so that equation (2.24) becomes:

$$\begin{aligned} dv &= \varepsilon_{pqr} F_{pI} \delta_{1I} dX_1 F_{qJ} \delta_{2J} dX_2 F_{rK} \delta_{3K} dX_3 \\ &= \varepsilon_{pqr} F_{p1} F_{q2} F_{r3} dX_1 dX_2 dX_3 . \end{aligned}$$

It may easily be verified that the determinant of \mathbf{F} is given by $\det \mathbf{F} = \varepsilon_{pqr} F_{p1} F_{q2} F_{r3}$. In view of this and equation (2.23) we may write:

$$dv = (\det \mathbf{F}) dV .$$

The determinant of the deformation gradient, $\det \mathbf{F}$, thus has a key role in relating reference and spatial measures of volume. It is known as the *Jacobian* and denoted J so that,

$$J \equiv \det \mathbf{F} , \quad (2.25)$$

and

$$dv = J dV . \quad (2.26)$$

We see therefore that the Jacobian at some material point and time represents the ratio between deformed and current volumes locally. For physical reasons this ratio cannot be negative - otherwise negative volumes would arise. Likewise $\det \mathbf{F}$ must

be non-zero so that \mathbf{F}^{-1} exists and the motion is reversible. Thus the Jacobian is everywhere and always positive. i.e.

$$J(\mathbf{X}, t) > 0 \quad \forall \mathbf{X}, t \quad (2.27)$$

It is useful to obtain the material time derivative of the Jacobian. Using the chain rule we may write

$$\dot{J} = \frac{\partial J}{\partial \mathbf{F}} : \dot{\mathbf{F}} = \frac{\partial(\det \mathbf{F})}{\partial \mathbf{F}} : \dot{\mathbf{F}} .$$

Now by a well known result in tensor calculus (see e.g. [52] pp 41),

$$\frac{\partial(\det \mathbf{F})}{\partial \mathbf{F}} = (\det \mathbf{F}) \mathbf{F}^{-\text{T}} = J \mathbf{F}^{-\text{T}} ,$$

so that,

$$\begin{aligned} \dot{J} &= J \mathbf{F}^{-\text{T}} : \dot{\mathbf{F}} \\ &= J \mathbf{F}^{-\text{T}} : (\dot{\mathbf{F}} \mathbf{F}^{-1} \mathbf{F}) \\ &= J (\mathbf{F}^{-\text{T}} \mathbf{F}) : (\dot{\mathbf{F}} \mathbf{F}^{-1}) \\ &= J \mathbf{I} : (\dot{\mathbf{F}} \mathbf{F}^{-1}) . \end{aligned} \quad (2.28)$$

Recalling equation (2.17),

$$\dot{\mathbf{F}} \mathbf{F}^{-1} = \nabla \mathbf{v} ,$$

allows (2.28) to be rewritten as,

$$\dot{J} = J \mathbf{I} : \nabla \mathbf{v} .$$

Finally recognising that $\mathbf{I} : \nabla(\bullet)$ is equal to the divergence with respect to spatial coordinates, $\nabla \cdot (\bullet)$, we obtain the following expression for the total time derivative of the Jacobian:

$$\dot{J} = J \nabla \cdot \mathbf{v} . \quad (2.29)$$

Area

Consider now an elemental surface in the undeformed body with area vector $d\mathbf{S}$. We may construct a reference volume element dV by forming the scalar product of $d\mathbf{S}$ with an arbitrary infinitesimal vector $d\mathbf{X}$. Thus we have,

$$dV = d\mathbf{S} \cdot d\mathbf{X} . \quad (2.30)$$

Under deformation the surface element maps to a spatial surface element with an area vector we shall denote $d\mathbf{s}$. The arbitrary vector $d\mathbf{X}$ maps to $\mathbf{F}d\mathbf{X}$ and the deformed volume element is given by

$$dv = d\mathbf{s} \cdot \mathbf{F}d\mathbf{X} .$$

However from equation (2.26) dv may also be expressed as

$$dv = JdV ,$$

so that we may write,

$$JdV = d\mathbf{s} \cdot \mathbf{F}d\mathbf{X} .$$

Using equation (2.30) to substitute for dV gives:

$$Jd\mathbf{S} \cdot d\mathbf{X} = d\mathbf{s} \cdot \mathbf{F}d\mathbf{X} . \quad (2.31)$$

Now by definition of the transpose operation \mathbf{F} must satisfy,

$$\mathbf{u} \cdot \mathbf{F}\mathbf{v} = \mathbf{F}^T\mathbf{u} \cdot \mathbf{v}$$

for any two vectors \mathbf{u} and \mathbf{v} . We may apply this identity to the right hand side of equation (2.31) to obtain,

$$\begin{aligned} Jd\mathbf{S} \cdot d\mathbf{X} &= \mathbf{F}^T d\mathbf{s} \cdot d\mathbf{X} \\ \Leftrightarrow (Jd\mathbf{S} - \mathbf{F}^T d\mathbf{s}) &= 0 . \end{aligned}$$

Since this holds for any $d\mathbf{X}$ the term in brackets must vanish identically. Thus

$$Jd\mathbf{S} = \mathbf{F}^T d\mathbf{s} .$$

Re-arranging we arrive finally at *Nanson's formula*

$$d\mathbf{s} = J\mathbf{F}^{-T}d\mathbf{S} \quad (2.32)$$

which describes the important relation between infinitesimal surface area vectors in the reference configuration to the corresponding area vectors in the current configuration.

2.3.7 Polar decomposition of the deformation gradient

It is sometimes useful to express the deformation gradient as the product of a tensor representing a rotation and a tensor which is positive definite and symmetric.

More formally, it may be shown (see for example [52] chapter 2) that for every time and position in a motion there exist unique tensors \mathbf{R} , \mathbf{U} and \mathbf{V} such that

$$\mathbf{F} = \mathbf{R}\mathbf{U}, \quad (2.33)$$

$$\mathbf{F} = \mathbf{V}\mathbf{R}, \quad (2.34)$$

$$\mathbf{R}\mathbf{R}^T = \mathbf{I} \quad \text{and} \quad \det \mathbf{R} = 1 \quad (\text{i.e. } \mathbf{R} \text{ is proper orthogonal}), \quad (2.35)$$

$$\mathbf{U}^T = \mathbf{U} \quad \text{and} \quad \mathbf{U} \text{ positive definite}, \quad (2.36)$$

$$\mathbf{V}^T = \mathbf{V} \quad \text{and} \quad \mathbf{V} \text{ positive definite}, \quad (2.37)$$

where \mathbf{I} is the identity tensor. Equation (2.33) is referred to as the *right polar decomposition* of \mathbf{F} with the symmetric, positive definite tensor \mathbf{U} known as the *right stretch tensor*. Equation (2.34) represents the *left polar decomposition* and introduces the *left stretch tensor* \mathbf{V} which like the right stretch is positive definite and symmetric.

Like \mathbf{F} itself, the *rotation tensor*, \mathbf{R} , is a two point tensor acting on tangent vectors to the material position to give tangent vectors in the spatial description. By contrast the stretches are one point tensors. The right stretch, \mathbf{U} , maps material tangents to material tangents while the left stretch, \mathbf{V} , maps spatial tangent vectors to other spatial tangents. For this reason \mathbf{U} and \mathbf{V} are also known as the *material stretch tensor* and the *spatial stretch tensor* respectively.

The proper orthogonality of \mathbf{R} ensures that it preserves the length of vectors and can be interpreted as a local rigid rotation about the origin. To find a similar geometrical interpretation of the stretch tensors we note that their symmetry ensures, by the spectral theorem, that each has an orthonormal set of normalised eigenvectors with real eigenvalues. We may use these respective sets of eigenvectors as orthonormal bases and construct the spectral decomposition of each stretch tensor as follows,

$$\mathbf{U} = \sum_{\alpha=1}^3 \Lambda_{\alpha} \mathbf{N}_{\alpha} \otimes \mathbf{N}_{\alpha} \quad (2.38)$$

$$\mathbf{V} = \sum_{\alpha=1}^3 \lambda_{\alpha} \mathbf{n}_{\alpha} \otimes \mathbf{n}_{\alpha} \quad (2.39)$$

where \mathbf{N}_{α} and \mathbf{n}_{α} are the unit eigenvectors of \mathbf{U} and \mathbf{V} corresponding to eigenvalues Λ_{α} and λ_{α} respectively. i.e.

$$\mathbf{U}\mathbf{N}_{\alpha} = \Lambda_{\alpha} \mathbf{N}_{\alpha} \quad (2.40)$$

$$\mathbf{V}\mathbf{n}_{\alpha} = \lambda_{\alpha} \mathbf{n}_{\alpha}. \quad (2.41)$$

However from equations (2.33), (2.34) and (2.35) $\mathbf{V} = \mathbf{R}\mathbf{U}\mathbf{R}^T$ and we may write

$$\mathbf{V}(\mathbf{R}\mathbf{N}_\alpha) = \mathbf{R}\mathbf{U}\mathbf{R}^T\mathbf{R}\mathbf{N}_\alpha \quad (2.42)$$

$$= \mathbf{R}\mathbf{U}\mathbf{N}_\alpha \quad (2.43)$$

$$= \Lambda_\alpha (\mathbf{R}\mathbf{N}_\alpha) . \quad (2.44)$$

Comparing this with equation (2.41) we may make the following identifications

$$\mathbf{n}_\alpha = \mathbf{R}\mathbf{N}_\alpha \quad (2.45)$$

$$\lambda_\alpha = \Lambda_\alpha . \quad (2.46)$$

The mutual eigenvalues of \mathbf{U} and \mathbf{V} , henceforth denoted λ_α , are known as the *principal stretches*. Note that since \mathbf{U} and \mathbf{V} are positive definite, by definition, each eigenvalue is strictly positive.

In order to appreciate the geometrical effect of \mathbf{U} acting upon an infinitesimal material vector $d\mathbf{X}$ we use the eigen-basis $\{\mathbf{N}_1, \mathbf{N}_2, \mathbf{N}_3\}$ to write,

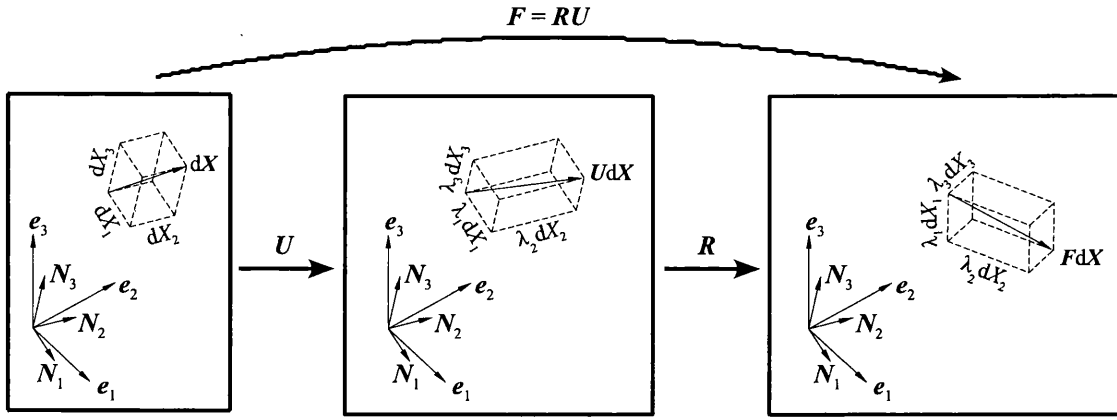
$$d\mathbf{X} = dX_1\mathbf{N}_1 + dX_2\mathbf{N}_2 + dX_3\mathbf{N}_3 ,$$

where $dX_1 = d\mathbf{X} \cdot \mathbf{N}_1$ and so on. We may imagine a cuboid in the material configuration with edges $dX_1\mathbf{N}_1$, $dX_2\mathbf{N}_2$, and $dX_3\mathbf{N}_3$ as illustrated on the left of figure 2.4. Applying the right stretch tensor to $d\mathbf{x}$ in this form then gives:

$$\begin{aligned} \mathbf{U}d\mathbf{X} &= dX_1\mathbf{U}\mathbf{N}_1 + dX_2\mathbf{U}\mathbf{N}_2 + dX_3\mathbf{U}\mathbf{N}_3 \\ &= \lambda_1 dX_1\mathbf{N}_1 + \lambda_2 dX_2\mathbf{N}_2 + \lambda_3 dX_3\mathbf{N}_3 . \end{aligned}$$

We now see that in the eigen-basis of \mathbf{U} each component of $d\mathbf{X}$ has been scaled or stretched by a factor equal to the corresponding eigenvalue. The material cuboid is transformed into a distorted cuboid as shown in the middle part of figure 2.4 but the right angles between edges remain. Only the lengths of sides are stretched. This is the reason for \mathbf{U} being called a stretch tensor. The full mapping \mathbf{F} is completed by applying \mathbf{R} to the stretched cuboid. This preserves its the shape and size but rotates it in space. The right hand side of figure 2.4 illustrates the effect.

The left polar decomposition, $\mathbf{F} = \mathbf{V}\mathbf{R}$ may be analysed in a similar way except that we should consider an element parallel to the eigen-basis of \mathbf{V} , $\{\mathbf{n}_1, \mathbf{n}_2, \mathbf{n}_3\}$. This time the rigid rotation is applied first. Only then is the element stretched along its axes by the eigenvalues λ_1 , λ_2 , and λ_3 .

Figure 2.4: Right polar decomposition of \mathbf{F} .

2.3.8 Strain Tensors

The deformation gradient has been introduced in section 2.3.4. This two point tensor relates infinitesimal changes in material position to corresponding infinitesimal changes in current position and is usually taken as the fundamental tensor describing deformation. However it is often useful to characterise a motion in terms of tensors which refer exclusively to either material or material descriptions. A number of such *strain tensors* may be constructed from the deformation gradient and are introduced in the following sections.

Material strain tensors

The *right Cauchy-Green tensor* is defined as follows:

$$\mathbf{C} = \mathbf{F}^T \mathbf{F} . \quad (2.47)$$

It is obvious from this definition that \mathbf{C} is symmetric.

The geometrical significance of the right Cauchy-Green tensor may be appreciated if we examine the ratio of the lengths of deformed to undeformed differential position vectors. Consider an infinitesimal change in material position $d\mathbf{X}$ with length dX and direction \mathbf{N} (i.e. $d\mathbf{X} = dX\mathbf{N}$) which deforms under a motion to the spatial line element $d\mathbf{x}$. To first order $d\mathbf{x} = \mathbf{F}d\mathbf{X} = dX\mathbf{F}\mathbf{N}$, so that we may write the square

of the ratio of lengths as:

$$\begin{aligned}
 \frac{|\mathrm{d}\mathbf{x}|^2}{|\mathrm{d}\mathbf{X}|^2} &= \frac{\mathrm{d}\mathbf{x} \cdot \mathrm{d}\mathbf{x}}{\mathrm{d}\mathbf{X} \cdot \mathrm{d}\mathbf{X}} \\
 &= \frac{(\mathrm{d}X \mathbf{F} \mathbf{N}) \cdot (\mathrm{d}X \mathbf{F} \mathbf{N})}{\mathrm{d}X^2} \\
 &= \mathbf{N}^T \mathbf{C} \mathbf{N} .
 \end{aligned} \tag{2.48}$$

The local ratio of deformed to undeformed lengths is known as the stretch, λ in the material direction \mathbf{N} . The Cauchy-Green tensor therefore relates the square of the stretch to the stretch direction via equation (2.48).

The right Cauchy-Green tensor may be expressed in terms of the right stretch tensor \mathbf{U} by inserting the right polar decomposition $\mathbf{F} = \mathbf{R}\mathbf{U}$ into definition (2.47) to obtain,

$$\begin{aligned}
 \mathbf{C} &= (\mathbf{R}\mathbf{U})^T \mathbf{R}\mathbf{U} = \mathbf{U}^T \mathbf{R}^T \mathbf{R} \mathbf{U} \\
 &= \mathbf{U}^2 ,
 \end{aligned} \tag{2.49}$$

where we have used the orthogonality of \mathbf{R} .

It is obvious from equation (2.49) that for any normalised eigenvector, \mathbf{N}_A , of \mathbf{U} with corresponding eigenvalue λ_A ,

$$\mathbf{C} \mathbf{N}_A = \mathbf{U}^2 \mathbf{N}_A = \lambda_A^2 \mathbf{N}_A$$

Therefore \mathbf{C} and \mathbf{U} share the same eigenbasis, $(\mathbf{N}_1, \mathbf{N}_2, \mathbf{N}_3)$ but the corresponding eigenvalues of \mathbf{C} are the square of those of \mathbf{U} . It follows from this that the right Cauchy-Green tensor may be represented in terms of the common eigenbasis as follows:

$$\mathbf{C} = \sum_{A=1}^3 \lambda_A^2 \mathbf{N}_A \otimes \mathbf{N}_A . \tag{2.50}$$

Other material strain tensors include the *Piola deformation tensor*, defined as the inverse of the right Cauchy-Green Tensor:

$$\mathbf{B} = \mathbf{C}^{-1} = \mathbf{F}^{-1} \mathbf{F}^{-T} \tag{2.51}$$

and the *Green-Lagrange strain tensor*, given by:

$$\mathbf{E} = \frac{1}{2}(\mathbf{C} - \mathbf{I}) = \frac{1}{2}(\mathbf{F}^T \mathbf{F} - \mathbf{I}) , \tag{2.52}$$

where \mathbf{I} is the second order identity tensor.

The Green-Lagrange tensor arises naturally when considering the difference between the square of the length of an infinitesimal line element in the deformed configuration and the square of its length in the original reference configuration. Working to first order we have

$$\begin{aligned}
 dx^2 - dX^2 &\simeq \mathbf{F}d\mathbf{X} \cdot \mathbf{F}d\mathbf{X} - d\mathbf{X} \cdot d\mathbf{X} \\
 &= d\mathbf{X} \cdot \mathbf{F}^T \mathbf{F} d\mathbf{X} - d\mathbf{X} \cdot d\mathbf{X} \\
 &= d\mathbf{X} \cdot (\mathbf{F}^T \mathbf{F} - \mathbf{I}) d\mathbf{X} \\
 &= 2d\mathbf{X} \cdot \mathbf{E} d\mathbf{X} .
 \end{aligned}$$

Recalling equation (2.49) we may express \mathbf{E} in terms of the material stretch tensor thus:

$$\mathbf{E} = \frac{1}{2}(\mathbf{U}^2 - \mathbf{I}) . \quad (2.53)$$

In this form the Green-Lagrange strain may be placed in a family of Lagrangian strain tensors defined by

$$\mathbf{E}^{(n)} = \begin{cases} \frac{1}{n}(\mathbf{U}^n - \mathbf{I}) & n \neq 0 \\ \ln[\mathbf{U}] & n = 0 \end{cases} , \quad (2.54)$$

$\mathbf{E} = \mathbf{E}^{(2)}$ being obtained by setting $n = 2$. Other examples of the class are the *Almansi* tensor $\mathbf{E}^{(-1)}$, the *Hencky* tensor $\mathbf{E}^{(0)}$ and the *Biot* tensor $\mathbf{E}^{(1)}$.

Spatial strain tensors

The *left Cauchy-Green tensor* is defined by:

$$\mathbf{b} = \mathbf{F} \mathbf{F}^T . \quad (2.55)$$

Like its Lagrangian counterpart, the right Cauchy-Green tensor, \mathbf{b} is symmetric and can be rewritten using the polar decomposition of \mathbf{F} . This time the left polar decomposition, $\mathbf{F} = \mathbf{V} \mathbf{R}$, is used to give \mathbf{b} in terms of the left stretch tensor \mathbf{V} thus:

$$\mathbf{V} = \mathbf{V} \mathbf{R} (\mathbf{V} \mathbf{R})^T = \mathbf{V} \mathbf{R} \mathbf{R}^T \mathbf{V}^T = \mathbf{V}^2 . \quad (2.56)$$

It follows that \mathbf{b} shares eigenvectors with \mathbf{V} but with corresponding eigenvalues squared. Furthermore \mathbf{b} may be represented in terms of the eigenprojection of \mathbf{V} . In a spatial analogue to equation (2.50) we have:

$$\mathbf{b} = \sum_{a=1}^3 \lambda_a^2 \mathbf{n}_a \otimes \mathbf{n}_a . \quad (2.57)$$

The spatial counterpart to the Green-Lagrange strain is known as the *Almansi strain tensor* and is defined as:

$$\mathbf{e} = \frac{1}{2}(\mathbf{I} - \mathbf{b}^{-1}) = \frac{1}{2}(\mathbf{I} - \mathbf{F}^{-\mathrm{T}}\mathbf{F}^{-1}), \quad (2.58)$$

or in terms of the left stretch tensor:

$$\mathbf{e} = \frac{1}{2}(\mathbf{I} - \mathbf{V}^{-2}). \quad (2.59)$$

The Almansi strain belongs to a family of *Eulerian strain tensors* defined by:

$$\mathbf{e}^{(n)} = \begin{cases} \frac{1}{n}(\mathbf{V}^n - \mathbf{I}) & n \neq 0 \\ \ln[\mathbf{V}] & n = 0 \end{cases}. \quad (2.60)$$

2.4 Forces and Stresses

Having established a mathematical description of the motion of a continuum body we now seek a similar framework in which to discuss the associated forces that act upon the body.

2.4.1 Distributed Forces

As previously discussed matter in continuum mechanics is considered to be distributed through space in a smooth continuous way. Likewise continuum theory also requires us to conceive of forces acting on the matter which are distributed rather than discrete in nature. Two types of such distributed forces may be distinguished: *surface tractions* and *body forces*.

Contact forces and surface tractions

Of fundamental importance in continuum mechanics is the concept of *contact forces*. These are forces acting on a continuum body which are applied at the boundary surface of the body and which arise from material on the exterior side of the bounding surface. The body in question may constitute the entire body under consideration in a given problem or a part of it.

The concept of contact forces has no place in an atomistic view of nature where forces are exchanged between particles at a distance. It is an idealisation of continuum physics to account for forces that are significant only over a range which is short in comparison to the scales of interest.

Once the notion of contact forces has been adopted it makes sense to consider the force per unit area acting on a given oriented surface. Figure 2.5 represents a general body occupying the region Ω_0 in its reference configuration mapped at some instance t by $\chi(t)$ to its deformed configuration occupying the spatial region Ω . In the deformed configuration, illustrated on the right hand side, the arbitrary closed surface \mathcal{S} lies within Ω and has outward normal \mathbf{n} at some spatial point \mathbf{x} . A neighbourhood of surface points around \mathbf{x} is shown with area δS . The net contact force applied over this surface element and acting on the matter within \mathcal{S} is denoted $\delta \mathbf{f}$. The *true* or *Cauchy traction*, \mathbf{t} is then defined as

$$\mathbf{t} = \lim_{\delta s \rightarrow 0} \frac{\delta \mathbf{f}}{\delta s} . \quad (2.61)$$

It is assumed that this limit exists for any oriented surface in the continuum body. The total contact force acting on a body is then found by integrating the Cauchy tractions over the boundary surface of its current configuration. A further assumption, known as Cauchy's postulate, is the statement that the traction at any given point on any oriented surface at any given instant depends only on the normal to the surface. That is to say that the traction on two or more surfaces which are parallel and coincident at some point is the same at that point regardless of their curvature. We may therefore write

$$\mathbf{t} = \mathbf{t}(\mathbf{x}, \mathbf{n}, t) . \quad (2.62)$$

It is also possible to define a traction field which refers to the reference configuration. If the surface element experiencing force $\delta \mathbf{f}$ originated from an undeformed surface element around material point \mathbf{X} with area δS and normal \mathbf{N} , as shown on the left of figure 2.5, then the first Piola-Kirchhoff traction is given by,

$$\mathbf{T}(\mathbf{X}, \mathbf{N}, t) = \lim_{\delta S \rightarrow 0} \frac{\delta \mathbf{f}}{\delta S} . \quad (2.63)$$

Body Forces

In addition to contact forces applied to their surfaces, bodies may also be subject to forces applied throughout their volumes. These so called *body forces* arise from remote influences outwith the body and do not include boundary tractions. If an element around spatial point \mathbf{x} with volume δv in the current configuration is subject to a force $\delta \mathbf{f}$ at time t then the body force at \mathbf{x} is defined as

$$\mathbf{b}(\mathbf{x}, t) = \lim_{\delta v \rightarrow 0} \frac{\delta \mathbf{f}}{\delta v} . \quad (2.64)$$

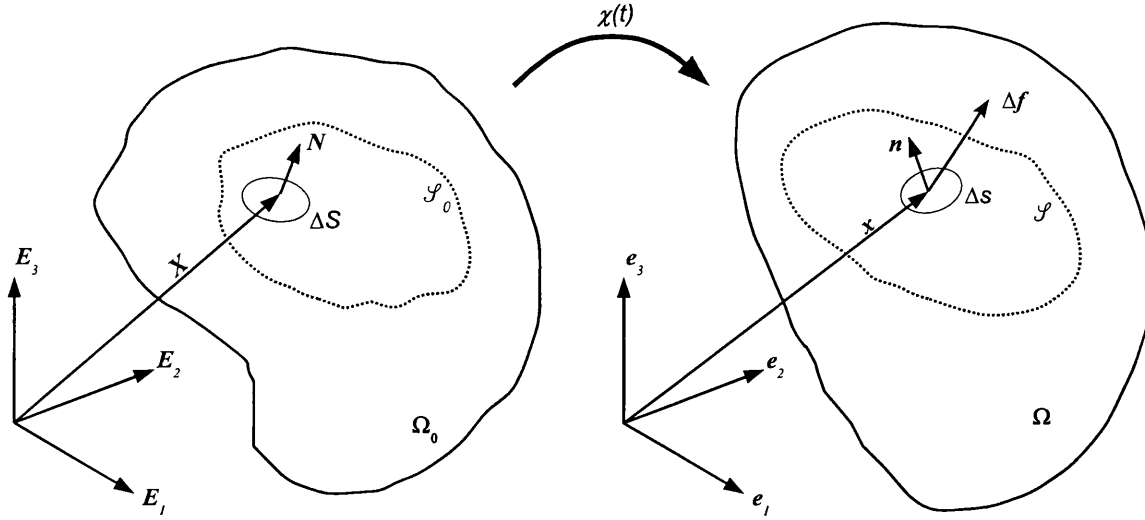


Figure 2.5: Traction on an infinitesimal surface element in the reference and deformed configurations.

More precisely equation (2.64) defines the body force with respect to current volume. It is also possible to define the body force with respect to reference volume from,

$$\mathbf{B}(\mathbf{X}, t) = \lim_{\delta V \rightarrow 0} \frac{\delta \mathbf{f}}{\delta V}, \quad (2.65)$$

where \mathbf{X} is the material point corresponding to \mathbf{x} and δV is the reference volume of the element with spatial volume δv . Some authors also refer to force per unit mass as body force. Note also that \mathbf{b} and \mathbf{B} have previously been used to denote the left Cauchy-Green and right Piola deformation tensors respectively but in future equations it should be clear from the context which usage is being followed.

Internal and External Forces

It is important in the solution of problems concerning the motion a continuum body to distinguish between *internal forces* and *external forces*.

Internal forces are the forces acting on elements of a body due to the effect of the rest of the body. These are the forces that hold a solid together and stop it collapsing in on itself. It is assumed that all such forces can be accounted for by internal surface tractions. This amounts to an assumption that internal forces are essentially local so that remote parts of a body do not act upon each other directly.

External forces are the forces acting on a body from all sources outwith the body. These may be body forces applied throughout the volume of the body or boundary

tractions applied to its bounding surface. A common example of the former is the gravitational attraction of a large external mass. A typical boundary traction is the pressure of a fluid acting on the inside of a solid cylinder. In this example the fluid or the cylinder might be the object of study. Thus what constitutes internal and external actions depends on the problem in question since this defines the continuum body to be studied.

2.4.2 The Cauchy Stress Tensor

It may be shown that the Cauchy traction, \mathbf{t} , depends linearly on the normal \mathbf{n} to the surface under consideration. The relationship is therefore characterised by a second order tensor, termed the *Cauchy* or *true stress tensor* and denoted by $\boldsymbol{\sigma}$. Hence we may write

$$\mathbf{t}(\mathbf{x}, \mathbf{n}, t) = \boldsymbol{\sigma}(\mathbf{x}, t)\mathbf{n}. \quad (2.66)$$

This crucial result is variously known as Cauchy's stress theorem or simply Cauchy's law. The proof, which may be found in many texts (e.g. the appendix to chapter 3 in [12]), is obtained by considering the balance of momentum of an infinitesimal volume element within the continuum.

2.4.3 The First Piola-Kirchhoff Stress Tensor

We now seek the material analogue to equation (2.66). That is an expression relating the first Piola-Kirchhoff traction, $\mathbf{T}(\mathbf{X}, \mathbf{N}, t)$, to the normal surface direction, \mathbf{N} , in the reference configuration.

From equations (2.61) and (2.63) it may be seen that the force $\delta\mathbf{f}$ acting on an infinitesimal surface element may be expressed either in terms of the deformed element area δs and the Cauchy traction \mathbf{t} or in terms of the undeformed area of the same element, δS and the first Piola-Kirchhoff traction \mathbf{T} . Thus we may write,

$$\delta\mathbf{f} = \delta s \mathbf{t}(\mathbf{x}(\mathbf{X}, t), \mathbf{n}, t) = \delta S \mathbf{T}(\mathbf{X}, \mathbf{N}, t).$$

Substituting for \mathbf{t} from equation (2.66) introduces the Cauchy stress and gives,

$$\delta s \boldsymbol{\sigma} \mathbf{n} = \delta S \mathbf{T}(\mathbf{N}), \quad (2.67)$$

where for clarity we drop the explicit dependence on position and time. Recalling equation (2.32) (Nanson's formula) we may relate the deformed and undeformed

elemental areas via the deformation gradient, \mathbf{F} , thus,

$$\delta s \mathbf{n} = J \mathbf{F}^{-T} \delta S \mathbf{N} .$$

Substituting for $\delta s \mathbf{n}$ in the right hand side of equation (2.67) and cancelling the common factor δS gives,

$$\mathbf{T}(\mathbf{N}) = (J \boldsymbol{\sigma} \mathbf{F}^{-T}) \mathbf{N} .$$

Thus just as the Cauchy traction is linearly dependent on the spatial normal so the first Piola-Kirchhoff has a linear dependence on the Lagrangian normal. The first Piola-Kirchhoff stress tensor is defined as,

$$\mathbf{P} = J \boldsymbol{\sigma} \mathbf{F}^{-T} , \quad (2.68)$$

so that we may write,

$$\mathbf{T}(\mathbf{X}, \mathbf{N}, t) = \mathbf{P}(\mathbf{X}, t) \mathbf{N} . \quad (2.69)$$

2.4.4 Other Stress Tensors

A variety of other stress tensors may be defined in terms of the Cauchy stress. Two of the more commonly encountered examples follow.

The Second Piola-Kirchhoff Stress Tensor

$$\mathbf{S} = J \mathbf{F}^{-1} \boldsymbol{\sigma} \mathbf{F}^{-T} \quad (2.70)$$

The Kirchhoff Stress Tensor

$$\boldsymbol{\tau} = J \boldsymbol{\sigma} \quad (2.71)$$

2.5 Conservation Principles

We now seek to formulate some of the fundamental physical laws governing the *mechanical* behaviour of continua. Note that thermodynamic principles will not be addressed.

2.5.1 Conservation of Mass

The *Lagrangian* or *reference mass density* at material point \mathbf{X} is defined as,

$$\rho_0(\mathbf{X}) = \lim_{\delta V \rightarrow 0} \frac{\delta M}{\delta V} , \quad (2.72)$$

where δM is the mass contained within the infinitesimal material volume element δV around \mathbf{X} .

If at some time t , the reference volume element has deformed into a spatial element with volume v at the point $\mathbf{x} = \chi(\mathbf{X}, t)$ then the *Eulerian* or *current mass density* is defined by

$$\rho(\mathbf{x}, t) = \lim_{\delta v \rightarrow 0} \frac{\delta m}{\delta v} , \quad (2.73)$$

where δm is the mass contained within δv .

Now since the spatial volume element δv represents the volume occupied by the same matter originally contained within δV in the reference configuration it follows that if mass is conserved then

$$\delta m = \delta M .$$

Recalling equation (2.26) we may also relate current and deformed volume elements via the Jacobian, $J = \det F$, thus

$$\delta v = J \delta V ,$$

so that the Eulerian density may be written,

$$\rho(\mathbf{x}, t) = \lim_{\delta V \rightarrow 0} \frac{\delta M}{J \delta V} .$$

Hence Eulerian and Lagrangian densities are related by,

$$\rho_0 = J \rho . \quad (2.74)$$

where of course ρ_0 , ρ and J are evaluated at corresponding material and spatial points. This equation expresses the principle of mass conservation for a continuum.

An equivalent statement of mass conservation may be obtained in terms of the Eulerian density and velocity fields alone without explicit reference to the reference density. Consider firstly that the Lagrangian density is independent of time so that its material time derivative vanishes. In view of equation (2.74) this means that

$$\begin{aligned} \frac{D(J\rho)}{Dt} &= 0 \\ \Leftrightarrow \dot{J}\rho + J\dot{\rho} &= 0 . \end{aligned} \quad (2.75)$$

Now the material time derivative of J is given by equation (2.29) as

$$\dot{J} = J \nabla \cdot \mathbf{v} ,$$

where \mathbf{I} is the second order identity tensor and \mathbf{v} the velocity field. Thus equation (2.75) becomes,

$$\rho J \nabla \cdot \mathbf{v} + J \dot{\rho} = 0 .$$

The second term on the left of equation (2.5.1) may be expanded using expression (2.9) for the material time derivative of a spatial field so that,

$$\begin{aligned} \rho J \nabla \cdot \mathbf{v} + J \left(\frac{\partial \rho}{\partial t} + \nabla \rho \cdot \mathbf{v} \right) &= 0 \\ \Leftrightarrow \frac{\partial \rho}{\partial t} + \rho \nabla \cdot \mathbf{v} + \nabla \rho \cdot \mathbf{v} &= 0 . \end{aligned}$$

Finally using the chain rule the last two terms on the left hand side may be consolidated to give,

$$\frac{\partial \rho}{\partial t} + \nabla \cdot (\rho \mathbf{v}) = 0 . \quad (2.76)$$

Equation (2.76), sometimes known as the continuity equation, represents an expression of the principle of mass conservation in wholly spatial terms.

2.5.2 Balance of Linear Momentum

In classical mechanics the motion of a particle is governed by Newton's second law which equates the rate of change of the particle's momentum to the force acting upon it. This principle may be generalised to continuum mechanics by considering the total linear momentum of a continuum body,

$$\mathbf{L}(t) = \int_{\Omega} \rho \mathbf{v} dv \quad (2.77)$$

and the sum of the all forces acting on the body, $\mathbf{f}(t)$. We require every constituent particle of the body to obey Newton's second law, so in the aggregate we have,

$$\dot{\mathbf{L}}(t) = \mathbf{f}(t) . \quad (2.78)$$

Now the body will be subject to internal and external forces. However if Newton's third law holds, stating that forces between particles are equal and opposite, then internal forces will cancel each other out in the sum over the body. In this case the

total force on the body equals the sum of all external forces which may be external surface tractions, $\mathbf{t}(\mathbf{x}, t)$ or body forces $\mathbf{b}(\mathbf{x}, t)$. Thus we have

$$\mathbf{f} = \mathbf{f}^{external} = \int_{\partial\Omega} \mathbf{t} dv + \int_{\Omega} \mathbf{b} dv.$$

Assuming that the traction may be derived from a stress tensor field $\boldsymbol{\sigma}$ and applying the divergence theorem we obtain,

$$\mathbf{f} = \int_{\Omega} (\text{div} \boldsymbol{\sigma} + \mathbf{b}) dv. \quad (2.79)$$

Returning to consider the left hand side of equation (2.78), it is convenient to obtain the Lagrangian representation of the total momentum integral. Recalling (2.26) and (2.74), $dv = JdV$ and $\rho_0 = J\rho$, it follows that

$$\rho dv = \rho_0 dV, \quad (2.80)$$

so that equation (2.77) becomes

$$\mathbf{L} = \int_{\Omega_0} \rho_0 \mathbf{v} dV. \quad (2.81)$$

Since Ω_0 and ρ_0 are both independent of time we may readily differentiate to obtain

$$\dot{\mathbf{L}} = \int_{\Omega_0} \rho_0 \dot{\mathbf{v}} dV. \quad (2.82)$$

Using (2.80) again, this may be expressed in the spatial description as

$$\dot{\mathbf{L}} = \int_{\Omega} \rho \dot{\mathbf{v}} dv. \quad (2.83)$$

With equations (2.79) and (2.83) at hand, the linear balance equation (2.78) may be rewritten as

$$\int_{\Omega} (\text{div} \boldsymbol{\sigma} + \mathbf{b} - \rho \dot{\mathbf{v}}) dv = 0. \quad (2.84)$$

This equality holds for any domain of integration. It follows that the integrand must be zero everywhere and we finally obtain *Cauchy's first equation of motion*,

$$\text{div} \boldsymbol{\sigma} + \mathbf{b} - \rho \dot{\mathbf{v}} = 0. \quad (2.85)$$

It can be shown that the equivalent expression of (2.85) in the material description is given by

$$\text{Div} \mathbf{P} + \mathbf{B} - \rho \dot{\mathbf{V}} dV = 0, \quad (2.86)$$

where Div indicates the material divergence (the divergence with respect to reference coordinates), \mathbf{B} is the body force per unit undeformed volume and \mathbf{V} is simply the velocity expressed as a function of reference position.

2.5.3 Balance of Angular Momentum

The total angular momentum of a body is given in the spatial formulation by

$$\mathbf{J} = \int_{\Omega} (\mathbf{x} \times \rho \mathbf{v}) dv ,$$

and equivalently in terms of integration in the material domain by

$$\mathbf{J} = \int_{\Omega_0} (\mathbf{x} \times \rho_0 \mathbf{v}) dV ,$$

where as before (2.80) has been used to switch between spatial and material formulations. In the latter form we may readily differentiate with respect to time to obtain the rate of change as,

$$\begin{aligned} \dot{\mathbf{J}} &= \int_{\Omega_0} (\dot{\mathbf{x}} \times \rho_0 \mathbf{v} + \mathbf{x} \times \rho_0 \dot{\mathbf{v}}) dV \\ &= \int_{\Omega_0} (\mathbf{x} \times \rho_0 \dot{\mathbf{v}}) dV . \end{aligned}$$

Using (2.80) again the spatial equivalent is obtained as:

$$\dot{\mathbf{J}} = \int_{\Omega} (\mathbf{x} \times \rho \dot{\mathbf{v}}) dv .$$

Invoking linear momentum balance for each integral element we may say that $\rho \dot{\mathbf{v}} dv = \mathbf{f}(\mathbf{x}) dv$ where $\mathbf{f}(\mathbf{x}) dv$ is the net force acting on element dv at spatial position \mathbf{x} . This force will be made up of internal and external contributions. However if it is assumed that internal forces between particles are not only equal and opposite but also directed along the line joining interacting particles² then the moments of these forces will cancel out in the integral. In this case we need only consider external forces which may be surface tractions \mathbf{t} or body forces \mathbf{b} . The balance of angular momentum for the body may thus be expressed as

$$\int_{\Omega} (\mathbf{x} \times \rho \dot{\mathbf{v}}) dv = \int_{\partial\Omega} (\mathbf{x} \times \mathbf{t}) da + \int_{\Omega} (\mathbf{x} \times \mathbf{b}) dv .$$

Assuming that the traction may be derived from a stress field $\boldsymbol{\sigma}$ this becomes

$$\int_{\Omega} (\mathbf{x} \times \rho \dot{\mathbf{v}}) dv = \int_{\partial\Omega} (\mathbf{x} \times \boldsymbol{\sigma} \mathbf{n}) da + \int_{\Omega} (\mathbf{x} \times \mathbf{b}) dv ,$$

²This condition is sometimes referred to as the *strong law of action and reaction* in distinction to the *weak law of action and reaction* whereby forces are equal and opposite but not necessarily central [38]. Such forces do exist but will not be considered here.

where \mathbf{n} is unit normal to the boundary surface $\partial\Omega$. Applying the divergence theorem to the first term on the right hand side leads to

$$\int_{\Omega} (\mathbf{x} \times \rho \dot{\mathbf{v}}) dv = \int_{\Omega} (\mathbf{x} \times \operatorname{div} \boldsymbol{\sigma} - \boldsymbol{\varepsilon} : \boldsymbol{\sigma}) dv + \int_{\Omega} (\mathbf{x} \times \mathbf{b}) dv ,$$

where we have introduced the permutation tensor defined by $\boldsymbol{\varepsilon} = \varepsilon_{ijk} \mathbf{e}_i \otimes \mathbf{e}_j \otimes \mathbf{e}_k$.

Rearranging yields

$$\int_{\Omega} \boldsymbol{\varepsilon} : \boldsymbol{\sigma} dv = \int_{\Omega} \mathbf{x} \times (\operatorname{div} \boldsymbol{\sigma} + \mathbf{b} - \rho \dot{\mathbf{v}}) dv . \quad (2.87)$$

In view of the Cauchy's first equation of motion (2.85) the right hand side above must vanish and since (2.87) holds for any domain Ω it follows that

$$\boldsymbol{\varepsilon} : \boldsymbol{\sigma} = 0 .$$

It may easily be verified that this holds if and only if $\boldsymbol{\sigma}$ is symmetric and so we finally may write

$$\boldsymbol{\sigma}^T = \boldsymbol{\sigma} . \quad (2.88)$$

This important equation expresses the conservation of angular momentum and is known as *Cauchy's second equation of motion*.

2.5.4 Balance of mechanical energy

It follows from the balance of momentum laws that the rate of work done by external forces on a body must equal the rate of work done by the internal forces plus the rate of change of the total kinetic energy of the body. To see how this comes about consider firstly the rate of work done by tractions on the boundary surface. Over an infinitesimal deformed surface element δs the rate of work done by traction \mathbf{t} will be $(\mathbf{t} \delta s) \cdot \mathbf{v}$. Thus the total power of the external surface tractions is $\int_{\partial\Omega} \mathbf{t} \cdot \mathbf{v} ds$. Expressing the traction in terms of the Cauchy stress and surface normal, $\mathbf{t} = \boldsymbol{\sigma} \mathbf{n}$, and using the divergence theorem we may rewrite this power term as

$$\int_{\partial\Omega} \mathbf{t} \cdot \mathbf{v} ds = \int_{\Omega} (\operatorname{div} \boldsymbol{\sigma} \cdot \mathbf{v} + \boldsymbol{\sigma} : \nabla \mathbf{v}) dv .$$

Now from Cauchy's first equation of motion (2.85) we may subtract the vanishing term $(\operatorname{div} \boldsymbol{\sigma} + \mathbf{b} - \rho \dot{\mathbf{v}}) \cdot \mathbf{v}$ to the integrand above without changing the result to obtain

$$\begin{aligned} \int_{\partial\Omega} \mathbf{t} \cdot \mathbf{v} ds &= \int_{\Omega} \{ \operatorname{div} \boldsymbol{\sigma} \cdot \mathbf{v} + \boldsymbol{\sigma} : \nabla \mathbf{v} - (\operatorname{div} \boldsymbol{\sigma} + \mathbf{b} - \rho \dot{\mathbf{v}}) \cdot \mathbf{v} \} dv \\ &= \int_{\Omega} \{ \boldsymbol{\sigma} : \mathbf{l} - \mathbf{b} \cdot \mathbf{v} + \rho \dot{\mathbf{v}} \cdot \mathbf{v} \} dv , \end{aligned}$$

where in the last step we have introduced the spatial velocity gradient \mathbf{l} which by definition (2.15) equals $\nabla \mathbf{v}$. Since $\boldsymbol{\sigma}$ is symmetric by Cauchy's second equation of motion (2.88) we can replace \mathbf{l} by its symmetric part, the rate of deformation tensor \mathbf{d} . Noting also that $\dot{\mathbf{v}} \cdot \mathbf{v} = \frac{D}{Dt}(\frac{1}{2}\mathbf{v} \cdot \mathbf{v})$ we may rearrange the last equation to obtain

$$\int_{\partial\Omega} \mathbf{t} \cdot \mathbf{v} ds + \int_{\Omega} \mathbf{b} \cdot \mathbf{v} dv = \int_{\Omega} \boldsymbol{\sigma} : \mathbf{d} dv + \int_{\Omega} \rho \frac{D}{Dt}(\frac{1}{2}\mathbf{v} \cdot \mathbf{v}) dv .$$

By use of (2.26) and (2.74) we take the material time derivative outside the integral so that

$$\int_{\partial\Omega} \mathbf{t} \cdot \mathbf{v} ds + \int_{\Omega} \mathbf{b} \cdot \mathbf{v} dv = \int_{\Omega} \boldsymbol{\sigma} : \mathbf{d} dv + \frac{D}{Dt} \left(\int_{\Omega} \rho \frac{1}{2} \mathbf{v} \cdot \mathbf{v} \right) dv . \quad (2.89)$$

This equation represents the balance of mechanical energy. The left hand side represents the rate of work done by external forces (surface tractions and body forces). The second term on the right is the rate of change of the total kinetic energy within Ω . This leaves the first term on the right $\int_{\Omega} \boldsymbol{\sigma} : \mathbf{d} dv$ which we identify as the rate of work done by internal forces or total stress power. It may be shown that the stress power has equivalent representation in terms of the first Piola-Kirchhoff stress as

$$\int_{\Omega} \boldsymbol{\sigma} : \mathbf{d} dv = \int_{\Omega_0} \mathbf{P} : \mathbf{F} dV . \quad (2.90)$$

In view of (2.90) $\boldsymbol{\sigma}$ and \mathbf{P} are said to be work conjugate to \mathbf{d} and \mathbf{F} respectively.

2.5.5 Principle of Virtual Work

The statement of linear momentum balance provided by equation (2.85) is expressed in the so called strong form. It relates local values of the field variables and their derivatives in a point wise fashion. Conservation of momentum can also be expressed in a wholly equivalent weak formulation in terms of a global functional of the relevant fields. The weak form of momentum conservation provides the basis of most finite element method solutions to problems in solid mechanics.

Virtual Work in the Spatial Description

We begin by invoking an arbitrary spatial vector field, $\boldsymbol{\eta}(\mathbf{x})$, with the dimensions of distance. These *virtual displacements*, as they are known, are purely notional and are independent of time. Taking the dot product of equation (2.85) with $\boldsymbol{\eta}$ and integrating over the volume domain, Ω , of the body gives:

$$\int_{\Omega} (\text{div} \boldsymbol{\sigma} + \mathbf{b} - \rho \dot{\mathbf{v}}) \cdot \boldsymbol{\eta} dv = 0 \quad \text{for arbitrary } \boldsymbol{\eta}. \quad (2.91)$$

Equation (2.85) clearly implies equation (2.91) as it states that $(\text{div} \boldsymbol{\sigma} + \mathbf{b} - \rho \dot{\mathbf{v}})$ vanishes everywhere. Conversely equation (2.91) can only hold for every $\boldsymbol{\eta}$ if the term in brackets is identically zero, so that (2.91) implies equation (2.85).

Rearranging gives:

$$\int_{\Omega} [\text{div} \boldsymbol{\sigma} \cdot \boldsymbol{\eta} + (\mathbf{b} - \rho \dot{\mathbf{v}}) \cdot \boldsymbol{\eta}] dv = 0 \quad \text{for arbitrary } \boldsymbol{\eta}. \quad (2.92)$$

Considering the first term of the integrand, we have:

$$\begin{aligned} \text{div} \boldsymbol{\sigma} \cdot \boldsymbol{\eta} &= \frac{\partial \sigma_{ij}}{\partial x_j} \eta_i \\ &= \frac{\partial}{\partial x_j} (\sigma_{ij} \eta_i) - \sigma_{ij} \frac{\partial \eta_i}{\partial x_j} \\ &= \text{div}(\boldsymbol{\sigma} \boldsymbol{\eta}) - \boldsymbol{\sigma} : \nabla \boldsymbol{\eta}. \end{aligned}$$

Substituting into equation (2.92) gives:

$$\int_{\Omega} [\text{div}(\boldsymbol{\sigma} \boldsymbol{\eta}) - \boldsymbol{\sigma} : \nabla \boldsymbol{\eta} + (\mathbf{b} - \rho \dot{\mathbf{v}}) \cdot \boldsymbol{\eta}] dv = 0 \quad \text{for arbitrary } \boldsymbol{\eta}.$$

Application of the divergence theorem to the first term of the integrand yields:

$$\int_{\partial \Omega} (\boldsymbol{\sigma} \boldsymbol{\eta}) \cdot \mathbf{n} ds - \int_{\Omega} [\boldsymbol{\sigma} : \nabla \boldsymbol{\eta} - (\mathbf{b} - \rho \dot{\mathbf{v}}) \cdot \boldsymbol{\eta}] dv = 0 \quad \text{for arbitrary } \boldsymbol{\eta}. \quad (2.93)$$

The first integrand may be rewritten thus:

$$\begin{aligned} (\boldsymbol{\sigma} \boldsymbol{\eta}) \cdot \mathbf{n} &= \sigma_{ij} \eta_j n_i \\ &= \sigma_{ji} n_i \eta_j \quad \text{since } \boldsymbol{\sigma} \text{ is symmetric} \\ &= (\boldsymbol{\sigma} \mathbf{n}) \cdot \boldsymbol{\eta}, \end{aligned}$$

so that equation (2.93) becomes:

$$\int_{\partial \Omega} (\boldsymbol{\sigma} \mathbf{n}) \cdot \boldsymbol{\eta} ds - \int_{\Omega} [\boldsymbol{\sigma} : \nabla \boldsymbol{\eta} - (\mathbf{b} - \rho \dot{\mathbf{v}}) \cdot \boldsymbol{\eta}] dv = 0 \quad \text{for arbitrary } \boldsymbol{\eta}. \quad (2.94)$$

On the boundary $\boldsymbol{\sigma} \mathbf{n} = \mathbf{t}$, where \mathbf{t} is the applied boundary traction. Thus we obtain the *virtual work equation in the spatial description*:

$$\int_{\partial \Omega} \mathbf{t} \cdot \boldsymbol{\eta} ds - \int_{\Omega} [\boldsymbol{\sigma} : \nabla \boldsymbol{\eta} - (\mathbf{b} - \rho \dot{\mathbf{v}}) \cdot \boldsymbol{\eta}] dv = 0 \quad \text{for arbitrary } \boldsymbol{\eta}. \quad (2.95)$$

If $\dot{\mathbf{v}} = 0$ everywhere the body is in static equilibrium and equation (2.95) simplifies to:

$$\int_{\partial \Omega} \mathbf{t} \cdot \boldsymbol{\eta} ds - \int_{\Omega} [\boldsymbol{\sigma} : \nabla \boldsymbol{\eta} - \mathbf{b} \cdot \boldsymbol{\eta}] dv = 0 \quad \text{for arbitrary } \boldsymbol{\eta}, \quad (2.96)$$

Virtual Work in the Material Description

The principle of virtual work may also be expressed in terms of material quantities. Firstly we introduce the body force per unit reference volume, $\mathbf{B} = J\mathbf{b}$, the surface traction per unit reference area, $\mathbf{T} = \frac{ds}{dS}\mathbf{t}$ (the first Piola-Kirchhoff traction), and the material density, $\rho_0 = J\rho$, so that using relation (2.26) equation (2.95) becomes:

$$\int_{\partial\Omega_0} \mathbf{T} \cdot \boldsymbol{\eta} dS - \int_{\Omega_0} [J\boldsymbol{\sigma} : \nabla \boldsymbol{\eta} - (\mathbf{B} - \rho_0 \dot{\mathbf{V}}) \cdot \boldsymbol{\eta}] dV = 0 \quad \text{for arbitrary } \boldsymbol{\eta}, \quad (2.97)$$

where $\mathbf{V}(\mathbf{X}) = \mathbf{v}(\mathbf{x})$. Considering the integrand of the second term in isolation:

$$\begin{aligned} J\boldsymbol{\sigma} : \nabla \boldsymbol{\eta} &= J\sigma_{ij} \frac{\partial \eta_i}{\partial x_j} \\ &= J\sigma_{ij} \frac{\partial \eta_i}{\partial X_k} \frac{\partial X_k}{\partial x_j} \\ &= J\boldsymbol{\sigma} \mathbf{F}^{-T} : \nabla_0 \boldsymbol{\eta}. \end{aligned}$$

Recalling equation (2.68), $\mathbf{P} = J\boldsymbol{\sigma} \mathbf{F}^{-T}$, we obtain:

$$J\boldsymbol{\sigma} : \nabla \boldsymbol{\eta} = \mathbf{P} : \nabla_0 \boldsymbol{\eta}, \quad (2.98)$$

so that equation (2.97) becomes:

$$\int_{\partial\Omega_0} \mathbf{T} \cdot \boldsymbol{\eta} dS - \int_{\Omega_0} [\mathbf{P} : \nabla_0 \boldsymbol{\eta} - (\mathbf{B} - \rho_0 \dot{\mathbf{V}}) \cdot \boldsymbol{\eta}] dV = 0 \quad \text{for arbitrary } \boldsymbol{\eta}, \quad (2.99)$$

which expresses the *principle of virtual work in the material form*.

In the case of static equilibrium, $\dot{\mathbf{V}} = 0$, equation (2.99) simplifies to:

$$\int_{\partial\Omega_0} \mathbf{T} \cdot \boldsymbol{\eta} ds - \int_{\Omega_0} [\mathbf{P} : \nabla_0 \boldsymbol{\eta} - \mathbf{B} \cdot \boldsymbol{\eta}] dV = 0 \quad \text{for arbitrary } \boldsymbol{\eta}. \quad (2.100)$$

2.6 Constitutive Laws

In previous sections principles governing the motion of continua have been expounded without making any distinction between different types of material. Experience shows that two bodies differing only in their material composition will deform differently under the same system of external forces. This is due to differing relationships between stress and deformation. The role of constitutive theory is to formulate material specific laws which model these relationships. Moreover the problem of solving the equations of motion is not well posed without specifying a constitutive relationship.

In this section three principles which inform the formulation of constitutive laws (following [119] for instance) are set out. We shall treat these as axiomatic³. Following this we consider some special classes of constitutive models. Finally a small selection of specific material models are described.

2.6.1 Fundamental principles of constitutive theory

Determinism

At any given time the stress at a point in a body is determined by the history of the motion of the body up to that instant. In terms of the Cauchy stress this means we can write

$$\boldsymbol{\sigma}(\mathbf{X}, t) = \boldsymbol{\varsigma}(\boldsymbol{\chi}^t; \mathbf{X}, t) , \quad (2.101)$$

where $\boldsymbol{\varsigma}$ is a functional of the history of the motion, $\boldsymbol{\chi}^t$ as well as a function of material position \mathbf{X} and time t . Formally $\boldsymbol{\chi}^t$ represents the restriction of the motion function $\boldsymbol{\chi}(\mathbf{X}, \tau)$ to the range $-\infty < \tau \leq t$. In other words only the *past* experience of a body influences its stress response. Note that here $\boldsymbol{\chi}^t$ indicates the history of the motion of the whole body not just the trajectory of the particle at \mathbf{X} .

Equivalently in terms of the first Piola-Kirchhoff stress we write

$$\mathbf{P}(\mathbf{X}, t) = \mathfrak{P}(\boldsymbol{\chi}^t; \mathbf{X}, t) . \quad (2.102)$$

Localism

The principle of local action states that the stress at material point \mathbf{X} depends only on the motion within a small neighbourhood of \mathbf{X} . The motion of distant particles is thus assumed to have no influence. This rules out considering long range forces such as gravity being considered as internal forces. If two motion histories $\boldsymbol{\chi}^t$ and $\bar{\boldsymbol{\chi}}^t$ are identical within an arbitrarily small neighbourhood $\mathcal{N}(\mathbf{X})$ of \mathbf{X} then the stress at \mathbf{X} must be the same no matter how $\boldsymbol{\chi}^t$ and $\bar{\boldsymbol{\chi}}^t$ differ outside $\mathcal{N}(\mathbf{X})$. This may be expressed formally as:

$$\begin{aligned} [\boldsymbol{\chi}(\mathbf{X}', \tau) = \bar{\boldsymbol{\chi}}(\mathbf{X}', \tau) \quad \forall \mathbf{X}' \in \mathcal{N}(\mathbf{X}), \tau \leq t] \\ \Rightarrow [\mathfrak{P}(\boldsymbol{\chi}^t; \mathbf{X}, t) = \mathfrak{P}(\bar{\boldsymbol{\chi}}^t; \mathbf{X}, t)] . \end{aligned} \quad (2.103)$$

³The fundamental nature of the principles of localism and material frame invariance have been questioned in the literature. For instance Ryskin [98] rejects the strict validity of frame indifference pointing to the violation of Newton's laws in non inertial frames of reference. However for the purposes of the present work the principles assumed in this section are at least close enough approximations if not fundamental truths of nature.

Material Objectivity

In loose terms the *principle of material frame indifference* or *material objectivity* requires that constitutive laws are the same for all observers of a body undergoing deformation. A more precise account of the principle requires us to consider the way in which measurements in different frames of reference relate to each other.

We begin by introducing the notion of a *Euclidean transformation*. This relates the spatial position, \mathbf{x} , and time t , measured by observer, \mathcal{O} , to the spatial position, $\bar{\mathbf{x}}$, and time, \bar{t} , measured by a second observer, $\bar{\mathcal{O}}$, according the following equations:

$$\bar{\mathbf{x}}(\mathbf{X}, t) = \mathbf{c}(t) + \mathbf{Q}(t)\mathbf{x}(\mathbf{X}, t) \quad ; \quad \bar{t} = t + \tau, \quad (2.104)$$

where $\mathbf{Q}(t)$ is an orthogonal second rank tensor (representing a rotation) and $\mathbf{c}(t)$ is the displacement of the $\bar{\mathcal{O}}$'s origin relative to \mathcal{O} 's.

It may be easily shown that any displacement $\mathbf{u} = \mathbf{y} - \mathbf{x}$, where \mathbf{y} and \mathbf{x} are positions, transforms according to:

$$\bar{\mathbf{u}} = \bar{\mathbf{y}} - \bar{\mathbf{x}} = \mathbf{Q}(t)\mathbf{u}. \quad (2.105)$$

Any spatial vector field which transforms in this way between observers is termed an *objective vector field*.

The distance between \mathbf{x} and \mathbf{y} , $\sqrt{\mathbf{u} \cdot \mathbf{u}}$, has the same value in both frames. i.e.

$$\bar{\mathbf{u}} \cdot \bar{\mathbf{u}} = \mathbf{Q}(t)\mathbf{u} \cdot \mathbf{Q}(t)\mathbf{u} = \mathbf{Q}(t)\mathbf{Q}(t)^T \mathbf{u} \cdot \mathbf{u} = \mathbf{u} \cdot \mathbf{u}. \quad (2.106)$$

A scalar variable which, like distance, remains the same in every Euclidian frame of reference is known as an *objective scalar field*.

Consider next the spatial gradient of an objective vector field, \mathbf{v} , given by observer \mathcal{O} as:

$$\nabla \mathbf{v} = \frac{\partial \mathbf{v}}{\partial \mathbf{x}}.$$

Observer $\bar{\mathcal{O}}$ will measure the gradient of the same field as:

$$\bar{\nabla} \bar{\mathbf{v}} = \frac{\partial \bar{\mathbf{v}}}{\partial \bar{\mathbf{x}}} = \frac{\partial \bar{\mathbf{v}}}{\partial \mathbf{x}} \frac{\partial \mathbf{x}}{\partial \bar{\mathbf{x}}}.$$

Since \mathbf{v} is objective, $\bar{\mathbf{v}} = \mathbf{Q}(t)\mathbf{v}$, so that $\frac{\partial \bar{\mathbf{v}}}{\partial \mathbf{x}} = \mathbf{Q}(t)\frac{\partial \mathbf{v}}{\partial \mathbf{x}}$. It follows from equation (2.104) that $\frac{\partial \mathbf{x}}{\partial \bar{\mathbf{x}}} = \mathbf{Q}^T$. Thus the gradient transforms according to:

$$\bar{\nabla} \bar{\mathbf{v}} = \mathbf{Q}(\nabla \mathbf{v}) \mathbf{Q}^T. \quad (2.107)$$

A spatial second rank tensor which transforms in this way is known as an *objective tensor field*. For instance it can be shown that Cauchy stress is objective so that:

$$\bar{\sigma} = Q\sigma Q^T. \quad (2.108)$$

In general a spatial tensor field of rank n , $\mathbf{u}_1 \otimes \mathbf{u}_2 \otimes \cdots \otimes \mathbf{u}_n$ is called an *objective tensor field* if under a Euclidean transformation it changes according to the following rule:

$$\overline{(\mathbf{u}_1 \otimes \mathbf{u}_2 \otimes \cdots \otimes \mathbf{u}_n)} = Q\mathbf{u}_1 \otimes Q\mathbf{u}_2 \otimes \cdots \otimes Q\mathbf{u}_n. \quad (2.109)$$

Equations (2.105), and (2.107) are special cases of this.

The first Piola-Kirchhoff stress tensor field is also considered to be objective but as a two point tensor it may be shown to transform according to

$$\bar{P} = QP. \quad (2.110)$$

The displacement gradient is also an objective two point tensor and transforms in the following way:

$$\bar{F} = \frac{\partial \bar{x}}{\partial \bar{X}} = \frac{\partial}{\partial X}(c + Qx) = QF. \quad (2.111)$$

We now state the *principle of material objectivity* in the following terms:

If a motion $\mathbf{x} = \varphi(\mathbf{X}, t)$ and associated stress field σ as measured in one frame of reference satisfies a valid constitutive equation then the transformed motion and stress $(\bar{\varphi}, \bar{\sigma})$ measured by another Euclidean observer must also satisfy the same equation.

In terms of the constitutive Cauchy stress functional \mathfrak{s} we may say that if the constitutive equation

$$\sigma(\mathbf{X}, t) = \mathfrak{s}(\chi^t; \mathbf{X}, t), \quad (2.112)$$

holds for the frame of reference of observer \mathcal{O} then it follows that the same functional \mathfrak{s} is valid for any other observer $\bar{\mathcal{O}}$ so that

$$\bar{\sigma}(\mathbf{X}, t) = \mathfrak{s}(\bar{\chi}^t; \mathbf{X}, t), \quad (2.113)$$

where $\bar{\chi}^t$ is the history of the motion observed by $\bar{\mathcal{O}}$ (i.e. χ^t subjected to the Euclidean transformation (2.104)). In view of (2.108) we may write

$$Q\mathfrak{s}(\chi^t; \mathbf{X}, t)Q^T = \mathfrak{s}(\bar{\chi}^t; \mathbf{X}, t). \quad (2.114)$$

Equivalently in terms of the first Piola-Kirchhoff stress the objectivity condition becomes

$$\mathbf{Q}\mathfrak{P}(\chi^t; \mathbf{X}, t) = \mathfrak{P}(\bar{\chi}^t; \mathbf{X}, t) . \quad (2.115)$$

Any constitutive law which does not satisfy this condition is frame dependent and must be considered invalid.

2.6.2 Special classes of constitutive law

Simple Materials

A material whose stress response to all deformation histories may be inferred from its response to all homogeneous deformation histories is termed a *simple material*. We mean by a homogeneous deformation history one in which the deformation gradient at any given time is uniform throughout the body. It follows that the stress response at some material point depends only on the history of the deformation at that point. In other words the constitutive equation for a simple material takes the form

$$\boldsymbol{\sigma}(\mathbf{X}, t) = \mathfrak{s}(\mathbf{F}^t(\mathbf{X}); \mathbf{X}, t) , \quad (2.116)$$

where $\mathbf{F}^t(\mathbf{X})$ is the history of the deformation gradient experienced at material point \mathbf{X} . Note that since the gradient \mathbf{F} is defined with respect to a reference configuration the functional \mathfrak{s} depends on the choice of this reference configuration.

The constitutive relation (2.116) clearly satisfies the principles of determinism and locality automatically. The principle of material objectivity requires that

$$\mathbf{Q}\mathfrak{s}(\mathbf{F}^t)\mathbf{Q}^T = \mathfrak{s}(\mathbf{Q}\mathbf{F}^t) , \quad (2.117)$$

holds for all rotations \mathbf{Q} and all \mathbf{F} where the dependencies on \mathbf{X} and t are now understood. Applying the right polar decomposition (2.33) to the deformation history on the right hand side we obtain

$$\mathbf{Q}\mathfrak{s}(\mathbf{F}^t)\mathbf{Q}^T = \mathfrak{s}(\mathbf{Q}\mathbf{R}^t\mathbf{U}^t) . \quad (2.118)$$

Since \mathbf{R} is always proper orthogonal this must hold for $\mathbf{Q}(t) = (\mathbf{R}^t)^T$ and so after rearranging we obtain

$$\mathfrak{s}(\mathbf{F}^t) = \mathbf{R}^t \mathfrak{s}(\mathbf{U}^t)(\mathbf{R}^t)^T . \quad (2.119)$$

Materials with internal variables

The dependence of the stress on the entire history of the motion is the most general form of constitutive relation but in practice too complicated to deal with in solving real problems. This difficulty is avoided in material models which employ *internal variables*. The stress response for such models depends only on the *current* state of the body as characterised by the current configuration and instantaneous values of a finite number of internal variables. These internal variables evolve in time according to rules prescribed for the model. They can be thought of as encapsulating the essential features of the deformation history which influence the present behaviour.

The stress dependence for a simple material with a set of internal variables α may be written

$$\sigma = \mathfrak{s}(\mathbf{F}(\mathbf{X}, t), \mathbf{X}, t, \alpha) . \quad (2.120)$$

Cauchy elastic materials

A simple material whose stress response at any point depends only on the current deformation gradient at that point is known as a *Cauchy elastic material*. The path of the motion experienced by a body of such material in deforming from the reference to the current configurations is immaterial. The general constitutive relation for a Cauchy elastic material takes the form

$$\sigma = \mathfrak{s}(\mathbf{F}(\mathbf{X}, t), \mathbf{X}) . \quad (2.121)$$

Note that the function \mathfrak{s} does not depend explicitly on t since the stress response is path independent and therefore cannot depend on the time taken to reach the current configuration.

Hyperelasticity

An important subset of the elastic materials is made up by so called *hyperelastic materials*. These are defined by the existence of a scalar field, $\Psi(\mathbf{F}, \mathbf{X})$, known as the free-energy function, from which the first Piola-Kirchhoff stress may be derived according to:

$$\mathbf{P}(\mathbf{X}, t) = \rho_0 \frac{\partial \Psi(\mathbf{F}, \mathbf{X})}{\partial \mathbf{F}} , \quad (2.122)$$

where ρ_0 is the material density. Some authors refer to hyperelastic materials as *Green elastic materials*.

The free-energy represents a potential energy per unit mass. An equivalent function known as the *Helmholtz free-energy function* ($\Psi_H = \rho_0^{-1}\Psi$) and representing energy per unit reference volume is sometimes used instead. In this alternative formulation, the equivalent of equation (2.122) may be written without the mass density ρ_0 .

A homogeneous material has a free-energy function which has no direct dependence on position, \mathbf{X} . That is Ψ has the same functional dependence on \mathbf{F} throughout the material. This is not to say that Ψ has the same value at everywhere since \mathbf{F} in general varies with position. A free-energy function that only depends on \mathbf{F} is referred to as a *strain-energy* or *stored-energy function*.

Other stress tensors may readily be derived from the free-energy function.

Cauchy Stress Tensor:

$$\boldsymbol{\sigma} = J^{-1} \mathbf{P} \mathbf{F}^T = \frac{\rho_0}{J} \frac{\partial \Psi}{\partial \mathbf{F}} \mathbf{F}^T. \quad (2.123)$$

Kirchhoff Stress Tensor:

$$\boldsymbol{\tau} = J \boldsymbol{\sigma} = \rho_0 \frac{\partial \Psi}{\partial \mathbf{F}} \mathbf{F}^T. \quad (2.124)$$

Second Piola-Kirchhoff Stress Tensor:

$$\mathbf{S} = J \mathbf{F}^{-1} \boldsymbol{\sigma} \mathbf{F}^{-T} = \rho_0 \mathbf{F}^{-1} \frac{\partial \Psi}{\partial \mathbf{F}}. \quad (2.125)$$

It follows from the principle of material objectivity that any arbitrary choice of Ψ as a function of \mathbf{F} is not valid. In fact it can be shown that Ψ must only depend on \mathbf{F} through the right Cauchy-Green tensor $\mathbf{C} = \mathbf{F} \mathbf{F}^T$. ie. there exists a function $\check{\Psi}$ such that:

$$\Psi(\mathbf{F}) = \check{\Psi}(\mathbf{C}).$$

The function $\check{\Psi}$ is referred to as the reduced form of the free-energy function Ψ .

The stress relations (2.122), (2.123) and (2.124) (2.125) may be rewritten in the reduced form.

First Piola-Kirchhoff Stress Tensor:

$$\mathbf{P} = 2 \mathbf{F} \rho_0 \frac{\partial \check{\Psi}}{\partial \mathbf{C}}, \quad (2.126)$$

Cauchy Stress Tensor:

$$\boldsymbol{\sigma} = \frac{2\rho_0}{J} \mathbf{F} \frac{\partial \check{\Psi}}{\partial \mathbf{C}} \mathbf{F}^T. \quad (2.127)$$

Kirchhoff Stress Tensor:

$$\boldsymbol{\tau} = 2\rho_0 \mathbf{F} \frac{\partial \check{\Psi}}{\partial \mathbf{C}} \mathbf{F}^T . \quad (2.128)$$

Second Piola-Kirchhoff Stress Tensor:

$$\mathbf{S} = 2\rho_0 \frac{\partial \check{\Psi}}{\partial \mathbf{C}} . \quad (2.129)$$

2.6.3 Material symmetry

In general the constitutive functionals \mathfrak{s} and \mathfrak{P} are particular to the choice of reference configuration. However for some materials there exists a set of reference configurations which have the same constitutive functional. Such materials are said to exhibit a degree of material symmetry.

We focus on Cauchy elastic materials and consider a motion with respect to two different reference configurations. Figure 2.6 illustrates the mappings $\mathbf{x} = \boldsymbol{\chi}(\mathbf{X})$ and $\mathbf{x} = \boldsymbol{\chi}'(\mathbf{X}')$ from the two reference configurations to the same current configuration. The mapping between the two reference configurations from \mathbf{X}' to \mathbf{X} is denoted by $\boldsymbol{\kappa}$ and is given by $\boldsymbol{\kappa} = \boldsymbol{\chi}^{-1}(\boldsymbol{\chi}'(\mathbf{X}'))$. Now if the Cauchy elastic stress response function \mathfrak{s} is the same for the two reference configurations then we have

$$\mathfrak{s}(\mathbf{F}) = \mathfrak{s}(\mathbf{F}') , \quad (2.130)$$

where \mathbf{F} is the deformation gradient $\text{Grad}\boldsymbol{\chi}(\mathbf{X}, t)$ and \mathbf{F}' is the deformation gradient $\text{Grad}\boldsymbol{\chi}'(\mathbf{X}', t)$. However by the chain rule \mathbf{F}' is given by

$$\mathbf{F}' = \frac{\partial \mathbf{x}}{\partial \mathbf{X}'} = \frac{\partial \mathbf{x}}{\partial \mathbf{X}} \frac{\partial \mathbf{X}}{\partial \mathbf{X}'} = \mathbf{F} \text{Grad}\boldsymbol{\kappa}(\mathbf{X}') = \mathbf{F} \mathbf{K} , \quad (2.131)$$

where \mathbf{K} is the gradient of $\boldsymbol{\kappa}(\mathbf{X}')$. Substituting for \mathbf{F}' in (2.130) gives

$$\mathfrak{s}(\mathbf{F}) = \mathfrak{s}(\mathbf{F} \mathbf{K}) . \quad (2.132)$$

We denote by \mathcal{G} the set of all invertible tensors \mathbf{K} which satisfy (2.132) for arbitrary \mathbf{F} . It is easily shown that \mathcal{G} contains an inverse for each member as well as the identity tensor and that it is closed under tensor multiplication. Hence in mathematical terms the set \mathcal{G} is a group termed the *symmetry group* of the response function \mathfrak{s} .

The symmetry condition may also be expressed in terms of the first Piola-Kirchhoff stress and its response function \mathfrak{P} . Unlike the Cauchy stress $\boldsymbol{\sigma}$, the first Piola-Kirchhoff stress itself depends on the choice of reference configuration. Thus we have \mathbf{P} representing the current state of stress with respect to the reference configuration

with coordinates \mathbf{X} and \mathbf{P}' representing the same current state with respect to the second reference configuration with coordinates \mathbf{X}' . Using the standard relation (2.68) between first Piola-Kirchhoff and Cauchy stress tensors \mathbf{P} is obtained from the stress response function \mathfrak{P}

$$\mathbf{P} = \mathfrak{P}(\mathbf{F}) = \det \mathbf{F} \mathfrak{s}(\mathbf{F}) \mathbf{F}^{-\text{T}}, \quad (2.133)$$

defined in terms of the Cauchy response function \mathfrak{s} . Similarly \mathbf{P}' may be obtained by evaluating the stress response function \mathfrak{P}' with respect to the second reference configuration:

$$\mathbf{P}' = \mathfrak{P}'(\mathbf{F}') = \det \mathbf{F}' \mathfrak{s}'(\mathbf{F}') (\mathbf{F}')^{-\text{T}}. \quad (2.134)$$

where $\mathbf{F}' = \mathbf{F}\mathbf{K}$ as before and \mathfrak{s}' is the Cauchy response function with respect to this second reference configuration. Suppose that \mathbf{K} belongs to \mathcal{G} , the symmetry group of the Cauchy stress response function \mathfrak{s} so that $\mathfrak{s}'(\mathbf{F}') = \mathfrak{s}(\mathbf{F}') = \mathfrak{s}(\mathbf{F}\mathbf{K}) = \mathfrak{s}(\mathbf{F})$. In this case

$$\mathfrak{P}'(\mathbf{F}') = \mathfrak{P}(\mathbf{F}') \quad (2.135)$$

and the right hand side of equation (2.134) becomes

$$\det(\mathbf{F}\mathbf{K}) \mathfrak{s}(\mathbf{F})(\mathbf{F}\mathbf{K})^{-\text{T}} = \det \mathbf{K} \det \mathbf{F} \mathfrak{s}(\mathbf{F}) \mathbf{F}^{-\text{T}} \mathbf{K}^{-\text{T}} = \det \mathbf{K} \mathfrak{P}(\mathbf{F}) \mathbf{K}^{-\text{T}}. \quad (2.136)$$

Thus we obtain the symmetry condition

$$\mathfrak{P}(\mathbf{F}\mathbf{K}) = \det \mathbf{K} \mathfrak{P}(\mathbf{F}) \mathbf{K}^{-\text{T}}, \quad (2.137)$$

that is satisfied by all \mathbf{K} in the symmetry group \mathcal{G} common to \mathfrak{s} and \mathfrak{P} . Commonly \mathbf{K} represents a rotation so that $\det \mathbf{K} = 1$ and $\mathbf{K}^{-1} = \mathbf{K}^{\text{T}}$. In this case (2.137) simplifies to

$$\mathfrak{P}(\mathbf{F}\mathbf{K}) = \mathfrak{P}(\mathbf{F}) \mathbf{K}. \quad (2.138)$$

Noll's rule

We consider again the Cauchy stress response functions \mathfrak{s} and $\bar{\mathfrak{s}}$ for the same material with respect to two different reference configurations χ_0 and $\bar{\chi}_0$ respectively. However it is not assumed that the gradient \mathbf{L} of the mapping from χ_0 to $\bar{\chi}_0$ is a member of the symmetry group \mathcal{G} of \mathfrak{s} . The current deformation has gradients \mathbf{F} and $\bar{\mathbf{F}} = \mathbf{F}\mathbf{L}$ with respect to the two reference configurations and we may write

$$\mathfrak{s}(\mathbf{F}) = \bar{\mathfrak{s}}(\bar{\mathbf{F}}), \quad (2.139)$$

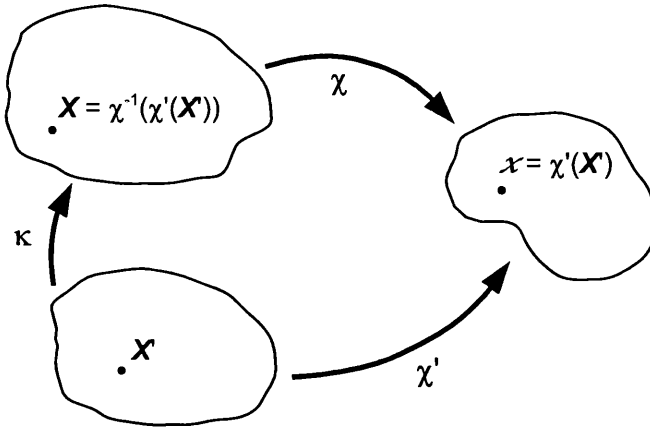


Figure 2.6: Change of reference configuration.

for arbitrary deformation gradient \mathbf{F} . The left hand side above may be re-expressed thus

$$\mathfrak{s}(\mathbf{F}) = \mathfrak{s}(\bar{\mathbf{F}}\mathbf{L}^{-1}) \quad (2.140)$$

$$= \mathfrak{s}(\bar{\mathbf{F}}\mathbf{L}^{-1}\mathbf{K}) \quad \text{where } \mathbf{K} \in \mathcal{G} \quad (2.141)$$

$$= \bar{\mathfrak{s}}(\bar{\mathbf{F}}\mathbf{L}^{-1}\mathbf{K}\mathbf{L}); \quad (2.142)$$

Taking (2.139) and (2.139) together we see that

$$\bar{\mathfrak{s}}(\bar{\mathbf{F}}) = \bar{\mathfrak{s}}(\bar{\mathbf{F}}\mathbf{L}^{-1}\mathbf{K}\mathbf{L}), \quad (2.143)$$

and thus the set of tensors of the form $\mathbf{L}^{-1}\mathbf{K}\mathbf{L}$ makes up the symmetry group $\bar{\mathcal{G}}$ say for the response function $\bar{\mathfrak{s}}$. In other words the symmetry groups associated with the two reference configurations are related by

$$\bar{\mathcal{G}} = \mathbf{L}^{-1}\mathcal{G}\mathbf{L} \quad (2.144)$$

This result is known as *Noll's rule*.

Isotropy

A material model whose symmetry group contains all rotations is said to be *isotropic*. An isotropic Cauchy elastic model thus has a Cauchy stress response function that satisfies

$$\mathfrak{s}(\mathbf{F}) = \mathfrak{s}(\mathbf{F}\mathbf{Q}) \quad \text{for all invertible } \mathbf{F} \text{ and rotations } \mathbf{Q}. \quad (2.145)$$

In terms of the first Piola-Kirchhoff stress function \mathfrak{P} this condition may equivalently be written

$$\mathfrak{P}(\mathbf{F})\mathbf{Q} = \mathfrak{s}(\mathbf{F}\mathbf{Q}) \quad \text{for all invertible } \mathbf{F} \text{ and rotations } \mathbf{Q}. \quad (2.146)$$

For a hyperelastic material it may be shown that isotropy in conjunction with the requirement of objectivity requires that the strain-energy may be expressed as a function of the principal invariants of the left Cauchy Green tensor $\mathbf{b} = \mathbf{F}\mathbf{F}^T$. Accordingly we may write

$$\Psi = \bar{\Psi}(\mathbf{b}) = \bar{\Psi}(I_1, I_2, I_3), \quad (2.147)$$

where

$$I_1 = \text{tr}[\mathbf{b}], \quad I_2 = \frac{1}{2}\{I_1^2 - \text{tr}[\mathbf{b}^2]\}, \quad I_3 = \det \mathbf{b}. \quad (2.148)$$

The Kirchhoff stress may be derived from this potential according to:

$$\boldsymbol{\tau} = 2\rho_0 \frac{\partial \bar{\Psi}}{\partial \mathbf{b}}. \quad (2.149)$$

The stress $\boldsymbol{\tau}$ is an isotropic function of \mathbf{b} . Using this fact it can be shown that $\boldsymbol{\tau}$ can be expressed as:

$$\boldsymbol{\tau} = J(\beta_{-1}\mathbf{b}^{-1} + \beta_0\mathbf{I} + \beta_1\mathbf{b}), \quad (2.150)$$

where:

$$\begin{aligned} \beta_{-1} &= 2\rho_0 \sqrt{I_3} \frac{\partial \bar{\Psi}}{\partial I_2} \\ \beta_0 &= \frac{2\rho_0}{\sqrt{I_3}} \left[I_2 \frac{\partial \bar{\Psi}}{\partial I_2} + I_3 \frac{\partial \bar{\Psi}}{\partial I_3} \right] \\ \beta_1 &= \frac{2\rho_0}{\sqrt{I_3}} \frac{\partial \bar{\Psi}}{\partial I_1} \end{aligned}$$

are known as the elastic response functions.

Another important way in which the strain-energy function may be represented is in terms of the principal stretches λ_1 , λ_2 and λ_3 . Recall that these are the eigenvalues of the stretch tensors (\mathbf{U} or \mathbf{V}) obtained from the polar decomposition of the deformation gradient. In this formulation the strain-energy is written as:

$$\Psi = \hat{\Psi}(\lambda_1, \lambda_2, \lambda_3), \quad (2.151)$$

and the principal Kirchhoff stresses, τ_i (the eigenvalues of the Kirchhoff stress tensor), are derived from:

$$\tau_i = \rho \lambda_i \frac{\partial \hat{\Psi}}{\partial \lambda_i}. \quad (2.152)$$

The full Kirchhoff stress tensor may be recovered from the principal values by means of its spectral representation:

$$\boldsymbol{\tau} = \sum_{i=1}^3 \tau_i \mathbf{n}_i \otimes \mathbf{n}_i , \quad (2.153)$$

where \mathbf{n}_i are the normalised eigenvectors of \mathbf{b} .

2.6.4 Some examples of Hyperelastic Material Models

Saint Venant-Kirchhoff Model

This is one of the simplest hyperelastic constitutive models. The strain-energy function is given by:

$$\begin{aligned} \Psi &= \frac{\lambda}{2\rho_0} (\text{tr} \mathbf{E})^2 + \frac{\mu}{\rho_0} \mathbf{E} : \mathbf{E} \\ &= \frac{\lambda}{8\rho_0} (\text{tr} \mathbf{C})^2 - \left(\frac{3\lambda}{4\rho_0} + \frac{\mu}{2\rho_0} \right) \text{tr} \mathbf{C} + \frac{\mu}{4\rho_0} \mathbf{C} : \mathbf{C} + \left(\frac{9\lambda}{8\rho_0} + \frac{3\mu}{4\rho_0} \right) , \end{aligned} \quad (2.154)$$

where $\mathbf{E} = \frac{1}{2}(\mathbf{C} - \mathbf{I}) = \frac{1}{2}(\mathbf{F}\mathbf{F}^T - \mathbf{I})$ is the Green-Lagrange strain tensor, and λ and μ are the Lamé coefficients familiar from small strain linear elasticity.

This yields the second Piola-Kirchhoff stress as:

$$\begin{aligned} \mathbf{S} = 2\rho_0 \frac{\partial \Psi}{\partial \mathbf{C}} &= \left[\frac{\lambda}{2} \text{tr} \mathbf{C} - \frac{3\lambda}{2} - \mu \right] \mathbf{I} - \mu \mathbf{C} \\ &= \lambda (\text{tr} \mathbf{E}) \mathbf{I} + 2\mu \mathbf{E} , \end{aligned} \quad (2.155)$$

The Saint Venant-Kirchhoff constitutive law is one of the older material models but is little used in large deformation mechanics.

Hencky Model

This model is due to Hencky [45] and is intended to be applied to vulcanised rubber. The strain-energy is most conveniently expressed in terms of the *Eulerian logarithmic strain tensor*, defined as:

$$\boldsymbol{\varepsilon} = \frac{1}{2} \ln \mathbf{b} , \quad (2.156)$$

where $\mathbf{b} = \mathbf{F}\mathbf{F}^T$ is the left Cauchy Green tensor.

In terms of $\boldsymbol{\varepsilon}$ the Hencky strain-energy function is defined as:

$$\Psi = \frac{1}{2\rho_0} \boldsymbol{\varepsilon} : \mathbf{D} : \boldsymbol{\varepsilon} , \quad (2.157)$$

where \mathbf{D} is the rank 4 tensor given, in terms of material constants G and K , by:

$$\mathbf{D} = 2G\mathbf{I} + (K - \frac{2}{3}G)\mathbf{I} \otimes \mathbf{I} . \quad (2.158)$$

Note that \mathbf{D} has the same form as the small strain elasticity tensor.

It can be shown that the Kirchhoff stress tensor derived from the Hencky free-energy function admits the particularly simple representation:

$$\boldsymbol{\tau} = \mathbf{D} : \boldsymbol{\varepsilon} . \quad (2.159)$$

Ogden Model

The Ogden model [84] has proved successful in modeling rubber-like materials at very large strains. The Ogden strain-energy function is expressed in terms of the principal stretches, λ_1 , λ_2 and λ_3 (the eigenvalues of the stretch tensor \mathbf{U} or \mathbf{V}). The general function takes the form:

$$\Psi = \frac{1}{\rho_0} \sum_p^N \frac{\mu_p}{\alpha_p} (\lambda_1^{\alpha_p} + \lambda_2^{\alpha_p} + \lambda_3^{\alpha_p} - 3) , \quad (2.160)$$

where the constants μ_p and α_p constitute a set of shear modulae and dimensionless powers respectively. The positive integer N determines the number of terms in the series.

Originally perfect incompressibility was assumed. This imposes the constraint on the principal stretches that their product should equal one.

However a modified version known as the *regularised Ogden model* allows for compressibility. This is based on the *isochoric/volumetric decomposition* of the deformation gradient:

$$\mathbf{F} = \mathbf{F}_{iso}\mathbf{F}_v = \mathbf{F}_v\mathbf{F}_{iso} , \quad (2.161)$$

where the *isochoric component*, \mathbf{F}_{iso} , is given by:

$$\mathbf{F}_{iso} = J^{-\frac{1}{3}}\mathbf{F} , \quad (2.162)$$

and the *volumetric component* \mathbf{F}_v is given by:

$$\mathbf{F}_v = J^{\frac{1}{3}}\mathbf{I} . \quad (2.163)$$

Clearly $\det(\mathbf{F}_{iso}) = 1$ so that the isochoric component preserves volume.

On the basis of this split, the *isochoric left Cauchy-Green tensor* is defined as:

$$\mathbf{b}_{iso} = \mathbf{F}_{iso}\mathbf{F}_{iso}^T , \quad (2.164)$$

and the *isochoric stretch tensor* is given by:

$$\mathbf{V}_{iso} = \sqrt{\mathbf{b}_{iso}} , \quad (2.165)$$

with eigenvectors λ_1^* , λ_2^* and λ_3^* known as the *principal isochoric stretches*. It can be easily shown that these are related to the principal stretches according to:

$$\lambda_1^* = \frac{\lambda_i}{J^{\frac{1}{3}}} = \frac{\lambda_i}{(\lambda_1 \lambda_2 \lambda_3)^{\frac{1}{3}}} . \quad (2.166)$$

The regularised Ogden strain-energy function is expressed in terms of the isochoric principal stretches by:

$$\Psi = \frac{1}{\rho_0} \sum_p^N \frac{\mu_p}{\alpha_p} [(\lambda_1^*)^{\alpha_p} + (\lambda_2^*)^{\alpha_p} + (\lambda_3^*)^{\alpha_p} - 3] + \frac{1}{2} K (\ln J)^2 . \quad (2.167)$$

From this potential the following expression for the i^{th} principal Kirchhoff stress is derived:

$$\begin{aligned} \tau_i &= \rho_0 \lambda_i \frac{\partial \Psi}{\partial \lambda_i} \\ &= \rho_0 \lambda_i \left(\frac{\partial \Psi}{\partial \lambda_1^*} \frac{\partial \lambda_1^*}{\partial \lambda_i} + \frac{\partial \Psi}{\partial \lambda_2^*} \frac{\partial \lambda_2^*}{\partial \lambda_i} + \frac{\partial \Psi}{\partial \lambda_3^*} \frac{\partial \lambda_3^*}{\partial \lambda_i} + \frac{\partial \Psi}{\partial J} \frac{\partial J}{\partial \lambda_i} \right) , \end{aligned} \quad (2.168)$$

where no summation is implied by repeated indices.

This yields the principal Kirchhoff stress, in terms of the principal stretches and Jacobian, as:

$$\tau_i = \sum_{p=1}^N \mu_p J^{\frac{\alpha_p}{3}} \left[\lambda_i^{\alpha_p} - \frac{1}{3} (\lambda_1^{\alpha_p} + \lambda_2^{\alpha_p} + \lambda_3^{\alpha_p}) \right] + K \ln J . \quad (2.169)$$

2.7 The Quasi-Static Initial Boundary Value Problem

In this section we formulate the problem of determining the motion of a body given its initial state and the constitutive laws governing its stress response. It is assumed that the body is subject to certain known constraints on its boundary displacements and some prescribed external forces. We seek the displacement field $\mathbf{u}(\mathbf{x}, t)$ such that the balance of momentum is maintained. The formulation is presented in variational form based on the virtual work principle introduced in section 2.5.5. This form is well suited to the application of the finite element method.

In the next subsection we describe the boundary conditions applied to the problem. Following this the problem is stated in equivalent Eulerian and Lagrangian terms. Note that we only consider here the conventional mixture of prescribed forces and boundary constraints that are found in most texts. In subsequent chapters we shall deal with a wider variety of constraints which form an essential part of the homogenisation procedure.

2.7.1 Conventional boundary conditions

Figure 2.7 illustrates the motion of a continuum body subject to a system of prescribed constraints. The body occupies its reference configuration Ω_0 at time t_0 . The boundary of the reference domain, $\partial\Omega_0$, is split into two parts $\partial\Omega_0^u$ and $\partial\Omega_0^t$ which map onto $\partial\Omega^u(t)$ and $\partial\Omega^t(t)$ respectively as the motion progresses. It is assumed that these two parts do not overlap and that their union makes up the whole boundary. The following constraints are to be enforced:

Boundary tractions.

At each instant of the motion the Cauchy traction over $\partial\Omega^t$ is explicitly prescribed. That is for a given function $\bar{\mathbf{t}}$ we have

$$[\mathbf{t}(\mathbf{x}, t') = \bar{\mathbf{t}}(\mathbf{x}, t') \quad \forall \mathbf{x} \in \partial\Omega^t(t')] \quad \forall t' \in [t_0, t]. \quad (2.170)$$

The prescription of boundary tractions is often known as the *natural boundary condition*.

Boundary displacements.

The displacements over $\partial\Omega^u$ are given by

$$[\mathbf{u}(\mathbf{x}, t') = \bar{\mathbf{u}}(\mathbf{x}, t') \quad \forall \mathbf{x} \in \partial\Omega^u(t')] \quad \forall t' \in [t_0, t]. \quad (2.171)$$

This constraint is known as the *essential boundary condition*. Sufficiently regular fields that satisfy this condition define the set of kinematically admissible displacement fields:

$$\mathcal{K} = \{ \mathbf{u} : \Omega \times \mathbb{R} \rightarrow \mathcal{U} \mid \mathbf{u}(\mathbf{x}, t) = \bar{\mathbf{u}}(\mathbf{x}, t') \quad \forall \mathbf{x} \in \partial\Omega^u(t'), \forall t' \in [t_0, t] \}, \quad (2.172)$$

where \mathcal{U} is the space of a displacement vectors.

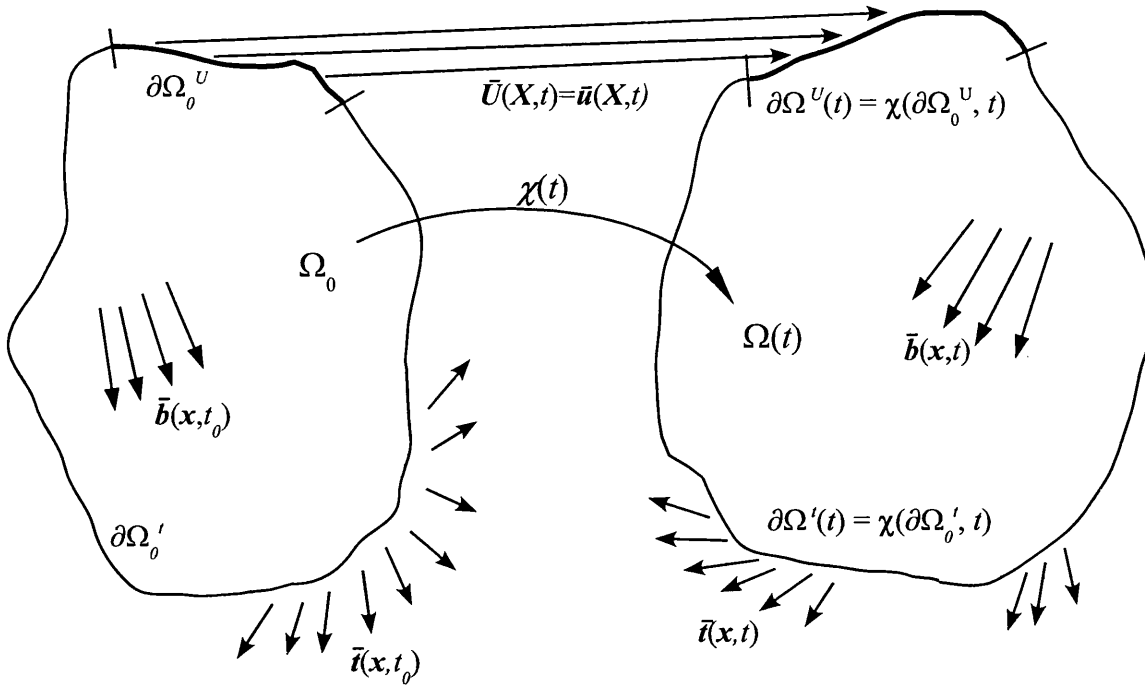


Figure 2.7: Schematic representation of conventional initial and boundary constraints.

Body forces

The history of body forces acting on the body is given by

$$[\mathbf{b}(\mathbf{x}, t') = \bar{\mathbf{b}}(\mathbf{x}, t') \quad \forall \mathbf{x} \in \Omega(t')] \quad \forall t' \in [t_0, t] . \quad (2.173)$$

Initial conditions

If the constitutive model for the body is formulated in terms of internal variables α then their initial values are fully specified according to

$$\alpha(\mathbf{X}, t_0) = \alpha_0(\mathbf{X}) \quad \forall \mathbf{X} \in \Omega_0 . \quad (2.174)$$

2.7.2 The Mechanical Quasi-static I.B.V.P. - Spatial Description

With reference to the definitions of the previous subsections we now define the problem in spatial terms as follows.

Problem 2.7.2

Given:

- \mathfrak{s} – the constitutive Cauchy stress functional
- $\alpha(t_0)$ – the initial values of the internal variables of \mathfrak{s}
- \mathcal{K} – the space of kinematically admissible displacements
- $\bar{\mathbf{t}}(\mathbf{x}, t)$ – prescribed boundary traction on $\partial\Omega^t$
- $\bar{\mathbf{b}}(\mathbf{x}, t)$ – prescribed body force

find the kinematically admissible displacement field, $\mathbf{u} \in \mathcal{K}$, that solves the *virtual work equation*:

$$\int_{\Omega(t)} [\boldsymbol{\sigma}(t) : \nabla \boldsymbol{\eta} - \bar{\mathbf{b}}(t) \cdot \boldsymbol{\eta}] dv - \int_{\partial\Omega^t(t)} \bar{\mathbf{t}}(t) \cdot \boldsymbol{\eta} da = 0 \quad \forall \boldsymbol{\eta} \in \mathcal{V}_t, \quad (2.175)$$

such that everywhere and at each instant the Cauchy stress $\boldsymbol{\sigma}$ satisfies the constitutive law characterised by the functional \mathfrak{s} and where the space of virtual displacements at time t is defined as:

$$\mathcal{V}_t = \{\boldsymbol{\eta} : \Omega(t) \rightarrow \mathcal{U} \mid \boldsymbol{\eta}(\mathbf{x}) = \mathbf{0} \quad \forall \mathbf{x} \in \partial\Omega^u(t)\}.$$

Note that equation (2.175) differs from the equilibrium equation (2.96) by the term $\int_{\partial\Omega^u(t)} \bar{\mathbf{t}}(t) \cdot \boldsymbol{\eta} da$. However because we insist that $\boldsymbol{\eta}$ is zero on the part of the boundary with prescribed displacements, $\partial\Omega^u(t)$, this term vanishes. This is important since $\bar{\mathbf{t}}$ is not known *a priori* over this domain.

2.7.3 The Mechanical Quasi-static IBVP - Material Description

The following expression of the equilibrium problem formulated using the material version of the virtual work equation is equivalent to the spatial problem 2.7.2.

Problem 2.7.3

Given:

- \mathfrak{P} – the constitutive first Piola-Kirchhoff stress functional
- $\alpha(t_0)$ – the initial values of the internal variables of \mathfrak{P}
- \mathcal{K} – the space of kinematically admissible displacements
- $\bar{\mathbf{T}}(\mathbf{X}, t)$ – prescribed first Piola-Kirchhoff traction on $\partial\Omega_0^t$
- $\bar{\mathbf{B}}(\mathbf{X}, t)$ – prescribed body force per unit undeformed volume

find the kinematically admissible displacement field, $\mathbf{U} \in \mathcal{K}$, that solves the *virtual work equation*:

$$\int_{\Omega_0(t)} [\mathbf{P}(t) : \nabla_0 \boldsymbol{\eta} - \bar{\mathbf{B}}(t) \cdot \boldsymbol{\eta}] dV - \int_{\partial\Omega_0^t(t)} \bar{\mathbf{T}}(t) \cdot \boldsymbol{\eta} dA = 0 \quad \forall \boldsymbol{\eta} \in \mathcal{V}_t, \quad (2.176)$$

such that everywhere and at each instant the first Piola-Kirchhoff stress \mathbf{P} satisfies the constitutive law characterised by the functional \mathfrak{P} and where the space of virtual displacements at time t is defined as:

$$\mathcal{V}_t = \{ \boldsymbol{\eta} : \Omega(t) \rightarrow \mathcal{U} \mid \boldsymbol{\eta}(\mathbf{X}) = \mathbf{0} \quad \forall \mathbf{X} \in \partial\Omega_0^u(t) \} .$$

Chapter 3

Review of the finite element method

This chapter presents a concise description of the finite element method as it is used to solve quasi-static problems in non-linear mechanics of the type specified in 2.7. Attention is restricted to quasi-static applications.

The typical strategy employed in solving such problems is to find a way of approximating the continuous governing equations by a set of linear equations. This involves the use of three types of approximation within the overall algorithm:

- **Spatial discretisation.** This is the fundamental finite element procedure whereby the continuum body is divided into a mesh of nodes and elements. Field variables are interpolated between nodal values on the basis of assumed shape functions.
- **Temporal discretisation.** Under time varying prescribed loads and displacements it is necessary to solve history dependent constitutive laws in an incremental way.
- **Linearisation.** The basis of the numerical solution (by the Newton Raphson method or similar) of the equilibrium equation is the linearisation of the virtual work expression.

In this chapter each of the aspects mentioned above will be discussed. In the final section an overview of a complete algorithm will be presented.

The material discussed represents some well established techniques and is drawn from references [4, 17, 127].

3.1 Spatial Discretisation

Fundamental to any finite element implementation is the discretisation of the domain, Ω_0 , of the continuum body in space. This procedure consists of dividing the body, in its reference configuration, into a finite number of subregions. These are normally polyhedra (polygons in two dimensional problems or simply line segments in one dimensional cases) and are generally irregularly shaped for convenience according to the details of the specific problem. If the body has a curved boundary then the union of plane faced polyhedra can only approximate the overall domain.

In addition to this volumetric division a finite number of points within Ω_0 are selected as *nodes*. A node may lie on the boundary between two subregions or at a vertex where three or more subregions meet, or it may be located in the interior of a subregion. Typically when polyhedra are used to subdivide the domain, a node is placed at each vertex.

Together the pattern of subdivision and nodal assignments is known as the mesh. The choice of mesh is made to suit each specific problem.

3.1.1 Parametric Finite Elements

Each of the subregions is mapped onto a standardised *finite element*. This is a topographically similar shape, existing in its own space, that is isomorphic to the material subregion. That is a one to one correspondence can be established between each point in the material subregion and a point belonging to the element. In particular one can identify a nodal point in the element corresponding to each node in the material subregion.

Typically the mesh consists of a set of irregular polyhedra which are mapped onto regular polyhedra. For simplicity it is natural to choose the subregions of the mesh so that they all map onto to a single element shape or a small number of them. For instance one might divide the body into irregular skewed tetrahedra of arbitrary sizes that could then all be mapped onto a standard regular tetrahedron.

The finite element is equipped with its own coordinate system. These coordinates are usually referred to as the *element parameters* and usually range from -1 to 1 over the element domain. Since the mesh subregion and the parametric element are isomorphic to each other, the material coordinates of each point, \mathbf{X} , of a subregion

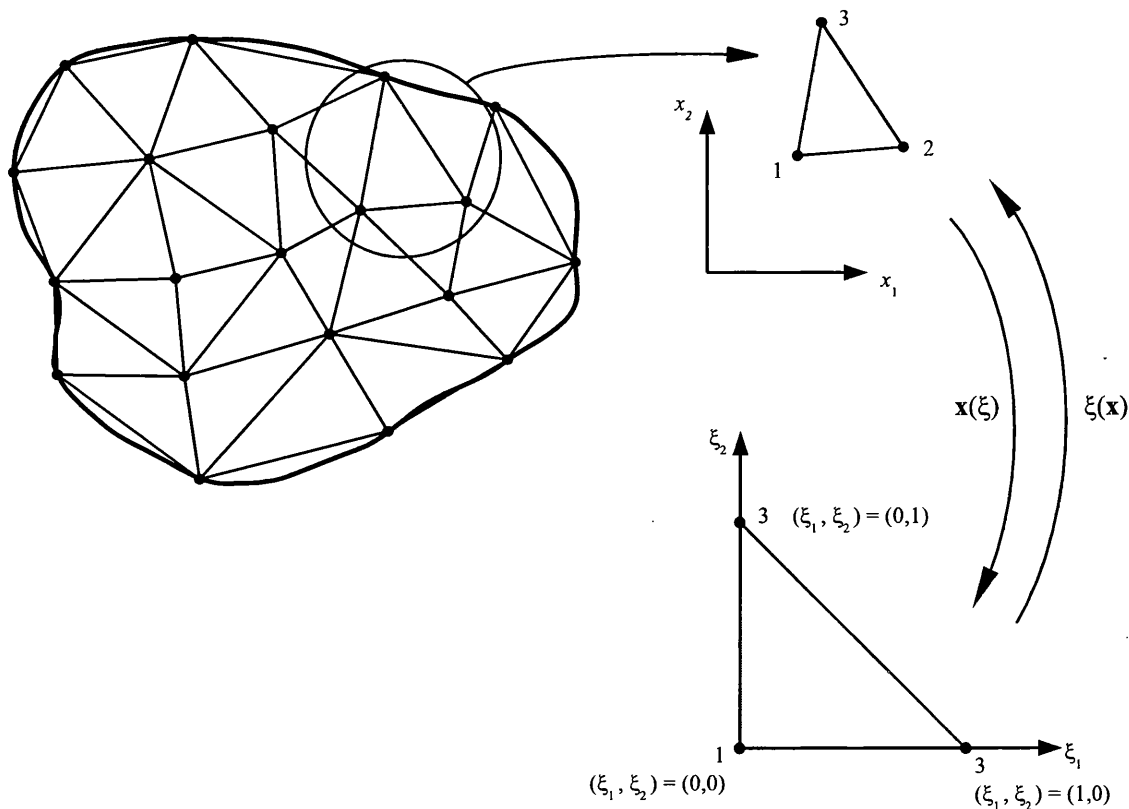


Figure 3.1: Triangular meshing of a two dimensional domain and mapping to a standard triangle.

may be expressed as an invertible function of the element parameters, ξ . i.e.

$$\mathbf{X} = \mathbf{X}(\xi) \quad \text{and} \quad \xi = \xi(\mathbf{X}) . \quad (3.1)$$

There is more than one way to map one region onto another. Thus the choice of the function relating the real world coordinates to the element parameters is an essential part of the specification of a finite element. This is the role of the shape functions which are discussed in the next subsection.

In two dimensional problems the simplest element shape is a triangle. Figure 3.1 illustrates the triangular meshing of a two dimensional domain and shows how an individual skewed triangle in the mesh maps onto a standard triangular element.

Note that although up to now we have reserved the term ‘element’ for the parameterised shape in abstract space in distinction to the subregion of the actual body domain. However in general usage the term may be used to refer to both the mesh element and its isomorphic counterpart the parameterised element.

3.1.2 Shape Functions

As previously stated, in order to properly define the parametric element it is necessary to define the mapping between the body coordinates and the element parameters. This is done firstly by identifying each node in the mesh element with one node in the parametric element in a one to one correspondence. We then introduce the so called *shape functions* or *interpolation functions*. These are a set of single valued dimensionless functions of the element parameters. The number of shape functions is equal the number of nodes in the element. Each function is associated with a different node and defined such that it takes a value of one when evaluated at that node and is zero at every other node. i.e.

$$N_i(\boldsymbol{\xi}^{(j)}) = \delta_{ij}, \quad \forall i, j = 1, \dots, n, \quad (3.2)$$

where N_i is the shape function associated with node i , $\boldsymbol{\xi}^{(j)} = (\xi_1^{(j)}, \xi_2^{(j)}, \dots, \xi_n^{(j)})$ represents the vector of parametric coordinates of node j and n is the number of nodes in the element.

The shape functions can be used to write the material coordinates, $\mathbf{X}(\boldsymbol{\xi})$, of any point in the mesh element, $\boldsymbol{\xi}$, in terms of a sum of the shape functions weighted by the nodal coordinates. This is done as follows:

$$\mathbf{X}(\boldsymbol{\xi}) = \sum_{i=1}^n \mathbf{X}^{(i)} N_i(\boldsymbol{\xi}), \quad (3.3)$$

where $\mathbf{X}^{(i)}$ is the position vector of the i^{th} node. Condition (3.2) ensures compatibility at each node:

$$\mathbf{X}(\boldsymbol{\xi}^{(i)}) = \mathbf{X}^{(i)}. \quad (3.4)$$

A point with parametric coordinates $\boldsymbol{\xi}$ is associated with the material particle at $\mathbf{X}(\boldsymbol{\xi})$. It is assumed that the corresponding spatial position, \mathbf{x} , in the subsequent motion is given by a similar function of the nodal values:

$$\mathbf{x}(\boldsymbol{\xi}) = \sum_{i=1}^n \mathbf{x}^{(i)} N_i(\boldsymbol{\xi}), \quad (3.5)$$

where $\mathbf{x}^{(i)}$ is the current position vector of the i^{th} node. Note that, in this equation, the shape functions are independent of time so that the evolution of the motion is effected solely by changes in the nodal values.

3.1.3 Interpolation - Isoparametric Formulation

The essence of the finite element method is the interpolation of field variables between nodal points.

Equation (3.5), introduced in the previous subsection, is effectively an interpolation formula for global position coordinates. This provides a template for interpolating any field variable, within an element, from its nodal values in terms of the element parameters. Accordingly an arbitrary field, ϕ say, may be approximated by:

$$\phi(\xi) = \sum_{i=1}^n \phi^{(i)} N_i(\xi) , \quad (3.6)$$

where $\phi^{(i)}$ is the value of ϕ at node i .

In the context of displacement based formulations it is necessary to interpolate displacement, \mathbf{u} , at any point in an element from the values at the nodes, $\mathbf{u}^{(i)}$. Following equation (3.6) this can be done using:

$$\mathbf{u}(\xi) = \sum_{i=1}^n \mathbf{u}^{(i)} N_i(\xi) . \quad (3.7)$$

A finite element formulation which in this way uses the same form of interpolation formula for positional coordinates as for the displacement field, in terms of the element parameters, is termed an *isoparametric formulation*.

In the *Galerkin* formulation the shape functions are also used to interpolate the virtual displacement field from the nodal values $\eta^{(i)}$ so that

$$\eta(\xi) = \sum_{i=1}^n \eta^{(i)} N_i(\xi) . \quad (3.8)$$

3.1.4 Deformation Gradient and Strains

Having established an approximation for the displacement field in terms of discrete nodal values, the next step is to obtain discretised expressions for whatever strain measures are required by the initial value boundary problem. These are most conveniently obtained as expressions of the gradient of the displacement. This approach requires us to differentiate equation (3.7) with respect to position. In component form, using the chain rule, we obtain:

$$\frac{\partial u_i}{\partial x_j} = \sum_{p=1}^n \sum_{q=1}^3 u_i^{(p)} \frac{\partial N_p}{\partial \xi_q} \frac{\partial \xi_q}{\partial x_j} . \quad (3.9)$$

The first multiplicative term on the right hand side of equation (3.9), $\frac{\partial N_p}{\partial \xi_q}$ may always be obtained directly as a function of ξ since the specification of the finite element includes an explicit definition of each shape function.

The second term is obtained by considering its inverse, $\frac{\partial x_j}{\partial \xi_q}$. This may be obtained directly by differentiating equation(3.5):

$$\frac{\partial x_j}{\partial \xi_q} = \sum_{i=1}^n \mathbf{x}^{(i)} \frac{\partial N_i}{\partial \xi_q} . \quad (3.10)$$

The matrix, \mathbf{J} , with components given by:

$$J_{qj} = \frac{\partial x_j}{\partial \xi_q} , \quad (3.11)$$

is termed the *Jacobian operator* for the relation between spatial coordinates and element parameters. Given the nodal positions, $\mathbf{x}^{(i)}$, the Jacobian may be evaluated at any parametric position using equation (3.10). Inverting \mathbf{J} allows the second term of equation (3.9) to be expressed as:

$$\frac{\partial \xi_q}{\partial x_j} = J_{jq}^{-1} . \quad (3.12)$$

Thus equation (3.9) becomes:

$$\frac{\partial u_i}{\partial x_j} = \sum_{p=1}^n \left[\sum_{q=1}^3 \frac{\partial N_p}{\partial \xi_q} J_{jq}^{-1} \right] u_i^{(p)} . \quad (3.13)$$

This equation shows that, assuming isoparametric interpolation, the components of the gradient of the displacement, $(\nabla \mathbf{u})_{ij} = \frac{\partial u_i}{\partial x_j}$, can be obtained as an explicit function of the nodal displacements. Recalling equation (2.13) from chapter 2:

$$\mathbf{F}(\mathbf{x}, t) = (\mathbf{I} - \nabla \mathbf{u}(\mathbf{x}, t))^{-1} ,$$

it can be seen that the components of the deformation gradient, \mathbf{F} , may also be obtained in the discretised approximation as functions of nodal displacements. Through \mathbf{F} all the strain measures and the constitutive I.V.P. may be discretised.

The gradient of the virtual displacement field, with components $[\nabla \boldsymbol{\eta}]_{ij} = \frac{\partial \eta_i}{\partial x_j}$, which appears in the virtual work equation (2.175) may be obtained in terms of nodal values, $\eta_i^{(p)}$, in exactly the same way as \mathbf{u} :

$$\frac{\partial \eta_i}{\partial x_j} = \sum_{p=1}^n \left[\sum_{q=1}^3 \frac{\partial N_p}{\partial \xi_q} J_{jq}^{-1} \right] \eta_i^{(p)} . \quad (3.14)$$

We have seen therefore that the all the unknown fields required in the spatial formulation of the initial value boundary problem may be discretised in terms of nodal values of displacement (actual and virtual). This is the essential process in the finite element method that allows a variational statement (2.175) in terms of a continuous function of position to be transformed into an equation relating a finite number of discrete variables. In other words the degrees of freedom in the problem are reduced from infinite to finite in number.

The material gradients $\nabla_0 \mathbf{U} = \frac{\partial \mathbf{U}}{\partial \mathbf{X}}$ and $\nabla_0 \boldsymbol{\eta} = \frac{\partial \boldsymbol{\eta}}{\partial \mathbf{X}}$ required in the Lagrangian formulation may be discretised in a similar way:

$$\frac{\partial U_i}{\partial X_j} = \sum_{p=1}^n \left[\sum_{q=1}^3 \frac{\partial N_p}{\partial \xi_q} J_{0jq}^{-1} \right] U_i^{(p)} ; \quad \frac{\partial \eta_i}{\partial X_j} = \sum_{p=1}^n \left[\sum_{q=1}^3 \frac{\partial N_p}{\partial \xi_q} J_{0jq}^{-1} \right] \eta_i^{(p)} , \quad (3.15)$$

where \mathbf{J}_0 is the Jacobian operator evaluated at the initial time with components given by:

$$J_{0qj} = \frac{\partial X_j}{\partial \xi_q} . \quad (3.16)$$

3.1.5 Integration

We have seen that the unknown fields in the I.B.V.P. can be discretised. However in order to evaluate the terms in the virtual work equation it remains to integrate the discretised field expressions over the whole volume of the body.

In principle we can obtain each integrand as an explicit function of the nodal displacements, the element parameters and, in order to range over the whole body, some index to identify the particular element which includes the point of evaluation. However integration must be performed with respect to spatial volume. This is achieved in two stages.

Firstly each of the whole body integrals is expressed as the sum of integrals over each mesh element. It then remains to transform each element integral with respect to spatial volume to an integral with respect to the element parameters. It can be shown that this is achieved using:

$$dv = (\det \mathbf{J}) d\xi_1 d\xi_2 d\xi_3 , \quad (3.17)$$

where $\det \mathbf{J}$ is the determinant of the Jacobian matrix defined by equation (3.11).

It is possible now to obtain expressions for the required global integrals, in terms of nodal displacements, by explicit integration. However in practice many choices

of shape functions give rise to overcomplicated formulae. Therefore *numerical integration* is usually used. The favoured method is Gaussian quadrature whereby an integral is approximated by a weighted sum of the form:

$$\int_{-1}^1 \int_{-1}^1 \int_{-1}^1 f(\xi_1, \xi_2, \xi_3) d\xi_1 d\xi_2 d\xi_3 = \sum_{i,j,k=1}^p \omega_{ijk} f(\xi_1^{(i)}, \xi_2^{(j)}, \xi_3^{(k)}) , \quad (3.18)$$

where $(\xi_1^{(i)}, \xi_2^{(j)}, \xi_3^{(k)})$ are the coordinates of a $p \times p$ grid of sampling points and ω_{ijk} are the corresponding weights. The weights and sampling coordinates are calculated by insisting that equation (3.18) exactly integrates polynomials of the highest possible order, but may be obtained from standard tables. Generally the larger the value of p , the greater the accuracy of the approximation. However sometimes a low number of sampling points is deliberately chosen because experience has shown that in certain cases the error from numerical integration can compensate for errors from spatial discretisation and thereby improve the overall solution. This so called reduced integration technique has been used for example to overcome the problem of shear locking in plate analysis [126].

3.1.6 Voigt Notation

It is convenient in finite element codes to store the nodal values of displacement as column matrices. According to the so called *Voigt notation*, element nodal displacements are expressed as:

$$[\mathbf{u}^{(e)}] = [u_1^{(1)}, u_2^{(1)}, u_3^{(1)}, u_1^{(2)}, u_2^{(2)}, u_3^{(2)}, \dots, u_1^{(n)}, u_2^{(n)}, u_3^{(n)}]^T , \quad (3.19)$$

where $u_k^{(i)}$ represents the k^{th} component of the displacement of the node numbered i in the *element* numbering scheme and n is the number of nodes in the element. A full three dimensional problem is assumed so that the column matrix, $[\mathbf{u}]^{(e)}$, has $3n$ components.

Global nodal displacements are given as:

$$[\mathbf{u}] = [u_1^{(1)}, u_2^{(1)}, u_3^{(1)}, u_1^{(2)}, u_2^{(2)}, u_3^{(2)}, \dots, u_1^{(N)}, u_2^{(N)}, u_3^{(N)}]^T , \quad (3.20)$$

where $u_k^{(i)}$ now represents the k^{th} component of the displacement of *global* node number i and N is the overall number of nodes in the element.

Column matrices, $[\boldsymbol{\eta}^{(e)}]$ and $[\boldsymbol{\eta}]$, may be similarly defined to represent element and global virtual displacements.

Rank 2 tensors, such as the displacement gradient tensor, $(\nabla \mathbf{u})_{ij} = \frac{\partial u_i}{\partial x_j}$, and the Cauchy stress, $\boldsymbol{\sigma}$, are also represented as column matrices:

$$[\nabla \mathbf{u}] = \begin{bmatrix} \frac{\partial u_1}{\partial x_1} \\ \frac{\partial u_2}{\partial x_2} \\ \frac{\partial u_3}{\partial x_3} \\ \frac{\partial u_1}{\partial x_2} \\ \frac{\partial u_1}{\partial x_3} \\ \frac{\partial u_2}{\partial x_1} \\ \frac{\partial u_2}{\partial x_3} \\ \frac{\partial u_3}{\partial x_1} \\ \frac{\partial u_3}{\partial x_2} \end{bmatrix} ; \quad [\boldsymbol{\sigma}] = \begin{bmatrix} \sigma_{11} \\ \sigma_{22} \\ \sigma_{33} \\ \sigma_{12} \\ \sigma_{13} \\ \sigma_{21} \\ \sigma_{23} \\ \sigma_{31} \\ \sigma_{32} \end{bmatrix} , \quad (3.21)$$

with components arranged according to some ordering convention. The order of components above does not follow a standard convention but as long as ordering is consistent within an algorithm the choice is unimportant. Note that the symmetry of the Cauchy stress tensor means that six components are sufficient in three dimensional problems. However we retain all nine components so that we can write the double contraction of stress and virtual displacement gradient in matrix form:

$$\boldsymbol{\sigma} : \nabla \mathbf{u} = [\nabla \mathbf{u}]^T [\boldsymbol{\sigma}] \quad (3.22)$$

Using the notation introduced above the equation for the discretised displacement gradient, (3.13), may be written in matrix form:

$$[\nabla \mathbf{u}] = \mathbf{G}[\mathbf{u}^{(e)}] , \quad (3.23)$$

where the $3n \times 9$ matrix \mathbf{G} , termed the *discrete spatial gradient operator* is given by:

$$\mathbf{G} = \begin{bmatrix} N_{1,1} & 0 & 0 & N_{2,1} & 0 & 0 & \dots & N_{n,1} & 0 & 0 \\ 0 & N_{1,2} & 0 & 0 & N_{2,2} & 0 & \dots & 0 & N_{n,2} & 0 \\ 0 & 0 & N_{1,3} & 0 & 0 & N_{2,3} & \dots & 0 & 0 & N_{n,3} \\ N_{1,2} & 0 & 0 & N_{2,2} & 0 & 0 & \dots & N_{n,2} & 0 & 0 \\ N_{1,3} & 0 & 0 & N_{2,3} & 0 & 0 & \dots & N_{n,3} & 0 & 0 \\ 0 & N_{1,1} & 0 & 0 & N_{2,1} & 0 & \dots & 0 & N_{n,1} & 0 \\ 0 & N_{1,3} & 0 & 0 & N_{2,3} & 0 & \dots & 0 & N_{n,3} & 0 \\ 0 & 0 & N_{1,1} & 0 & 0 & N_{2,1} & \dots & 0 & 0 & N_{n,1} \\ 0 & 0 & N_{1,2} & 0 & 0 & N_{2,2} & \dots & 0 & 0 & N_{n,2} \end{bmatrix} , \quad (3.24)$$

with the derivative of shape function p with respect to global cartesian coordinate j given by:

$$N_{p,j} = \sum_{q=1}^3 \frac{\partial N_p}{\partial \xi_q} J_{jq}^{-1} . \quad (3.25)$$

Likewise the discretised virtual displacement is given by

$$[\nabla \boldsymbol{\eta}] = \mathbf{G}[\boldsymbol{\eta}^{(e)}] . \quad (3.26)$$

The *discrete material gradient* may be defined as

$$\mathbf{G}_0 = \begin{bmatrix} N_{1,1} & 0 & 0 & N_{2,1} & 0 & 0 & \dots & N_{n,1} & 0 & 0 \\ 0 & N_{1,2} & 0 & 0 & N_{2,2} & 0 & \dots & 0 & N_{n,2} & 0 \\ 0 & 0 & N_{1,3} & 0 & 0 & N_{2,3} & \dots & 0 & 0 & N_{n,3} \\ N_{1,2} & 0 & 0 & N_{2,2} & 0 & 0 & \dots & N_{n,2} & 0 & 0 \\ N_{1,3} & 0 & 0 & N_{2,3} & 0 & 0 & \dots & N_{n,3} & 0 & 0 \\ 0 & N_{1,1} & 0 & 0 & N_{2,1} & 0 & \dots & 0 & N_{n,1} & 0 \\ 0 & N_{1,3} & 0 & 0 & N_{2,3} & 0 & \dots & 0 & N_{n,3} & 0 \\ 0 & 0 & N_{1,1} & 0 & 0 & N_{2,1} & \dots & 0 & 0 & N_{n,1} \\ 0 & 0 & N_{1,2} & 0 & 0 & N_{2,2} & \dots & 0 & 0 & N_{n,2} \end{bmatrix} , \quad (3.27)$$

where the material shape function derivatives are given by

$$N_{p,j} = \sum_{q=1}^3 \frac{\partial N_p}{\partial \xi_q} J_{0jq}^{-1} , \quad (3.28)$$

allowing the discretised material derivatives of actual and virtual displacement fields to be written in matrix form as

$$[\nabla_0 \mathbf{U}] = \mathbf{G}_0[\mathbf{U}^{(e)}] \quad \text{and} \quad [\nabla_0 \boldsymbol{\eta}] = \mathbf{G}_0[\boldsymbol{\eta}^{(e)}] . \quad (3.29)$$

3.2 Temporal Discretisation

Time dependence is present in the quasi static initial boundary value problem only through variation in the applied loads $\bar{\mathbf{b}}$ and $\bar{\mathbf{t}}$, or the essential boundary conditions. However if an elastic constitutive law is used, time will not play an integral part in the solution algorithm. This is because at any given time the stress may be found from the current deformation without reference to the previous motion. Therefore, at each value of time, the I.B.V.P. becomes a series of independent boundary value problems. The time variable does need to be discretised into a finite number of steps,

so that we have only a finite number of these time-independent problems to solve, but the discretisation does not affect the solution algorithm.

The situation is different when we are dealing with inelastic material models, such as plasticity. In such cases the constitutive initial value problem depends on the history of deformation. Therefore in order to evaluate the current stress, as required in the virtual work equation, it would be necessary to trace the motion continuously back in time to the initial configuration. It is not generally possible to do this because finding the deformation at each intermediate time requires the solution of an I.V.B.P. in itself. In short the constitutive initial value problem and the solution of the virtual work equation are coupled problems. The way round this difficulty lies in discretising time and solving the problem in incremental steps.

We begin by dividing the overall time interval, $[t_0, t]$, into $(n+1)$ steps, $(t_0, t_1, t_2, \dots, t_n = t)$. At each of these points in time, the body force, \mathbf{b} , surface traction, \mathbf{t} , and prescribed displacements are specified. We seek to solve the virtual work equation (2.175) at time t_i for all i . In order to do this we need to evaluate the current Cauchy stress field, $\boldsymbol{\sigma}$, or equivalently the first Piola-Kirchhoff stress, \mathbf{P} . Assuming that all the state variables (displacement, stress and internal variables) have been obtained at time t_{i-1} , this is generally done by solving a constitutive initial value problem with initial values defined at t_{i-1} . In other words the constitutive I.V.P. is solved over the incremental time step $[t_{i-1}, t_i]$ rather than $[t_0, t_i]$. We still do not know how the motion evolves over the smaller interval and so cannot solve the incremental constitutive I.V.P. exactly. Instead the strategy is to assume that the deformation gradient \mathbf{F} evolves in a prescribed way. That is the history over the time increment is obtained by interpolation between $\mathbf{F}(t_{i-1})$ and $\mathbf{F}(t_i)$. On this basis an approximate estimate of the current stress may be obtained. For a simple material with internal variables we may formally write the current cauchy stress at time station , t_i , as:

$$\boldsymbol{\sigma}(t_i) = \boldsymbol{\sigma}_i \approx \hat{\boldsymbol{\sigma}}(\boldsymbol{\alpha}_{i-1}, \mathbf{F}(t_i)) , \quad (3.30)$$

where $\hat{\boldsymbol{\sigma}}(\boldsymbol{\alpha}_{i-1}, \mathbf{F}_i)$ represents the result of an appropriate numerical solution to the constitutive initial value problem with initial values $\boldsymbol{\alpha}_{i-1}$. The approximation $\hat{\boldsymbol{\sigma}}$ is termed the *incremental constitutive function*.

Using the incremental constitutive function we may recast the I.B.V.P. in incremental form. Substituting $\hat{\boldsymbol{\sigma}}$ for the true $\boldsymbol{\sigma}$, we obtain the *incremental mechanical quasi-static boundary value problem*:

Given the field values of the internal variables, α_{i-1} , the body force field, $\bar{\mathbf{b}}(t_i)$, the surface tractions, $\bar{\mathbf{t}}(t_i)$ and the prescribed displacements defining the set of kinematically admissible displacement fields, \mathcal{X}_i , all at time t_i , find the displacement field, $\mathbf{u}(t_i) \in \mathcal{X}_i$, that solves the **variational equilibrium equation**:

$$\begin{aligned} \int_{\Omega(t_i)} [\hat{\boldsymbol{\sigma}}(\alpha_{i-1}, \mathbf{F}(\mathbf{u}(t_i)) : \nabla \boldsymbol{\eta} - \bar{\mathbf{b}}(t_i) \cdot \boldsymbol{\eta}] dv \\ - \int_{\partial\Omega^t(t_i)} \bar{\mathbf{t}}(t_i) \cdot \boldsymbol{\eta} da = 0 \quad \forall \boldsymbol{\eta} \in \mathcal{V}_{t_i}, \end{aligned} \quad (3.31)$$

where $\hat{\boldsymbol{\sigma}}$ is the incremental constitutive function, $\mathbf{F}(\mathbf{u}(t_i)) = \mathbf{I} + \nabla_0 \mathbf{U}$ and the space of virtual displacements at time t , \mathcal{V}_{t_i} is defined as:

$$\mathcal{V}_{t_i} = \{ \boldsymbol{\eta} : \Omega(t) \rightarrow \mathcal{U} \mid \boldsymbol{\eta}(\mathbf{x}) = 0, \mathbf{x} \in \partial\Omega^U(t_i) \}.$$

This incremental approach represents one of the major approximations used in the numerical solution of nonlinear problems. The amount of error introduced will depend on the nature of the constitutive law and the algorithm used to approximate it over each time step. Cauchy elastic materials present a special case where the stress response is generally an explicit function of the current deformation. Time discretisation does not induce any error for such materials and indeed is not required if only the final deformation is of interest. Path dependent materials, on the other hand, require a degree of approximation.

Accuracy depends additionally on the details of the time discretisation used. One would expect the error in the incremental stress response function to reduce as the time step, $(t_i - t_{i-1})$, is reduced. In the simplest algorithms these steps are fixed but it is possible to adapt them in the light of intermediate results. Thus when the incremental boundary value problem is tackled by means of an iterative solution procedure and convergence cannot be attained, it can be advantageous to cut the size of the time step and try again.

3.3 Linearisation

3.3.1 Newton-Raphson Method

We have seen that the virtual work equation (2.175) may be approximated at discrete time station, t_i , by equation (3.31),

$$\int_{\Omega(t_i)} [\hat{\boldsymbol{\sigma}} : \nabla \boldsymbol{\eta} - \bar{\mathbf{b}}(t_i) \cdot \boldsymbol{\eta}] dv - \int_{\partial\Omega^t(t_i)} \bar{\mathbf{t}}(t_i) \cdot \boldsymbol{\eta} da = 0 \quad \forall \boldsymbol{\eta} \in \mathcal{V}_{t_i}.$$

Now since $\hat{\sigma}$ depends on \mathbf{u} (through \mathbf{F}) it follows that the left hand side of this equation is a functional of the real and virtual displacement fields, \mathbf{u} and $\boldsymbol{\eta}$ respectively. Denoting this virtual work functional as W we may write:

$$W(\mathbf{u}, \boldsymbol{\eta}) = \int_{\Omega} [\hat{\sigma} : \nabla \boldsymbol{\eta} - \bar{\mathbf{b}} \cdot \boldsymbol{\eta}] dv - \int_{\partial\Omega^t} \bar{\mathbf{t}} \cdot \boldsymbol{\eta} da, \quad (3.32)$$

where we have dropped the explicit time dependence since all variables are evaluated at $t = t_i$. Equation (3.31) then becomes:

$$W(\mathbf{u}, \boldsymbol{\eta}) = 0 \quad \forall \boldsymbol{\eta} \in \mathcal{V}_{t_i}. \quad (3.33)$$

Often W is nonlinear in \mathbf{u} and equation (3.33) cannot be solved analytically even if we were to discretise it spatially. Therefore in general an approximate numerical solution is sought. The most commonly used algorithm is the well known *Newton-Raphson method*.

This is an iterative procedure whereby a sequence of approximations to the solution field is calculated from:

$$\mathbf{u}_k = \mathbf{u}_{k-1} + \delta \mathbf{u}_k, \quad (3.34)$$

where $\delta \mathbf{u}_k$ is the solution of the *linearisation* of equation (3.33) with respect to \mathbf{u} :

$$W(\mathbf{u}_{k-1}, \boldsymbol{\eta}) + DW(\mathbf{u}_{k-1}, \boldsymbol{\eta})[\delta \mathbf{u}_k] = 0. \quad (3.35)$$

Here $DW(\mathbf{u}_{k-1}, \boldsymbol{\eta})[\delta \mathbf{u}_k]$ is the directional derivative of the functional W about \mathbf{u}_{k-1} in the ‘direction’ $\delta \mathbf{u}_k$. Note of course that \mathbf{u}_{k-1} , \mathbf{u}_k and $\delta \mathbf{u}_k$ are vector valued *functions* of position.

3.3.2 Linearisation of Virtual Work

In order to use the Newton-Raphson method (or any of the other solution procedures based on linearisation) it is necessary to find the directional derivative of the time discrete virtual work functional W .

The directional derivative of W is by definition:

$$DW(\mathbf{u}, \boldsymbol{\eta})[\delta \mathbf{u}] = \left. \frac{d}{d\epsilon} \right|_{\epsilon=0} W(\mathbf{u} + \epsilon(\delta \mathbf{u}), \boldsymbol{\eta}). \quad (3.36)$$

It turns out to be more convenient to express the virtual work in the material form:

$$W(\mathbf{u}, \boldsymbol{\eta}) = \int_{\Omega_0} [\hat{\mathbf{P}} : \nabla_0 \boldsymbol{\eta} - \bar{\mathbf{B}} \cdot \boldsymbol{\eta}] dV - \int_{\partial\Omega_0^t} \bar{\mathbf{T}} \cdot \boldsymbol{\eta} dA, \quad (3.37)$$

where $\hat{\mathbf{P}} = J\hat{\boldsymbol{\sigma}}\mathbf{F}^{-T}$ is the first Piola-Kirchhoff stress corresponding to the incremental constitutive function $\hat{\boldsymbol{\sigma}}$. Then we may write:

$$DW(\mathbf{u}, \boldsymbol{\eta})[\delta\mathbf{u}] = \left. \frac{d}{d\epsilon} \right|_{\epsilon=0} \left(\int_{\Omega_0} [\hat{\mathbf{P}} : \nabla_0 \boldsymbol{\eta} - \bar{\mathbf{B}} \cdot \boldsymbol{\eta}] dV - \int_{\partial\Omega_0^t} \bar{\mathbf{T}} \cdot \boldsymbol{\eta} dA \right). \quad (3.38)$$

For simplicity we assume that the prescribed body force, $\bar{\mathbf{B}}$, and traction, $\bar{\mathbf{T}}$, are both independent of deformation. It should be noted however that many real life loads will not satisfy this condition. Air pressure for instance will act normal to the current boundary surface. In such cases the external load terms need to be linearised. If we proceed with the assumption nonetheless, then the two terms in (3.38) vanish and the equation simplifies to:

$$\begin{aligned} DW(\mathbf{u}, \boldsymbol{\eta})[\delta\mathbf{u}] &= \left. \frac{d}{d\epsilon} \right|_{\epsilon=0} \int_{\Omega_0} \hat{\mathbf{P}} : \nabla_0 \boldsymbol{\eta} dV \\ &= \int_{\Omega_0} \left(\left. \frac{d}{d\epsilon} \right|_{\epsilon=0} \hat{\mathbf{P}} \right) : \nabla_0 \boldsymbol{\eta} dV. \end{aligned} \quad (3.39)$$

The last step follows since $\boldsymbol{\eta}$ is independent of the displacement field. Now, $\hat{\mathbf{P}}$ depends on \mathbf{u} through the deformation gradient, \mathbf{F} , so that we may use the chain rule to write:

$$\begin{aligned} \left. \frac{d}{d\epsilon} \right|_{\epsilon=0} \hat{\mathbf{P}} &= \left. \frac{d}{d\epsilon} \right|_{\epsilon=0} \hat{\mathbf{P}}(\mathbf{F}(\mathbf{u} + \epsilon\delta\mathbf{u})) \\ &= \frac{\partial \hat{\mathbf{P}}}{\partial \mathbf{F}} : \left. \frac{d}{d\epsilon} \right|_{\epsilon=0} \mathbf{F}(\mathbf{u} + \epsilon\delta\mathbf{u}). \end{aligned} \quad (3.40)$$

Recalling expression (2.12) for \mathbf{F} in terms of \mathbf{U} , and noting that $\mathbf{U}(\mathbf{X}, t) = \mathbf{u}(\mathbf{x}, t)$ we have,

$$\begin{aligned} \left. \frac{d}{d\epsilon} \right|_{\epsilon=0} \mathbf{F}(\mathbf{u} + \epsilon\delta\mathbf{u}) &= \left. \frac{d}{d\epsilon} \right|_{\epsilon=0} (\mathbf{I} + \nabla_0(\mathbf{u} + \epsilon\delta\mathbf{u})) \\ &= \nabla_0(\delta\mathbf{u}), \end{aligned} \quad (3.41)$$

so that (3.39) becomes:

$$DW(\mathbf{u}, \boldsymbol{\eta})[\delta\mathbf{u}] = \int_{\Omega_0} \frac{\partial \hat{\mathbf{P}}}{\partial \mathbf{F}} : \nabla_0(\delta\mathbf{u}) : \nabla_0 \boldsymbol{\eta} dV. \quad (3.42)$$

Now,

$$\nabla_0(\delta\mathbf{u}) = \frac{\partial(\delta\mathbf{u})}{\partial \mathbf{X}} = \frac{\partial(\delta\mathbf{u})}{\partial \mathbf{x}} \frac{\partial \mathbf{x}}{\partial \mathbf{X}} = \nabla(\delta\mathbf{u})\mathbf{F}, \quad (3.43)$$

and similarly

$$\nabla_0 \boldsymbol{\eta} = \nabla \boldsymbol{\eta} \mathbf{F}. \quad (3.44)$$

Therefore, using $dV = J^{-1}dv$, we may express the integral in equation (3.42) over the spatial domain:

$$DW(\mathbf{u}, \boldsymbol{\eta})[\delta \mathbf{u}] = \int_{\Omega} J^{-1} \frac{\partial \hat{\mathbf{P}}}{\partial \mathbf{F}} : (\nabla(\delta \mathbf{u}) \mathbf{F}) : (\nabla \boldsymbol{\eta} \mathbf{F}) dv . \quad (3.45)$$

In component notation this may be written:

$$\begin{aligned} DW(\mathbf{u}, \boldsymbol{\eta})[\delta \mathbf{u}] &= \int_{\Omega} J^{-1} \left[\frac{\partial \hat{\mathbf{P}}}{\partial \mathbf{F}} \right]_{ipkq} [\nabla(\delta \mathbf{u})]_{kl} F_{lq} [\nabla \boldsymbol{\eta}]_{ij} F_{jp} dv \\ &= \int_{\Omega} \left(J^{-1} \frac{\partial \hat{P}_{ip}}{\partial F_{kq}} F_{jp} F_{lq} \right) [\nabla(\delta \mathbf{u})]_{kl} [\nabla \boldsymbol{\eta}]_{ij} dv \\ &= \int_{\Omega} \mathbf{a} : \nabla(\delta \mathbf{u}) : \nabla \boldsymbol{\eta} dv , \end{aligned} \quad (3.46)$$

where we have introduced the *spatial tangent modulus*, defined in component form by:

$$a_{ijkl} = J^{-1} \frac{\partial \hat{P}_{ip}}{\partial F_{kq}} F_{jp} F_{lq} . \quad (3.47)$$

The first Piola-Kirchhoff stress, $\hat{\mathbf{P}}$, may, recalling definitions (2.68) and (2.71) be expressed in terms of the (incremental) Kirchhoff stress tensor as:

$$\hat{\mathbf{P}} = J \hat{\boldsymbol{\sigma}} \mathbf{F}^{-T} = \hat{\boldsymbol{\tau}} \mathbf{F}^{-T} . \quad (3.48)$$

Thus:

$$\begin{aligned} a_{ijkl} &= J^{-1} \frac{\partial}{\partial F_{kq}} (\hat{\tau}_{ia} F_{ap}^{-T}) F_{jp} F_{lq} \\ &= J^{-1} \frac{\partial \hat{\tau}_{ia}}{\partial F_{kq}} F_{lq} F_{jp} F_{pa}^{-1} + J^{-1} \frac{\partial F_{pa}^{-1}}{\partial F_{kq}} \hat{\tau}_{ia} F_{jp} F_{lq} \\ &= J^{-1} \frac{\partial \hat{\tau}_{ia}}{\partial F_{kq}} F_{lq} \delta_{ja} - J^{-1} F_{pk}^{-1} F_{qa}^{-1} \hat{\tau}_{ia} F_{jp} F_{lq} \\ &= J^{-1} \frac{\partial \hat{\tau}_{ij}}{\partial F_{kq}} F_{lq} - J^{-1} \hat{\tau}_{ia} \delta_{jk} \delta_{la} \\ &= J^{-1} \frac{\partial \hat{\tau}_{ij}}{\partial F_{kq}} F_{lq} - \hat{\sigma}_{il} \delta_{jk} , \end{aligned} \quad (3.49)$$

where we have used the identity $[\partial \mathbf{T}^{-1} / \partial \mathbf{T}]_{pakq} = -T_{pk}^{-1} T_{qa}^{-1}$, valid for an invertible tensor, \mathbf{T} . In Voigt notation, using the ordering convention adopted in 3.21, the

tangent modulus \mathbf{a} assumes the matrix form

$$[\mathbf{a}] = \begin{bmatrix} a_{1111} & a_{1122} & a_{1133} & a_{1112} & a_{1113} & a_{1121} & a_{1123} & a_{1131} & a_{1132} \\ a_{2211} & a_{2222} & a_{2233} & a_{2212} & a_{2213} & a_{2221} & a_{2223} & a_{2231} & a_{2232} \\ a_{3311} & a_{3322} & a_{3333} & a_{3312} & a_{3313} & a_{3321} & a_{3323} & a_{3331} & a_{3332} \\ a_{1211} & a_{1222} & a_{1233} & a_{1212} & a_{1213} & a_{1221} & a_{1223} & a_{1231} & a_{1232} \\ a_{1311} & a_{1322} & a_{1333} & a_{1312} & a_{1313} & a_{1321} & a_{1323} & a_{1331} & a_{1332} \\ a_{2111} & a_{2122} & a_{2133} & a_{2112} & a_{2113} & a_{2121} & a_{2123} & a_{2131} & a_{2132} \\ a_{2311} & a_{2322} & a_{2333} & a_{2312} & a_{2313} & a_{2321} & a_{2323} & a_{2331} & a_{2332} \\ a_{3111} & a_{3122} & a_{3133} & a_{3112} & a_{3113} & a_{3121} & a_{3123} & a_{3131} & a_{3132} \\ a_{3211} & a_{3222} & a_{3233} & a_{3212} & a_{3213} & a_{3221} & a_{3223} & a_{3231} & a_{3232} \end{bmatrix}. \quad (3.50)$$

Equation (3.46) with the spatial tangent modulus, \mathbf{a} , defined by equation (3.49) allows us to implement the Newton-Raphson scheme. However in order to use (3.49) it is necessary to have the derivative $\frac{\partial \boldsymbol{\tau}}{\partial \mathbf{F}}$. This tensor field depends on the material of the continuum and so the tangent modulus must be derived from the constitutive law that is to be used. A selection of tangent moduli can be found in Chapter 13 of reference [17] for hyperelastic materials.

Note that throughout this discussion on the linearisation of the virtual work functional, we have written each stress tensor with a hat over its symbol. This is a reminder that we have been dealing with stresses obtained from the *incremental* response function, which does not necessarily satisfy the constitutive laws exactly. Tangent moduli obtained in this way are said to be *consistent* with the algorithm used to obtain the stress response over each time increment. The distinction is only important with dissipative materials since elastic models normally allow an explicit stress response to be obtained.

3.3.3 Spatial Discretisation of Virtual Work

In the context of a finite element algorithm, equation (3.46) for the directional derivative of the virtual work functional needs to be expressed in discretised form. That is in terms of nodal displacement values. This is done on an element by element

basis. In terms of the Voigt notation introduced in subsection 3.1.6, we may write:

$$\begin{aligned}
 DW(\mathbf{u}, \boldsymbol{\eta})[\delta \mathbf{u}] &= \sum_{\text{elements}} \int_{\Omega^{(e)}} [\boldsymbol{\eta}^{(e)}]^T \mathbf{G}^T[\mathbf{a}] \mathbf{G}[\delta \mathbf{u}^{(e)}] dv \\
 &= \sum_{\text{elements}} [\boldsymbol{\eta}^{(e)}]^T \left(\int_{\Omega^{(e)}} \mathbf{G}^T[\mathbf{a}] \mathbf{G} dv \right) [\delta \mathbf{u}^{(e)}] \\
 &= \sum_{\text{elements}} [\boldsymbol{\eta}^{(e)}]^T \mathbf{K}^{(e)} [\delta \mathbf{u}^{(e)}], \tag{3.51}
 \end{aligned}$$

where $\Omega^{(e)}$ is the volume domain of a single element, $[\delta \mathbf{u}^{(e)}]$ is the array of element nodal displacement adjustments and the *element stiffness matrix*, $\mathbf{K}^{(e)}$, is given by:

$$\mathbf{K}^{(e)} = \int_{\Omega^{(e)}} \mathbf{G}^T[\mathbf{a}] \mathbf{G} dv. \tag{3.52}$$

We can write equation (3.51) in terms of the global nodal displacements as:

$$DW(\mathbf{u}, \boldsymbol{\eta})[\delta \mathbf{u}] = [\boldsymbol{\eta}]^T \mathbf{K} [\delta \mathbf{u}], \tag{3.53}$$

where \mathbf{K} is the global stiffness matrix obtained by summing all the terms in the element stiffness matrices while respecting the correspondence between global and element nodes. Note that in practice the integration in (3.52) is performed by Gaussian quadrature so that \mathbf{G} and \mathbf{a} need only be evaluated at the sampling points in each element.

In a similar fashion a discretised matrix representation of the incremental virtual work functional may be obtained. Consider firstly the stress term:

$$\begin{aligned}
 \int_{\Omega} \hat{\boldsymbol{\sigma}} : \nabla \boldsymbol{\eta} dv &= \sum_{\text{elements}} \int_{\Omega^{(e)}} [\nabla \boldsymbol{\eta}]^T [\hat{\boldsymbol{\sigma}}] dv \\
 &= \sum_{\text{elements}} \int_{\Omega^{(e)}} [\boldsymbol{\eta}^{(e)}]^T \mathbf{G}^T[\hat{\boldsymbol{\sigma}}] dv \\
 &= [\boldsymbol{\eta}]^T \mathbf{A}_e \int_{\Omega^{(e)}} \mathbf{G}^T[\hat{\boldsymbol{\sigma}}] dv \\
 &= [\boldsymbol{\eta}]^T [\mathbf{F}^{\text{int}}], \tag{3.54}
 \end{aligned}$$

where the *finite element assembly operator* \mathbf{A}_e effects the assembly of a global matrix with components obtained by summing all local degrees of freedom corresponding to the same global degree of freedom. The *global internal force vector*, $[\mathbf{F}^{\text{int}}]$, is also introduced above and is defined by:

$$[\mathbf{F}^{\text{int}}] = \mathbf{A}_e \int_{\Omega^{(e)}} \mathbf{G}^T[\hat{\boldsymbol{\sigma}}] dv. \tag{3.55}$$

The body force and traction terms may also be discretised:

$$\begin{aligned}
\int_{\Omega} \bar{\mathbf{b}} \cdot \boldsymbol{\eta} dv + \int_{\partial\Omega^t} \bar{\mathbf{t}} \cdot \boldsymbol{\eta} da &= \sum_{elements} \int_{\Omega^{(e)}} \bar{\mathbf{b}} \cdot \left(\sum_i^n \boldsymbol{\eta}^{(i)} N^{(i)} \right) dv \\
&\quad + \sum_{elements} \int_{\partial\Omega^{(e)} \cap \partial\Omega^t} \bar{\mathbf{t}} \cdot \left(\sum_i^n \boldsymbol{\eta}^{(i)} N^{(i)} \right) da \\
&= \sum_{elements} \sum_i^n \boldsymbol{\eta}^{(i)} \cdot \left(\int_{\Omega^{(e)}} N^{(i)} \bar{\mathbf{b}} dv + \int_{\partial\Omega^{(e)} \cap \partial\Omega^t} N^{(i)} \bar{\mathbf{t}} da \right) \\
&= [\boldsymbol{\eta}]^T \mathbf{A}_e \left(\int_{\Omega^{(e)}} N^{(i)} \bar{\mathbf{b}} dv + \int_{\partial\Omega^{(e)} \cap \partial\Omega^t} N^{(i)} \bar{\mathbf{t}} da \right) \\
&= [\boldsymbol{\eta}]^T [\mathbf{F}^{ext}] ,
\end{aligned} \tag{3.56}$$

where the *global external force vector*, $[\mathbf{F}^{ext}]$, is defined by:

$$[\mathbf{F}^{ext}] = \mathbf{A}_e \left(\int_{\Omega^{(e)}} N^{(i)} \bar{\mathbf{b}} dv + \int_{\partial\Omega^{(e)} \cap \partial\Omega^t} N^{(i)} \bar{\mathbf{t}} da \right) . \tag{3.57}$$

Combining the stress, body force and traction terms we obtain the following discretised matrix expression for the incremental virtual work functional:

$$\begin{aligned}
W(\mathbf{u}, \boldsymbol{\eta}) &= \int_{\Omega} [\hat{\boldsymbol{\sigma}} : \nabla \boldsymbol{\eta} - \bar{\mathbf{b}} \cdot \boldsymbol{\eta}] dv - \int_{\partial\Omega^t} \bar{\mathbf{t}} \cdot \boldsymbol{\eta} da \\
&= [\boldsymbol{\eta}]^T \{ [\mathbf{F}^{int}] - [\mathbf{F}^{ext}] \} .
\end{aligned} \tag{3.58}$$

Using equations (3.51) and (3.58) the linearisation of the virtual work equation (3.35), used in the Newton-Raphson method, becomes:

$$[\boldsymbol{\eta}]^T \{ [\mathbf{F}_{k-1}^{int}] - [\mathbf{F}_{k-1}^{ext}] \} + [\boldsymbol{\eta}]^T \mathbf{K}_{k-1} [\mathbf{u}_k] = 0 , \tag{3.59}$$

where the subscripts on \mathbf{F}^{int} , \mathbf{F}^{ext} and \mathbf{K} indicate that they are evaluated as functions of displacement \mathbf{u}_{k-1} . Since $\boldsymbol{\eta}$ is an arbitrary field, this reduces to;

$$\mathbf{K}_{k-1} [\delta \mathbf{u}_k] = - \{ [\mathbf{F}_{k-1}^{int}] - [\mathbf{F}_{k-1}^{ext}] \} . \tag{3.60}$$

The bracketed term on the right hand side is known as the *residual* of the virtual work equation (evaluated for displacement \mathbf{u}_{k-1}) and should vanish when the virtual work equation is satisfied. The Newton-Raphson scheme is considered to have converged when the residual evaluated at the latest estimate of \mathbf{u} is zero to within a specified tolerance.

Discretisation of virtual work in Lagrangian formulation

In Lagrangian terms the expression for the element stiffness matrix equivalent to equation (3.52) is

$$\mathbf{K}^{(e)} = \int_{\Omega_0^{(e)}} \mathbf{G}_0^T \left[\frac{\partial \hat{\mathbf{P}}}{\partial \mathbf{F}} \right] \mathbf{G}_0 \, dV, \quad (3.61)$$

where $\left[\frac{\partial \hat{\mathbf{P}}}{\partial \mathbf{F}} \right]$ is the Voigt matrix representation of the tensor $\frac{\partial \hat{\mathbf{P}}}{\partial \mathbf{F}}$. Equally the global internal and external force vectors may be written

$$[\mathbf{F}^{\text{int}}] = \mathbf{A}_e \int_{\Omega_0^{(e)}} \mathbf{G}_0^T [\hat{\mathbf{P}}] dV \quad (3.62)$$

$$[\mathbf{F}^{\text{ext}}] = \mathbf{A}_e \left(\int_{\Omega_0^{(e)}} N^{(i)} \bar{\mathbf{B}} dV + \int_{\partial\Omega_0^{(e)} \cap \partial\Omega_0^t} N^{(i)} \bar{\mathbf{T}} dA \right). \quad (3.63)$$

Equations (3.61), (3.62) and (3.63) provide an alternative way of evaluating $\mathbf{K}^{(e)}$, $[\mathbf{F}^{\text{int}}]$ and $[\mathbf{F}^{\text{ext}}]$ respectively. The global stiffness matrix, discretised virtual work (3.58), discretised directional derivative of the virtual work (3.53) and Newton-Raphson equation (3.60) follow as in the spatial formulation.

3.4 Overall Algorithm

Figure 3.2 represents a schematic overview of a suitable algorithm to solve the initial boundary value problem.

There are two principal repeated loops in the process - an iterative loop to implement the Newton-Raphson method is nested within an incremental loop performed for each pseudo-time step.

The principal difference between the illustrated algorithm and a corresponding process for the solution of small displacement linear problems is that the evaluation of the system stiffness, carried out in step 2, needs to be performed at each iterative step. In the fully linear small displacement case it is assumed that the stiffness does not change significantly with the small changes in configuration. Therefore it can be evaluated once before entering the Newton-Raphson loop. Hence a saving in computational effort is obtained over the present scheme.

Alternative numerical schemes to the full Newton-Raphson method are sometimes used for nonlinear problems in order to reduce the time spent calculating the stiffness matrix. These are the *modified Newton methods*. In the simplest of these, the *initial stiffness method*, \mathbf{K} is calculated just once on the basis of the initial configuration

and stresses and used throughout the iterations and time increments. Alternatively \mathbf{K} may be re-evaluated at the start of each increment or each time after a certain number of increments. There is of course a price to pay for not working always with the most up to date stiffness. This comes in the reduced speed of convergence of the iterative solution procedure. Savings in computational time spent evaluating \mathbf{K} in the modified methods are often outweighed by the loss of quadratic convergence that the full Newton-Raphson scheme should enjoy.

A more sophisticated enhancement to the Newton-Raphson method is the arc-length method. This is a procedure designed to overcome difficulties encountered with unstable equilibria in the solution of the virtual work problem. We shall not discuss the method here except to comment that the basis of solution remains approximation by linearisation.

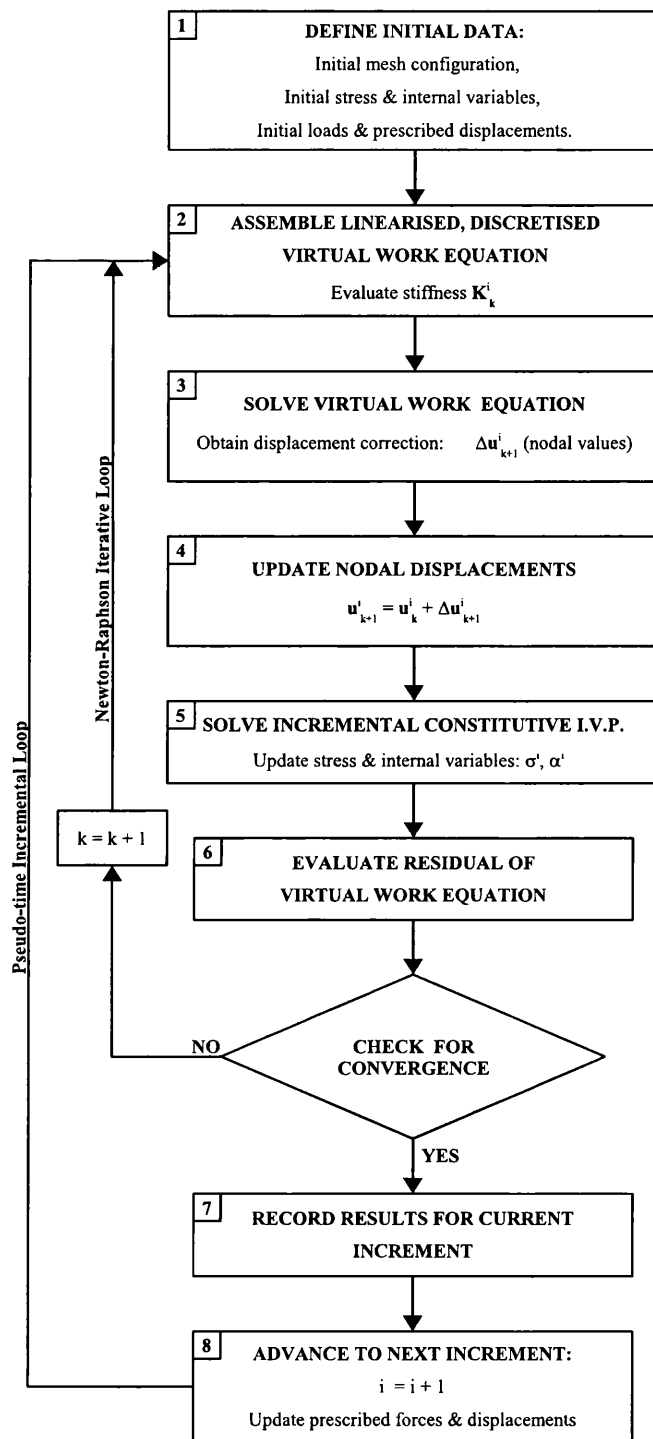


Figure 3.2: An algorithm to solve nonlinear quasi-static mechanical problems.

Chapter 4

Computational homogenisation

4.1 Introduction

This chapter is concerned with the formulation of homogenised constitutive models. These attempt to represent a heterogeneous material as a macroscopic continuum whose stress response at any point is derived from the behaviour of a small domain representing the local microstructure. This microscopic domain is known as a *representative volume element* (RVE). We adopt a deformation driven approach. Accordingly the homogenised constitutive model defines the macroscopic stress response to a macroscopic deformation gradient history as the average microscopic stress over the RVE when it is in equilibrium and subject to some chosen kinematical constraints. Among these constraints is the crucial condition that the average deformation gradient history should equal the given macroscopic deformation gradient history. The homogenised response is thus obtained through the solution of a microscopic boundary value problem on the RVE.

In this chapter we follow [16] in developing the homogenization procedure in terms of variational equations. We begin by introducing the fundamental concepts required of the theory. These are then used to describe the equilibrium problem for the minimum kinematical constraint and its use in defining a homogenised constitutive law. Alternative boundary conditions are discussed in subsequent sections. Following this some observations on the relationship between the symmetry of the RVE and the material symmetry of the homogenised constitutive response are offered. The final section of the chapter provides details of how the homogenisation procedure may be discretised and carried out using the finite element method.

4.2 The representative volume element

At each point $\mathbf{X} \in \Omega_0$ in the reference configuration of the macroscopic body \mathcal{B} we associate a *representative volume element* usually abbreviated to *RVE*. This is a microscopic continuum body chosen to be statistically representative of the local microstructure and occupying a neighbourhood around \mathbf{X} which is small in comparison to the macroscopic body. Figure 4.1 illustrates the concept. The Lagrangian position of a point within the microscopic domain $\Omega_{\mu 0}$ is denoted by \mathbf{Y} . The boundary of $\Omega_{\mu 0}$ is denoted $\partial\Omega_{\mu 0}$ and its reference volume is V_μ .

Note that we use the terms microscopic and macroscopic only to distinguish the scale of the RVE from that of the overall body and not to imply any absolute scale. The characteristic length of the RVE should be much smaller than that of macro body but large enough compared to atomic structures so that the continuum hypothesis may be applied.

The geometry of each RVE and the constitutive laws governing its constituents are assumed to be known. Thus \mathfrak{P}_μ , the functional giving the microscopic first Piola-Kirchhoff stress according to

$$\mathbf{P}_\mu(\mathbf{Y}) = \mathfrak{P}_\mu(\mathbf{F}_\mu^t; \mathbf{Y}), \quad (4.1)$$

is fully specified over the whole RVE in terms of the history of the microscopic deformation gradient \mathbf{F}_μ^t at point \mathbf{Y} . Here we assume that the micro-constituents are simple materials. In general the RVE may contain different solid phases as well voids. However we shall develop the homogenisation problem on the assumption that there are no voids present. This simplifies the required equations somewhat without losing sight of the main principles.

The vital concept of the RVE is discussed more fully in [83].

4.3 Definition of averaged quantities

The volume average of a general field quantity over the RVE with respect to the reference configuration is defined by

$$\langle \bullet \rangle_0 = \frac{1}{V_\mu} \int_{\Omega_{\mu 0}} \bullet dV. \quad (4.2)$$

Of particular importance are the average microscopic deformation gradient

$$\langle \mathbf{F}_\mu \rangle_0 = \frac{1}{V_\mu} \int_{\Omega_{\mu 0}} \mathbf{F}_\mu(\mathbf{Y}) dV, \quad (4.3)$$

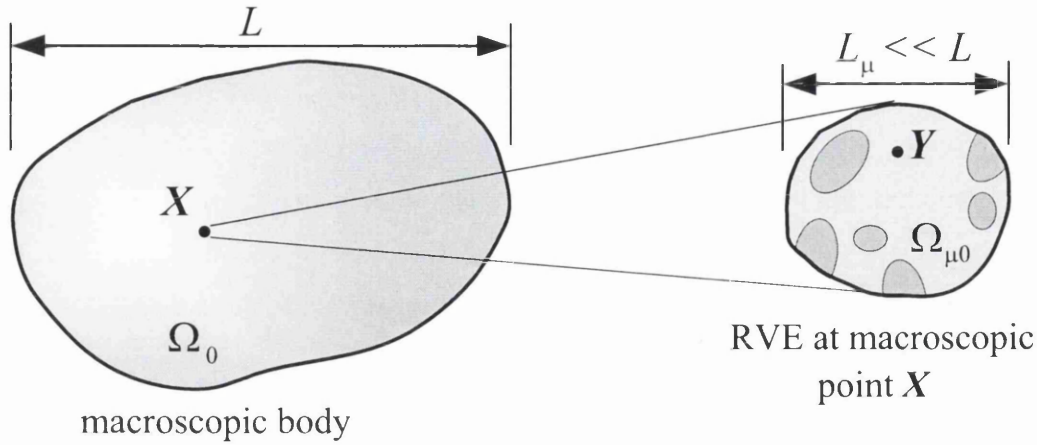


Figure 4.1: Volume element representing microstructure at reference point \mathbf{X} in a macroscopic body.

and the average first Piola-Kirchhoff stress

$$\langle \mathbf{P}_\mu \rangle_0 = \frac{1}{V_\mu} \int_{\Omega_{\mu 0}} \mathbf{P}_\mu(\mathbf{Y}) dV, \quad (4.4)$$

where we use the subscript μ to indicate fields defined over the microscopic RVE domain.

It is sometimes useful to express the average stress in terms of boundary values. This can be achieved as follows

$$\begin{aligned} \frac{1}{V_\mu} \int_{\Omega_{\mu 0}} \mathbf{P}_\mu dV &= \frac{1}{V_\mu} \int_{\Omega_{\mu 0}} \mathbf{P}_\mu \mathbf{I} dV \\ &= \frac{1}{V_\mu} \int_{\Omega_{\mu 0}} \mathbf{P}_\mu (\nabla_{\mathbf{Y}} \mathbf{Y})^T dV \\ &= \frac{1}{V_\mu} \int_{\partial\Omega_{\mu 0}} (\mathbf{P}_\mu \mathbf{N}) \otimes \mathbf{Y} dA - \frac{1}{V_\mu} \int_{\Omega_{\mu 0}} (\text{Div}_{\mathbf{Y}} \mathbf{P}_\mu) \otimes \mathbf{Y} dV, \end{aligned} \quad (4.5)$$

where integration by parts has been used for the last step and $\nabla_{\mathbf{Y}}$ and $\text{Div}_{\mathbf{Y}}$ are the material gradient and divergence respectively with respect to microscopic reference position \mathbf{Y} .

One could equally adopt a spatial formulation in terms of the average of the microscopic Cauchy stress $\boldsymbol{\sigma}_\mu$ with respect to *deformed* volume

$$\langle \boldsymbol{\sigma}_\mu \rangle = \frac{1}{v_\mu} \int_{\Omega_\mu} \boldsymbol{\sigma}_\mu dv, \quad (4.6)$$

where v_μ is the volume of the deformed RVE occupying the region Ω_μ . However it should be noted that such spatially averaged stress is not mechanically equivalent to

the materially averaged stress (4.4) in the sense that in general

$$\langle \boldsymbol{\sigma}_\mu \rangle \neq \frac{1}{\det(\langle \mathbf{F}_\mu \rangle_0)} \langle \mathbf{P}_\mu \rangle_0 \langle \mathbf{F}_\mu \rangle_0^T \quad (4.7)$$

That is to say that the usual relationship between Cauchy stress and first Piola-Kirchhoff stress (2.68) does not necessarily extend to their averages. In some special cases equality in expression (4.7) can be proved [16] however in the present work we shall only use material averaging.

4.4 Split between homogeneous deformation and fluctuations

The deformed position of the particle previously at \mathbf{Y} in the reference configuration is denoted $\mathbf{y}(\mathbf{Y}, t) = \mathbf{Y} + \mathbf{U}_\mu(\mathbf{Y}, t)$. It proves to be useful to split this into two parts: the first representing a homogeneous deformation with deformation gradient equal to the macroscopic deformation gradient $\mathbf{F}(\mathbf{X}, t)$ and the second a remainder term known as the *displacement fluctuation*. Accordingly we write

$$\mathbf{y}(\mathbf{Y}, t) = \mathbf{F}(\mathbf{X}, t)\mathbf{Y} + \tilde{\mathbf{U}}_\mu(\mathbf{Y}, t), \quad (4.8)$$

where $\tilde{\mathbf{U}}_\mu$ denotes the field of displacement fluctuations. Similarly the total displacement \mathbf{U}_μ may be split into a part associated with the homogeneous deformation and the fluctuation part so that

$$\mathbf{U}_\mu = \mathbf{y} - \mathbf{Y} = (\mathbf{F} - \mathbf{I})\mathbf{Y} + \tilde{\mathbf{U}}_\mu, \quad (4.9)$$

where for simplicity of presentation we have dropped the explicit functional dependency on \mathbf{X} , \mathbf{Y} and t . The additive split also leads to the following expression for the microscopic deformation gradient

$$\mathbf{F}_\mu = \nabla_{\mathbf{Y}} \mathbf{y} = \mathbf{F} + \nabla_{\mathbf{Y}} \tilde{\mathbf{U}}_\mu. \quad (4.10)$$

where $\nabla_{\mathbf{Y}}$ represents the material gradient with respect to the microscopic reference position \mathbf{Y} .

4.5 Equilibrium of the RVE

In the absence of constraints the equilibrium of the RVE is expressed in the strong form as

$$\begin{cases} \text{Div}_{\mathbf{Y}} \mathbf{P}_\mu + \mathbf{B}_\mu = \mathbf{0} & \text{in } \Omega_{\mu 0} \\ \mathbf{P}_\mu \mathbf{N} + \mathbf{T}_\mu = \mathbf{0} & \text{on } \partial\Omega_{\mu 0} \end{cases}, \quad (4.11)$$

where \mathbf{B}_μ is the body force per unit reference volume, \mathbf{T}_μ is the traction per unit reference area on the boundary surface having normal \mathbf{N} and $\text{Div}_{\mathbf{Y}}$ represents the divergence with respect to reference position \mathbf{Y} . The equivalent statement of equilibrium in the weak or variational form is the virtual work equation,

$$\int_{\Omega_{\mu 0}} \mathbf{P}_\mu : \nabla_{\mathbf{Y}} \boldsymbol{\eta} dV - \int_{\Omega_{\mu 0}} \mathbf{B}_\mu \cdot \boldsymbol{\eta} dV - \int_{\partial\Omega_{\mu 0}} \mathbf{T}_\mu \cdot \boldsymbol{\eta} dA = 0 \quad \forall \boldsymbol{\eta} \in \mathcal{V}_\mu, \quad (4.12)$$

where \mathcal{V}_μ is the space of kinematically admissible variations in the displacement field. This space has not been specified yet but will be defined by the kinematic constraints applied to the RVE.

4.6 Constraints

Two fundamental constraints are imposed on the motion of the RVE. The first of these is the kinematical constraint that ensures that the motion of the RVE is driven by the history of the macroscopic deformation. The second enforces consistency between microscopic and macroscopic stress power. Further kinematical constraints may be applied to obtain different classes of homogenised constitutive models.

4.6.1 Prescribed average deformation gradient – the minimal kinematic constraint

In the deformation driven approach to homogenisation, as adopted in this chapter and throughout the thesis, the average deformation gradient history is taken as a given. That is to say that at all times the average of the microscopic deformation gradient field is constrained to be equal to the prescribed macroscopic value $\mathbf{F}(\mathbf{X}, t)$:

$$\langle \mathbf{F}_\mu \rangle_0 = \mathbf{F}. \quad (4.13)$$

Equation (4.13) represents the *minimal* kinematic constraint that needs to be applied to the RVE in the formulation of a deformation driven homogenised constitutive

model. Further kinematic constraints may be imposed as long as (4.13) remains in force.

The minimal constraint may be expressed in terms of displacement fluctuations on the RVE boundary. To see this equation (4.10), reflecting the additive split in the displacement field, is used to substitute for \mathbf{F}_μ in the kinematic constraint equation (4.13) leading to:

$$\begin{aligned}
& \langle \mathbf{F} + \nabla_{\mathbf{Y}} \tilde{\mathbf{U}}_\mu \rangle_0 = \mathbf{F} \\
& \Leftrightarrow \frac{1}{V_\mu} \int_{\Omega_{\mu 0}} [\mathbf{F} + \nabla_{\mathbf{Y}} \tilde{\mathbf{U}}_\mu] dV = \mathbf{F} \\
& \Leftrightarrow \int_{\Omega_{\mu 0}} \nabla_{\mathbf{Y}} \tilde{\mathbf{U}}_\mu dV = \mathbf{0} \\
& \Leftrightarrow \int_{\partial\Omega_{\mu 0}} \tilde{\mathbf{U}}_\mu \otimes \mathbf{N} dA = \mathbf{0}, \tag{4.14}
\end{aligned}$$

where the last step follows from use of the divergence theorem. Equation (4.14) represents a restatement of the essential kinematic constraint (4.13).

4.6.2 Kinematically admissible fluctuations under the minimal constraint

We define the set of minimally constrained kinematically admissible fluctuations as those fields $\tilde{\mathbf{U}}_\mu(\mathbf{Y})$ that satisfy (4.14). Denoting this set by \mathcal{K}_μ^* we write this definition formally as

$$\mathcal{K}_\mu^* \equiv \left\{ \tilde{\mathbf{U}}_\mu, \text{ sufficiently regular } \mid \int_{\partial\Omega_{\mu 0}} \tilde{\mathbf{U}}_\mu \otimes \mathbf{N} dA = \mathbf{0} \right\}, \tag{4.15}$$

where by “sufficiently regular” we mean that the field is smooth and regular enough that all required operations on it are well defined. It may easily be shown that \mathcal{K}_μ^* constitutes a vector space. The set of minimally constrained kinematically admissible total displacements is now given by

$$\mathcal{K}_\mu^* \equiv \left\{ \mathbf{U}_\mu = (\mathbf{F} - \mathbf{I})\mathbf{Y} + \tilde{\mathbf{U}}_\mu \mid \tilde{\mathbf{U}}_\mu \in \mathcal{K}_\mu^* \right\}, \tag{4.16}$$

We may also define the set of virtual displacements consistent with the minimum kinematic constraint in terms of \mathcal{K}_μ^* . These are variations in the kinematically admissible displacement fields and so any virtual displacement may be expressed as a difference between two admissible displacements. Accordingly we write the set of

minimally constraint kinematically admissible virtual displacements as

$$\mathcal{V}_\mu^* \equiv \{ \boldsymbol{\eta} = \dot{\mathbf{U}}_1 - \mathbf{U}_2 \mid \mathbf{U}_1, \mathbf{U}_2 \in \mathcal{K}_\mu^* \} , \quad (4.17)$$

which in view of the definition of $\tilde{\mathcal{K}}_\mu^*$ (4.16) is equivalent to

$$\mathcal{V}_\mu^* \equiv \{ \boldsymbol{\eta} = \tilde{\mathbf{U}}_1 - \tilde{\mathbf{U}}_2 \mid \tilde{\mathbf{U}}_1, \tilde{\mathbf{U}}_2 \in \tilde{\mathcal{K}}_\mu^* \} . \quad (4.18)$$

However given that $\tilde{\mathcal{K}}_\mu^*$ is clearly closed under addition and subtraction we have simply

$$\mathcal{V}_\mu^* = \tilde{\mathcal{K}}_\mu^* . \quad (4.19)$$

It shall also be useful to consider the fluctuation velocities $\dot{\tilde{\mathbf{U}}}_\mu$. It is easy to see that the velocities of kinematically admissible fluctuations under the minimal constraint satisfy the rate form of equation (4.14):

$$\int_{\partial\Omega_{\mu 0}} \dot{\tilde{\mathbf{U}}}_\mu \otimes \mathbf{N} dA = \mathbf{0} . \quad (4.20)$$

In other words $\tilde{\mathbf{U}}_\mu$ and $\dot{\tilde{\mathbf{U}}}_\mu$ satisfy the same constraint equation. Thus the set of minimally constrained kinematically admissible fluctuation velocities is equal to $\tilde{\mathcal{K}}_\mu^*$ – the same space occupied by minimally constrained admissible fluctuations and virtual displacements.

4.6.3 Admissible fluctuations under general kinematic constraints

In defining any homogenised constitutive model kinematical constraints are applied to the RVE in order to define a well posed equilibrium problem. These impose restrictions on the allowable deformed configurations and define the set $\tilde{\mathcal{K}}_\mu$ of kinematically admissible displacement fluctuation fields. Specific examples of such constraints are described later in this chapter. However the essential kinematical constraint expressed equivalently by equations (4.13) and (4.14) must always be satisfied. It follows that any kinematically admissible fluctuation field must belong to the minimally constrained set $\tilde{\mathcal{K}}_\mu^* = \mathcal{V}_\mu^*$. In other words

$$\tilde{\mathcal{K}}_\mu \subset \mathcal{V}_\mu^* . \quad (4.21)$$

The corresponding set of kinematically admissible displacement fields is readily obtained as

$$\mathcal{K}_\mu \equiv \{ \mathbf{U}_\mu = (\mathbf{F} - \mathbf{I})\mathbf{Y} + \tilde{\mathbf{U}}_\mu \mid \tilde{\mathbf{U}}_\mu \in \tilde{\mathcal{V}}_\mu \} , \quad (4.22)$$

and clearly in view of (4.21) and the definition (4.16) of \mathcal{K}_μ^*

$$\mathcal{K}_\mu \subset \mathcal{K}_\mu^* . \quad (4.23)$$

Under the same constraints the set of kinematically admissible virtual displacements is given by

$$\begin{aligned} \mathcal{V}_\mu &\equiv \{ \boldsymbol{\eta} = \mathbf{U}_1 - \mathbf{U}_2 \mid \mathbf{U}_1, \mathbf{U}_2 \in \mathcal{K}_\mu \} \\ &= \left\{ \boldsymbol{\eta} = \tilde{\mathbf{U}}_1 - \tilde{\mathbf{U}}_2 \mid \tilde{\mathbf{U}}_1, \tilde{\mathbf{U}}_2 \in \tilde{\mathcal{K}}_\mu \right\} . \end{aligned} \quad (4.24)$$

Assuming that the set $\tilde{\mathcal{K}}_\mu$ is closed under subtraction then we have

$$\mathcal{V}_\mu = \tilde{\mathcal{K}}_\mu . \quad (4.25)$$

We shall also assume that just as all minimally constrained admissible fluctuation velocities belong to the minimally constrained set of virtual displacements, in the case of general constraints every kinematically admissible fluctuation velocity $\dot{\tilde{\mathbf{U}}}_\mu$ satisfies

$$\dot{\tilde{\mathbf{U}}}_\mu \in \mathcal{V}_\mu . \quad (4.26)$$

4.6.4 The Hill-Mandel principle

The Hill-Mandel principle of macro-homogeneity [47,48,70] is a requirement, based on physical considerations, that the average microscopic stress power over the RVE should equal the stress power derived from the averaged stress and its conjugate averaged deformation gradient. In the present finite deformation context this condition is expressed by

$$\langle \mathbf{P}_\mu : \dot{\mathbf{F}}_\mu \rangle_0 = \langle \mathbf{P}_\mu \rangle_0 : \langle \dot{\mathbf{F}}_\mu \rangle_0 , \quad (4.27)$$

which must be satisfied for all microscopic stress fields \mathbf{P}_μ in equilibrium and all microscopic deformation gradient fields \mathbf{F}_μ that are consistent with the kinematic constraints. Note that since time differentiation and material averaging are interchangeable, $\langle \dot{\mathbf{F}}_\mu \rangle_0$ is equal to the material time derivative of $\langle \mathbf{F}_\mu \rangle_0$.

The additive split described in section 4.4 is also useful in simplifying the expression of the Hill-Mandel principle. Using the material time derivative of equation

(4.10) to substitute for \mathbf{F}_μ in (4.27) gives

$$\begin{aligned}
& \langle \mathbf{P}_\mu : (\dot{\mathbf{F}} + \nabla_{\mathbf{Y}} \dot{\mathbf{U}}_\mu) \rangle_0 = \langle \mathbf{P}_\mu \rangle_0 : \langle \dot{\mathbf{F}}_\mu \rangle_0 \\
& \Leftrightarrow \langle \mathbf{P}_\mu : \dot{\mathbf{F}} \rangle_0 + \frac{1}{V_\mu} \int_{\Omega_{\mu 0}} \mathbf{P}_\mu : \nabla_{\mathbf{Y}} \dot{\mathbf{U}}_\mu dV = \langle \mathbf{P}_\mu \rangle_0 : \langle \dot{\mathbf{F}}_\mu \rangle_0 \\
& \Leftrightarrow \langle \mathbf{P}_\mu \rangle_0 : \langle \dot{\mathbf{F}}_\mu \rangle_0 + \frac{1}{V_\mu} \int_{\Omega_{\mu 0}} \mathbf{P}_\mu : \nabla_{\mathbf{Y}} \dot{\mathbf{U}}_\mu dV = \langle \mathbf{P}_\mu \rangle_0 : \langle \dot{\mathbf{F}}_\mu \rangle_0 \\
& \Leftrightarrow \int_{\Omega_{\mu 0}} \mathbf{P}_\mu : \nabla_{\mathbf{Y}} \dot{\mathbf{U}}_\mu dV = 0.
\end{aligned} \tag{4.28}$$

Integrating this last equation by parts leads to

$$\int_{\partial\Omega_{\mu 0}} (\mathbf{P}_\mu \mathbf{N}) \cdot \dot{\mathbf{U}}_\mu dA - \int_{\Omega_{\mu 0}} (\text{Div}_{\mathbf{Y}} \mathbf{P}_\mu) \cdot \dot{\mathbf{U}}_\mu dV = 0. \tag{4.29}$$

This equation must hold for each kinematically admissible field $\dot{\mathbf{U}}_\mu$. In view of (4.26) equation (4.29) may be written as

$$\int_{\partial\Omega_{\mu 0}} (\mathbf{P}_\mu \mathbf{N}) \cdot \boldsymbol{\eta} dA - \int_{\Omega_{\mu 0}} (\text{Div}_{\mathbf{Y}} \mathbf{P}_\mu) \cdot \boldsymbol{\eta} dV = 0 \quad \forall \boldsymbol{\eta} \in \mathcal{V}_\mu. \tag{4.30}$$

The equilibrium equations in their strong form (4.11) may be used to substitute for $\mathbf{P}_\mu \mathbf{N}$ and $\text{Div}_{\mathbf{Y}} \mathbf{P}_\mu$ to obtain

$$\int_{\partial\Omega_{\mu 0}} \mathbf{T}_\mu \cdot \boldsymbol{\eta} dA - \int_{\Omega_{\mu 0}} \mathbf{B}_\mu \cdot \boldsymbol{\eta} dV = 0 \quad \forall \boldsymbol{\eta} \in \mathcal{V}_\mu. \tag{4.31}$$

It suffices to set the field $\boldsymbol{\eta}$ to zero ($\mathbf{0} \in \mathcal{V}_\mu$) on the interior and boundary of $\Omega_{\mu 0}$ in turn to establish that each of the two terms in (4.31) above must vanish separately. That is

$$\int_{\partial\Omega_{\mu 0}} \mathbf{T}_\mu \cdot \boldsymbol{\eta} dA = 0 \quad \forall \boldsymbol{\eta} \in \mathcal{V}_\mu \tag{4.32}$$

$$\int_{\Omega_{\mu 0}} \mathbf{B}_\mu \cdot \boldsymbol{\eta} dV = 0 \quad \forall \boldsymbol{\eta} \in \mathcal{V}_\mu, \tag{4.33}$$

so that body forces and tractions are seen to be reaction forces required by the kinematic constraints.

We may use equations (4.32) and (4.33) to simplify the virtual work equilibrium equation (4.12) thus obtaining

$$\int_{\Omega_{\mu 0}} \mathbf{P}_\mu : \nabla_{\mathbf{Y}} \boldsymbol{\eta} dV = 0 \quad \forall \boldsymbol{\eta} \in \mathcal{V}_\mu, \tag{4.34}$$

4.7 The RVE equilibrium problem

We may now define the *RVE equilibrium problem* as the task of finding the history of displacement fluctuations that at all times conform to the chosen kinematic constraints and give rise to microscopic stresses which satisfy the Hill-Mandel principle and maintain the equilibrium of the RVE. The variational expression of this problem is shown in box 1.

Box 1: Variational statement of the RVE equilibrium problem

Given:

1. the geometrical and constitutive details of the RVE domain $\Omega_{\mu 0}$ (including the microscopic constitutive functional \mathfrak{P}_{μ} everywhere in the RVE),
2. the history of the macroscopic deformation \mathbf{F}^t
and
3. the definition of the space of kinematically admissible microscopic fluctuations \mathcal{V}_{μ} , where $\mathcal{V}_{\mu} \subset \left\{ \boldsymbol{\eta}, \text{ sufficiently regular} \mid \int_{\partial\Omega_{\mu 0}} \boldsymbol{\eta} \otimes \mathbf{N} dA = 0 \right\}$

find the history of microscopic displacement fluctuation fields $\tilde{\mathbf{U}}_{\mu} \in \mathcal{V}_{\mu}$ that satisfies

$$\int_{\Omega_{\mu 0}} \mathfrak{P}_{\mu}([\mathbf{F} + \nabla_{\mathbf{Y}} \tilde{\mathbf{U}}_{\mu}]^t) : \nabla_{\mathbf{Y}} \boldsymbol{\eta} dV = 0 \quad \forall \boldsymbol{\eta} \in \mathcal{V}_{\mu}$$

at each instant in the history of the macroscopic deformation gradient.

4.8 The homogenised constitutive functional

The *homogenised constitutive functional* is defined in the present context as the functional $\bar{\mathfrak{P}}$ which for a given macroscopic deformation history returns the average first Piola-Kirchhoff stress $\langle \mathbf{P}_{\mu} \rangle_0$ derived from the solution of the RVE equilibrium problem. Formally we write that the macroscopic first Piola-Kirchhoff stress is given by:

$$\mathbf{P} = \bar{\mathfrak{P}}(\mathbf{F}^t; \mathbf{X}) = \langle \mathfrak{P}_{\mu}([\mathbf{F} + \nabla_{\mathbf{Y}} \tilde{\mathbf{U}}_{\mu}]^t; \mathbf{Y}) \rangle_0, \quad (4.35)$$

where $\tilde{\mathbf{U}}_{\mu}^t$ solves the RVE equilibrium problem (Box 1).

4.9 Homogenisation with elastic and hyperelastic micro-constituents

The homogenised constitutive response always defines a simple material since the history of the macroscopic deformation gradient wholly determines the stress. Furthermore if the RVE is made up entirely from Cauchy elastic materials then clearly the homogenised stress is also independent of the deformation history and is itself Cauchy elastic.

If the micro-constituents of the RVE are all hyperelastic then there exists a microscopic strain energy field (per unit volume) such that

$$\mathbf{P}_\mu = \frac{\partial \Psi_\mu}{\partial \mathbf{F}_\mu}, \quad (4.36)$$

everywhere in the RVE. We may use this expression in the Hill Mandel equation (4.27) to obtain

$$\begin{aligned} \mathbf{P} : \dot{\mathbf{F}} &= \frac{1}{V_\mu} \int_{\Omega_{\mu 0}} \frac{\partial \Psi_\mu}{\partial \mathbf{F}_\mu} : \dot{\mathbf{F}}_\mu dV \\ &= \frac{1}{V_\mu} \int_{\Omega_{\mu 0}} \dot{\Psi}_\mu dV \\ &= \frac{D \langle \Psi_\mu \rangle_0}{Dt}. \end{aligned} \quad (4.37)$$

Integrating with respect to time gives

$$\langle \Psi_\mu \rangle_0 = \int \mathbf{P} : \dot{\mathbf{F}} dt, \quad (4.38)$$

so that

$$\begin{aligned} \frac{\partial \langle \Psi_\mu \rangle_0}{\partial \mathbf{F}} &= \frac{\partial}{\partial \mathbf{F}} \left(\int \mathbf{P} : \dot{\mathbf{F}} dt \right) \\ &= \int \frac{\partial \mathbf{P}}{\partial \mathbf{F}} : \dot{\mathbf{F}} dt + \int \mathbf{P} : \frac{\partial \dot{\mathbf{F}}}{\partial \mathbf{F}} dt \\ &= \mathbf{P}. \end{aligned} \quad (4.39)$$

Thus provided the RVE is composed of hyperelastic constituents the homogenised constitutive model is itself hyperelastic with a macroscopic strain energy function defined by

$$\Psi = \langle \Psi_\mu \rangle_0, \quad (4.40)$$

and the macroscopic first Piola-Kirchhoff stress is given by

$$\mathbf{P} = \frac{\partial \Psi}{\partial \mathbf{F}}. \quad (4.41)$$

4.10 Some specific kinematic constraints

The homogenised macroscopic model depends not only on the geometrical and constitutive details of the RVE but also on the chosen kinematical constraints applied to it. In this section we review four constraint conditions commonly encountered in the literature. Each of these defines a class of homogenised constitutive functionals and is characterised by the definition of the set of kinematically virtual displacements \mathcal{V}_μ . As explained in section 4.6.3 the set of kinematically admissible displacement fluctuations is identical to this.

Following conventional usage we sometimes refer to the kinematical constraints as boundary conditions although in one case displacements are constrained at the interior of the RVE as well as on its boundary.

4.10.1 The minimal constraint: uniform traction on boundary

The minimal kinematic constraint has already been introduced in sections 4.6.1 and 4.6.2. It is defined by the following set of kinematically admissible virtual displacements (equal to the set of admissible displacement fluctuations)

$$\mathcal{V}_\mu^{\text{tract}} = \tilde{\mathcal{K}}_\mu^* \equiv \left\{ \boldsymbol{\eta}, \text{ sufficiently regular} \mid \int_{\partial\Omega_{\mu 0}} \boldsymbol{\eta} \otimes \mathbf{N} dA = \mathbf{0} \right\}. \quad (4.42)$$

Body forces under the minimum kinematic constraint

We consider again the variational statement of the Hill-Mandel principle represented by equations (4.32) and (4.33). Under the minimal constraint equation (4.33) becomes

$$\int_{\Omega_{\mu 0}} \mathbf{B}_\mu \cdot \boldsymbol{\eta} dV = 0 \quad \forall \boldsymbol{\eta} \in \mathcal{V}_\mu^{\text{tract}},$$

and noting that $\boldsymbol{\eta} \in \mathcal{V}_\mu^{\text{tract}}$ is only constrained on the boundary surface $\partial\Omega_{\mu 0}$ it follows that

$$\mathbf{B}_\mu(\mathbf{Y}) = \mathbf{0} \quad \forall \mathbf{Y} \in \Omega_{\mu 0}. \quad (4.43)$$

Note that in some treatments of the subject the absence of body forces is taken as an assumption and the Hill-Mandel principle is verified on this basis. Here the Hill-Mandel principle is taken as an axiom from which (4.43) follows.

Surface tractions under the minimum kinematic constraint

Consider next the other Hill-Mandel variational equation (4.32) which for $\mathcal{V}_\mu = \mathcal{V}_\mu^{\text{tract}}$ is written

$$\int_{\partial\Omega_{\mu 0}} \mathbf{T}_\mu \cdot \boldsymbol{\eta} dA = \int_{\partial\Omega_{\mu 0}} (\mathbf{P}_\mu \mathbf{N}) \cdot \boldsymbol{\eta} dA = 0 \quad \forall \boldsymbol{\eta} \in \mathcal{V}_\mu^{\text{tract}},$$

It may be shown (see appendix in [16]) that this leads to the conclusion that

$$\mathbf{P}_\mu(\mathbf{Y}, t) \mathbf{N}(\mathbf{Y}) = \mathbf{P}(\mathbf{X}, t) \mathbf{N}(\mathbf{Y}) \quad \forall \mathbf{Y} \in \partial\Omega_{\mu 0}. \quad (4.44)$$

That is the traction on the boundary of the RVE is equal to the traction of the average stress. This result is often taken as a definition of the so called *uniform traction boundary condition* which is an alternative name for the minimal kinematic constraint.

The proof of (4.44) requires us to consider the microscopic vector fields \mathbf{N}_1 , \mathbf{N}_2 and \mathbf{N}_3 which represent respectively the normal to the RVE boundary $\partial\Omega_{\mu 0}$ and some choices of vectors tangential to $\partial\Omega_{\mu 0}$ such that $(\mathbf{N}_1, \mathbf{N}_2, \mathbf{N}_3)$ forms a local orthonormal basis at each point on the boundary. We then consider the uniform 2^{nd} rank tensor \mathbf{Q} that satisfies

$$\mathbf{Q} : \int_{\partial\Omega_{\mu 0}} \mathbf{Z} \otimes \mathbf{N}_1 dA = \int_{\partial\Omega_{\mu 0}} \mathbf{P}_\mu : \mathbf{Z} \otimes \mathbf{N}_1 dA, \quad (4.45)$$

where the third order tensor \mathbf{Z} is given by

$$\mathbf{Z} = \sum_{i=1}^3 \mathbf{N}_i \otimes \mathbf{N}_1 \otimes \mathbf{N}_i. \quad (4.46)$$

The existence of \mathbf{Z} is guaranteed by the invertibility of $\int_{\partial\Omega_{\mu 0}} \mathbf{Z} \otimes \mathbf{N} dA$ which is assured for a closed boundary $\partial\Omega_{\mu 0}$ (see appendix of [16]). Now rearranging (4.45) gives

$$\int_{\partial\Omega_{\mu 0}} (\mathbf{P}_\mu - \mathbf{Q}) : \mathbf{Z} \otimes \mathbf{N}_1 dA = 0, \quad (4.47)$$

from which it follows that the vector $(\mathbf{P}_\mu - \mathbf{Q}) : \mathbf{Z}$ belongs to the set of kinematically admissible virtual displacements $\mathcal{V}_\mu^{\text{tract}}$. We can therefore obtain from (4.44) the

particular case

$$\begin{aligned}
& \int_{\partial\Omega_{\mu 0}} (\mathbf{P}_\mu \mathbf{N}_1) \cdot [(\mathbf{P}_\mu - \mathbf{Q}) : \mathbf{Z}] dA = 0 \\
& \Rightarrow \int_{\partial\Omega_{\mu 0}} \mathbf{P}_\mu : [(\mathbf{P}_\mu - \mathbf{Q}) : \mathbf{Z} \otimes \mathbf{N}_1] dA = 0 \\
& \Rightarrow \int_{\partial\Omega_{\mu 0}} (\mathbf{Q} + \mathbf{P}_\mu - \mathbf{Q}) : [(\mathbf{P}_\mu - \mathbf{Q}) : \mathbf{Z} \otimes \mathbf{N}_1] dA = 0 \\
& \Rightarrow \mathbf{Q} : \int_{\partial\Omega_{\mu 0}} (\mathbf{P}_\mu - \mathbf{Q}) : \mathbf{Z} \otimes \mathbf{N}_1 dA \tag{4.48}
\end{aligned}$$

$$+ \int_{\partial\Omega_{\mu 0}} (\mathbf{P}_\mu - \mathbf{Q}) : [(\mathbf{P}_\mu - \mathbf{Q}) : \mathbf{Z} \otimes \mathbf{N}_1] dA = 0, \tag{4.49}$$

In light of equation (4.47) the first term above vanishes. Introducing $\tilde{\mathbf{P}}_\mu = \mathbf{P}_\mu - \mathbf{Q}$ we are left with

$$\int_{\partial\Omega_{\mu 0}} \tilde{\mathbf{P}}_\mu : [\tilde{\mathbf{P}}_\mu : \mathbf{Z} \otimes \mathbf{N}_1] dA = 0. \tag{4.50}$$

Expanding this from the definition of \mathbf{Z} (4.46) gives

$$\begin{aligned}
& \sum_{i=1}^3 \int_{\partial\Omega_{\mu 0}} \tilde{\mathbf{P}}_\mu : (\tilde{\mathbf{P}}_\mu : \mathbf{N}_i \otimes \mathbf{N}_1 \otimes \mathbf{N}_i \otimes \mathbf{N}_1) dA = 0 \\
& \Rightarrow \sum_{i=1}^3 \int_{\partial\Omega_{\mu 0}} (\tilde{\mathbf{P}}_\mu : \mathbf{N}_i \otimes \mathbf{N}_1)^2 dA = 0. \tag{4.51}
\end{aligned}$$

Since (4.51) is a sum and integral of non-negative terms it follows that each integrand vanishes so that

$$\tilde{\mathbf{P}}_\mu : \mathbf{N}_i \otimes \mathbf{N}_1 = 0 \quad \text{for } i = 1, 2, 3. \tag{4.52}$$

Hence

$$\begin{aligned}
& \sum_{i=1}^3 (\tilde{\mathbf{P}}_\mu : \mathbf{N}_i \otimes \mathbf{N}_1) \mathbf{N}_i = \tilde{\mathbf{P}}_\mu \mathbf{N}_1 = \mathbf{0} \\
& \Rightarrow \mathbf{P}_\mu \mathbf{N}_1 = \mathbf{Q} \mathbf{N}_1. \tag{4.53}
\end{aligned}$$

Now from (4.43) the body force over the RVE is zero so expression (4.5) for the average first Piola-Kirchhoff stress becomes with the use of (4.53)

$$\begin{aligned}
\mathbf{P} &= \frac{1}{V_\mu} \int_{\partial\Omega_{\mu 0}} (\mathbf{Q}_\mu \mathbf{N}) \otimes \mathbf{Y} dA \\
&= \mathbf{Q}_\mu \frac{1}{V_\mu} \int_{\partial\Omega_{\mu 0}} \mathbf{N} \otimes \mathbf{Y} dA \\
&= \mathbf{Q}_\mu \frac{1}{V_\mu} \int_{\Omega_{\mu 0}} (\nabla_{\mathbf{Y}} \mathbf{Y})^T dV \\
&= \mathbf{Q}_\mu, \tag{4.54}
\end{aligned}$$

where we now write \mathbf{N} instead of \mathbf{N}_1 for the normal to the boundary surface. Thus on the boundary the stress is uniformly equal to the average/macroscopic stress and from (4.53) we finally obtain (4.44)

$$\mathbf{P}_\mu(\mathbf{Y}, t)\mathbf{N}(\mathbf{Y}) = \mathbf{P}(\mathbf{X}, t)\mathbf{N}(\mathbf{Y}) \quad \forall \mathbf{Y} \in \partial\Omega_{\mu 0}. \quad (4.55)$$

4.10.2 The periodic boundary condition

The *periodic boundary condition* is motivated by consideration of materials which have a repetitive microstructure. That is to say microscopic structures that, in the terminology of crystallography, may be described by a *Bravais Lattice* and an associated *primitive cell* [2]. A Bravais lattice is defined as a set of position vectors of the form

$$\mathbf{r} = n_1\mathbf{a}_1 + n_2\mathbf{a}_2 + n_3\mathbf{a}_3, \quad (4.56)$$

where n_1 , n_2 and n_3 are arbitrary integers and \mathbf{a}_1 , \mathbf{a}_2 and \mathbf{a}_3 are specified vectors known as *primitive vectors*¹. The primitive vectors must be linearly independent so that they span \mathbb{R}^3 . A primitive cell on the other hand is a region of space which when translated by all the vectors of a Bravais lattice fills up all of \mathbb{R}^3 without overlapping or leaving any gaps. The whole periodic structure is thus obtained by describing a pattern over a primitive cell and repeating it at every lattice point. Note that different sets of primitive vectors may describe the same Bravais lattice. Likewise different primitive cells may occupy the same lattice. Thus when trying to describe a periodic pattern or structure neither the choice of primitive vectors nor the choice of primitive cell is unique. Figure 4.2(a) illustrates a two dimensional example of a periodic pattern. Two alternative sets of primitive vectors are drawn over the pattern. Figures 4.2(b) and 4.2(c) show two primitive cells (along with internal design) that generate the pattern in 4.2(a).

In the context of homogenisation theory we consider an RVE which occupies a primitive cell of a Bravais lattice appropriate to the periodic microstructure of the material to be modeled. Such an RVE is sometimes known as a representative unit cell. Replicating the RVE at each lattice point generates the complete microstructure. Under deformation it is assumed that the new configuration retains its periodicity. In order to make this assumption more precise and to see how it leads to a constraint on the boundary displacements we consider an RVE occupying a primitive cell $\Omega_{\mu 0}$

¹Some authors [74] use the term *periodicity frame* to refer to the basis of primitive vectors.

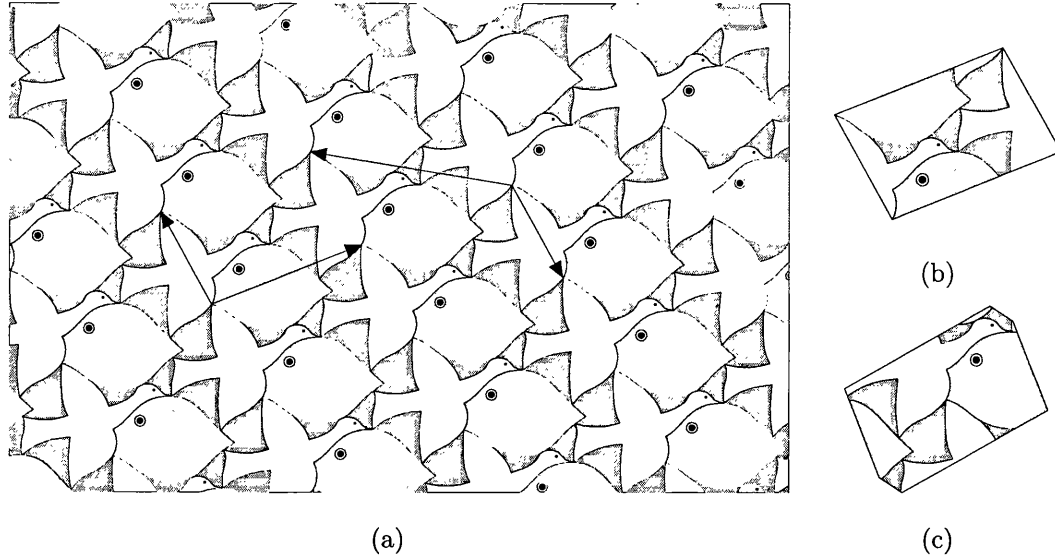


Figure 4.2: (a) A two dimensional periodic pattern with two choices of primitive vector sets indicated (after M.C. Escher). (b) & (c) Two primitive cells which, with the internal patterns shown, will generate the global pattern in (a).

with boundary $\partial\Omega_{\mu 0}$ that lies within an array of identical cells populating the Bravais lattice \mathcal{B} . Figure 4.3(a) shows the case of a two dimensional hexagonal pattern as an example but our discussion is quite general. Let $\Gamma_k^+ \subset \partial\Omega_{\mu 0}$ be the boundary between $\Omega_{\mu 0}$ and one of the neighbouring unit cells B_k^+ and let $\mathbf{r}_k \in \mathcal{B}$ be the translation vector that maps $\Omega_{\mu 0}$ onto B_k^+ (the significance of the superscripts and subscripts will shortly become apparent). Now Γ_k^+ may be considered common to $\Omega_{\mu 0}$ and B_k^+ so under the reverse translation $-\mathbf{r}_k$ which maps B_k^+ onto $\Omega_{\mu 0}$ it is mapped onto another part of $\partial\Omega_{\mu 0}$ which we denote Γ_k^- . Thus there are two distinct portions of the RVE boundary Γ_k^+ and Γ_k^- which correspond with each other through the translation \mathbf{r}_k . In a similar fashion the remaining cells adjacent to $\Omega_{\mu 0}$ may be grouped in pairs (B_i^-, B_i^+) which share with $\Omega_{\mu 0}$ the respective boundaries Γ_i^+ and Γ_i^- such that,

$$\bigcup_{i=1}^n (\Gamma_i^- \cup \Gamma_i^+) = \partial\Omega_{\mu 0}, \quad (4.57)$$

where n is the number of pairs of neighbouring cells and

$$\mathbf{Y}_i^- = \mathbf{Y}_i^+ - \mathbf{r}_i \in \Gamma_i^- \quad \forall \mathbf{Y}_i^+ \in \Gamma_i^+ \quad (4.58)$$

and

$$\mathbf{Y}_i^+ = \mathbf{Y}_i^- + \mathbf{r}_i \in \Gamma_i^+ \quad \forall \mathbf{Y}_i^- \in \Gamma_i^-, \quad (4.59)$$

for each i . Since Γ_i^+ and Γ_i^- are rigid translations of each other they necessarily have normals which at corresponding points \mathbf{Y}_i^- and \mathbf{Y}_i^+ are parallel but (defined in the outward direction from $\Omega_{\mu 0}$) opposite in sense. In other words

$$\mathbf{N}(\mathbf{Y}_i^-) = -\mathbf{N}(\mathbf{Y}_i^+) \quad \forall \mathbf{Y}_i^- \in \Gamma_i^-, \mathbf{Y}_i^+ \in \Gamma_i^+. \quad (4.60)$$

Having established the partition of the boundary and the pairing of boundary points described above we may now define the periodic boundary condition as the restriction that the deformed configuration of the RVE should maintain the periodicity of the reference configuration imposed by equations (4.58) and (4.59). That is to say

$$\mathbf{y}(\mathbf{Y}_i^-) = \mathbf{y}(\mathbf{Y}_i^+) - \mathbf{r}'_i \quad \forall \mathbf{Y}_i^- \in \Gamma_i^-, \mathbf{Y}_i^+ \in \Gamma_i^+, \quad (4.61)$$

for each i and for some \mathbf{r}'_i . This definition is more conveniently recast in terms of displacement fluctuations without reference to the translation vectors \mathbf{r}'_i . It is easily shown that equation (4.61) is equivalent to

$$\tilde{U}_\mu(\mathbf{Y}_i^-) = \tilde{U}_\mu(\mathbf{Y}_i^+) \quad \forall \mathbf{Y}_i^- \in \Gamma_i^-, \mathbf{Y}_i^+ \in \Gamma_i^+, \quad (4.62)$$

for each i . Figure 4.3(b) illustrates periodic fluctuations on the boundary of a hexagonal cell. Equation (4.62) may be written more compactly without reference to the partition of the boundary as

$$\tilde{U}_\mu(\mathbf{Y}^-) = \tilde{U}_\mu(\mathbf{Y}^+) \quad \forall \text{ corresponding pairs } \mathbf{Y}^-, \mathbf{Y}^+ \in \partial\Omega_{\mu 0}, \quad (4.63)$$

where by corresponding pairs \mathbf{Y}^- and \mathbf{Y}^+ we refer to the pairing of all boundary points established by applying equations (4.58) and (4.59) to all the parts of the boundary.

Now any kinematic constraint used to formulate the RVE equilibrium problem defining a homogenised constitutive model must satisfy the minimal kinematic constraint (4.14). It turns out that any periodic fluctuation field satisfying (4.63) automatically satisfies (4.14). In order to see this we use the boundary partition (4.57) to split the integral on the right hand side of (4.14):

$$\int_{\partial\Omega_{\mu 0}} \tilde{U}_\mu \otimes \mathbf{N} dA = \sum_{i=1}^n \left[\int_{\Gamma_i^-} \tilde{U}_\mu(\mathbf{Y}_i^-) \otimes \mathbf{N}(\mathbf{Y}_i^-) dA + \int_{\Gamma_i^+} \tilde{U}_\mu(\mathbf{Y}_i^+) \otimes \mathbf{N}(\mathbf{Y}_i^+) dA \right]. \quad (4.64)$$

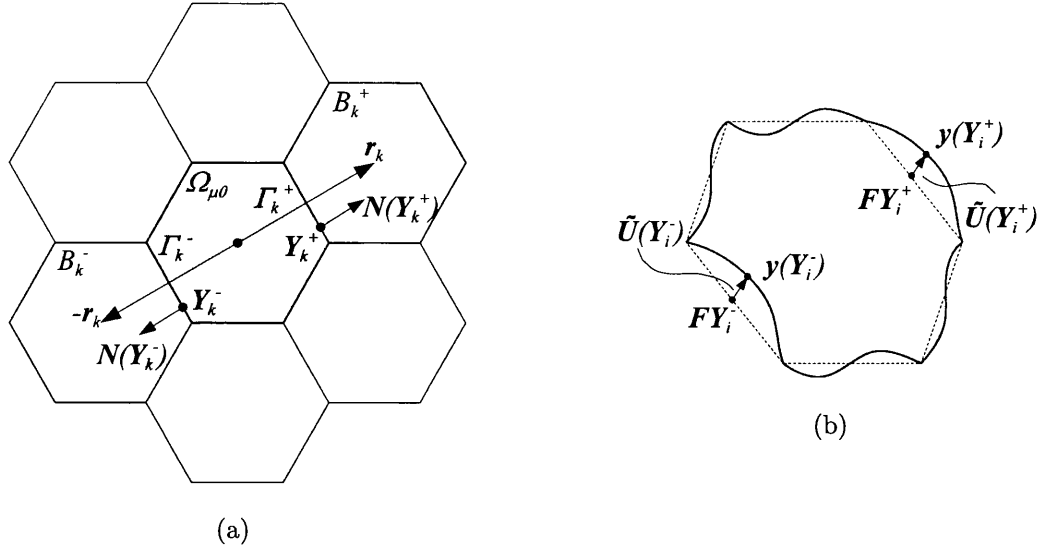


Figure 4.3: (a) A two dimensional hexagonal cell and its neighbours. A pair of corresponding boundary points is indicated. (b) Periodic deformation of a hexagonal cell showing displacement fluctuations at corresponding boundary points.

In view of (4.59) we may write

$$\begin{aligned}
 \int_{\partial\Omega_{\mu 0}} \tilde{U}_\mu \otimes N dA &= \sum_{i=1}^n \left[\int_{\Gamma_i^-} \tilde{U}_\mu(Y_i^-) \otimes N(Y_i^-) dA + \right. \\
 &\quad \left. \int_{\Gamma_i^-} \tilde{U}_\mu(Y_i^- + r_i) \otimes N(Y_i^- + r_i) dA \right] \\
 &= \sum_{i=1}^n \int_{\Gamma_i^-} \left[\tilde{U}_\mu(Y_i^-) \otimes N(Y_i^-) + \right. \\
 &\quad \left. \tilde{U}_\mu(Y_i^- + r_i) \otimes N(Y_i^- + r_i) \right] dA. \quad (4.65)
 \end{aligned}$$

Using the periodicity of the fluctuations (4.62) and the anti-periodicity of the boundary normals (4.60) this implies

$$\begin{aligned}
 \int_{\partial\Omega_{\mu 0}} \tilde{U}_\mu \otimes N dA &= \sum_{i=1}^n \int_{\Gamma_i^-} \left[\tilde{U}_\mu(Y_i^-) \otimes N(Y_i^-) - \tilde{U}_\mu(Y_i^-) \otimes N(Y_i^-) \right] dA \\
 &= \mathbf{0}, \quad (4.66)
 \end{aligned}$$

which is an expression of the minimum kinematic constraint.

We now define the set of kinematically admissible virtual displacement fields for the periodic condition as

$$\begin{aligned}
 \mathcal{V}_\mu^{\text{per}} &\equiv \{ \boldsymbol{\eta}, \text{ sufficiently regular} \mid \boldsymbol{\eta}(Y^-) = \boldsymbol{\eta}(Y^+) \\
 &\quad \forall \text{ corresponding pairs } Y^-, Y^+ \in \partial\Omega_{\mu 0} \}. \quad (4.67)
 \end{aligned}$$

As ever this is the same as the set of kinematically admissible displacement fluctuations. It has been established that all fluctuations in $\mathcal{V}_\mu^{\text{per}}$ satisfy the minimum constraint (uniform traction condition) and so

$$\mathcal{V}_\mu^{\text{per}} \subset \mathcal{V}_\mu^{\text{tract}} \quad (4.68)$$

as required for deformation driven homogenisation.

Body forces and surface tractions under the periodic boundary condition

Under the periodic constraint the variational form of the Hill-Mandel principle expressed in equations (4.32) and (4.33) specialises to

$$\int_{\partial\Omega_{\mu 0}} \mathbf{T}_\mu \cdot \boldsymbol{\eta} dA = 0 \quad \forall \boldsymbol{\eta} \in \mathcal{V}_\mu^{\text{per}} \quad (4.69)$$

$$\int_{\Omega_{\mu 0}} \mathbf{B}_\mu \cdot \boldsymbol{\eta} dV = 0 \quad \forall \boldsymbol{\eta} \in \mathcal{V}_\mu^{\text{per}}. \quad (4.70)$$

As with the uniform traction condition, the definition of $\mathcal{V}_\mu^{\text{per}}$ places no restrictions on fields inside the RVE. Thus equation (4.70) implies that

$$\mathbf{B}_\mu(\mathbf{Y}) = \mathbf{0} \quad \forall \mathbf{Y} \in \Omega_{\mu 0}, \quad (4.71)$$

so that once again body forces must vanish.

Using the partition of the boundary into corresponding pairs we may write the left hand side of equation (4.69) as

$$\begin{aligned} \int_{\partial\Omega_{\mu 0}} \mathbf{T}_\mu \cdot \boldsymbol{\eta} dA &= \sum_{i=1}^n \left[\int_{\Gamma_i^-} \mathbf{T}_\mu(\mathbf{Y}_i^-) \cdot \boldsymbol{\eta}(\mathbf{Y}_i^-) dA + \int_{\Gamma_i^+} \mathbf{T}_\mu(\mathbf{Y}_i^+) \cdot \boldsymbol{\eta}(\mathbf{Y}_i^+) dA \right] \\ &= \sum_{i=1}^n \int_{\Gamma_i^-} [\mathbf{T}_\mu(\mathbf{Y}_i^-) \cdot \boldsymbol{\eta}(\mathbf{Y}_i^-) + \mathbf{T}_\mu(\mathbf{Y}_i^+) \cdot \boldsymbol{\eta}(\mathbf{Y}_i^+)] dA. \end{aligned} \quad (4.72)$$

As long as $\boldsymbol{\eta}$ is in $\mathcal{V}_\mu^{\text{tract}}$ then $\boldsymbol{\eta}(\mathbf{Y}_i^-) = \boldsymbol{\eta}(\mathbf{Y}_i^+)$ and we have

$$\begin{aligned} \int_{\partial\Omega_{\mu 0}} \mathbf{T}_\mu \cdot \boldsymbol{\eta} dA &= \sum_{i=1}^n \int_{\Gamma_i^-} [\mathbf{T}_\mu(\mathbf{Y}_i^-) + \mathbf{T}_\mu(\mathbf{Y}_i^+)] \cdot \boldsymbol{\eta}(\mathbf{Y}_i^-) dA \\ &= \int_{\Gamma^-} [\mathbf{T}_\mu(\mathbf{Y}^-) + \mathbf{T}_\mu(\mathbf{Y}^+)] \cdot \boldsymbol{\eta}(\mathbf{Y}^-) dA, \end{aligned} \quad (4.73)$$

where Γ^- is the union of all Γ_i^- . Substituting this expression into equation (4.69) gives

$$\int_{\Gamma^-} [\mathbf{T}_\mu(\mathbf{Y}^-) + \mathbf{T}_\mu(\mathbf{Y}^+)] \cdot \boldsymbol{\eta}(\mathbf{Y}^-) dA = 0 \quad \forall \boldsymbol{\eta} \in \mathcal{V}_\mu^{\text{per}}, \quad (4.74)$$

and since fields $\boldsymbol{\eta} \in \mathcal{V}_\mu^{\text{per}}$ are unconstrained when restricted to Γ^- it follows that

$$\mathbf{T}_\mu(\mathbf{Y}^-) + \mathbf{T}_\mu(\mathbf{Y}^+) = \mathbf{0} \quad \forall \text{ corresponding pairs } \mathbf{Y}^-, \mathbf{Y}^+ \in \partial\Omega_{\mu 0}. \quad (4.75)$$

Thus the periodic boundary condition requires that boundary surface tractions should be anti-periodic. Some authors [74] adopt equation (4.75) as part of the definition of the periodic boundary condition and then verify the Hill-Mandel principle. We treat the Hill-Mandel principle as an axiom from which anti-periodicity of tractions follows.

4.10.3 The linear boundary condition

The *linear boundary condition* requires that the deformed shape of the boundary of the RVE should be given by the linear relation

$$\mathbf{y}(\mathbf{Y}) = \mathbf{F}\mathbf{Y} \quad \forall \mathbf{Y} \in \partial\Omega_{\mu 0}, \quad (4.76)$$

where \mathbf{F} is the macroscopic deformation gradient independent of \mathbf{Y} . We recognise in this equation an essential boundary condition of the type (2.171) used in the conventional boundary value problem described in section 2.7. In terms of displacement fluctuations ($\tilde{\mathbf{U}}_\mu = \mathbf{y} - \mathbf{F}\mathbf{Y}$) equation (4.76) is obviously equivalent to

$$\tilde{\mathbf{U}}(\mathbf{Y})_\mu = \mathbf{0} \quad \forall \mathbf{Y} \in \partial\Omega_{\mu 0}. \quad (4.77)$$

On the basis of (4.77) we define the set of kinematically admissible displacement fluctuations and virtual displacements as

$$\mathcal{V}_\mu^{\text{lin}} \equiv \{\boldsymbol{\eta}, \text{ sufficiently regular} \mid \boldsymbol{\eta}(\mathbf{Y}) = \mathbf{0} \ \forall \mathbf{Y} \in \partial\Omega_{\mu 0}\}. \quad (4.78)$$

Any field of displacement fluctuations that vanishes on the RVE boundary must trivially satisfy the periodicity condition (4.63). Thus any member of $\mathcal{V}_\mu^{\text{lin}}$ is also in $\mathcal{V}_\mu^{\text{per}}$ which is itself a subset of $\mathcal{V}_\mu^{\text{tract}}$ and so the minimum kinematic constraint is automatically satisfied. Accordingly we write

$$\mathcal{V}_\mu^{\text{lin}} \subset \mathcal{V}_\mu^{\text{per}} \subset \mathcal{V}_\mu^{\text{tract}}. \quad (4.79)$$

Body forces and surface tractions under the linear boundary condition

In the case of the linear boundary condition the variational Hill-Mandel equations (4.32) and (4.33) become

$$\int_{\partial\Omega_{\mu 0}} \mathbf{T}_\mu \cdot \boldsymbol{\eta} dA = 0 \quad \forall \boldsymbol{\eta} \in \mathcal{V}_\mu^{\text{lin}} \quad (4.80)$$

$$\int_{\Omega_{\mu 0}} \mathbf{B}_\mu \cdot \boldsymbol{\eta} dV = 0 \quad \forall \boldsymbol{\eta} \in \mathcal{V}_\mu^{\text{lin}}. \quad (4.81)$$

Since $\mathcal{V}_\mu^{\text{lin}}$ only constrains fields on the RVE boundary, equation (4.81) implies that

$$\mathbf{B}_\mu(\mathbf{Y}) = \mathbf{0} \quad \forall \mathbf{Y} \in \Omega_{\mu 0}. \quad (4.82)$$

Thus all body forces must be vanish as they do under the minimum and periodic constraints.

Equation (4.80) on the other hand is satisfied trivially for any boundary traction field and places no restriction on \mathbf{T}_μ . Once the equilibrium problem has been solved \mathbf{T}_μ may be calculated as a reaction force enforcing the constraint.

4.10.4 The Taylor condition

The *Taylor* or *Voigt condition* is the simplest and most prescriptive of all kinematic constraints and has long been used in analytical treatments of homogenisation [111, 123]. It fully prescribes the deformed configuration according to

$$\mathbf{y}(\mathbf{Y}) = \mathbf{F}\mathbf{Y} \quad \forall \mathbf{Y} \in \Omega_{\mu 0}, \quad (4.83)$$

Clearly the microscopic deformation gradient \mathbf{F}_μ of such a configuration is uniformly equal to the macroscopic deformation gradient \mathbf{F} . Hence the average microscopic deformation gradient $\langle \mathbf{F}_\mu \rangle_0$ is also equal to \mathbf{F} and the minimum kinematic constraint in the form (4.13) is trivially satisfied.

In terms of displacement fluctuations the Taylor constraint is written

$$\tilde{\mathbf{U}}(\mathbf{Y}) = \mathbf{0} \quad \forall \mathbf{Y} \in \Omega_{\mu 0}, \quad (4.84)$$

so that the set of kinematically admissible fluctuations and the set of admissible virtual displacement are both given by

$$\mathcal{V}_\mu^{\text{Tay}} \equiv \{\mathbf{0}\}. \quad (4.85)$$

Obviously the fluctuation field that vanishes everywhere in the RVE is a particular case of a field that vanishes on the boundary and in so doing satisfies the linear boundary condition (4.77). It follows that

$$\mathcal{V}_\mu^{\text{Tay}} \subset \mathcal{V}_\mu^{\text{lin}} \subset \mathcal{V}_\mu^{\text{per}} \subset \mathcal{V}_\mu^{\text{tract}}. \quad (4.86)$$

Note that under the Taylor condition the RVE equilibrium problem is degenerate in the sense that the kinematic constraint in itself explicitly provides the complete solution without further process.

Body forces and surface tractions under the Taylor condition

The Hill-Mandel variational equations (4.32) and (4.33) are trivially satisfied for the vanishing Taylor virtual displacement field without placing any restrictions on the body force or surface traction fields. These must be obtained as reaction forces in the equilibrium problem. That is to say they are derived from the microscopic stress field evaluated for the fully prescribed deformed RVE configuration.

4.11 Observations on the symmetry of homogenised constitutive models

4.11.1 Symmetry of the RVE



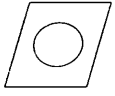

Intuitively one expects symmetry properties possessed by the RVE to be shared by the homogenised constitutive relation. It is shown in the following that this is indeed the case provided the kinematic constraints do not violate the symmetry. For simplicity attention is restricted to RVEs made up of Cauchy elastic materials.

We consider an RVE with reference domain $\Omega_{\mu 0}$ made up of Cauchy elastic materials defined by the functional $\mathfrak{P}_\mu(F_\mu, Y)$. Suppose that the RVE has the following properties

$$\left. \begin{array}{l} QY \in \Omega_{\mu 0} \\ \mathfrak{P}_\mu(F_\mu(Y)Q, Q^T Y) = \mathfrak{P}_\mu(F_\mu(Y), Y)Q \end{array} \right\} \forall Y \in \Omega_{\mu 0}, \text{ invertible } F_\mu \text{ and } Q \in \mathcal{S}, \quad (4.87)$$

where \mathcal{S} is a group of invertible tensors characterising the symmetry of the RVE. The condition (4.87)₁ ensures the symmetry of the RVE domain and requires that

Box 2: Sets of kinematically admissible virtual displacements for various constraints. Examples of admissible deformed configurations for an initially square RVE with a central circle are illustrated.

Uniform traction boundary condition $\mathcal{V}_\mu^{\text{tract}} \equiv \left\{ \boldsymbol{\eta}, \text{ sufficiently regular } \mid \int_{\partial\Omega_{\mu 0}} \boldsymbol{\eta} \otimes \mathbf{N} dA = \mathbf{0} \right\}$	
Periodic boundary condition $\mathcal{V}_\mu^{\text{per}} \equiv \left\{ \boldsymbol{\eta}, \text{ sufficiently regular } \mid \boldsymbol{\eta}(\mathbf{Y}^-) = \boldsymbol{\eta}(\mathbf{Y}^+) \right.$ $\quad \left. \forall \text{ corresponding pairs } \mathbf{Y}^-, \mathbf{Y}^+ \in \partial\Omega_{\mu 0} \right\}$ $\subset \mathcal{V}_\mu^{\text{tract}}$	
Linear boundary condition $\mathcal{V}_\mu^{\text{lin}} \equiv \left\{ \boldsymbol{\eta}, \text{ sufficiently regular } \mid \boldsymbol{\eta}(\mathbf{Y}) = \mathbf{0} \ \forall \mathbf{Y} \in \partial\Omega_{\mu 0} \right\}$ $\subset \mathcal{V}_\mu^{\text{per}} \subset \mathcal{V}_\mu^{\text{tract}}$	
Taylor condition $\mathcal{V}_\mu^{\text{Tay}} \equiv \{ \mathbf{0} \}$ $\subset \mathcal{V}_\mu^{\text{lin}} \subset \mathcal{V}_\mu^{\text{per}} \subset \mathcal{V}_\mu^{\text{tract}}$	

volume and distances are preserved under the transformation \mathbf{Q} . It follows that \mathbf{Q} must be orthogonal with unit determinant:

$$\mathbf{Q}^{-1} = \mathbf{Q}^T ; \quad |\det \mathbf{Q}| = 1 , \quad (4.88)$$

so that \mathbf{Q} represents either a rotation or a reflection. Note that if the two conditions in (4.87) hold for \mathbf{Q} they also hold for $\mathbf{Q}^{-1} = \mathbf{Q}^T$ and so $\mathbf{Q} \in \mathcal{S} \Rightarrow \mathbf{Q}^T \in \mathcal{S}$.

The second condition (4.87)₂ concerns the material symmetry of the constituents of the RVE and their distribution. If the symmetry group of the microscopic constitutive function everywhere contains \mathcal{S} as a subset then (4.87)₂ simplifies to

$$\mathfrak{P}_\mu(\mathbf{F}_\mu(\mathbf{Y}), \mathbf{Q}^T \mathbf{Y}) = \mathfrak{P}_\mu(\mathbf{F}_\mu(\mathbf{Y}), \mathbf{Y}) \quad \forall \mathbf{Y} \in \Omega_{\mu 0}, \text{ invertible } \mathbf{F}_\mu \text{ and } \mathbf{Q} \in \mathcal{S} , \quad (4.89)$$

which expresses the symmetry of the material distribution within the RVE.

We now wish to establish if the homogenised response of an RVE possessing the symmetry of (4.87) to an arbitrary macroscopic deformation tensor \mathbf{F} is the same as the response to the modified deformation tensor $\mathbf{F}\mathbf{Q}$ for all $\mathbf{Q} \in \mathcal{S}$. In other words does $\bar{\mathfrak{P}}(\mathbf{F}\mathbf{Q})$ equal $\bar{\mathfrak{P}}(\mathbf{F})\mathbf{Q}$?

We begin by considering the RVE equilibrium problem that defines $\bar{\mathfrak{P}}$. Suppose that $\tilde{\mathbf{U}}_\mu$ and $\tilde{\mathbf{U}}'_\mu$ are the microscopic deformation fields that solve the RVE equilibrium problems with macroscopic \mathbf{F} and $\mathbf{F}\mathbf{Q}$ respectively. Then the following equilibrium equations must be satisfied

$$\int_{\Omega_{\mu 0}} \mathfrak{P}_\mu(\mathbf{F} + \nabla_{\mathbf{Y}} \tilde{\mathbf{U}}_\mu(\mathbf{Y}), \mathbf{Y}) : \nabla_{\mathbf{Y}} \boldsymbol{\eta}(\mathbf{Y}) \, dV = 0 \quad \forall \boldsymbol{\eta} \in \mathcal{V}_\mu \quad (4.90)$$

$$\int_{\Omega_{\mu 0}} \mathfrak{P}_\mu(\mathbf{F}\mathbf{Q} + \nabla_{\mathbf{Y}} \tilde{\mathbf{U}}'_\mu(\mathbf{Y}), \mathbf{Y}) : \nabla_{\mathbf{Y}} \boldsymbol{\eta}(\mathbf{Y}) \, dV = 0 \quad \forall \boldsymbol{\eta} \in \mathcal{V}_\mu. \quad (4.91)$$

Now with the change of integration variable to $\mathbf{Y}' = \mathbf{Q}\mathbf{Y}$ the volume element becomes $dV' = \det \mathbf{Q} dV$ and we write equation 4.91 as

$$\int_{\Omega'_{\mu 0}} \mathfrak{P}_\mu(\mathbf{F}\mathbf{Q} + \nabla_{\mathbf{Y}'} \tilde{\mathbf{U}}'_\mu(\mathbf{Q}^T \mathbf{Y}'), \mathbf{Q}^T \mathbf{Y}') : \nabla_{\mathbf{Y}'} \boldsymbol{\eta}(\mathbf{Q}^T \mathbf{Y}') \, dV' = 0 \quad \forall \boldsymbol{\eta} \in \mathcal{V}_\mu, \quad (4.92)$$

where $\Omega'_{\mu 0}$ is the RVE domain occupied by \mathbf{Y}' and we have used the fact that $|\det \mathbf{Q}| = 1$. However it follows from the symmetry condition 4.87₁ and the invertibility of \mathbf{Q} that

$$\Omega'_{\mu 0} = \Omega_{\mu 0} \quad (4.93)$$

Moreover the gradient with respect to \mathbf{Y} may be expressed as²

$$\nabla_{\mathbf{Y}}(\bullet) = \frac{\partial \bullet}{\partial \mathbf{Y}} = \frac{\partial \bullet}{\partial \mathbf{Y}'} \frac{\partial \mathbf{Y}'}{\partial \mathbf{Y}} = \nabla_{\mathbf{Y}'}(\bullet) \mathbf{Q}. \quad (4.94)$$

Therefore the equilibrium equation 4.92 may be written

$$\int_{\Omega_{\mu 0}} \mathfrak{P}_\mu \left(\left[\mathbf{F} + \nabla_{\mathbf{Y}'} \tilde{\mathbf{U}}'_\mu(\mathbf{Q}^T \mathbf{Y}') \right] \mathbf{Q}, \mathbf{Q}^T \mathbf{Y}' \right) : (\nabla_{\mathbf{Y}'} \boldsymbol{\eta}(\mathbf{Q}^T \mathbf{Y}') \mathbf{Q}) \, dV' = 0 \quad \forall \boldsymbol{\eta} \in \mathcal{V}_\mu, \quad (4.95)$$

which in view of the second symmetry condition (4.87)₂ is equivalent to

$$\int_{\Omega_{\mu 0}} \mathfrak{P}_\mu \left(\mathbf{F} + \nabla_{\mathbf{Y}'} \tilde{\mathbf{U}}'_\mu(\mathbf{Q}^T \mathbf{Y}'), \mathbf{Y}' \right) \mathbf{Q} : (\nabla_{\mathbf{Y}'} \boldsymbol{\eta}(\mathbf{Q}^T \mathbf{Y}') \mathbf{Q}) \, dV' = 0 \quad \forall \boldsymbol{\eta} \in \mathcal{V}_\mu. \quad (4.96)$$

Using the orthogonality of \mathbf{Q} this may be rewritten as

$$\int_{\Omega_{\mu 0}} \mathfrak{P}_\mu \left(\mathbf{F} + \nabla_{\mathbf{Y}'} \tilde{\mathbf{U}}'_\mu(\mathbf{Q}^T \mathbf{Y}'), \mathbf{Y}' \right) : \nabla_{\mathbf{Y}'} \boldsymbol{\eta}(\mathbf{Q}^T \mathbf{Y}') \, dV' = 0 \quad \forall \boldsymbol{\eta} \in \mathcal{V}_\mu. \quad (4.97)$$

²Note that $\nabla_{\mathbf{Y}} \boldsymbol{\eta}(\mathbf{f}(\mathbf{Y}))$ is taken to mean the gradient of the function $\boldsymbol{\eta}'(\mathbf{Y}) = \boldsymbol{\eta}(\mathbf{f}(\mathbf{Y}))$ with respect to \mathbf{Y} and not $\nabla_{\mathbf{Y}} \boldsymbol{\eta}(\mathbf{Y})$ evaluated at $\mathbf{Y} = \mathbf{f}(\mathbf{Y})$.



At this stage it is assumed that the set of kinematically admissible virtual displacements \mathcal{V}_μ possesses the following property:

$$\forall \boldsymbol{\eta} \in \mathcal{V}_\mu, \mathbf{Q} \in \mathcal{S}, \exists \boldsymbol{\eta}' \in \mathcal{V}_\mu \text{ such that } \nabla_{\mathbf{Y}} \boldsymbol{\eta}(\mathbf{Q}\mathbf{Y}) = \nabla_{\mathbf{Y}'} \boldsymbol{\eta}'(\mathbf{Y}) \quad \forall \mathbf{Y} \in \Omega_{\mu 0}. \quad (4.98)$$

Given the closure of $\Omega_{\mu 0}$ under each $\mathbf{Q} \in \mathcal{S}$ it is easily shown that this ensures that the set of all fields $\nabla_{\mathbf{Y}} \boldsymbol{\eta}(\mathbf{Q}^T \mathbf{Y})$ with $\boldsymbol{\eta} \in \mathcal{V}_\mu$ is the same as the set of all $\nabla_{\mathbf{Y}} \boldsymbol{\eta}(\mathbf{Y})$. Thus as long as the chosen kinematic constraints on the RVE satisfy the additional symmetry condition (4.98) then equation (4.97) has the following equivalent expression

$$\int_{\Omega_{\mu 0}} \mathfrak{P}_\mu \left(\mathbf{F} + \nabla_{\mathbf{Y}} \tilde{\mathbf{U}}'_\mu(\mathbf{Q}^T \mathbf{Y}), \mathbf{Y} \right) : \nabla_{\mathbf{Y}} \boldsymbol{\eta}(\mathbf{Y}) \, dV = 0 \quad \forall \boldsymbol{\eta} \in \mathcal{V}_\mu, \quad (4.99)$$

where the prime has been dropped from \mathbf{Y} the variable of integration. In this form the RVE equilibrium equation for a macroscopic deformation gradient of \mathbf{FQ} is seen to be the same as the equilibrium equation (4.90) for macroscopic deformation gradient \mathbf{F} except that $\tilde{\mathbf{U}}'_\mu(\mathbf{Q}^T \mathbf{Y})$ in the latter replaces $\tilde{\mathbf{U}}_\mu(\mathbf{Y})$ in the former. It follows that the solutions to the two equilibrium problems are related by

$$\tilde{\mathbf{U}}'_\mu(\mathbf{Q}^T \mathbf{Y}) = \tilde{\mathbf{U}}_\mu(\mathbf{Y}). \quad (4.100)$$

Consider now the homogenised stress response to the two macroscopic deformation gradients \mathbf{F} and \mathbf{FQ} where $\mathbf{Q} \in \mathcal{S}$. These are given respectively by

$$\bar{\mathfrak{P}}(\mathbf{F}) = \int_{\Omega_{\mu 0}} \mathfrak{P}_\mu(\mathbf{F} + \nabla_{\mathbf{Y}} \tilde{\mathbf{U}}_\mu(\mathbf{Y}), \mathbf{Y}) \, dV \quad (4.101)$$

$$\bar{\mathfrak{P}}(\mathbf{FQ}) = \int_{\Omega_{\mu 0}} \mathfrak{P}_\mu(\mathbf{FQ} + \nabla_{\mathbf{Y}} \tilde{\mathbf{U}}'_\mu(\mathbf{Y}), \mathbf{Y}) \, dV. \quad (4.102)$$

Once again the change of variable $\mathbf{Y}' = \mathbf{QY}$ may be used to express equation (4.102) as

$$\bar{\mathfrak{P}}(\mathbf{FQ}) = \int_{\Omega_{\mu 0}} \mathfrak{P}_\mu \left(\left[\mathbf{F} + \nabla_{\mathbf{Y}'} \tilde{\mathbf{U}}'_\mu(\mathbf{Q}^T \mathbf{Y}') \right] \mathbf{Q}, \mathbf{Q}^T \mathbf{Y}' \right) \, dV', \quad (4.103)$$

where (4.88)₂, (4.93) and (4.94) have been invoked as before. In view of the symmetry of the RVE material distribution (4.87)₂ this is equivalent to

$$\begin{aligned} \bar{\mathfrak{P}}(\mathbf{FQ}) &= \int_{\Omega_{\mu 0}} \mathfrak{P}_\mu \left(\mathbf{F} + \nabla_{\mathbf{Y}'} \tilde{\mathbf{U}}'_\mu(\mathbf{Q}^T \mathbf{Y}'), \mathbf{Y}' \right) \mathbf{Q} \, dV' \\ &= \int_{\Omega_{\mu 0}} \mathfrak{P}_\mu \left(\mathbf{F} + \nabla_{\mathbf{Y}'} \tilde{\mathbf{U}}_\mu(\mathbf{Y}'), \mathbf{Y}' \right) \, dV' \mathbf{Q}, \end{aligned} \quad (4.104)$$

and using equation (4.100) we obtain

$$\bar{\mathfrak{P}}(\mathbf{FQ}) = \int_{\Omega_{\mu 0}} \mathfrak{P}_\mu \left(\mathbf{F} + \nabla_{\mathbf{Y}'} \tilde{\mathbf{U}}_\mu(\mathbf{Y}'), \mathbf{Y}' \right) \, dV' \mathbf{Q}, \quad (4.105)$$

which holds for arbitrary $\mathbf{Q} \in \mathcal{S}$. Comparing this with equation (4.101) we find that

$$\bar{\mathfrak{P}}(\mathbf{F}\mathbf{Q}) = \bar{\mathfrak{P}}(\mathbf{F})\mathbf{Q} \quad \forall \mathbf{Q} \in \mathcal{S}. \quad (4.106)$$

Thus the symmetry group of the homogenised constitutive function contains every member of \mathcal{S} – the group of operations that characterise the symmetry of the RVE and kinematic constraints as defined by (4.87) and (4.98).

It remains to examine in turn each of the four kinematic constraints introduced previously (uniform traction, periodic, linear and Taylor conditions) to establish whether or not they satisfy the symmetry condition (4.98).

Symmetry of the minimum kinematic constraint

Consider a field $\boldsymbol{\eta}$ belonging to the set of kinematically admissible virtual displacements for the uniform traction boundary condition \mathcal{V}^{tract} but which is otherwise arbitrary. By the definition of \mathcal{V}^{tract} the field $\boldsymbol{\eta}$ must satisfy

$$\int_{\partial\Omega_{\mu 0}} \boldsymbol{\eta}(\mathbf{Y}) \otimes \mathbf{N} dA = \mathbf{0}, \quad (4.107)$$

This condition may be expressed equivalently using the divergence theorem as

$$\int_{\Omega_{\mu 0}} \nabla_{\mathbf{Y}} \boldsymbol{\eta}(\mathbf{Y}) dV = \mathbf{0}. \quad (4.108)$$

Now let $\boldsymbol{\eta}'$ be defined by

$$\boldsymbol{\eta}'(\mathbf{Y}) = \boldsymbol{\eta}(\mathbf{Q}\mathbf{Y}), \quad (4.109)$$

for arbitrary $\mathbf{Q} \in \mathcal{S}$ so that

$$\nabla_{\mathbf{Y}} \boldsymbol{\eta}'(\mathbf{Y}) = \nabla_{\mathbf{Y}} \boldsymbol{\eta}(\mathbf{Q}\mathbf{Y}). \quad (4.110)$$

Thus if it can be shown that $\boldsymbol{\eta}'$ is in \mathcal{V}^{tract} then the symmetry condition (4.98) must hold for the minimum kinematic constraint. We consider therefore the integral

$$\int_{\partial\Omega_{\mu 0}} \boldsymbol{\eta}'(\mathbf{Y}) \otimes \mathbf{N} dA = \int_{\Omega_{\mu 0}} \nabla_{\mathbf{Y}} \boldsymbol{\eta}'(\mathbf{Y}) dV.$$

Substituting from equation (4.110) gives

$$\int_{\partial\Omega_{\mu 0}} \boldsymbol{\eta}'(\mathbf{Y}) \otimes \mathbf{N} dA = \int_{\Omega_{\mu 0}} \nabla_{\mathbf{Y}} \boldsymbol{\eta}(\mathbf{Q}\mathbf{Y}) dV.$$

Using the substitution $\mathbf{Y}' = \mathbf{Q}\mathbf{Y}$, recalling (4.88)₁, (4.88)₂ and (4.93) and noting that $\nabla_{\mathbf{Y}}(\bullet) = \nabla_{\mathbf{Y}'}(\bullet)\mathbf{Q}$ the right hand side may be rewritten to give

$$\int_{\partial\Omega_{\mu 0}} \boldsymbol{\eta}'(\mathbf{Y}) \otimes \mathbf{N} dA = \int_{\Omega_{\mu 0}} \nabla_{\mathbf{Y}'} \boldsymbol{\eta}(\mathbf{Y}') dV' \mathbf{Q}.$$

However since $\boldsymbol{\eta} \in \mathcal{V}^{tract}$ and consequently satisfies equation (4.108) the right hand side above vanishes and we obtain

$$\int_{\partial\Omega_{\mu 0}} \boldsymbol{\eta}'(\mathbf{Y}) \otimes \mathbf{N} dA = \mathbf{0}. \quad (4.111)$$

Thus $\boldsymbol{\eta}'$ is also in \mathcal{V}^{tract} and so symmetry condition (4.98) holds. Hence the material symmetry of homogenised constitutive models based on the uniform traction boundary condition depends only on the symmetry of the RVE and is not limited by the kinematic constraint.

Symmetry of the periodic boundary condition

Consider firstly an arbitrary member $\boldsymbol{\eta}$ of the set of kinematically admissible virtual displacement fields \mathcal{V}_{μ}^{per} under the periodic boundary condition. According to the definition of \mathcal{V}_{μ}^{per} the field $\boldsymbol{\eta}$ must satisfy

$$\boldsymbol{\eta}(\mathbf{Y}^-) = \boldsymbol{\eta}(\mathbf{Y}^+) \quad \forall \text{ corresponding pairs } \mathbf{Y}^-, \mathbf{Y}^+ \in \partial\Omega_{\mu 0}. \quad (4.112)$$

Now $\mathbf{Q} \in \mathcal{S}$ represents a rigid transformation which maps the RVE domain onto itself. It follows that the points \mathbf{QY}^- and \mathbf{QY}^+ , where \mathbf{Y}^- and \mathbf{Y}^+ are corresponding boundary points, must also lie on the RVE boundary. Moreover \mathbf{Q} must preserve the relationships between matching boundary portions in such a way that \mathbf{QY}^- and \mathbf{QY}^+ constitute a matching pair. Thus

$$\boldsymbol{\eta}(\mathbf{QY}^-) = \boldsymbol{\eta}(\mathbf{QY}^+) \quad \forall \text{ corresponding pairs } \mathbf{Y}^-, \mathbf{Y}^+ \in \partial\Omega_{\mu 0}. \quad (4.113)$$

If we define $\boldsymbol{\eta}'$ by

$$\boldsymbol{\eta}'(\mathbf{Y}) = \boldsymbol{\eta}(\mathbf{QY}), \quad (4.114)$$

then we have from (4.113)

$$\boldsymbol{\eta}'(\mathbf{Y}^-) = \boldsymbol{\eta}'(\mathbf{Y}^+) \quad \forall \text{ corresponding pairs } \mathbf{Y}^-, \mathbf{Y}^+ \in \partial\Omega_{\mu 0}, \quad (4.115)$$

and so $\boldsymbol{\eta}' \in \mathcal{V}_{\mu}^{per}$.

It is obvious from the definition of $\boldsymbol{\eta}'$ that

$$\nabla_{\mathbf{Y}} \boldsymbol{\eta}'(\mathbf{Y}) = \nabla_{\mathbf{Y}} \boldsymbol{\eta}(\mathbf{QY}). \quad (4.116)$$

Thus for any $\boldsymbol{\eta} \in \mathcal{V}_{\mu}^{per}$ there is an $\boldsymbol{\eta}' \in \mathcal{V}_{\mu}^{per}$ that satisfies equation (4.116) and so the symmetry condition (4.98) holds for the periodic boundary condition.

Symmetry of the linear boundary condition

Under the linear boundary condition any $\boldsymbol{\eta}$ in the set \mathcal{V}_μ^{lin} of all kinematically admissible virtual displacements must vanish on the boundary. i.e.

$$\boldsymbol{\eta}(\mathbf{Y}) = \mathbf{0} \quad \forall \mathbf{Y} \in \Omega_{\mu 0}. \quad (4.117)$$

Now for any $\mathbf{Q} \in \mathcal{S}$, the point \mathbf{QY} must lie on the boundary if $\mathbf{Y} \in \Omega_{\mu 0}$. Thus

$$\boldsymbol{\eta}(\mathbf{QY}) = \mathbf{0} \quad \forall \mathbf{Y} \in \Omega_{\mu 0} \quad (4.118)$$

and if we define $\boldsymbol{\eta}'$ as before by

$$\boldsymbol{\eta}'(\mathbf{Y}) = \boldsymbol{\eta}(\mathbf{QY}), \quad (4.119)$$

then (4.118) implies

$$\boldsymbol{\eta}'(\mathbf{Y}) = \mathbf{0} \quad \forall \mathbf{Y} \in \Omega_{\mu 0}. \quad (4.120)$$

Thus $\boldsymbol{\eta}'$ is a member of \mathcal{V}_μ^{lin} .

Obviously from the definition of $\boldsymbol{\eta}'$

$$\nabla_{\mathbf{Y}} \boldsymbol{\eta}'(\mathbf{Y}) = \nabla_{\mathbf{Y}} \boldsymbol{\eta}(\mathbf{QY}). \quad (4.121)$$

and so we have a suitable $\boldsymbol{\eta}' \in \mathcal{V}_\mu^{lin}$ for each $\boldsymbol{\eta} \in \mathcal{V}_\mu^{lin}$ to satisfy the symmetry condition (4.98) for the linear boundary condition.

Symmetry of Taylor based models

Under the Taylor condition the virtual displacement field $\boldsymbol{\eta}$ is constrained to equal $\mathbf{0}$ uniformly over the RVE and so the symmetry condition (4.98) is satisfied trivially.

In fact Taylor based homogenised models generally display greater symmetry than the RVEs that define them. This can be seen from the definition of the homogenised constitutive functional (4.35) specialised to the case where $\tilde{\mathbf{U}}_\mu = \mathbf{0}$ and for Cauchy elastic materials

$$\text{Tay} \bar{\mathfrak{P}}(\mathbf{F}, \mathbf{X}) = \langle \mathfrak{P}_\mu(\mathbf{F}, \mathbf{Y}) \rangle_0. \quad (4.122)$$

If the microscopic constitutive functional has everywhere a symmetry group \mathcal{G} (or if \mathcal{G} is a common subset of various symmetry groups over the RVE) then

$$\mathfrak{P}_\mu(\mathbf{QF}, \mathbf{Y}) = \mathfrak{P}_\mu(\mathbf{F}, \mathbf{Y})\mathbf{Q} \quad \forall \mathbf{Q} \in \mathcal{G}, \quad (4.123)$$

where we assume \mathcal{G} consists of rotations only. Since the averaging operator $\langle \bullet \rangle_0$ is linear it follows from the definition (4.122) of ${}^{\text{Tay}}\bar{\mathfrak{P}}$ that

$${}^{\text{Tay}}\bar{\mathfrak{P}}(\mathbf{Q}\mathbf{F}, \mathbf{Y}) = {}^{\text{Tay}}\bar{\mathfrak{P}}(\mathbf{F}, \mathbf{Y})\mathbf{Q} \quad \forall \mathbf{Q} \in \mathcal{G}, \quad (4.124)$$

Thus under the Taylor kinematic constraint the homogenised stress response shares the symmetry properties of the micro-constituent materials regardless of asymmetries in the RVE.

4.12 Finite element discretisation of the homogenisation procedure

The RVE equilibrium problem may be solved by the finite element method outlined in chapter 3. If the RVE includes history dependent materials an incremental approach is adopted as described in section 3.2 whereby the history of deformation is broken down into a series of discrete time steps. At each time step an incremental boundary value problem is solved. If by contrast the RVE contains only elastic constituents then only a single boundary value problem is required. In either case it is necessary to solve one or more time independent quasi-static boundary value problems. This is achieved firstly by a spatial discretisation of the RVE domain in the conventional way introducing a finite number of nodes and elements. The discretised version of the virtual work equilibrium equation follows (cf. equation (3.58)):

$$[\boldsymbol{\eta}^T][\mathbf{F}^{\text{int}}] = 0, \quad (4.125)$$

where $[\mathbf{F}^{\text{int}}]$ is the internal force vector defined by equation (3.62) and $[\boldsymbol{\eta}]$ is the vector of nodal virtual displacements compatible with the kinematic constraints. Note that the external force vector $[\mathbf{F}^{\text{ext}}]$ appearing in equation (3.58) vanishes since by equations (4.32) and (4.33) the virtual work done by external forces is zero.

Now in view of the relationship (4.9) between total and fluctuation displacements the directional derivatives of the virtual work with respect to identical changes $\delta\mathbf{U}_\mu$ and $\delta\tilde{\mathbf{U}}_\mu$ in each variable are the same. It follows that a suitable Newton-Raphson scheme to solve equation (4.125) for the nodal fluctuation displacements may be obtained by simplifying equation (3.59) to obtain

$$[\tilde{\mathbf{U}}_k] = [\tilde{\mathbf{U}}]_{k-1} + [\delta\tilde{\mathbf{U}}]_k \quad (4.126)$$

$$[\boldsymbol{\eta}]^T \left\{ \mathbf{K}_{k-1}[\delta\tilde{\mathbf{U}}]_k + [\mathbf{F}^{\text{int}}]_{k-1} \right\} = 0, \quad (4.127)$$

where \mathbf{K}_{k-1} and $[\mathbf{F}^{\text{int}}]_{k-1}$ are the global stiffness and internal force vectors respectively both evaluated at $[\tilde{\mathbf{U}}]_{k-1}$. Note that the subscript μ has been dropped from the fluctuation displacements for clarity but we remain concerned with the microscopic level.

Thus the finite element procedure to solve the RVE equilibrium problem is much the same as that adopted to solve a conventional quasi-static boundary value problem with prescribed displacements and boundary tractions. The only difference is due to the unconventional kinematic constraints imposed on the RVE. In the following subsections we consider in turn each of the four constraints introduced in section 4.10 to see how the constraint conditions are discretised and how they affect the solution procedure.

Having solved the RVE equilibrium problem, the homogenisation procedure is completed by estimating the average first Piola-Kirchhoff stress over the RVE. This may be done using Gaussian quadrature, the stress at each Gauss point being obtained from the micro constitutive relation evaluated under the known displacement field.

Box 3 summarises the details developed in the following subsections for obtaining the homogenised response of an RVE by the finite element method under various kinematic constraints.

4.12.1 Uniform traction constraint: discretisation

Virtual displacement fields $\boldsymbol{\eta}$ that conform to the uniform boundary traction (minimum) constraint must by definition satisfy

$$\int_{\partial\Omega_{\mu 0}} \boldsymbol{\eta} \otimes \mathbf{N} dA = \mathbf{0}. \quad (4.128)$$

We wish to discretise this expression to obtain an equation constraining the vector of nodal virtual displacements, $[\boldsymbol{\eta}]$. We begin by splitting the RVE boundary into a sum of element boundaries so that

$$\int_{\partial\Omega_{\mu 0}} \boldsymbol{\eta} \otimes \mathbf{N} dA = \sum_{\text{elements}} \int_{\partial\Omega_0^e \cap \partial\Omega_{\mu 0}} \boldsymbol{\eta} \otimes \mathbf{N} dA. \quad (4.129)$$

Introducing the standard discretisation of $\boldsymbol{\eta}$,

$$\boldsymbol{\eta} = \sum_{i=1}^n H_i \boldsymbol{\eta}^{(i)} \quad (4.130)$$

where H_i and $\boldsymbol{\eta}^{(i)}$ are the i^{th} shape function and corresponding nodal value of $\boldsymbol{\eta}$ respectively, we obtain

$$\begin{aligned} \int_{\partial\Omega_{\mu 0}} \boldsymbol{\eta} \otimes \mathbf{N} dA &\approx \sum_{\text{elements}} \int_{\partial\Omega_0^{el} \cap \partial\Omega_{\mu 0}} \left(\sum_{i=1}^n H_i \boldsymbol{\eta}^{(i)} \right) \otimes \mathbf{N} dA \\ &= \sum_{\text{elements}} \sum_{i=1}^n \boldsymbol{\eta}^{(i)} \otimes \left(\int_{\partial\Omega_0^{el} \cap \partial\Omega_{\mu 0}} H_i \mathbf{N} dA \right). \end{aligned} \quad (4.131)$$

If the last bracketed term above is denoted by the vector $\mathbf{Z}^{(i)}$, i.e.

$$\mathbf{Z}^{(i)} \equiv \int_{\partial\Omega_0^{el} \cap \partial\Omega_{\mu 0}} H_i \mathbf{N} dA, \quad (4.132)$$

then the element term

$$\sum_{i=1}^n \boldsymbol{\eta}^{(i)} \otimes \left(\int_{\partial\Omega_0^{el} \cap \partial\Omega_{\mu 0}} H_i \mathbf{N} dA \right) \quad (4.133)$$

may be represented in Voigt notation by

$$\begin{bmatrix} Z_1^{(1)} & 0 & 0 & Z_1^{(2)} & 0 & 0 & \dots & Z_1^{(n)} & 0 & 0 \\ 0 & Z_2^{(1)} & 0 & 0 & Z_2^{(2)} & 0 & \dots & 0 & Z_2^{(n)} & 0 \\ 0 & 0 & Z_3^{(1)} & 0 & 0 & Z_3^{(2)} & \dots & 0 & 0 & Z_3^{(n)} \\ Z_2^{(1)} & 0 & 0 & Z_2^{(2)} & 0 & 0 & \dots & Z_2^{(n)} & 0 & 0 \\ Z_3^{(1)} & 0 & 0 & Z_3^{(2)} & 0 & 0 & \dots & Z_3^{(n)} & 0 & 0 \\ 0 & Z_1^{(1)} & 0 & 0 & Z_1^{(2)} & 0 & \dots & 0 & Z_1^{(n)} & 0 \\ 0 & Z_3^{(1)} & 0 & 0 & Z_3^{(2)} & 0 & \dots & 0 & Z_3^{(n)} & 0 \\ 0 & 0 & Z_1^{(1)} & 0 & 0 & Z_1^{(2)} & \dots & 0 & 0 & Z_1^{(n)} \\ 0 & 0 & Z_2^{(1)} & 0 & 0 & Z_2^{(2)} & \dots & 0 & 0 & Z_2^{(n)} \end{bmatrix} \begin{bmatrix} \eta_1^{(1)} \\ \eta_2^{(1)} \\ \eta_3^{(1)} \\ \eta_1^{(2)} \\ \eta_2^{(2)} \\ \eta_3^{(2)} \\ \vdots \\ \eta_1^{(n)} \\ \eta_2^{(n)} \\ \eta_3^{(n)} \end{bmatrix} \quad (4.134)$$

where we adopt the same component ordering convention used in chapter 3. The matrix of $\mathbf{Z}^{(i)}$ components on the left above represents an element constraint operator which may be denoted $\mathbf{C}^{(e)}$ so that the minimal constraint condition becomes

$$\sum_{\text{elements}} \mathbf{C}^{(e)} [\boldsymbol{\eta}^{(e)}] = \mathbf{0}, \quad (4.135)$$

where $[\boldsymbol{\eta}^{(e)}]$ is the vector of element nodal virtual displacements (the column vector on the left of (4.134)). A global constraint matrix \mathbf{C} (in 3-D $9 \times N$ where N is the total number of nodes) may be assembled with each element given as the sum of all terms of the element matrices $\mathbf{C}^{(e)}$ that correspond to the global node indices:

$$\mathbf{C} = \mathbf{A}_e \mathbf{C}^{(e)}. \quad (4.136)$$

In this way we obtain the global discretised expression of the constraint condition:

$$\mathbf{C}[\boldsymbol{\eta}] = \mathbf{0}, \quad (4.137)$$

where $[\boldsymbol{\eta}]$ is the global vector of nodal virtual displacements.

Now in order to rule out rigid body motions six suitable degrees of freedom (in 2-D problems three suffice) are chosen on the RVE boundary and we set

$$[\boldsymbol{\eta}_p] = \mathbf{0}, \quad (4.138)$$

where $[\boldsymbol{\eta}_p]$ denotes the vector of nodal virtual displacement components associated with the chosen prescribed degrees of freedom.

It is convenient to further partition the vector $[\boldsymbol{\eta}]$ as follows

$$[\boldsymbol{\eta}] = \begin{bmatrix} \boldsymbol{\eta}_i \\ \boldsymbol{\eta}_m \\ \boldsymbol{\eta}_d \\ \boldsymbol{\eta}_p \end{bmatrix}. \quad (4.139)$$

Here $[\boldsymbol{\eta}_i]$ are the degrees of freedom of $[\boldsymbol{\eta}]$ associated with internal nodes, $[\boldsymbol{\eta}_p]$ are the prescribed degrees of freedom as above, $[\boldsymbol{\eta}_d]$ are termed the dependent degrees of freedom and $[\boldsymbol{\eta}_m]$ are termed master degrees of freedom. The dependent degrees of freedom are any nine unprescribed boundary degrees of freedom (for a 3 dimensional problem³) such that the square sub-matrix \mathbf{C}_d of associated elements of \mathbf{C} is invertible. The master degrees of freedom are the remaining boundary components - neither in the prescribed or dependent sets. The significance of the nomenclature will become apparent shortly.

The partitioning is extended to the constraint matrix as follows

$$\mathbf{C} = \begin{bmatrix} \mathbf{C}_i & \mathbf{C}_m & \mathbf{C}_d & \mathbf{C}_p \end{bmatrix}, \quad (4.140)$$

so that the constraint equation may be written

$$\mathbf{C}_i[\boldsymbol{\eta}_i] + \mathbf{C}_m[\boldsymbol{\eta}_m] + \mathbf{C}_d[\boldsymbol{\eta}_d] + \mathbf{C}_p[\boldsymbol{\eta}_p] = \mathbf{0}, \quad (4.141)$$

Assuming only shape functions corresponding to nodes that lie on the boundary are non-zero on the boundary then all components of all $\mathbf{Z}^{(i)}$ are zero for internal nodes and so

$$\mathbf{C}_i = \mathbf{0}. \quad (4.142)$$

³The requisite number of dependent degrees of freedom equals the number of rows in \mathbf{C} . That is the square of the number of spatial dimensions - 9 in 3-D, 4 in 2-D. In this way the sub-matrix \mathbf{C}_d of dependent degrees of freedom is square.

In view of this and equation (4.138) the constraint equation simplifies to

$$\mathbf{C}_m[\boldsymbol{\eta}_m] + \mathbf{C}_d[\boldsymbol{\eta}_d] = \mathbf{0}. \quad (4.143)$$

Given that the matrix \mathbf{C}_d is square and invertible by choice of dependent degrees of freedom, then we finally obtain the following explicit expression for the dependent degrees of freedom in terms of the master degrees of freedom:

$$[\boldsymbol{\eta}_d] = -\mathbf{C}_d^{-1}\mathbf{C}_m[\boldsymbol{\eta}_m]. \quad (4.144)$$

Thus the dependent degrees of freedom may be wholly determined by the master degrees of freedom. The master degrees of freedom may, along with the interior degrees of freedom, be considered independent. It simplifies the subsequent treatment of the problem to group the interior and master degrees of freedom under the label of free or independent degrees of freedom:

$$[\boldsymbol{\eta}_f] = \begin{bmatrix} \boldsymbol{\eta}_i \\ \boldsymbol{\eta}_m \end{bmatrix}. \quad (4.145)$$

so that we may rewrite the dependency equation (4.144)

$$[\boldsymbol{\eta}_d] = \begin{bmatrix} \mathbf{0} & -\mathbf{C}_d^{-1}\mathbf{C}_m \end{bmatrix} \begin{bmatrix} \boldsymbol{\eta}_i \\ \boldsymbol{\eta}_m \end{bmatrix} = \mathbf{D}[\boldsymbol{\eta}_f], \quad (4.146)$$

where we have introduced the dependency matrix \mathbf{D} defined by

$$\mathbf{D} = \begin{bmatrix} \mathbf{D}_i & \mathbf{D}_m \end{bmatrix} = \begin{bmatrix} \mathbf{0} & -\mathbf{C}_d^{-1}\mathbf{C}_m \end{bmatrix}. \quad (4.147)$$

Thus under the uniform traction boundary condition we have 6 boundary degrees of freedom set to zero by (4.138) and a further 9 wholly determined through (4.146) by the remaining independent degrees of freedom.

In order to see how this affects the Newton-Raphson solution scheme we partition the stiffness matrix and fluctuation displacement vector in the same way as above. Equation (4.127) may thus be written

$$\begin{bmatrix} \boldsymbol{\eta}_f \\ \boldsymbol{\eta}_d \\ \boldsymbol{\eta}_p \end{bmatrix}^T \left\{ \begin{bmatrix} \mathbf{K}_{ff} & \mathbf{K}_{fd} & \mathbf{K}_{fp} \\ \mathbf{K}_{df} & \mathbf{K}_{dd} & \mathbf{K}_{dp} \\ \mathbf{K}_{pf} & \mathbf{K}_{pd} & \mathbf{K}_{pp} \end{bmatrix} \begin{bmatrix} \delta\tilde{\mathbf{U}}_f \\ \delta\tilde{\mathbf{U}}_d \\ \delta\tilde{\mathbf{U}}_p \end{bmatrix} + \begin{bmatrix} \mathbf{F}_f^{\text{int}} \\ \mathbf{F}_d^{\text{int}} \\ \mathbf{F}_p^{\text{int}} \end{bmatrix} \right\} = 0, \quad (4.148)$$

where the subscripts k and $(k-1)$ have been dropped for clarity and it is understood that \mathbf{K} and \mathbf{F}^{int} are evaluated at $\mathbf{U}_{k-1} = (\mathbf{F} - \mathbf{I})\mathbf{Y} + \tilde{\mathbf{U}}_{k-1}$. Now since the

fluctuation displacements must satisfy the same kinematic constraints as the virtual displacements it follows that

$$\delta \tilde{\mathbf{U}}_p = \mathbf{0} \quad (4.149)$$

$$\delta \tilde{\mathbf{U}}_d = \mathbf{D} \delta \tilde{\mathbf{U}}_f. \quad (4.150)$$

In view of this and equations (4.138) and (4.146) we may rewrite equation (4.148) as

$$\begin{bmatrix} \boldsymbol{\eta}_f \\ \mathbf{D}\boldsymbol{\eta}_f \\ \mathbf{0} \end{bmatrix}^T \left\{ \begin{bmatrix} \mathbf{K}_{ff} & \mathbf{K}_{fd} & \mathbf{K}_{fp} \\ \mathbf{K}_{df} & \mathbf{K}_{dd} & \mathbf{K}_{dp} \\ \mathbf{K}_{pf} & \mathbf{K}_{pd} & \mathbf{K}_{pp} \end{bmatrix} \begin{bmatrix} \delta \tilde{\mathbf{U}}_f \\ \mathbf{D} \delta \tilde{\mathbf{U}}_f \\ \mathbf{0} \end{bmatrix} + \begin{bmatrix} \mathbf{F}_f^{\text{int}} \\ \mathbf{F}_d^{\text{int}} \\ \mathbf{F}_p^{\text{int}} \end{bmatrix} \right\} = 0. \quad (4.151)$$

The zero term in the $[\boldsymbol{\eta}]$ vector allows the last row above to be eliminated to obtain

$$\begin{bmatrix} \boldsymbol{\eta}_f \\ \mathbf{D}\boldsymbol{\eta}_f \end{bmatrix}^T \left\{ \begin{bmatrix} \mathbf{K}_{ff} & \mathbf{K}_{fd} \\ \mathbf{K}_{df} & \mathbf{K}_{dd} \end{bmatrix} \begin{bmatrix} \delta \tilde{\mathbf{U}}_f \\ \mathbf{D} \delta \tilde{\mathbf{U}}_f \end{bmatrix} + \begin{bmatrix} \mathbf{F}_f^{\text{int}} \\ \mathbf{F}_d^{\text{int}} \end{bmatrix} \right\} = 0. \quad (4.152)$$

Next the two rows in the $\mathbf{K}[\delta \tilde{\mathbf{U}}]$ term may be combined to give

$$\begin{bmatrix} \boldsymbol{\eta}_f \\ \mathbf{D}\boldsymbol{\eta}_f \end{bmatrix}^T \left\{ \begin{bmatrix} \mathbf{K}_{ff} + \mathbf{K}_{fd}\mathbf{D} \\ \mathbf{K}_{df} + \mathbf{K}_{dd}\mathbf{D} \end{bmatrix} [\delta \tilde{\mathbf{U}}_f] + \begin{bmatrix} \mathbf{F}_f^{\text{int}} \\ \mathbf{F}_d^{\text{int}} \end{bmatrix} \right\} = 0. \quad (4.153)$$

Finally the terms multiplying $\boldsymbol{\eta}_f$ may be combined to obtain

$$\begin{aligned} [\boldsymbol{\eta}_f]^T \left\{ \begin{bmatrix} \mathbf{K}_{ff} + \mathbf{K}_{fd}\mathbf{D} + \mathbf{D}^T \mathbf{K}_{df} + \mathbf{D}^T \mathbf{K}_{dd} \mathbf{D} \end{bmatrix} [\delta \tilde{\mathbf{U}}_f] \right. \\ \left. + \begin{bmatrix} \mathbf{F}_f^{\text{int}} + \mathbf{D}^T \mathbf{F}_d^{\text{int}} \end{bmatrix} \right\} = 0. \end{aligned} \quad (4.154)$$

This must hold for arbitrary $\boldsymbol{\eta}_f$. Thus we obtain the following Newton-Raphson scheme

$$[\delta \tilde{\mathbf{U}}_f]_k = [\delta \tilde{\mathbf{U}}_f]_{k-1} + [\delta \tilde{\mathbf{U}}_f] \quad (4.155)$$

$$\begin{bmatrix} \mathbf{K}_{ff} + \mathbf{K}_{fd}\mathbf{D} + \mathbf{D}^T \mathbf{K}_{df} + \mathbf{D}^T \mathbf{K}_{dd} \mathbf{D} \end{bmatrix} [\delta \tilde{\mathbf{U}}_f] = - \begin{bmatrix} \mathbf{F}_f^{\text{int}} + \mathbf{D}^T \mathbf{F}_d^{\text{int}} \end{bmatrix}, \quad (4.156)$$

with the convergence condition, obtained by applying equations (4.138) and (4.146) to the discretised virtual work equation (4.125), given by

$$[\mathbf{F}_f^{\text{int}} + \mathbf{D}^T \mathbf{F}_d^{\text{int}}] = \mathbf{0}. \quad (4.157)$$

This iterative scheme may be used to obtain the internal and boundary independent nodal fluctuation displacements consistent with equilibrium and the uniform

traction boundary condition. The prescribed boundary degrees of freedom $\boldsymbol{\eta}_p$ are simply zero and the remaining dependent degrees of freedom are obtained from the dependency condition

$$[\tilde{\mathbf{U}}_d] = \mathbf{D} [\tilde{\mathbf{U}}_f] . \quad (4.158)$$

Thus the full vector of nodal fluctuation displacements $[\tilde{\mathbf{U}}_\mu]$ is obtained.

4.12.2 Periodic boundary condition: discretisation

Under the periodic constraint the boundary of the RVE is divided into a number of parts Γ_i^- , Γ_i^+ ($i = 1, \dots, n$) such that, for each i , Γ_i^- is a rigid translation of Γ_i^+ . Admissible virtual displacements and fluctuations at corresponding points \mathbf{Y}^- and \mathbf{Y}^+ on paired boundary portions must be equal. A finite element mesh may be constructed such that the nodes on each Γ_i^- have a one-to-one correspondence with the nodes on Γ_i^+ and are located at corresponding points. The periodic constraint applied to the discrete system consists of the condition that corresponding nodes experience the same displacement fluctuation⁴.

Rectangular RVE

We consider first of all the case of a two dimensional rectangular RVE. Figure 4.4 illustrates a possible finite element mesh. The vector of nodal fluctuations and nodal virtual displacements may be partitioned as follows;

$$[\tilde{\mathbf{U}}] = \begin{bmatrix} \tilde{\mathbf{U}}_i \\ \tilde{\mathbf{U}}_+ \\ \tilde{\mathbf{U}}_- \\ \tilde{\mathbf{U}}_v \end{bmatrix} \quad [\boldsymbol{\eta}] = \begin{bmatrix} \boldsymbol{\eta}_i \\ \boldsymbol{\eta}_+ \\ \boldsymbol{\eta}_- \\ \boldsymbol{\eta}_v \end{bmatrix} , \quad (4.159)$$

where the subscript i indicates degrees of freedom associated with internal nodes and v indicates degrees of freedom associated with nodes at the vertices of the RVE. The subscripts $+$ and $-$ label the degrees of freedom associated with boundary nodes, excluding the corners, that belong to $\Gamma^+ = \bigcup_i \Gamma_i^+$ and $\Gamma^- = \bigcup_i \Gamma_i^-$ respectively.

⁴Somer *et al.* [102] have proposed using a distinct discretisation of the RVE boundary especially for enforcing the periodic condition. Typically fewer boundary nodes are employed than appear in the main finite element mesh. Periodicity is enforced directly on these special nodes. Mesh nodes are controlled by interpolation between the periodic nodes. The method has the advantage that the mesh does not have to be created with nodes at corresponding boundary locations. More importantly it reduces the number of unconstrained degrees of freedom in the system and hence saves computational effort with only a small loss of accuracy.

The ordering of components in $[\tilde{\mathbf{U}}_+]$, $[\tilde{\mathbf{U}}_-]$, $[\boldsymbol{\eta}_+]$ and $[\boldsymbol{\eta}_-]$ respects the correspondence between paired boundary nodes so that the periodicity condition requires that

$$[\tilde{\mathbf{U}}_-] = [\tilde{\mathbf{U}}_+] \quad (4.160)$$

$$[\boldsymbol{\eta}_-] = [\boldsymbol{\eta}_+] \quad (4.161)$$

The corner nodes also lie on the boundary and are governed by the periodicity condition. However each vertex belongs to two distinct boundary portions. For the rectangular RVE in figure 4.4 this means that fluctuations at the corner labeled V1 must match those at corner V2 because the two nodes lie at corresponding points on Γ_1^- and Γ_1^+ . Since V1 is also one end of Γ_2^- the fluctuation must also be equal at V4 on Γ_2^+ . By similar argument fluctuations at V2 and V4 must match. Therefore periodic fluctuation displacements occurring at all four corners of a periodic rectangular RVE must be equal to each other. The same is obviously true of kinematically admissible virtual displacements.

Now in order to rule out rigid body motion of the RVE it is necessary in this 2-D example to fix three degrees of freedom (the 3-D case requires six fixed d.o.f.). It is convenient to choose corner nodes for this purpose. Since all eight degrees of freedom associated with the corner nodes must by the periodicity condition be the same it follows that fixing three of these fixes them all. Thus we may write

$$[\tilde{\mathbf{U}}_v] = \mathbf{0} \quad (4.162)$$

$$[\boldsymbol{\eta}_v] = \mathbf{0}. \quad (4.163)$$

It can now be seen that the degrees of freedom associated with the rectangular RVE under the periodic boundary condition may be divided into three types. Firstly there are those associated with the corner nodes that are fully prescribed. In order to conform with the nomenclature used in the discretisation of the uniform traction condition (subsection 4.12.1) we re-label these with the subscript p so that

$$[\tilde{\mathbf{U}}_p] \equiv [\tilde{\mathbf{U}}_v] = \mathbf{0} \quad (4.164)$$

$$[\boldsymbol{\eta}_p] \equiv [\boldsymbol{\eta}_v] = \mathbf{0}. \quad (4.165)$$

Secondly there are the degrees of freedom which may be considered free or independent. These consist of the components associated with interior nodes and one half of the paired boundary nodes. Choosing $\boldsymbol{\eta}_-$ and $\tilde{\mathbf{U}}_-$ to be independent and using the

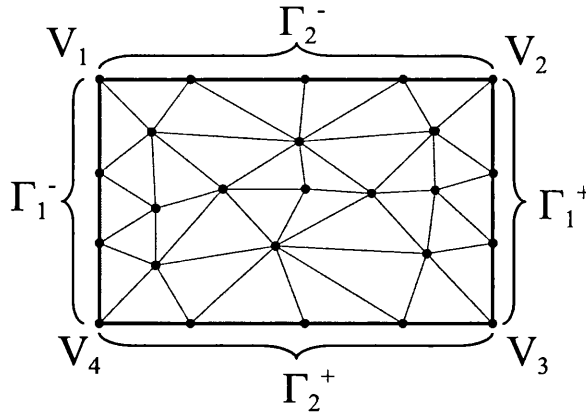


Figure 4.4: A finite element mesh for 2-D rectangular RVE under the periodic constraint.

subscript f to denote the collection of free components we may write

$$\begin{bmatrix} \tilde{\mathbf{U}}_f \end{bmatrix} \equiv \begin{bmatrix} \tilde{\mathbf{U}}_i \\ \tilde{\mathbf{U}}_- \end{bmatrix} \quad \text{and} \quad \begin{bmatrix} \boldsymbol{\eta}_f \end{bmatrix} \equiv \begin{bmatrix} \boldsymbol{\eta}_i \\ \boldsymbol{\eta}_- \end{bmatrix}. \quad (4.166)$$

Finally their remain $\boldsymbol{\eta}_+$ and $\tilde{\mathbf{U}}_+$. These are fully determined through the constraint equation (4.160) and may be termed dependent degrees of freedom with the subscript d so that we have

$$\begin{aligned} \begin{bmatrix} \tilde{\mathbf{U}}_d \end{bmatrix} &\equiv \begin{bmatrix} \tilde{\mathbf{U}}_+ \end{bmatrix} = \begin{bmatrix} \mathbf{0} & \mathbf{I} \end{bmatrix} \begin{bmatrix} \tilde{\mathbf{U}}_i \\ \tilde{\mathbf{U}}_- \end{bmatrix} \\ &= \mathbf{D} \begin{bmatrix} \tilde{\mathbf{U}}_f \end{bmatrix}, \end{aligned} \quad (4.167)$$

and

$$\begin{aligned} \begin{bmatrix} \boldsymbol{\eta}_d \end{bmatrix} &\equiv \begin{bmatrix} \boldsymbol{\eta}_+ \end{bmatrix} = \begin{bmatrix} \mathbf{0} & \mathbf{I} \end{bmatrix} \begin{bmatrix} \boldsymbol{\eta}_i \\ \boldsymbol{\eta}_- \end{bmatrix} \\ &= \mathbf{D} \begin{bmatrix} \boldsymbol{\eta}_f \end{bmatrix}, \end{aligned} \quad (4.168)$$

where the dependency matrix \mathbf{D} is defined by

$$\mathbf{D} \equiv \begin{bmatrix} \mathbf{D}_i & \mathbf{D}_- \end{bmatrix} = \begin{bmatrix} \mathbf{0} & \mathbf{I} \end{bmatrix}. \quad (4.169)$$

Thus we have identified prescribed, free and dependent degrees of freedom with a dependency equation linking the last two. The discretised problem is thus formulated in exactly the same terms as for the uniform boundary traction constraint (subsection

4.12.1 and the RVE equilibrium problem may be solved by the same Newton-Raphson scheme as before:

$$\left[\delta \tilde{\mathbf{U}}_f \right]_k = \left[\delta \tilde{\mathbf{U}}_f \right]_{k-1} + \left[\delta \tilde{\mathbf{U}}_f \right] \quad (4.170)$$

$$\left[\mathbf{K}_{ff} + \mathbf{K}_{fd} \mathbf{D} + \mathbf{D}^T \mathbf{K}_{df} + \mathbf{D}^T \mathbf{K}_{dd} \mathbf{D} \right] \left[\delta \tilde{\mathbf{U}}_f \right] = - \left[\mathbf{F}_f^{\text{int}} + \mathbf{D}^T \mathbf{F}_d^{\text{int}} \right] . \quad (4.171)$$

The only difference from the uniform traction condition lies in the choice of degrees of freedom that constitute the free, dependent and prescribed groups and in the definition (4.169) of the dependency matrix \mathbf{D} .

Arbitrarily shaped RVE

We have seen how the periodic condition acting on a two dimensional RVE may be discretised. The general case of an arbitrary shape may be treated in a similar fashion. There is only one complication. This manifests itself in how periodicity affects the vertices of the RVE - that is the nodes at which distinct portions $\Gamma_i^{+/-}$ of the RVE meet. Unlike the rectangular (or cuboid) case, in general all vertices are not constrained to undergo the same displacement fluctuation. Instead groups of vertices may be formed that must have equal fluctuations. We therefore have a more complicated interdependency between periodic nodal displacement fluctuations and between virtual displacements. Nevertheless it is still possible to define prescribed, free and dependent degrees of freedom along with a dependency equation and to solve the RVE equilibrium problem with a Newton-Raphson scheme in the form of (4.170).

It may easily be verified for instance that for the extruded hexagon in figure 4.5 vertices A, C, E, G, I and K must all have matching fluctuations. The remaining vertex fluctuations at B, D, F, H, J and L must also equal each other but need not be the same as the first group. Rigid body motion may be eliminated by fixing the first group of vertices thus defining the prescribed degrees of freedom. One of the remaining vertices, B say, may be chosen as a master node and grouped with the internal nodes to define the free set of degrees of freedom. The vertices D, F, H, J and L are then classified as dependent nodes. Thus in terms of kinematically admissible

virtual displacements we may write

$$\begin{aligned}
 [\eta_p] &\equiv \begin{bmatrix} \eta_A \\ \eta_C \\ \eta_E \\ \eta_G \\ \eta_I \\ \eta_K \end{bmatrix} & [\eta_f] &\equiv \begin{bmatrix} \eta_i \\ \eta_- \\ \eta_B \end{bmatrix} \\
 \text{and} \quad [\eta_d] &\equiv \begin{bmatrix} \eta_+ \\ \eta_D \\ \eta_F \\ \eta_H \\ \eta_J \\ \eta_L \end{bmatrix} = \underbrace{\begin{bmatrix} 0 & I & 0 \\ 0 & 0 & 1 \\ 0 & 0 & 1 \\ 0 & 0 & 1 \\ 0 & 0 & 1 \\ 0 & 0 & 1 \end{bmatrix}}_D \underbrace{\begin{bmatrix} \eta_i \\ \eta_- \\ \eta_B \end{bmatrix}}_{[\eta_f]} = D[\eta_f]
 \end{aligned}$$

with similar expressions for the displacement fluctuations. Thus an appropriate partition of the discretised system's degrees of freedom has been identified allowing the Newton-Raphson (4.170) scheme to be applied.

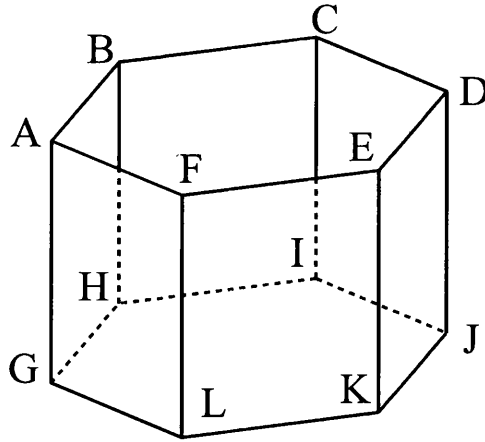


Figure 4.5: An RVE occupying an extruded hexagon.

4.12.3 Linear boundary condition: discretisation

Discretisation of the linear boundary condition is simple. It suffices to identify the boundary nodes and set the associated degrees of freedom of the virtual displacements and fluctuations to zero. Degrees of freedom associated with internal nodes are

unconstrained. Adopting the formulation used for the constant traction and periodic conditions, we have a prescribed set of degrees of freedom $[\boldsymbol{\eta}_p]$ and $[\tilde{\mathbf{U}}_p]$ associated with the boundary nodes and a free set of degrees of freedom $[\boldsymbol{\eta}_f]$ and $[\tilde{\mathbf{U}}_f]$ associated with internal nodes. The set of dependent degrees of freedom is empty. In order to conform with the previous formulation we may still write

$$[\boldsymbol{\eta}_d] = \mathbf{D}[\boldsymbol{\eta}_f] \quad \text{and} \quad [\tilde{\mathbf{U}}_d] = \mathbf{D}[\tilde{\mathbf{U}}_f],$$

where the dependency matrix \mathbf{D} is now taken to be the *empty matrix*⁵ $\mathbf{\emptyset}$. The RVE equilibrium problem is solved by the previous Newton-Raphson scheme (4.155) which with $\mathbf{D} = \mathbf{\emptyset}$ reduces to

$$\left[\delta \tilde{\mathbf{U}}_f \right]_k = \left[\delta \tilde{\mathbf{U}}_f \right]_{k-1} + \left[\delta \tilde{\mathbf{U}}_f \right] \quad (4.172)$$

$$\left[\mathbf{K}_{ff} \right] \left[\delta \tilde{\mathbf{U}}_f \right] = - \left[\mathbf{F}_f^{\text{int}} \right], \quad (4.173)$$

where the free nodes are the interior nodes:

$$\left[\tilde{\mathbf{U}}_f \right] = \left[\tilde{\mathbf{U}}_i \right]. \quad (4.174)$$

4.12.4 Taylor condition: discretisation

The Taylor condition is the simplest of all to deal with as there is no equilibrium problem to be solved to obtain the displacement field. We simply set all the nodal displacement fluctuations to zero. The Taylor case may be formulated in the same terms adopted for the previous kinematic constraints by defining the prescribed degrees of freedom as the set of all degrees of freedom with the free and dependent sets empty and the dependency matrix \mathbf{D} as an empty matrix.

4.13 Implementation of the computational homogenisation procedure

An implementation of the homogenisation procedure discussed in the preceding sections was coded in the commercially available MATLAB programming language. The structure of the resulting program, known as `microplast`, is illustrated in flow chart form by figure 4.6. Examples of homogenisation performed using the program

⁵That is to say the matrix which on multiplying any vector yields the empty set, on multiplying another matrix yields the empty matrix and on addition leaves other matrices unaffected.

Box 3: Summary of a finite element homogenisation procedure.

1. Partition the global degrees of freedom into independent, dependent and prescribed components according to the chosen kinematic constraint:

Constraint	prescribed (p)	dependent (d)	independent (f)
uniform traction	sufficient boundary d.o.f.s fluctuation to prevent rigid motion	any 9 (or 4 in 2-D) unprescribed boundary d.o.f.s such that \mathbf{C}_d is invertible	interior & remainder of boundary nodes
periodic (rectangular cell)	corner nodes	boundary nodes in Γ^- (not corners)	boundary nodes in Γ^+ (not corners) & interior nodes
linear	boundary nodes	none	interior nodes
Taylor	all degrees of freedom	none	none

2. Construct the dependency matrix \mathbf{D} according to the chosen kinematic constraint:

$$\begin{aligned}
 \text{uniform traction} &: \mathbf{D} = \begin{bmatrix} \mathbf{0} & -\mathbf{C}_d^{-1} \mathbf{C}_m \end{bmatrix} \\
 \text{periodic} &: \mathbf{D} = \begin{bmatrix} \mathbf{0} & \mathbf{I} \end{bmatrix} \quad (\text{rectangular cell}) \\
 \text{linear} &: \mathbf{D} = \mathbf{0} \\
 \text{Taylor} &: \mathbf{D} = \mathbf{0}
 \end{aligned}$$

where in the above \mathbf{C} is defined by (4.136), $\mathbf{0}$ is a matrix of zeros with n_d rows and n_{int} columns and \mathbf{I} is a $n_d \times n_d$ identity matrix (n_d & n_{int} being the number of dependent and interior degrees of freedom respectively).

3. Solve the reduced Newton-Raphson scheme for the independent fluctuation displacements $[\tilde{\mathbf{U}}_f]$:

$$\begin{aligned}
 [\delta \tilde{\mathbf{U}}_f]_k &= [\delta \tilde{\mathbf{U}}_f]_{k-1} + [\delta \tilde{\mathbf{U}}_f] \\
 \mathbf{K}_R [\delta \tilde{\mathbf{U}}_f] &= - [\mathbf{F}_f^{\text{int}} + \mathbf{D}^T \mathbf{F}_d^{\text{int}}] ,
 \end{aligned}$$

$$\text{where } \mathbf{K}_R = [\mathbf{K}_{ff} + \mathbf{K}_{fd} \mathbf{D} + \mathbf{D}^T \mathbf{K}_{df} + \mathbf{D}^T \mathbf{K}_{dd} \mathbf{D}] .$$

4. Calculate the average first Piola-Kirchhoff stress.

are provided in chapter 5. Further use of the program is made to carry out the homogenisation stages in chapters 6 and 7. These applications all use hyperelastic

RVE materials but the algorithm is suitable for general history dependent materials having an internal variable formulation.

In addition to the homogenisation steps already described in this chapter the program also uses an increment cutting feature whereby the size of the incremental step in the loading history is reduced if convergence of the Newton-Raphson algorithm cannot be attained within a reasonable number of iterations.

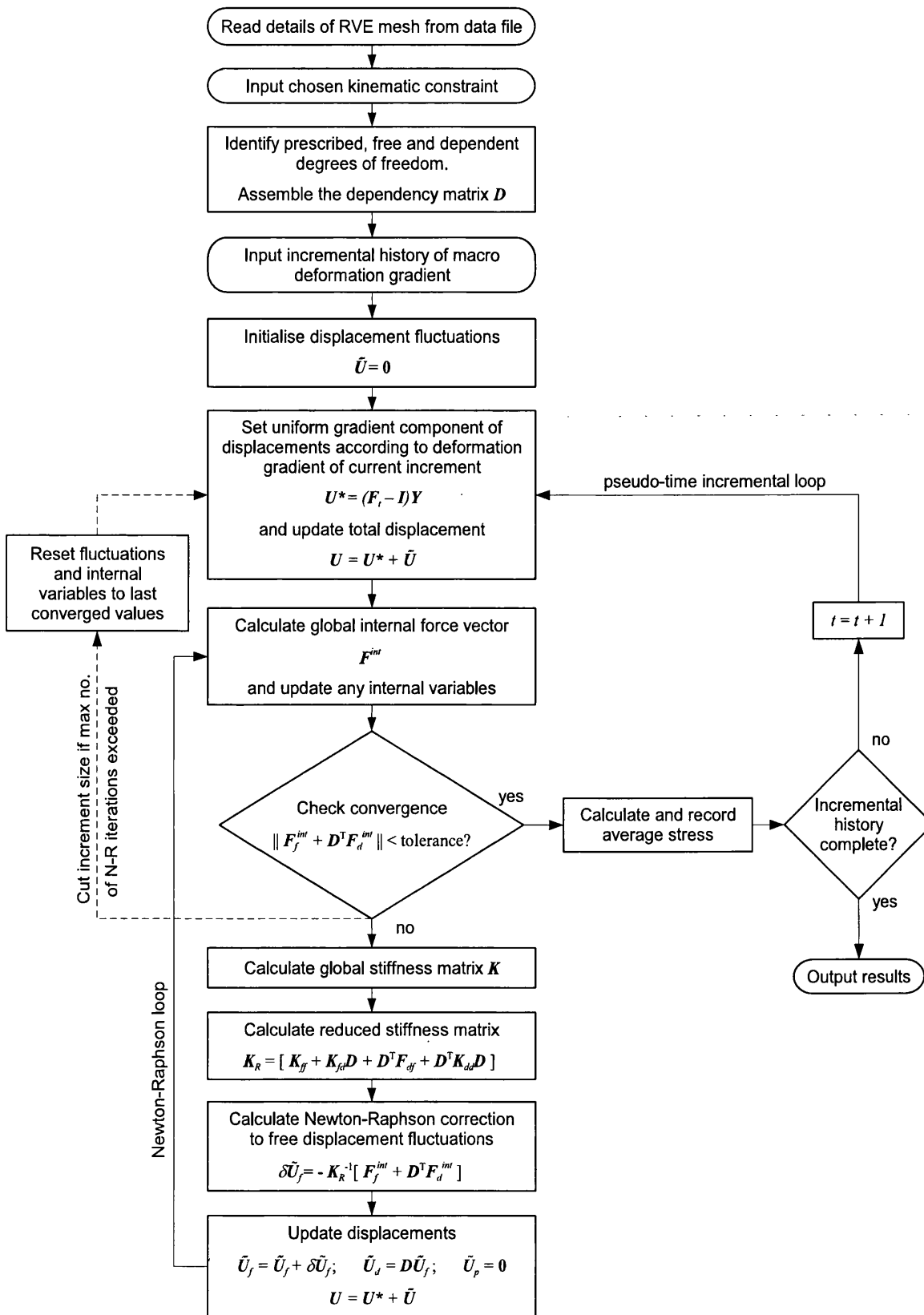


Figure 4.6: Flow chart for the program *microplast* – a finite element implementation of the computational homogenisation procedure.

Chapter 5

Application of computational homogenisation

5.1 Introduction

In this chapter a number of examples of microcell homogenisation using the `microplast` program described in chapter 4 are presented. The main objectives are to provide a degree of verification of the performance of the code and to investigate the relative behaviour of different meshes and boundary conditions.

With regard to the first of these objectives, it should be noted that while there are, in the context of small deformations, analytical solutions which approximate the average response of certain RVEs (e.g. Nemat-Nasser and Hori's analysis [83] may be compared to a microcell with a small circular elastic inclusion - see Partovi [91]), at large deformations such solutions are harder to find.

In the case of Taylor or linear boundary conditions the microcell boundary value problem is actually of the conventional kind with explicitly prescribed displacements and no applied forces. It is therefore possible to use an established finite element code on a given microcell mesh with appropriate fixed nodal displacements and compare results with the output of `microplast`. This was in fact done using the `HYPLAS` program described in de Souza, Perić and Owen [17] with a large selection of meshes. Although the results are not presented here, in all cases near perfect agreement was observed.

The performance of `microplast` with other boundary conditions is harder to corroborate. However there are certain characteristics of the homogenised behavior

of microstructures which may be expected a priori. Thus a degree of confidence in the program may be obtained if it produces results in accordance with these expectations. Some of these expectations are explored in the examples of this chapter.

5.2 Soft matrix with stiff inclusions

5.2.1 Problem definition

In this first example a square RVE or microcell was used consisting of five circular inclusions of varying diameter placed irregularly within a softer matrix. The matrix and inclusion materials were both of the Ogden type

$$\Psi = \sum_{p=1}^N \frac{\mu_p}{\alpha_p} (\lambda_1^{\alpha_p} + \lambda_2^{\alpha_p} + \lambda_3^{\alpha_p} - 3)$$

where λ_1 , λ_2 and λ_3 are the principal stretches of the motion and the respective parameters as follows:

- Matrix:

Incompressible Ogden

$N = 2$, $\mu_1 = 50$, $\mu_2 = -14$, $\alpha_1 = 2$ and $\alpha_2 = -2$

- Inclusions:

Incompressible Ogden

$N = 1$, $\mu_1 = 2000$ and $\alpha_1 = 2$

(This is the same as an incompressible neo-Hookean model with shear modulus $G = 2000$)

Plane stress was assumed and, using each of the four boundary conditions in turn (Taylor, linear, periodic and constant traction), an in-plane shear macro deformation gradient applied in increments from

$$\mathbf{F} = \begin{bmatrix} 1 & 0 \\ 0 & 1 \end{bmatrix}$$

to

$$\mathbf{F} = \begin{bmatrix} 1 & 1 \\ 0 & 1 \end{bmatrix}.$$

A mesh of linear three noded triangular elements was used and is illustrated in figure 5.1.

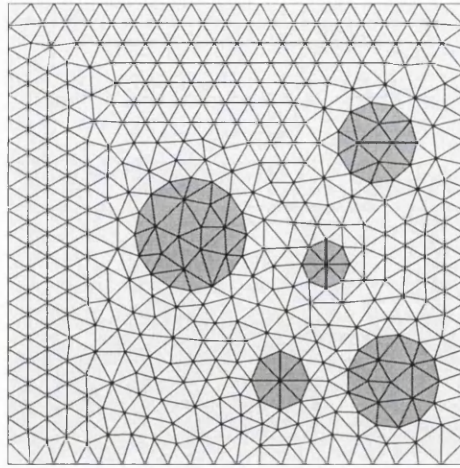


Figure 5.1: Undeformed mesh with 12% inclusions.

5.2.2 Results

Figure 5.2 shows on the left hand side the deformed shapes of the mesh under the full imposed macro deformation gradient for each of the boundary conditions and on the right corresponding contour plots of shear micro Cauchy stress. It can be seen in figure 5.2(a) that only under the Taylor condition do the inclusions become appreciably skewed. This is to be expected since by definition the Taylor condition insists on applying the same deformation uniformly and the inclusions do not need to be in equilibrium with matrix. The other three boundary conditions require the interior of the cell to be self equilibrating and so the stiff inclusions deform much less than the softer material surrounding them to reach the same stress. Also as expected figure 5.2(b) shows the edges of the cell remaining straight under a linear deformation while in figure 5.2(c) the deviation from a linear deformation on opposite edges matches as required by the periodic boundary condition.

Figure 5.3 shows the macro strain energy function, Ψ (that is the micro strain energy averaged over the cell with respect to reference volume), plotted against the deformation gradient component F_{12} . As expected the Taylor boundary condition, being the most prescriptive, produces the highest Ψ value followed in turn by the linear, periodic and constant traction conditions.

Since the curves in figure 5.3 plot Ψ against increasing F_{12} with the other deformation gradient components remaining constant, the gradients of these curves represent the partial derivative $\frac{\partial \Psi}{\partial F_{12}}$. Using the strain energy data, numerical estimates to the gradients were plotted in figure 5.4 against F_{12} . On the same graph are plotted curves

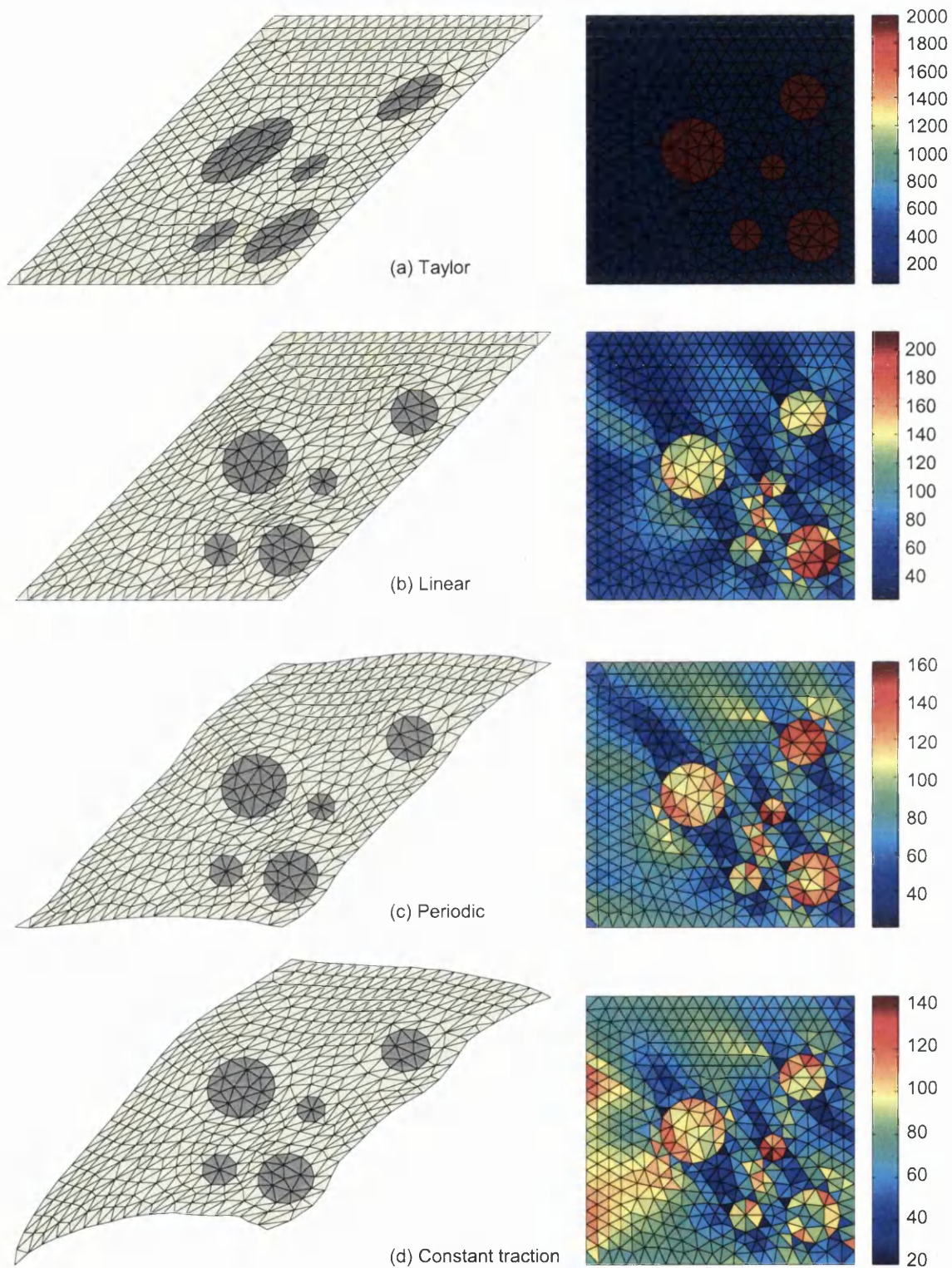


Figure 5.2: Deformed mesh shapes and plots of shear Cauchy stress (σ_{12}) under different boundary conditions.

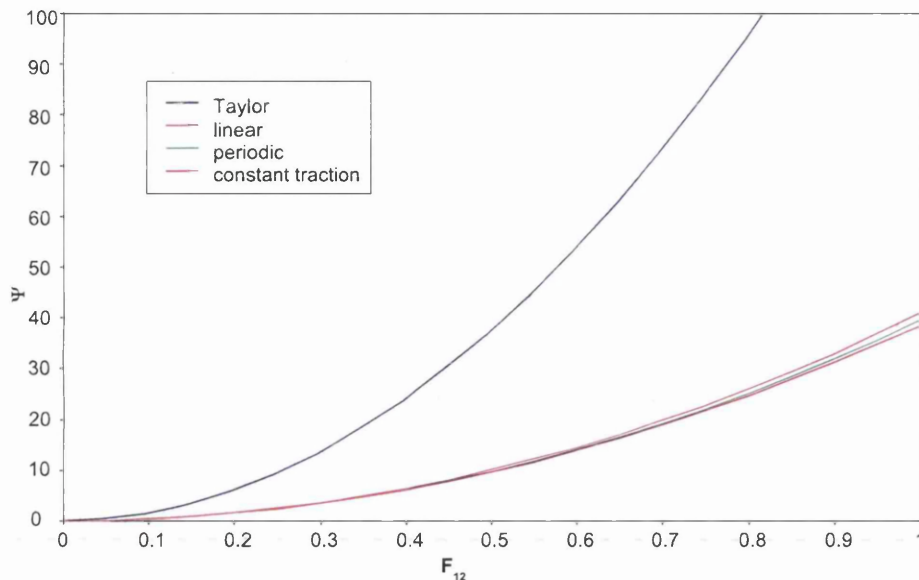


Figure 5.3: Macro strain energy under different boundary conditions.

of macro Piola Kirchhoff stress component P_{12} obtained directly from the `microplast` program. It is seen that the crosses representing the $\frac{\partial \Psi}{\partial F_{12}}$ estimates lie, to within a close tolerance, on the P_{12} curve corresponding to the same boundary condition. This confirms the fact that the averaged micro strain energy represents a true macro strain energy function in the sense that the macro stress \mathbf{P} may be derived from the macro strain energy according to

$$\mathbf{P} = \frac{\partial \Psi}{\partial \mathbf{F}}$$

as in single scale theory. In other words the homogenised stress response of a microcell with only hyperelastic constituents is itself hyperelastic.

5.3 Test of isotropy

A hyperelastic material model is considered isotropic relative to its reference configuration if the strain energy function satisfies

$$\Psi(\mathbf{F}) = \Psi(\mathbf{F}\mathbf{Q})$$

for all admissible deformation gradients \mathbf{F} and all orthogonal tensors \mathbf{Q} . In simple terms an isotropic material should respond the same whether or not a rotation is applied to it before deformation.

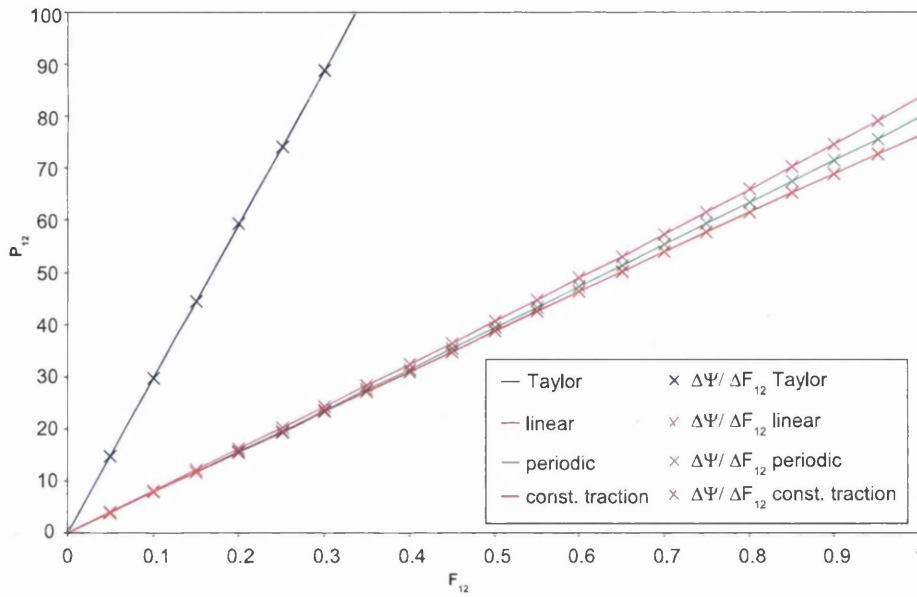


Figure 5.4: Shear component of first Piola Kirchhoff macro stress under different boundary conditions. The solid lines show the direct output of `microplast` while the crosses show a numerical approximation to $\frac{\partial \Psi}{\partial F_{12}}$ obtained from the macro strain energy i.e. the gradients to the curves in figure (5.3).

We do not generally expect the overall response of a RVE to display isotropy even if it is made up entirely of homogenous materials. In order to examine this assertion a microstructure made up wholly of isotropic hyperelastic material was subjected firstly to a range of biaxial deformations, \mathbf{F}_i , and then to the same set of deformations postmultiplied by a tensor representing a 35° rotation, $\mathbf{F}_i \mathbf{Q}$. The resulting homogenised strain energy functions were then compared.

5.3.1 Problem details

The microcell used for this problem consisted of a matrix of Ogden type material punctured by a highly asymmetric arrangement of circular holes making up 12% of the cell area. A mesh of 3 noded linear triangles was used as illustrated in figure 5.5. Matrix material parameters were as follows:

- Incompressible Ogden

$$\left(\Psi = \sum_{p=1}^N \frac{\mu_p}{\alpha_p} (\lambda_1^{\alpha_p} + \lambda_2^{\alpha_p} + \lambda_3^{\alpha_p} - 3) \right)$$

$$N = 2, \mu_1 = 50, \mu_2 = -14, \alpha_1 = 2 \text{ and } \alpha_2 = -2$$

The plane stress condition was assumed throughout.

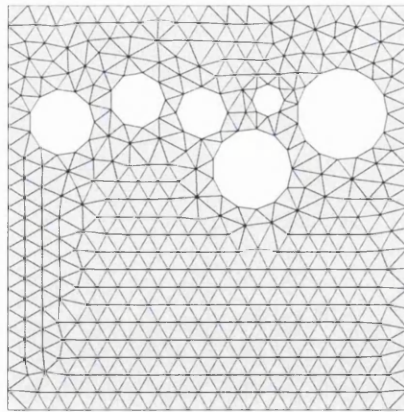


Figure 5.5: Mesh used to test isotropy of homogenised response.

Two sets of imposed deformations were applied to the microcell, the first a range of biaxial isochoric stretches of the form

$$\mathbf{F} = \begin{bmatrix} \lambda_1 & 0 & 0 \\ 0 & \lambda_2 & 0 \\ 0 & 0 & \lambda_1^{-1}\lambda_2^{-1} \end{bmatrix}$$

where λ_1 and λ_2 ranged from 1 to 1.5 and the second made up of the same deformation gradients composed with a rotation of 35° ,

$$\mathbf{F}' = \mathbf{F}\mathbf{Q} = \begin{bmatrix} \lambda_1 & 0 & 0 \\ 0 & \lambda_2 & 0 \\ 0 & 0 & \lambda_1^{-1}\lambda_2^{-1} \end{bmatrix} \begin{bmatrix} \cos 35^\circ & -\sin 35^\circ & 0 \\ \sin 35^\circ & \cos 35^\circ & 0 \\ 0 & 0 & 1 \end{bmatrix}.$$

The homogenised response to both sets of deformation gradients was calculated under the Taylor, linear, periodic and constant traction boundary conditions.

5.3.2 Results

In figure 5.6 the microcell response under each of the boundary conditions is illustrated separately by four contour plots of homogenised strain energy. In each plot the strain energy produced by the first range of deformations (the simple biaxial stretches) is shown by solid black contours. The strain energy contours from the second pre-rotated set of deformations are shown by broken red lines.

The black and red lines coincide in figure 5.6(a). This to be expected since by definition the micro deformation gradient is uniform across the cell leading to a uniform micro strain energy over the solid part. The homogenised strain energy, being

the average of the micro strain energy, is thus given by

$$\Psi(\mathbf{F}) = \frac{1}{V} \int_{\Omega_0} \Psi_\mu(\mathbf{F}) dV = \frac{V_{solid}}{V} \Psi_\mu(\mathbf{F})$$

and so retains the isotropy of the matrix material model.

Using the other three boundary conditions the unrotated and rotated deformation gradients give rise to differing strain energy contours. This observation confirms the fact that for linear, periodic and constant traction boundary conditions the isotropy of constituent materials is not in general preserved in the homogenised behaviour of the RVE. Therefore although the homogenised response is hyperelastic its strain energy function is not generally a unique function of the principle stretches of the motion.

5.4 Comparison of RVEs with varying void and inclusion ratios

In this example the relationship between homogenised response and volume ratio of voids and inclusions is examined. Two sets of square RVEs containing holes and inclusions respectively are considered. The example is suggested by a similar study in small strain by Partovi [91] in which linear elastic materials were considered. Partovi was able to compare homogenised results for Taylor and linear boundary conditions with analytical solutions by Nemat-Nasser and Hori [83] for voids and inclusions surrounded by extended an matrix. The analytic approach relates the void or inclusion ratio and the micro material parameters to derived elastic moduli which characterise the macro constitutive response. However as the theory only covers linear elastic micro constituents in small strain it cannot be used in the present work.

5.4.1 Problem details

The meshes used in this test are illustrated in figure 5.7. All elements are linear 3 node triangles and the plane stress condition was applied.

Material properties for the meshes with holes were as follows:

- Matrix:
Incompressible Ogden
 $N = 1$, $\mu_1 = 600$, and $\alpha_1 = 2$

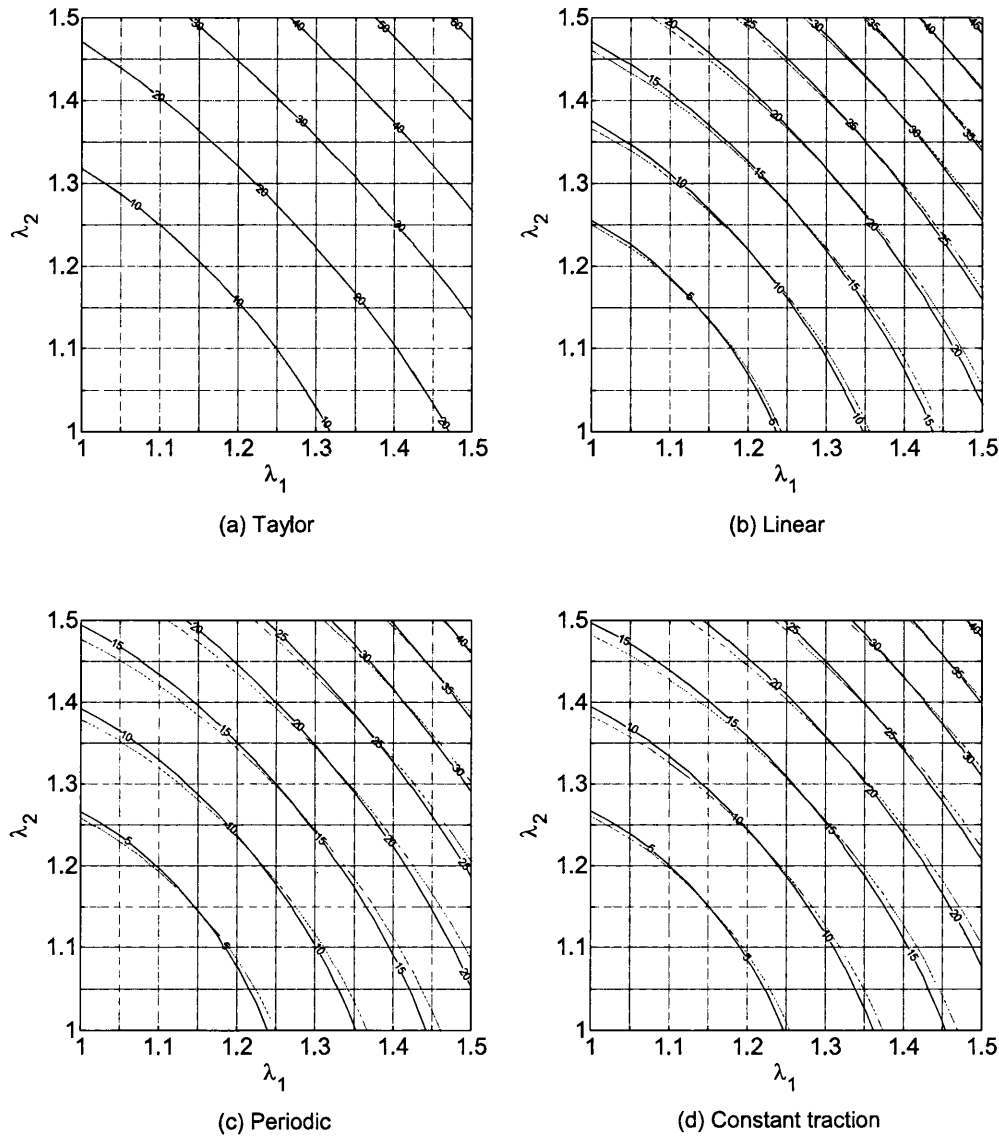


Figure 5.6: Contour plots of homogenised strain energy under each boundary condition. The solid black contours represent strain energy under biaxial deformations. The broken red lines correspond to the same biaxial deformations with a pre-rotation of 35° .

i.e. $\Psi = 300(\lambda_1^2 + \lambda_2^2 + \lambda_3^2 - 3)$

(This is the same as the incompressible neo-Hookean model, $\mathbf{P} = G\mathbf{F} - p\mathbf{F}^{-T}$, with shear modulus $G = 600$ and where p is a hydrostatic Cauchy pressure.)

The other set of microcells had a relatively soft neo-Hookean matrix with much stiffer neo-Hookean inclusions as follows:

- Matrix:

Incompressible Ogden

$N = 1$, $\mu_1 = 500$ and $\alpha_1 = 2$

i.e. $\Psi = 250(\lambda_1^2 + \lambda_2^2 + \lambda_3^2 - 3)$

(This is the same as the incompressible neo-Hookean model, $\mathbf{P} = G\mathbf{F} - p\mathbf{F}^{-T}$, with shear modulus $G = 500$.)

- Inclusions:

Incompressible Ogden

$N = 1$, $\mu_1 = 2000$ and $\alpha_1 = 2$

i.e. $\Psi = 1000(\lambda_1^2 + \lambda_2^2 + \lambda_3^2 - 3)$

(This is the same as the incompressible neo-Hookean model, $\mathbf{P} = G\mathbf{F} - p\mathbf{F}^{-T}$, with shear modulus $G = 2000$.)

The homogenised stress response of each RVE to an imposed macro deformation gradient of

$$F = \begin{bmatrix} 1 & 1 & 0 \\ 0 & 1 & 0 \\ 0 & 0 & 1 \end{bmatrix}$$

was calculated for the Taylor, linear, periodic and constant traction conditions.

5.4.2 Results

The shear component of the first Piola Kirchhoff macro stress, P_{12} , is plotted against void ratio in figure 5.8 for the set of perforated RVEs. Similarly figure 5.9 shows P_{12} plotted against inclusion ratio for the microcells with stiff inclusions. In both graphs the stress values have been divided by G_{matrix} , the shear modulus of the neo-Hookean matrix material. Note that for a pure shear deformation gradient of

$$F = \begin{bmatrix} 1 & 1 & 0 \\ 0 & 1 & 0 \\ 0 & 0 & 1 \end{bmatrix}$$

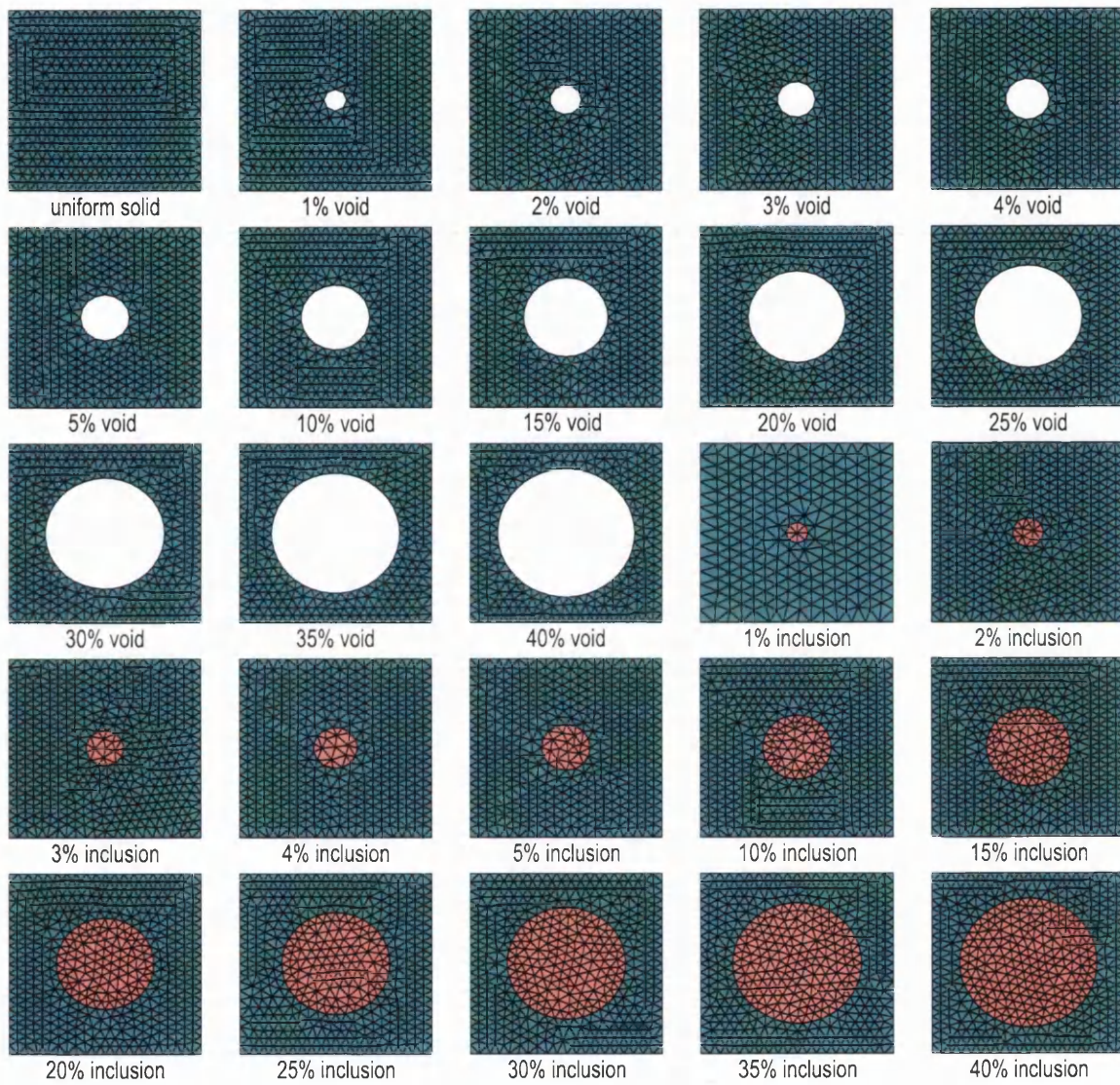


Figure 5.7: Regular meshes with varying ratios of voids and inclusions.

the neo-Hookean constitutive equation yields

$$P_{12} = GF_{12}$$

so that for the given macro deformation ($F_{12} = 1$) a uniform solid RVE (0% voids and 0% inclusions) should respond with a macro shear stress such that

$$\frac{P_{12}}{G_{matrix}} = 1.$$

and this is confirmed in both plots by the data points for zero void/inclusion ratio under all the boundary conditions.

Intuitively one would expect a softening of the homogenised response of the perforated cells as void ratio is increased. This is indeed observed with the negatively sloping P_{12}/G_{matrix} lines in figure 5.8 for all the boundary conditions. As the Taylor condition is equivalent to the law of mixtures it should lead to a linear relationship between macro stress and void ratio and this is confirmed by the straight blue line in figure 5.8. Indeed for this boundary condition the macro response is of the neo-Hookean form with an effective shear modulus equal to the ratio P_{12}/G_{matrix} . The other boundary conditions do not show a linear dependence of shear stress with void ratio. Instead a sharp decline at small void ratios becomes less steep as the ratio increases. Qualitatively this is a similar shape to that observed under the linear boundary condition by Partovi [91] working with linear elastic materials in small strain (periodic and constant traction conditions are not considered in [91]).

Just as one expects larger voids to soften the macro material, an increase in the size of stiff inclusions should stiffen the macro response. This is seen in figure 5.9 where the stress plots for all boundary conditions have positive slopes. Once again the Taylor plot is a straight line in agreement with the law of mixtures. By contrast the other three boundary conditions yield lines with slopes that increase with increasing inclusion ratio. This type of behaviour was also observed by Partovi [91] for linear elastic materials undergoing small deformations under different boundary conditions.

In both plots the familiar order of stiffness between boundary conditions is respected with the Taylor stress response always greater than the linear response which is greater than the periodic response which in turn exceeds the constant traction stress.

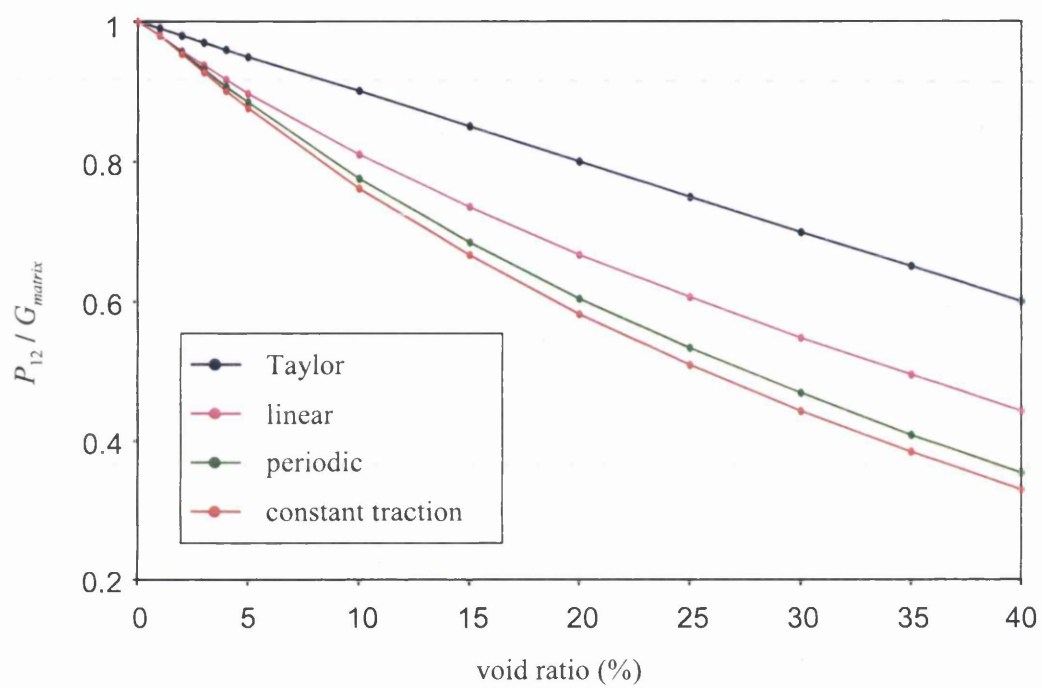


Figure 5.8: Results for RVEs with voids. The shear component of first Piola Kirchhoff stress, P_{12} is plotted against the void ratio. Stress values are scaled by G_{matrix} , the modulus of the neo-Hookean matrix material.

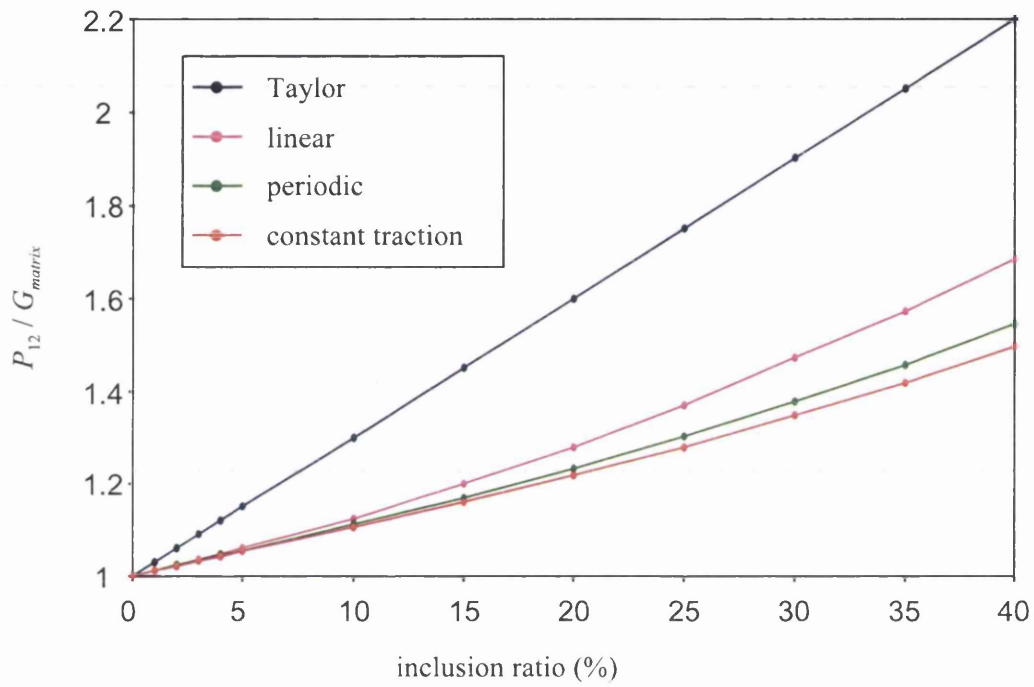


Figure 5.9: Results for RVEs with inclusions. The shear component of first Piola Kirchhoff stress, P_{12} is plotted against the inclusion ratio. Stress values are scaled by G_{matrix} , the modulus of the neo-Hookean matrix material.

5.5 Comparison of RVEs with varying densities of holes

5.5.1 Problem details

In this example the response of a series of RVEs all with the same void fraction but varying hole ‘densities’ was examined. The RVEs considered in the test were perforated with randomly placed circular holes. The diameters of the holes were also randomised but constrained to make up 15% of the cell area. For each RVE a maximum allowable diameter was set. This parameter controlled the ‘density’ of holes since a smaller maximum allowable diameter tends to lead to a larger number of smaller holes making up the required 15% area. In addition to the randomised meshes a regular mesh with a single central 15% hole was also included in the set of test cells. The nine meshes used are illustrated in figure 5.10. Linear 3 noded triangular elements were used throughout and in each case the following material was assigned to the the matrix elements:

- Incompressible Ogden

$$\left(\Psi = \sum_{p=1}^N \frac{\mu_p}{\alpha_p} (\lambda_1^{\alpha_p} + \lambda_2^{\alpha_p} + \lambda_3^{\alpha_p} - 3) \right)$$

$$N = 2, \mu_1 = 50, \mu_2 = -14, \alpha_1 = 2 \text{ and } \alpha_2 = -2$$

The homogenised response of each microcell under an imposed uniaxial deformation of

$$F = \begin{bmatrix} 2 & 0 & 0 \\ 0 & 1 & 0 \\ 0 & 0 & \frac{1}{2} \end{bmatrix}$$

was calculated by `microplast` assuming the plane stress condition. Calculations were repeated for each of the four familiar boundary conditions.

5.5.2 Results

Figure 5.11 shows the homogenised strain energy for each microcell plotted against the maximum allowed void diameter in the mesh with results for each boundary condition linked by a line of distinct colour. As already discussed the homogenised response under the Taylor condition depends only on the overall volume fraction of voids regardless of their spatial configuration. In this example all the meshes had the same percentage of voids so the macro strain energy should be the same for

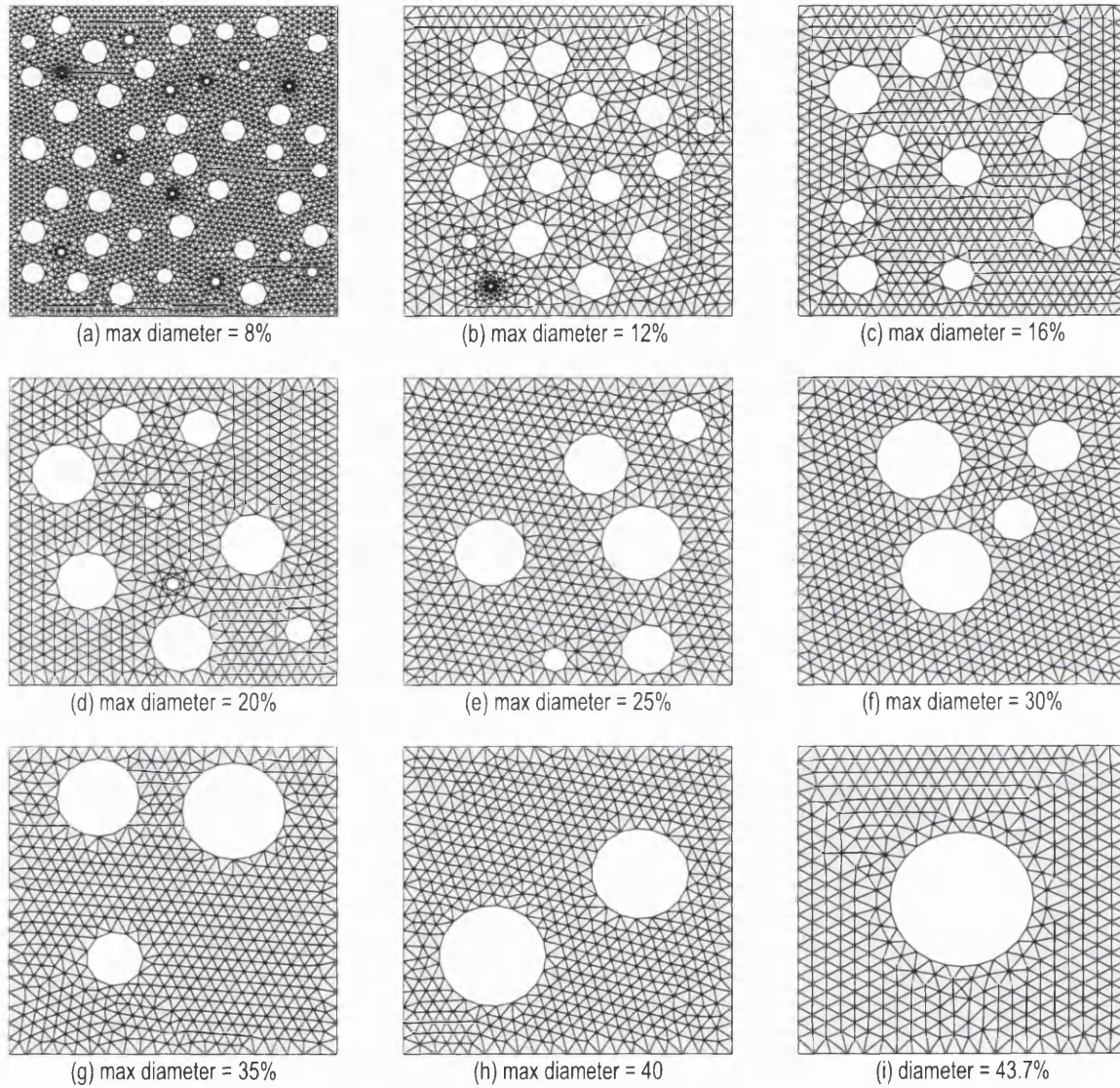


Figure 5.10: Microcells used to investigate the influence of hole density on homogenised response.

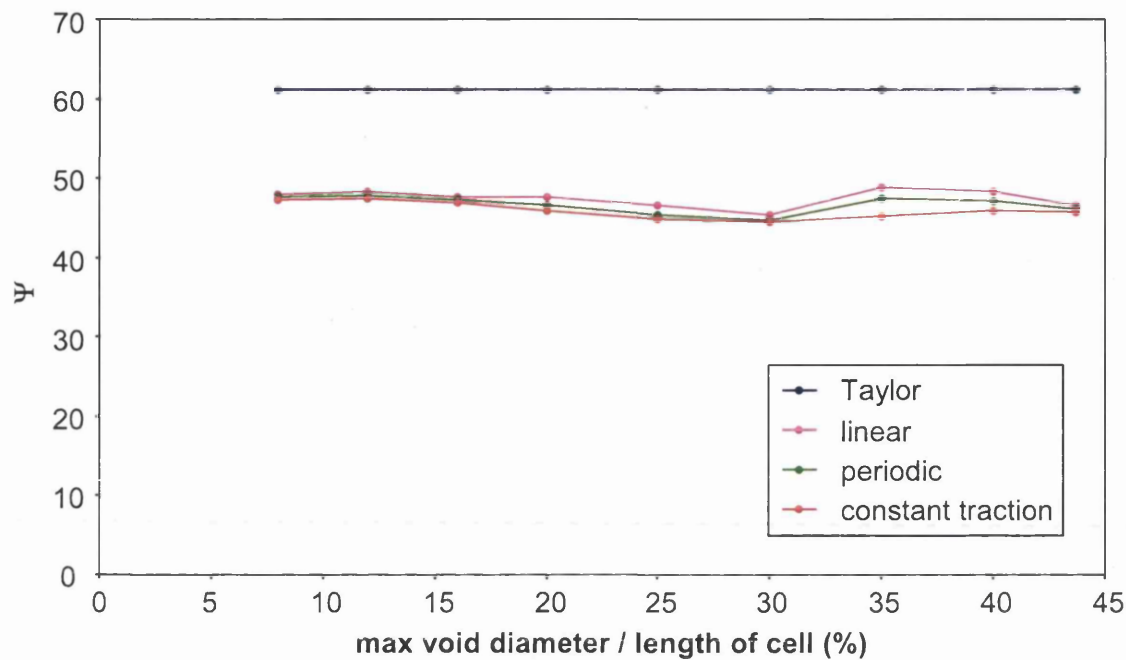


Figure 5.11: Homogenised strain energy plotted against the maximum allowable hole diameter in the RVEs of figure 5.10. Note that these diameters are not the maximum diameters actually found in the meshes but the limit set in generating the random distribution of diameters.

all of them under this boundary condition. The Taylor data points in figure 5.11 clearly conform to this expectation. Also as expected the Taylor strain energies are significantly higher than the strain energy values under the other boundary conditions for each mesh.

The results for the linear, periodic and constant traction boundary conditions are consistent with the expected order of stiffness with the strain energy under the periodic condition always lying between the corresponding results for the other two conditions. Beyond this observation it is hard to detect any pattern in the data. Partovi [92], working in a small deformation formulation, has compared an irregular dense mesh to a regular mesh with a single central hole, both meshes having 15% voids and an elasto-plastic matrix material. He observed that the stress responses under linear and periodic boundary conditions were markedly closer to each other for the dense mesh than the regular mesh. No similar effect is apparent in the results of the present study although it should be noted that Partovi's dense mesh was considerably denser than the densest mesh used here.

5.6 Comparison of regular and irregular void distributions

This example is based on a study described by Kouznetsova et al. [60] whereby the behaviour of regular and random micro structures were compared.

They considered ten random meshes with 12% circular voids and one regular mesh with a single central 12% void. The matrix of each RVE consisted of compressible Neo-Hookean material and the simulations were performed under the plane strain assumption. In these respects the present work has adopted the same procedure. However while the study in [60] only dealt with the periodic boundary condition the present work also considers the Taylor, linear and constant traction conditions. In addition the sizes and distribution of circular holes in the irregular meshes although randomised and maintaining a 12% void fraction is not identical between the two studies.

5.6.1 Problem details

In the present work eleven meshes were prepared as illustrated in figure 5.12. All elements are eight noded quadratic quadrilateral elements integrated with four Gauss points. The regular mesh (mesh 0) has a single circular hole centrally placed within a square matrix. The hole is sized so that its area makes up 12% of the overall area of the cell (i.e. the area of the square including the hole). The other ten irregular meshes (meshes 1-10) each contain a randomly generated distribution of circular voids. In each case the ratio of void area to overall cell area has been constrained to equal 12%. The constitutive model used for the matrix material was as follows:

- Compressible Neo-Hookean

$$\Psi = K (J - \log J) + \frac{1}{2}G (J^{-2/3} (\lambda_1^2 + \lambda_2^2 + \lambda_3^2) - 3)$$

$$G = 889, K = 2667$$

The plane strain condition was used and each mesh was subject to a uniaxial deformation with Green-Lagrange strain increasing in twenty increments from 0 to 0.2. That is a macro deformation gradient ranging from

$$\mathbf{F} = \begin{bmatrix} 1 & 0 \\ 0 & 1 \end{bmatrix}$$

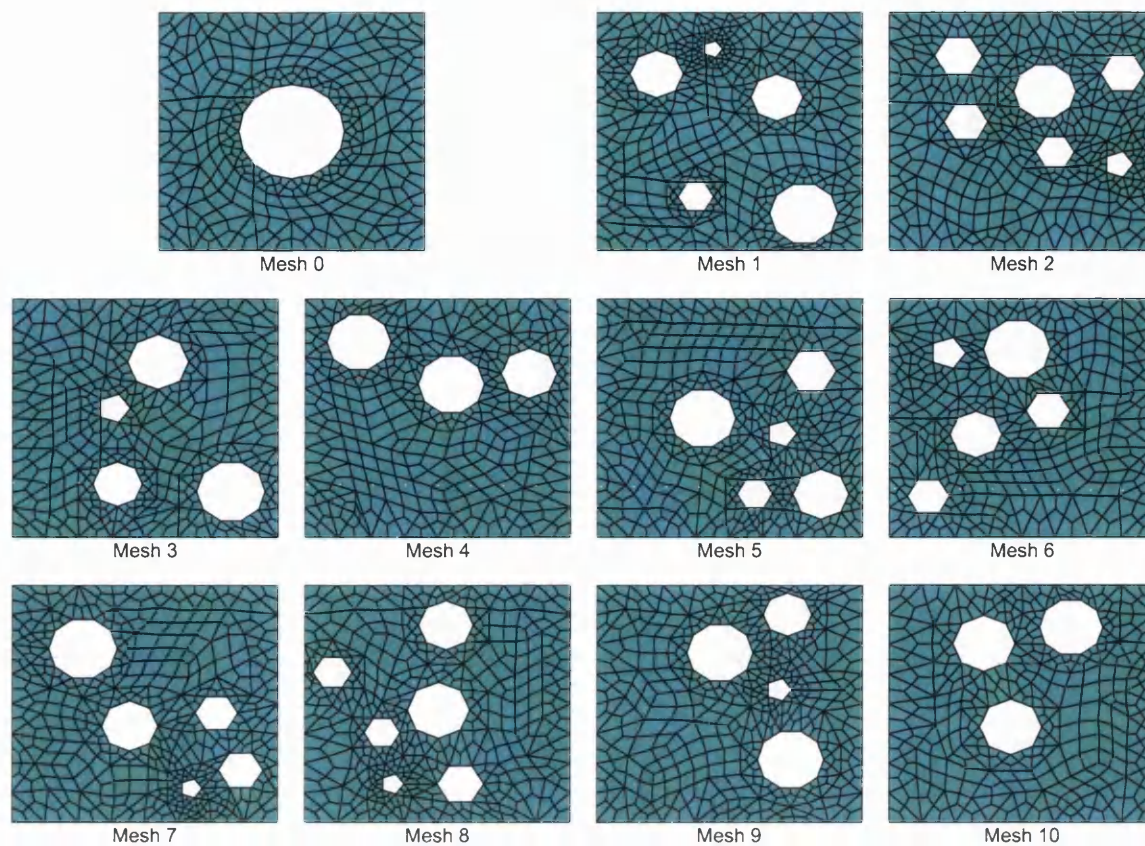


Figure 5.12: Regular and randomly generated irregular meshes.

to

$$\mathbf{F} = \begin{bmatrix} \sqrt{1.4} & 0 \\ 0 & 1 \end{bmatrix}$$

was imposed. This was done for each of the four boundary conditions in turn.

5.6.2 Results

Figure 5.13 shows the axial component of the first Piola Kirchhoff macro-stress, P_{11} , plotted against the corresponding axial component of the Green-Lagrange strain, E_{11} . For each boundary condition the average of the ten irregular meshes has been plotted along with results from regular mesh 0. Also shown as broken lines are the maximum and minimum stresses from the irregular meshes. Comparing the four graphs in figure 5.13 shows that as expected the Taylor boundary condition leads to the stiffest behaviour followed in turn by the linear, periodic and constant traction constraints. It can also be seen that there is no difference in homogenised behaviour between the different meshes under the Taylor condition. This is consistent with

theoretical considerations since the Taylor condition is equivalent to the law of mixtures whereby the averaged stress depends only on the volume fraction of the micro constituents which is the same for all the meshes.

Of particular interest is figure 5.13(c) illustrating the microcell response under the periodic condition as this can be compared directly with the results of Kouznetsova *et al.* (fig.8 in [60]). The stress curve for the regular mesh appears to be very similar to that plotted by Kouznetsova *et al.*, reaching approximately 370MPa at 20% strain. In the present work this regular mesh curve shows a slightly stiffer response than the average of the irregular meshes but is well within the envelope of irregular mesh responses. In the graph of Kouznetsova *et al.* the regular mesh response is more markedly stiffer than the averaged response with a curve lying just within the upper range of random mesh responses. It seems likely that this minor difference between the two studies is due to variations in the randomly chosen hole configurations. The sample size of ten is probably too small to remove variability between the averages of the two sets of meshes.

Under the linear boundary condition illustrated in figure 5.13(b) the regular mesh response curve lies just below the average curve. By contrast the regular mesh curve values for the constant traction condition in figure 5.13(d) are not only greater than the averaged values but exceed slightly the upper envelope of the irregular meshes. However the maximum differences between the averaged and regular stress responses under the linear, periodic and constant tractions are only 0.68%, 1.47% and 3.92% respectively (expressed as a percentage of the respective maximum averaged stress). Kouznetsova *et al.* [60], working with the periodic boundary condition, found that the difference between the response of the regular structure and the response averaged over their selection of random microcells did not exceed 2%. There is nothing in the present results to contradict the conclusion of the authors of [60] that the simplest RVE will usually provide averaged elastic properties to within an acceptable tolerance.

In the present results it was found that the order of stiffness of the individual meshes was similar but not identical between boundary conditions. It cannot therefore be concluded that if one mesh is stiffer than another under one boundary condition it will remain stiffer under a second boundary condition. In addition stress curves for different meshes under the same boundary condition occasionally crossed so it can no more be concluded that some microstructures are always stiffer than others under varying states of deformation.

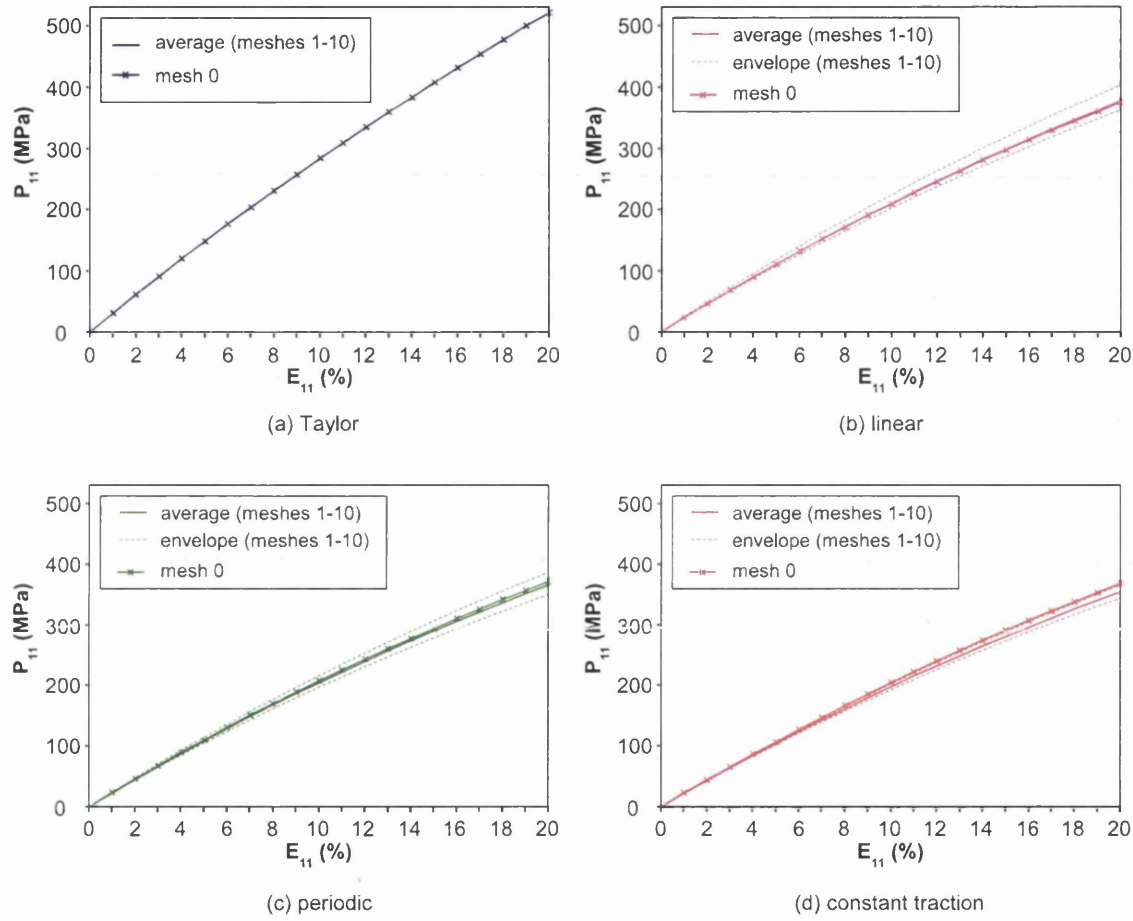


Figure 5.13: Axial first Piola Kirchhoff stress versus axial Green-Lagrange strain for a matrix of compressible neo-Hookean material in plane strain.

5.7 Conclusion

A number of examples have been provided which show that the `microplast` homogenisation code produces results which are at least in accord with those predictions that can be made a priori. Among the expectations confirmed it is observed that the expected relative stiffnesses of the responses under the four boundary conditions are respected. Also the Taylor condition is seen to replicate the law of mixtures and to preserve the isotropy of micro constituents in the macro response. This latter observation is not found to generalise to the other boundary conditions.

The numerical tests also allow a limited independent check on the `microplast` program as it appears to replicate the corresponding results of Kouznetsova [60].

Finally the examples briefly explore the effect of void/inclusion ratio, void density and void distribution on homogenised response. The examples are however very far from constituting an exhaustive exploration of these relations and are not intended as such. It is hard therefore to draw strong conclusions. We will content ourselves with observing that, excluding the Taylor condition, variation in the spatial configuration of micro constituents in constant proportions has an effect on the macro response that is complex but appears mostly to be outweighed by changes in the proportions of the micro constituents.

Chapter 6

Characterisation of homogenised properties by optimisation

6.1 Introduction

In this chapter we propose a constitutive modelling approach which makes use of computational homogenisation but yields an explicit macro model. Our attention is restricted to hyperelastic materials so that we seek macro models in the form of a conventional strain energy function (SEF). Instead of fitting model parameters to experimental results we consider optimising the parameters of a chosen canonical form of SEF to fit the homogenised response of a finite element model of a representative volume element calculated by the methods discussed in chapter 4. This procedure may potentially take into account micro-structural details more accurately than macro-models fitted phenomenologically but (once the optimisation is carried out) without the considerable computational expense of the fully coupled multi-scale method. It extends to the finite strain range the classical procedure adopted in linear elasticity whereby the elastic constants are determined from analyses of a linear elastic RVE. One notable feature of the proposed methodology is that it allows variations in micro-structure to be assessed but provides a constitutive model that can be relatively easily implemented in existing finite element codes.

The concept of deriving macroscopic material parameters from the detailed finite element modelling of an RVE has been used previously though less systematically. References may be found in chapter 1.

It is of course clear that the method considered in this chapter is a way of fitting

one model to another model without direct reference to empirical results. Thus in order to obtain a useful macro model we must have confidence in the validity of the representative model of the micro-structure. It is acknowledged that it is often difficult to obtain enough information at the micro level to construct a reliable micro model.

An outline of the procedure is provided by figure 6.1. Two principal aspects are apparent - homogenisation and optimisation. The homogenisation process has been discussed in detail in chapter 4. The application of optimisation to the present methodology is considered in section 6.2 below.

In section 6.3 an application of the method to composites with Ogden material microconstituents is presented. A more complex application in the field of arterial wall mechanics is described in chapter 7.

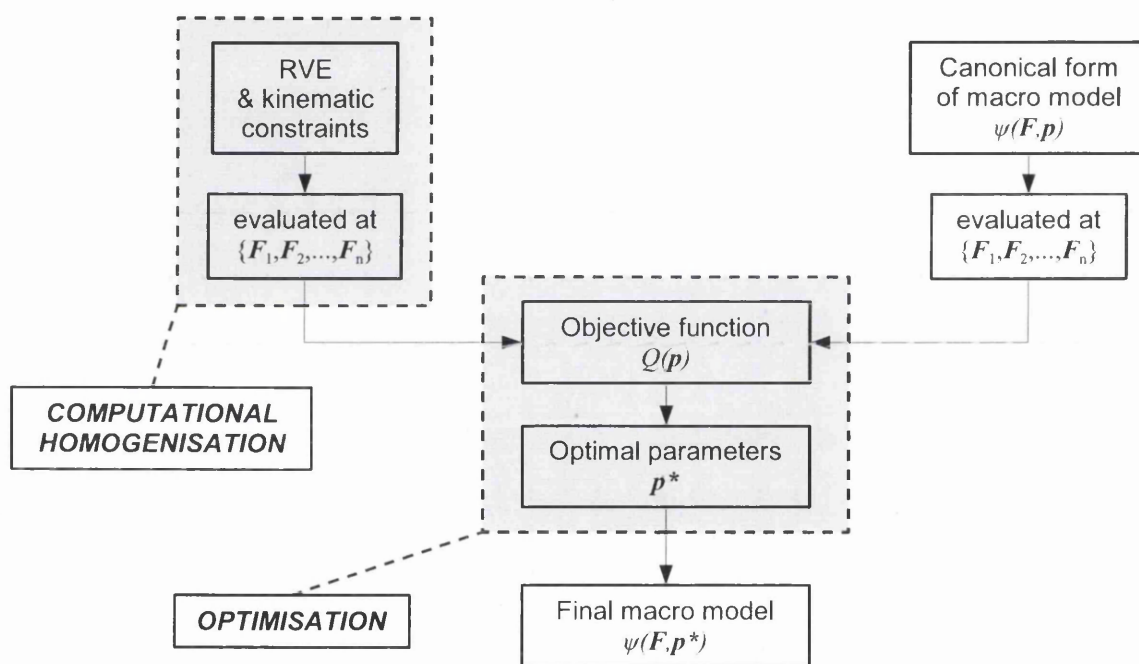


Figure 6.1: Outline of the procedure for fitting macroscopic models to homogenised data in hyperelasticity.

6.2 Optimisation of material parameters

The process of finding an optimal macro model to best approximate the homogenised micro response may be divided into a number of steps described in the following subsections.

6.2.1 Choice of the canonical form of the macro model

In the context of hyperelasticity choosing a macro model means proposing the functional dependence $\Psi(\mathbf{C}, \mathbf{p})$ of strain energy Ψ on the right Cauchy-Green tensor \mathbf{C} and a set \mathbf{p} of parameters to be optimised. Other equivalent formulations in terms of stress and other deformation measures are of course equally valid. We distinguish the ‘free’ parameters \mathbf{p} from any other constants in the strain energy function. It is of course a matter of choice as to which parameters are considered ‘free’ and which are fixed. Leaving more parameters free for optimisation will tend to produce a better fitting model but this has to be balanced against the increased computational difficulties in the optimisation procedure. Clearly the choice of function is of great importance - no amount of optimisation can make a straight line a good fit for a sine curve for instance. Equally an isotropic macro model is unlikely to be the best choice to approximate a microstructure with strongly anisotropic geometry.

6.2.2 Choice of objective function

In order to find the best fitting model it is necessary to define a measure of how well a candidate strain energy function approximates the homogenised micro cell response. Such a measure is provided by a scalar valued *objective function* which we shall denote Q . This is a function of the ‘free’ parameters and depends also on the macro model responses evaluated at a set number of deformations and the homogenised micro-cell responses to the same deformations. The objective function should be smaller in value the better the macro model is considered to fit the homogenised data so that the optimal parameters are those that minimise Q .

One suitable function has the form

$$Q(\mathbf{p}) = \sum_{i=1}^n \|\mathbf{S}(\mathbf{C}_i, \mathbf{p}) - \bar{\mathbf{S}}_i\|_2^2, \quad (6.1)$$

where \mathbf{S} is some measure of mechanical response (strain energy or stress), $\mathbf{C}_i (i = 1, n)$ represents a set of right Cauchy-Green tensors, $\bar{\mathbf{S}}_i$ is the homogenised response of the micro-cell to macro deformation \mathbf{C}_i and $\|\bullet\|_2$ denotes the 2-norm. Alternatives to (6.1) might employ a different norm or might weight each term in the sum differently if a good fit to certain deformations was favoured over others. It may be considered preferable to use a function based on relative values such as

$$Q(\mathbf{p}) = \sum_{i=1}^n \sum_{k=1}^m \left(\frac{S_k(\mathbf{C}_i, \mathbf{p})}{\bar{S}_{ki}} - 1 \right)^2, \quad (6.2)$$

where S_k and \bar{S}_{k_i} are the k^{th} components of \mathbf{S} and $\bar{\mathbf{S}}_i$ respectively and m is the total number of components. Of course (6.2) requires that \bar{S}_{k_i} is never zero. Compared with (6.1) this function would tend to favour a tighter absolute fit where \bar{S}_{k_i} takes on low values.

Of particular importance in specifying an objective function is the choice of deformations at which macro model and homogenised micro model responses are evaluated. The range of deformations covered and any weighting used should reflect the deformations experienced in problems of interest.

6.2.3 Optimisation procedure

The final step is to find the parameters \mathbf{p} which minimise the objective function Q . Since optimisation is by itself a large field in mathematics we shall not discuss this aspect in detail. Locating the minimum of an objective function of the form (6.1) is in general a non-linear least squares problem. Numerous well established means of solution are available (e.g. the Levenberg-Marquardt method [68,71]). These are iterative algorithms which cannot guarantee convergence to the global minimum. Moreover in practice it can be difficult with ill conditioned objective functions to achieve convergence at all. The more efficient methods require the gradient of the objective function to be evaluated at each iteration but this may be estimated numerically to avoid the potentially tedious differentiation of Q with respect to the parameters.

6.2.4 Sensitivity analysis

Although not an essential part of the parameter fitting procedure it is often valuable to assess the sensitivity of the objective function to changes in parameter values. Since the objective function depends on the parameters only through the stress or strain energy ($\mathbf{S}(\mathbf{C}_i, \mathbf{p})$ in (6.1)) this assessment may be made by considering the derivatives of \mathbf{S} with respect to the parameters \mathbf{p} . Ogden et al. [86] prefer to base their sensitivity analysis on the absolute values of the derivatives of stress with respect to relative parameter values. In the nomenclature of (6.1) they calculate $\left| \frac{p_i}{S_{k0}} \frac{\partial S_k}{\partial p_i} \right|$ where S_k is the k^{th} component of stress and S_{k0} is its value at some fixed set of parameters.

A sensitivity analysis should help identify those parameters which most strongly influence the objective function and may indicate potentially problematic cases where the objective function is overly sensitive to one or more parameters under certain

deformations. In such instances results may need to be treated with caution. It can also provide some insight into the distribution of residual errors across the range of trial deformations [86].

6.3 Application to composites of Ogden materials

In this section the concept of fitting a macroscopic model to homogenised data is applied to the case of a composite material consisting of a hexagonal array of circular inclusions embedded in a relatively soft matrix. Each of the two phases is governed by a different hyperelastic constitutive model of the Ogden type described in section 2.6.4. The overall behaviour of the composite is approximated in turn by Ogden models with 3 and 4 terms. The macroscopic parameters are fitted using a non linear least squares algorithm to homogenised results from uniaxial and biaxial tests on a two dimensional representative volume element.

The approach adopted in this section may be compared to the work of Ogden *et al.* [86] in which the Ogden model was fitted to data from actual experiments on sheets of rubber (assumed to be micro-homogeneous).

The fitted macro models are used in the finite element method solution of a macroscopic boundary value problem. Comparison is made with a fully coupled multiscale solution and a fine scale mesh representing the microstructure directly.

6.3.1 Finite element model of RVE

Figure 6.2 shows the 2-D finite element mesh constructed to represent the microstructure of the composite. Quadrilateral elements in plane stress with 8 nodes, bi-quadratic shape functions and 4 integration points each were used throughout. The constitutive models attributed to the two phases were each characterised by an Ogden strain energy function (per unit volume),

$$\Psi = \sum_p^N \frac{\mu_p}{\alpha_p} (\lambda_1^{\alpha_p} + \lambda_2^{\alpha_p} + \lambda_3^{\alpha_p} - 3), \quad (6.3)$$

with the following material parameters:

- *Matrix*

$$\begin{aligned}
N &= 3 \\
\mu_1 &= 3 & \alpha_1 &= 2 \\
\mu_2 &= -2 & \alpha_2 &= -2 \\
\mu_3 &= 5 & \alpha_3 &= 0.5
\end{aligned}$$

- *Circular inclusions*

$$\begin{aligned}
N &= 1 \\
\mu_1 &= 30 & \alpha_1 &= 2
\end{aligned}$$

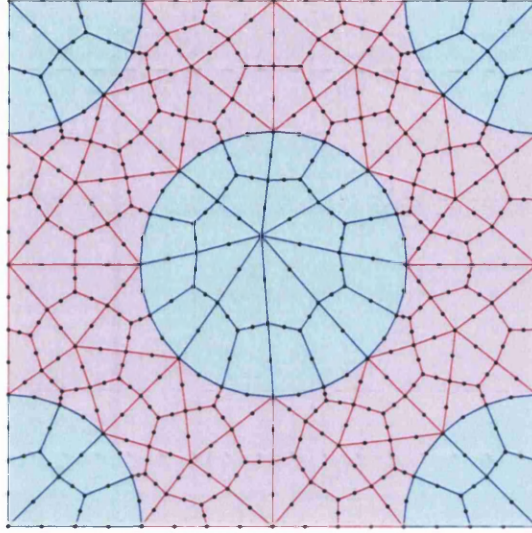


Figure 6.2: Finite element mesh of RVE.

6.3.2 Homogenised data sets

The RVE was subjected to the following two sequences of isochoric applied deformation gradients:

- Uniaxial tensile loading:

$$\mathbf{F}_k^{\text{ua}} = \begin{bmatrix} \lambda_k & 0 & 0 \\ 0 & 1 & 0 \\ 0 & 0 & \lambda_k^{-1} \end{bmatrix} \quad \text{where } \lambda_k = 1.0 + 0.2k \quad (k = 1, 2, \dots, 15) \quad (6.4)$$

- Equibiaxial tensile loading:

$$\mathbf{F}_k^{\text{eb}} = \begin{bmatrix} \lambda_k & 0 & 0 \\ 0 & \lambda_k & 0 \\ 0 & 0 & \lambda_k^{-2} \end{bmatrix} \quad \text{where } \lambda_k = 1.0 + 0.2k \quad (k = 1, 2, \dots, 15) \quad (6.5)$$

The corresponding homogenised first Piola-Kirchhoff stresses under the *periodic* boundary condition, ${}^{\text{per}}\bar{\mathfrak{P}}(\mathbf{F}_k^{\text{ua}})$ and ${}^{\text{per}}\bar{\mathfrak{P}}(\mathbf{F}_k^{\text{eb}})$, were calculated using the program `microplast` described in section 4.13. Of particular interest are the (1,1) components defined by

$$\bar{P}_k^{\text{ua}} = [{}^{\text{per}}\bar{\mathfrak{P}}(\mathbf{F}_k^{\text{ua}})]_{11} \quad (6.6)$$

$$\bar{P}_k^{\text{eb}} = [{}^{\text{per}}\bar{\mathfrak{P}}(\mathbf{F}_k^{\text{eb}})]_{11} , \quad (6.7)$$

as these are subsequently used in formulating the objective functions in subsection 6.3.3.

6.3.3 Macroscopic models and objective functions

The Ogden model, as used to describe the RVE constituent phases, was equally used as the canonical form of macroscopic constitutive relation to be optimised to fit the homogenised data. This is characterised by the strain energy function

$$\Psi = \sum_p^N \frac{\mu_p}{\alpha_p} (\lambda_1^{\alpha_p} + \lambda_2^{\alpha_p} + \lambda_3^{\alpha_p} - 3) , \quad (6.8)$$

in terms of principal stretches λ_1 , λ_2 and λ_3 . The cases of $N = 3$ and $N = 4$ were considered separately.

In the absence of internal constraints the first Piola-Kirchhoff stress derived from the energy function (6.8) is given by

$$\mathbf{P} = \sum_{i=1}^3 \frac{\partial \Psi}{\partial \lambda_i} \mathbf{n}_i \otimes \mathbf{n}_i , \quad (6.9)$$

where each \mathbf{n}_i is the unit eigenvector (principal direction) associated with λ_i . In the case of plane stress in the plane normal to \mathbf{n}_3 and with the constraint of incompress-

ibility ($\lambda_3 = (\lambda_1 \lambda_2)^{-1}$) the principal values of \mathbf{P} are given by

$$P_1 = \sum_{p=1}^N \mu_p \left(\lambda_1^{\alpha_p-1} - \lambda_1^{-\alpha_p-1} \lambda_2^{-\alpha_p} \right) \quad (6.10)$$

$$P_2 = \sum_{p=1}^N \mu_k \left(\lambda_2^{\alpha_p-1} - \lambda_1^{-\alpha_p} \lambda_2^{-\alpha_p-1} \right)$$

$$P_3 = 0. \quad (6.11)$$

Thus for uniaxial loading with deformation gradient in the form of equation (6.4) ($\lambda_1 = \lambda, \lambda_2 = 1$) the principal first Piola-Kirchhoff stress depends on the axial stretch λ , the number of Ogden terms N and the vectors of material parameters $\boldsymbol{\mu} = (\mu_1, \mu_2, \dots, \mu_N)$ and $\boldsymbol{\alpha} = (\alpha_1, \alpha_2, \dots, \alpha_N)$ according to

$$P^{\text{ua}}(\lambda, N, \boldsymbol{\mu}, \boldsymbol{\alpha}) = \sum_{p=1}^N \mu_p \left(\lambda^{\alpha_p-1} - \lambda^{-\alpha_p-1} \right). \quad (6.12)$$

For equibiaxial loading ($\lambda_1 = \lambda_2 = \lambda$) similar to equation (6.5) the two in plane principal first Piola-Kirchhoff stresses are equal and given by

$$P^{\text{eb}}(\lambda, N, \boldsymbol{\mu}, \boldsymbol{\alpha}) = \sum_{p=1}^N \mu_p \left(\lambda^{\alpha_p-1} - \lambda^{-2\alpha_p-1} \right). \quad (6.13)$$

Objective functions

Three objective functions were formulated to optimise the parameters $\boldsymbol{\mu}$ and $\boldsymbol{\alpha}$ of the Ogden model with $N = 3$.

The first based on the uniaxial tensile loading (6.4) is

$$Q_3^{\text{ua}}(\boldsymbol{\mu}, \boldsymbol{\alpha}) = \sum_{k=1}^{15} \left(P^{\text{ua}}(\lambda_k, 3, \boldsymbol{\mu}, \boldsymbol{\alpha}) - \bar{P}_k^{\text{ua}} \right)^2, \quad (6.14)$$

where P^{ua} is defined by equation (6.12), \bar{P}_k^{ua} is the (1,1) component of the homogenised stress from equation (6.6) and the uniaxial stretches are given by $\lambda_k = 1.0 + 0.2k$.

Similarly an objective function based on the equibiaxial tensile loading of (6.4) was defined as

$$Q_3^{\text{eb}}(\boldsymbol{\mu}, \boldsymbol{\alpha}) = \sum_{k=1}^{15} \left(P^{\text{eb}}(\lambda_k, 3, \boldsymbol{\mu}, \boldsymbol{\alpha}) - \bar{P}_k^{\text{eb}} \right)^2, \quad (6.15)$$

where P^{eb} and \bar{P}_k^{ua} are given by equations (6.13) and (6.7) respectively and the stretches (now equibiaxial) cover the same range $\lambda_k = 1.0 + 0.2k$, $k = 1, 2, \dots, 15$.

A third objective function was defined to fit the 3-term Ogden model to the uniaxial and biaxial data simultaneously:

$$Q_3^c(\boldsymbol{\mu}, \boldsymbol{\alpha}) = \sum_{k=1}^{15} \left\{ (P^{\text{ua}}(\lambda_k, 3, \boldsymbol{\mu}, \boldsymbol{\alpha}) - \bar{P}_k^{\text{ua}})^2 + (P^{\text{eb}}(\lambda_k, 3, \boldsymbol{\mu}, \boldsymbol{\alpha}) - \bar{P}_k^{\text{eb}})^2 \right\}. \quad (6.16)$$

A further 3 objective functions were defined to optimise the Ogden model with $N = 4$. These are completely identical to the functions Q_3^{ua} , Q_3^{eb} and Q_3^c above except that N is fixed at 4 in evaluating the macro stresses. Thus the following definitions were used:

$$Q_4^{\text{ua}}(\boldsymbol{\mu}, \boldsymbol{\alpha}) = \sum_{k=1}^{15} (P^{\text{ua}}(\lambda_k, 4, \boldsymbol{\mu}, \boldsymbol{\alpha}) - \bar{P}_k^{\text{ua}})^2 \quad (6.17)$$

$$Q_4^{\text{eb}}(\boldsymbol{\mu}, \boldsymbol{\alpha}) = \sum_{k=1}^{15} (P^{\text{eb}}(\lambda_k, 4, \boldsymbol{\mu}, \boldsymbol{\alpha}) - \bar{P}_k^{\text{eb}})^2 \quad (6.18)$$

$$Q_4^c(\boldsymbol{\mu}, \boldsymbol{\alpha}) = \sum_{k=1}^{15} \left\{ (P^{\text{ua}}(\lambda_k, 4, \boldsymbol{\mu}, \boldsymbol{\alpha}) - \bar{P}_k^{\text{ua}})^2 + (P^{\text{eb}}(\lambda_k, 4, \boldsymbol{\mu}, \boldsymbol{\alpha}) - \bar{P}_k^{\text{eb}})^2 \right\} \quad (6.19)$$

6.3.4 Optimisation procedure

Optimisation was performed using the function `lsqcurvefit` provided by the commercial software package *MATLAB*. The large-scale option was selected invoking a subspace trust region method based on the interior-reflective Newton algorithm described in [14, 15]. The procedure is an iterative one making successive guesses at the parameters in search of the minimising set of values. Convergence is deemed to have occurred if one of two conditions is attained. Either the infinity norm of the gradient of the objective function should be less than a tolerance value `TolFun` (set to 1e-8 for the present application) or the change in parameters calculated by the algorithm (a Newton type step) should be less than the tolerance `TolX` (set to 1e-8). The algorithm stops if convergence is obtained or after a maximum number of iterations (set to 10000) is exceeded.

Each of the six objective functions detailed in subsection 6.3.3 above were subject to the algorithm just described in order to obtain Ogden parameter sets $\boldsymbol{\mu}$ and $\boldsymbol{\alpha}$ to fit the homogenised data. In each case the procedure was repeated 100 times from different starting values of the parameters. The starting values for the μ_p and α_p parameters were randomly chosen within the ranges -30 to 30 and -5 to 5 respectively (c.f. μ and α values of the RVE constituent materials). Results are discussed in the sections that follow.

6.3.5 Results

Tables 6.1 to 6.6 show the results of optimisation of the Ogden model to fit the homogenised data using variously the objective functions Q_3^{ua} , Q_4^{ua} , Q_3^{eb} , Q_4^{eb} , Q_3^{c} and Q_4^{c} . The 100 starting values attempted in each case gave rise to a variety of parameter sets. These were either convergent values or the last updated parameter estimates yielded after the maximum allowed number of iterations. Each table lists the three distinct parameter sets that gave rise to the lowest three values of the objective function regardless of whether or not convergence occurred (only in one case – EB3-2 in table 6.3 – is a non-convergent set among the best three). The (μ_k, α_k) pairs in each set are written in order according to the size of the α_k values. Also listed are the corresponding residual values of the objective function.

Uniaxial deformations

Table 6.1 shows the results of optimisation of the Ogden model with $N = 3$ based on the uniaxial data using objective function Q_3^{eb} . Note that the three data sets, denoted UA3-1, UA3-2 and UA3-3, differ significantly but the corresponding residual values of the objective function are very close to each other.

Table 6.1: Parameters for the Ogden macro model with $N = 3$: optimisation based on uniaxial tension test

	UA3-1		UA3-2		UA3-3	
	μ_i	α_i	μ_i	α_i	μ_i	α_i
1	-41.1596	-0.2695	-21.8113	-3.4725	-18.5000	-3.4700
2	13.3286	3.4556	-40.3413	-0.2752	-37.9390	-0.2931
3	-11.1130	3.5366	-19.5990	3.5201	-16.2955	3.5265
res	0.04526		0.04527		0.04529	

Figure 6.3(a) shows a plot of first Piola-Kirchhoff stress versus uniaxial stretch for the Ogden model with each of the optimised parameter sets in table 6.1. The homogenised RVE stresses are also shown. Clearly the three data sets all provide a good fit to the homogenised data.

Figure 6.3(b) shows the relative errors between each of the fitted models and the homogenised stresses defined (similarly to [86]) by

$$\text{err}(\lambda_k) = \frac{|P^{\text{ua}}(\lambda_k, 3, \boldsymbol{\mu}, \boldsymbol{\alpha}) - \bar{P}_k^{\text{ua}}|}{|\max 0.5, \bar{P}_k^{\text{ua}}|}. \quad (6.20)$$

The 0.5 is included in the denominator to avoid division by small values when deformations are slight. From the graph the relative errors produced by the three data sets are virtually indistinguishable. This is a somewhat counterintuitive result since there are substantial differences between parameter values in the three sets. It may be that there exists a locus of points within the parameter space that yield essentially the same stresses in the uniaxial tensile test.

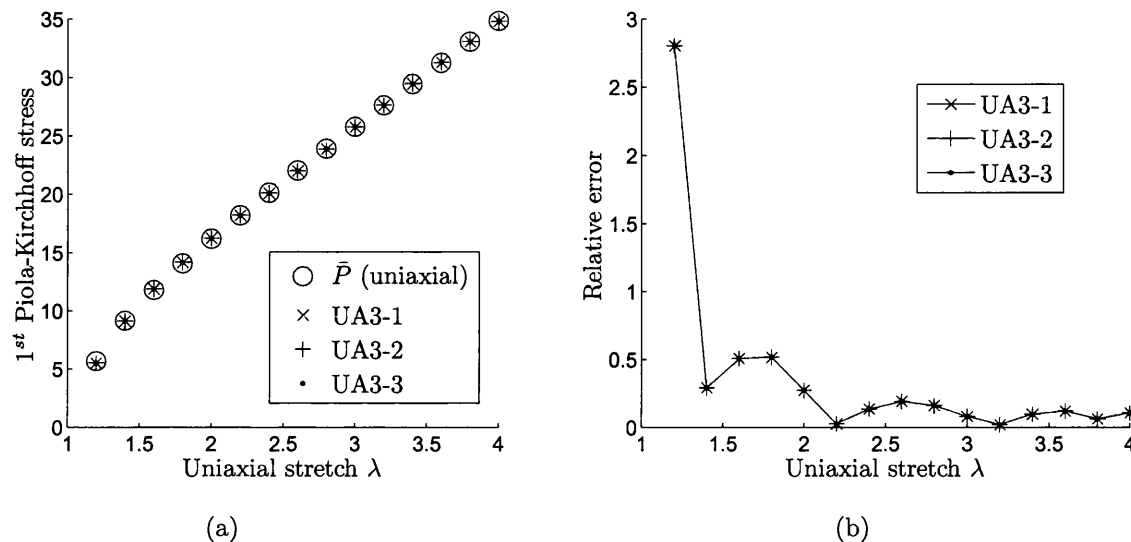


Figure 6.3: (a) 1st Piola-Kirchhoff stress curve for Ogden model with $N = 3$ fitted to uniaxial data. (b) Relative errors

In order to examine this phenomenon more closely figure 6.4 plots the value of the objective function Q_3^{eb} along a straight line through the parameter space linking the two fitted sets UA3-1 and UA3-2. The distance along the path is parameterised by the factor γ running from 0 to 1. Clearly in the space between UA3-1 and UA3-2 the Ogden model is not optimally fitted to the uniaxial homogenised data. Thus any locus of well fitting points in the parameter space is not as simple as a hyper-sphere. It may be that there is something akin to a level bottomed trough in the multi-dimensional objective function surface. Note that only the parameter sets with the three lowest residuals have been examined. Out of the 100 optimisation attempts with random starting values a further 20 sets were obtained with residual values within 1% of the overall minimum.

Note that under uniaxial deformation of the form (6.4) the axial stress, given by equation (6.12), is unchanged if the sign of *both* μ_p and α_p are reversed for any p . In light of this fact the parameter set UA3-1 is exactly equivalent to:

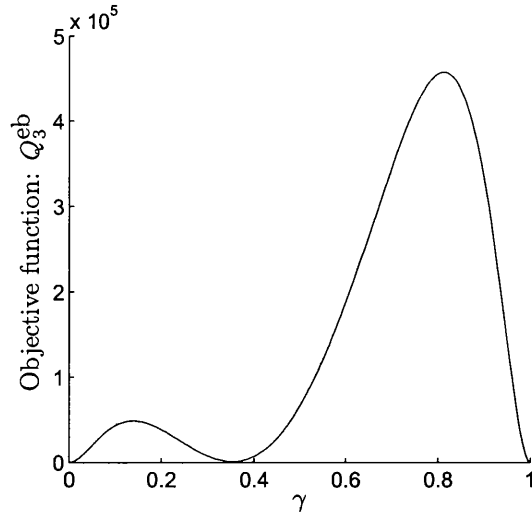


Figure 6.4: Objective function Q_3^{eb} evaluated along the straight line through the parameter space between optimised sets UA3-1 and UA3-2. The path is parameterised by the factor γ .

UA3-1b		
	μ_i	α_i
1	-13.3286	-3.4556
2	-41.1596	-0.2695
3	-11.1130	3.5366

Comparing this equivalent set to UA3-2 and UA3-3 it may be seen that corresponding α values are similar (within approximately 10%). However the corresponding μ values differ in some cases by about 70% so the invariance of P^{ua} under simultaneous reversal of sign in (μ_p, α_p) pairs does not entirely account for the similarity in behaviour of UA3-1, UA3-2 and UA3-3.

A further property of P^{ua} is that two parameter sets (μ, α) and $(\bar{\mu}, \bar{\alpha})$ yield the same stress if

$$\begin{aligned}
 \bar{\mu}_p &= \mu_p ; \quad \bar{\alpha}_p = \alpha_p & \forall p \neq j, k \\
 &\text{and} \\
 (\mu_j &= -\mu_k ; \quad \bar{\mu}_j = -\bar{\mu}_k ; \quad \alpha_j = \alpha_k ; \quad \bar{\alpha}_j = \bar{\alpha}_k) \\
 &\text{or} \\
 (\mu_j &= \mu_k ; \quad \bar{\mu}_j = \bar{\mu}_k ; \quad \alpha_j = -\alpha_k ; \quad \bar{\alpha}_j = -\bar{\alpha}_k).
 \end{aligned}
 \tag{6.21}$$

This is because either of the bracketed conditions above causes the particular sum-

mation terms j and k in the stress equation (6.12) to cancel each other out. We can see that the pairs (μ_1, α_1) and (μ_3, α_3) in parameter sets UA3-1b, UA3-2 and UA3-3 come fairly close to satisfying the second condition in brackets. Since the remaining (μ_2, α_2) values are quite close to each other the observed near equivalence of the three sets in the uniaxial test seems to be in some part explained by the symmetries of P^{ua} discussed above.

Table 6.2 shows the results of optimisation of the Ogden model with $N = 4$ using the uniaxial based objective function Q_4^{ua} . As with the $N = 3$ case the three best parameter sets, UA4-1, UA4-2 and UA4-3, differ significantly but yield very similar residual values of the objective function. Figure 6.5(b) illustrates the stress v stretch curves for each of three sets along with the homogenised response that is the target of optimisation. Clearly all three sets provide a good fit. A slight departure from the homogenised data may be noticed at low stretches. This is reflected in the plot of relative errors in figure 6.6(b). Once again the three best fitting parameter sets yield almost indistinguishable stress and error curves.

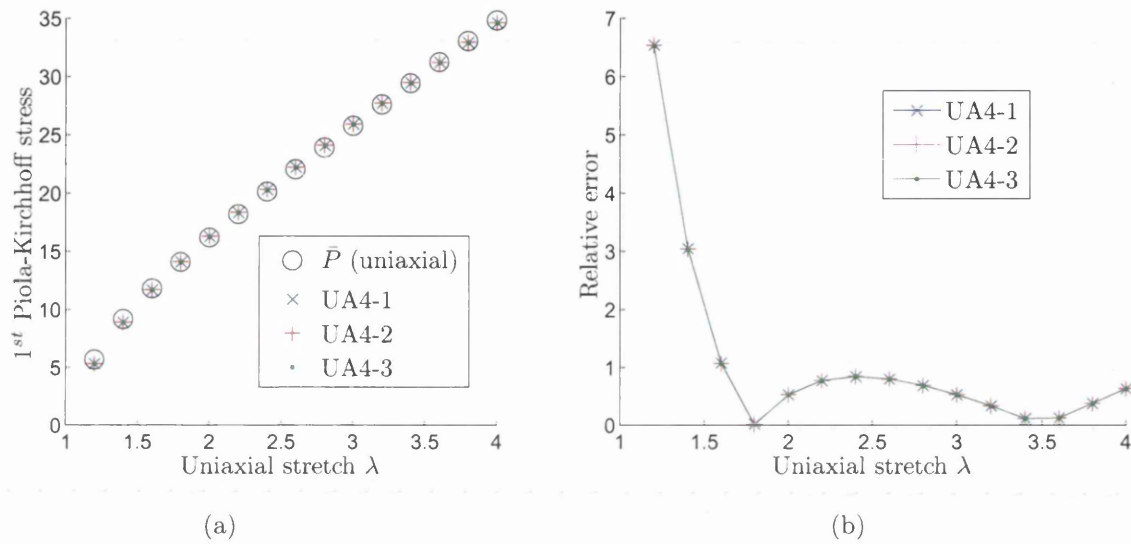
Note that the residual values of the objective function for the three parameter sets UA4-1, UA4-2 and UA4-3 are all larger than the residual values obtained by the $N = 3$ optimised sets UA3-1, UA3-2 and UA3-3. This is despite the fact that any set of parameters for the Ogden model with $N = 3$ may be extended by adding $\mu_4 = 0$ and $\alpha_4 = 1$ to obtain a parameter set for the Ogden model with $N = 4$ that yields exactly the same constitutive response. Thus the true minimum value of objective function Q_4^{eb} must be at least as small as the minimum of Q_3^{eb} . A comprehensive search of the parameter space for $N = 4$ would include the points UA3-1, UA3-2 and UA3-3 with added zero fourth terms and would yield at least as good a fit. That this has not occurred leads to the conclusion that the optimisation algorithm has failed to find the true optimal parameters for the case $N = 4$ even from 100 different starting values.

Equibiaxial deformations

The three best sets of parameters obtained from optimising the Ogden model with $N = 3$ to fit the homogenised RVE response under the equibiaxial deformations are shown in table 6.3. These were obtained using the objective function Q_3^{eb} . Note that residual values of this function are not comparable to the residual values in the uniaxial case since they relate to different objective data.

Table 6.2: Parameters for the Ogden macro model with $N = 4$: optimisation based on uniaxial tension test

	UA4-1		UA4-2		UA4-3	
	μ_i	α_i	μ_i	α_i	μ_i	α_i
1	-3.1164	-3.1266	-3.5855	-3.1217	-10.0036	-3.0838
2	-21.2338	-2.7469	14.9579	-2.9074	16.4081	-2.9990
3	21.2815	-2.8703	-14.4410	-2.7200	-9.4800	-2.6740
4	4.9906	2.0213	4.9932	2.0210	4.9885	2.0216
res	2.1395		2.1397		2.1403	

Figure 6.5: (a) 1st Piola-Kirchhoff stress curve for Ogden model with $N = 4$ fitted to uniaxial data. (b) Relative errors.

The stress curves yielded by the fitted models are plotted in figure 6.6(a) along with the homogenised response. As with the uniaxial data the three best fitting parameter sets are indistinguishable on the graph. The fit appears to be a good one overall. The relative errors are plotted in figure 6.6(b). The three parameter sets are more distinct than was the case with the uniaxial based optimisation but still close to each other.

The equivalent results for the $N = 4$ Ogden model are shown in table 6.4. The corresponding stress v stretch and relative error graphs are plotted in figures 6.7(a) and 6.7(b) respectively. The results are similar to those seen before in that the three best parameter sets produce very similar graphs. It is noticeable that the quality of fit, as characterised by the size of the residual value of the objective function, is not as

Table 6.3: Parameters for the Ogden macro model with $N = 3$: optimisation based on equibiaxial tension test

	EB3-1		EB3-2		EB3-3	
	μ_i	α_i	μ_i	α_i	μ_i	α_i
1	-1.5553×10^{-6}	-6.4337	-14.5042	-3.8573	-6.0509×10^{-8}	-7.4409
2	2.4926	-2.4991	14.5625	-3.8561	7.0991	4.1679
3	7.3304	4.3260	5.4102	3.8052	-1.8981	4.9681
res	0.7667		1.2237		1.3505	

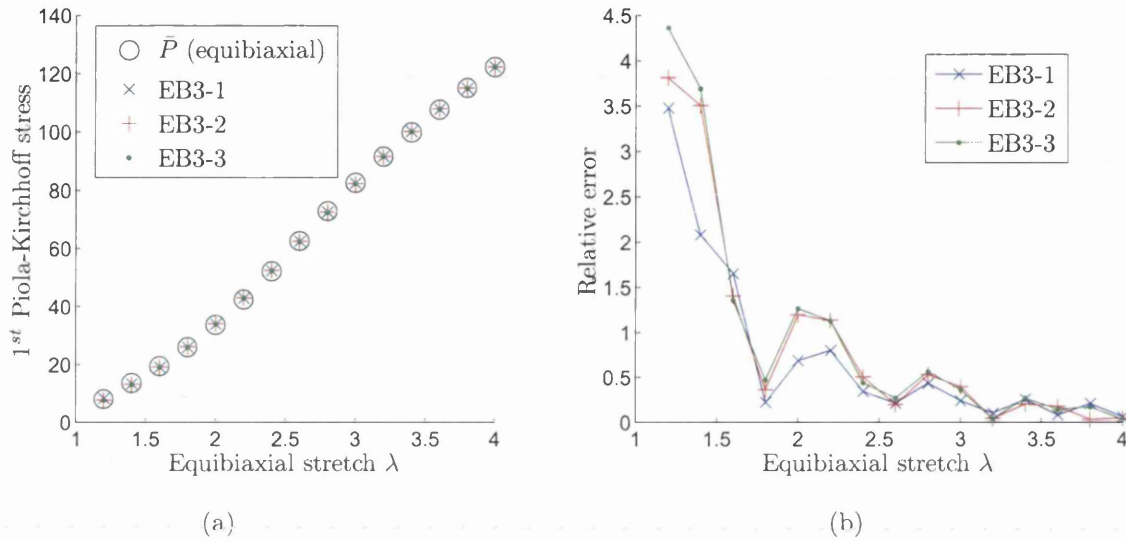


Figure 6.6: (a) 1st Piola-Kirchhoff stress curve for Ogden model with $N = 3$ fitted to equibiaxial data. (b) Relative errors.

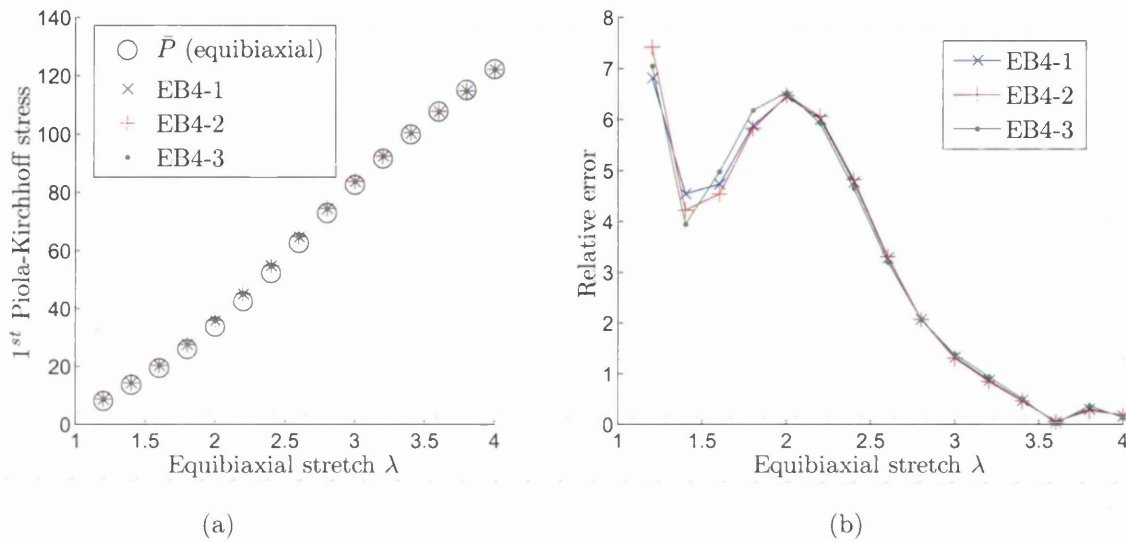
good as the that achieved with the $N = 3$ Ogden model. This phenomenon was observed with the uniaxial data and as argued previously indicates that the optimisation algorithm is not finding the best possible values of the material parameters.

Simultaneous optimisation to uniaxial and equibiaxial data

The results for the $N = 3$ Ogden model fitted simultaneously to the homogenised stress response of the RVE under uniaxial and biaxial deformations are recorded in table 6.5. The optimisation was performed using the objective function Q_3^c defined by equation (6.16). As before the best three sets of parameter values are given. The first Piola-Kirchhoff stresses arising from the optimised problems are plotted against the uniaxial stretches in figure 6.8(a) and against the equibiaxial stretches in figure 6.8(c). The corresponding relative errors are shown in figures 6.8(b) and 6.8(d)

Table 6.4: Parameters for the Ogden macro model with $N = 4$: optimisation based on equibiaxial tension test

	EB4-1		EB4-2		EB4-3	
	μ_i	α_i	μ_i	α_i	μ_i	α_i
1	-17.4934	-3.2046	-9.5302	-2.8892	-13.7414	-3.1653
2	20.3853	-2.6530	13.4390	-2.1965	15.6831	-3.1366
3	24.1891	5.0857	27.7228	4.7228	-92.5535	-0.04415
4	-16.8123	6.4117	-19.5790	5.5269	5.4660	4.9581
res	59.6319		59.7021		59.8593	

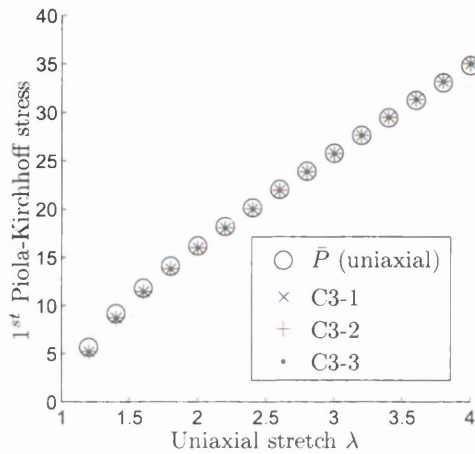
Figure 6.7: (a) 1st Piola-Kirchhoff stress curve for Ogden model with $N = 4$ fitted to equibiaxial data. (b) Relative errors.

respectively. It is evident that a good fit with the homogenised is obtained with all three parameter sets C3-1, C3-2 and C3-3. As observed in previous cases the three sets, although they contain different values to each other, yield very similar stresses under the deformations considered.

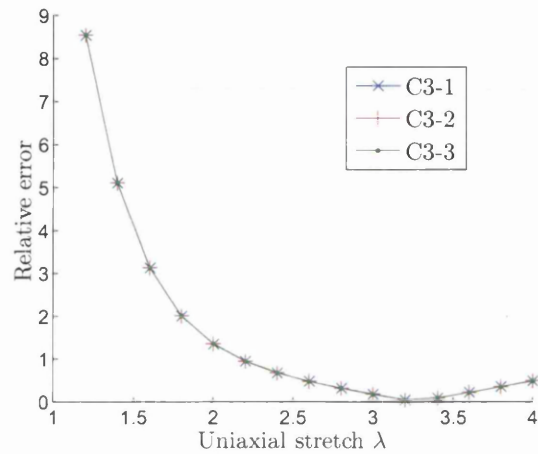
Comparing figure 6.8(b) to figure 6.3(b) we see that the relative errors are higher between the simultaneously fitted models, C3-1, C3-2 and C3-3, and the homogenised uniaxial data than between the models UA3-1, UA3-2 and UA3-3 and the same homogenised data. This is to be expected since the latter parameters are chosen to fit only the uniaxial data. Similarly one would expect the relative errors with respect to equibiaxial deformations to be larger from the simultaneous optimisations (figure 6.8(d)) than from the $N = 3$ Ogden parameters fitted to equibiaxial data alone

Table 6.5: Parameters for the Ogden macro model with $N = 3$: optimisation based on combined uniaxial and equibiaxial data

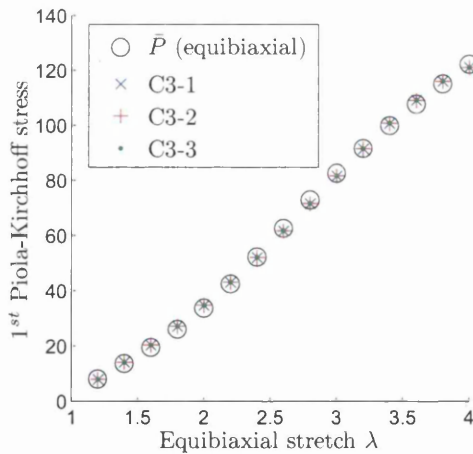
	C3-1		C3-2		C3-3	
	μ_i	α_i	μ_i	α_i	μ_i	α_i
1	19.6613	-2.3369	12.9142	-2.3481	9.0232	-2.3610
2	-23.0702	-2.2902	-16.3248	-2.2796	-12.4377	-2.2672
3	4.5578	2.1546	4.5565	2.1548	4.5526	2.1553
res	12.4167		12.4222		12.4230	



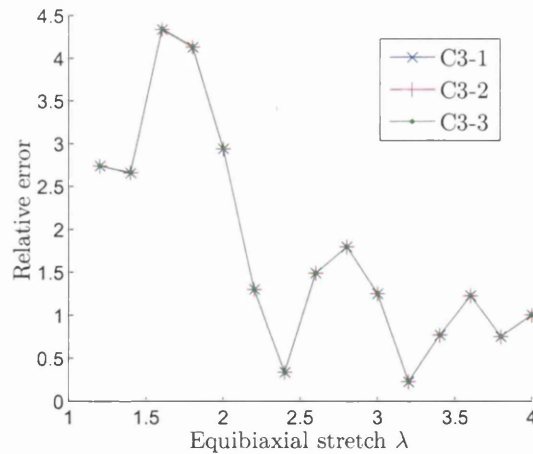
(a)



(b)



(c)



(d)

Figure 6.8: Results for Ogden model with $N = 3$ fitted to uniaxial and equibiaxial data simultaneously. (a)&(b) 1st Piola-Kirchhoff stresses and corresponding relative errors under uniaxial tension. (c)&(d) 1st Piola-Kirchhoff stresses and relative errors under equibiaxial tension.

(figure 6.6(b)). The error values appear similar in magnitude from inspection of the graph. However the sum of squared errors over the equibiaxial deformations (i.e. the objective function restricted to the biaxial terms) for C3-1, C3-2 and C3-3, is larger than the residuals for EB3-1, EB3-2 and EB3-3, as one would expect.

It is noticable that relative errors from C3-1, C3-2 and C3-3 with respect to equibiaxial data are mostly less than the relative errors from the $N = 4$ Ogden model fitted solely to the same equibiaxial data (figure 6.7(b)). This confirms the conclusion made earlier that the parameter sets EB4-1, EB4-2 and EB4-3 are not the best possible values.

Table 6.6 lists the sets parameters, C4-1, C4-2 and C4-3, for the Ogden model with $N = 4$ that yielded the three smallest values of the objective function Q_4^c from the 100 optimisation attempts. Q_4^c is defined by equation (6.19) and combines both uniaxial and equibiaxial data. The corresponding graphs of stress are plotted in figures 6.9(a) and 6.9(c) for uniaxial and equibiaxial deformations respectively. Visually a good fit is obtained over both deformation sets. Relative errors with respect to homogenised uniaxial and equibiaxial data are plotted on the adjacent graphs 6.9(b) and 6.9(d). The now familiar equivalence between the different parameter sets is apparent.

Table 6.6: Parameters for the Ogden macro model with $N = 4$: optimisation based on combined uniaxial and equibiaxial data

	C4-1		C4-2		C4-3	
	μ_i	α_i	μ_i	α_i	μ_i	α_i
1	-9.6072	-3.3523	-2.5758	-3.4090	-6.6799	-3.3727
2	16.8881	-3.2750	21.7750	-3.1824	12.3353	-3.2819
3	-8.7815	-3.0740	-20.7004	-3.1115	-7.1584	-3.0523
4	7.0277	1.8929	7.0265	1.8930	7.0248	1.8931
res	0.8247		0.8251		0.8254	

Comparing the combined optimisation over the uniaxial data to the solely uniaxially based optimisation with $N = 4$ we find that relative errors (figures 6.9(b) and 6.5(b)) follow a strikingly similar pattern. On the other hand the relative errors for the simultaneously optimised parameters over the equibiaxial deformations (figure 6.9(d)) are actually smaller than their counterparts fitted only to the equibiaxial data (figure 6.7(b)). As before we conclude that the optimisation algorithm has been ineffective in finding the true optimal parameter values to fit the equibiaxial data for the $N = 4$ Ogden model.

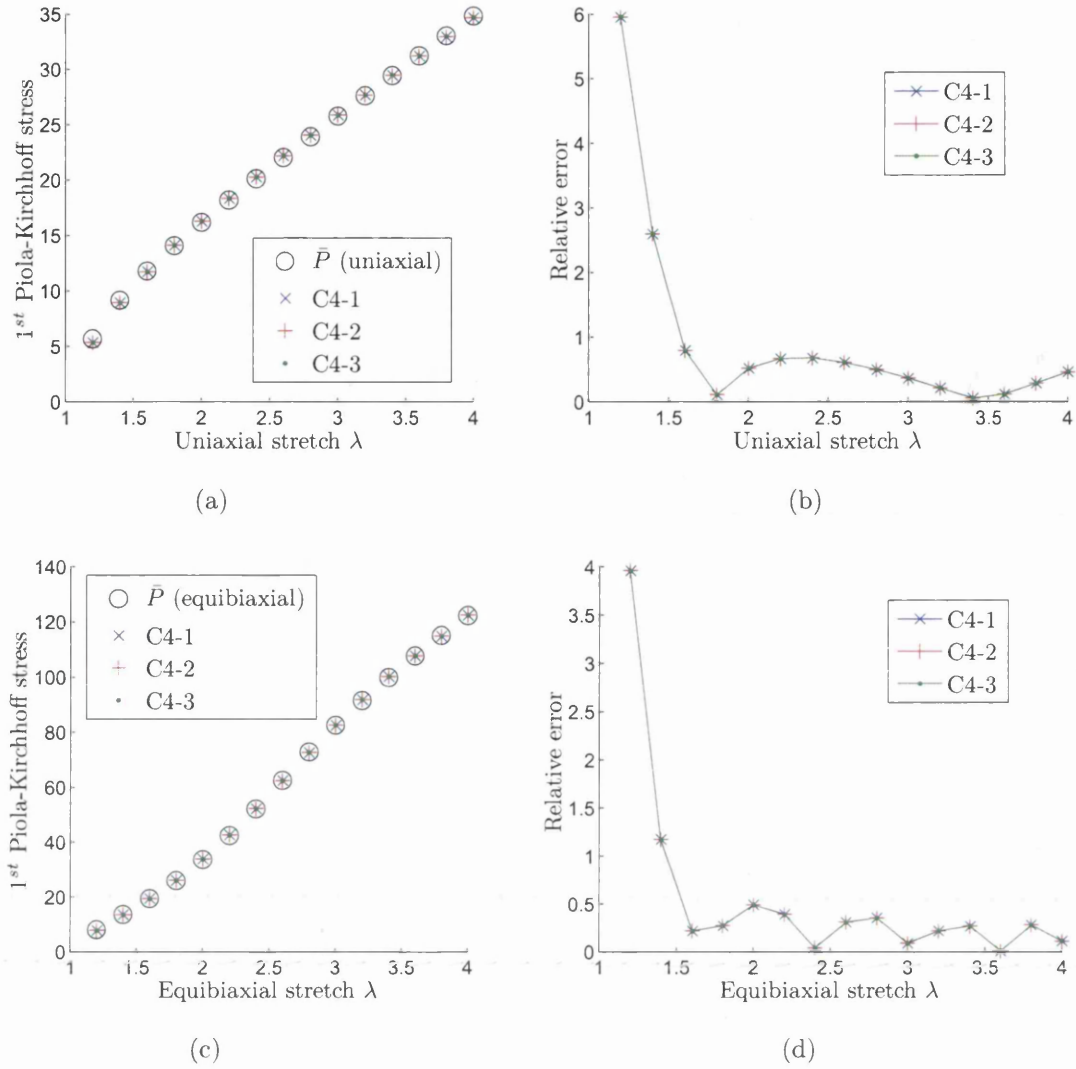


Figure 6.9: Results for Ogden model with $N = 4$ fitted to uniaxial and equibiaxial data simultaneously. (a)&(b) 1st Piola-Kirchhoff stresses and corresponding relative errors under uniaxial tension. (c)&(d) 1st Piola-Kirchhoff stresses and relative errors under equibiaxial tension.

The sums of squared errors obtained using C4-1, C4-2 and C4-3 with respect to the uniaxial data alone is found to be 0.2996, 0.2995 and 0.2993 respectively. The corresponding error sums with respect to equibiaxial data are 0.5252, 0.5256 and 0.5261 respectively. The relative errors on the other hand are generally smaller with respect to the equibiaxial data than with respect to the uniaxial data. This may be due simply to the fact that stresses tend to be higher under the set of equibiaxial deformations than under the uniaxial deformations. This means that the same relative error in the homogenised stress has a greater influence on the objective function in

the equibiaxial range than in the uniaxial range. Therefore if contributions from one or the other deformation range is not favoured in minimising the objective function *relative errors* will tend to be smaller over the equibiaxial stretches.

Finally we note that a slightly better fit is obtained using the Ogden model with $N = 4$ than with $N = 3$ as one might expect having more parameters free for optimisation. This is true considering each deformation range (uniaxial and equibiaxial) separately.

6.3.6 Sensitivity analysis

The sensitivity of each objective function to changes in the Ogden material parameters may be assessed by evaluating its partial derivatives with respect to each of the parameters. The relevant derivatives with respect to the μ_p parameters are given by

$$\frac{\partial Q_N^{\text{ua}}}{\partial \mu_p} = 2 \sum_{k=1}^{15} (P^{\text{ua}}(\lambda_k, N, \boldsymbol{\mu}, \boldsymbol{\alpha}) - \bar{P}_k^{\text{ua}}) \frac{\partial P^{\text{ua}}}{\partial \mu_p} \quad (6.22)$$

$$\frac{\partial Q_N^{\text{eb}}}{\partial \mu_p} = 2 \sum_{k=1}^{15} (P^{\text{eb}}(\lambda_k, N, \boldsymbol{\mu}, \boldsymbol{\alpha}) - \bar{P}_k^{\text{eb}}) \frac{\partial P^{\text{eb}}}{\partial \mu_p} \quad (6.23)$$

$$\begin{aligned} \frac{\partial Q_N^{\text{c}}}{\partial \mu_p} = 2 \sum_{k=1}^{15} \left\{ (P^{\text{ua}}(\lambda_k, N, \boldsymbol{\mu}, \boldsymbol{\alpha}) - \bar{P}_k^{\text{ua}}) \frac{\partial P^{\text{ua}}}{\partial \mu_p} + \right. \\ \left. (P^{\text{eb}}(\lambda_k, N, \boldsymbol{\mu}, \boldsymbol{\alpha}) - \bar{P}_k^{\text{eb}}) \frac{\partial P^{\text{eb}}}{\partial \mu_p} \right\} \end{aligned} \quad (6.24)$$

and with respect to each α_p by

$$\frac{\partial Q_N^{\text{ua}}}{\partial \alpha_p} = 2 \sum_{k=1}^{15} (P^{\text{ua}}(\lambda_k, N, \boldsymbol{\mu}, \boldsymbol{\alpha}) - \bar{P}_k^{\text{ua}}) \frac{\partial P^{\text{ua}}}{\partial \alpha_p} \quad (6.25)$$

$$\frac{\partial Q_N^{\text{eb}}}{\partial \alpha_p} = 2 \sum_{k=1}^{15} (P^{\text{eb}}(\lambda_k, N, \boldsymbol{\mu}, \boldsymbol{\alpha}) - \bar{P}_k^{\text{eb}}) \frac{\partial P^{\text{eb}}}{\partial \alpha_p} \quad (6.26)$$

$$\begin{aligned} \frac{\partial Q_N^{\text{c}}}{\partial \alpha_p} = 2 \sum_{k=1}^{15} \left\{ (P^{\text{ua}}(\lambda_k, N, \boldsymbol{\mu}, \boldsymbol{\alpha}) - \bar{P}_k^{\text{ua}}) \frac{\partial P^{\text{ua}}}{\partial \alpha_p} + \right. \\ \left. (P^{\text{eb}}(\lambda_k, N, \boldsymbol{\mu}, \boldsymbol{\alpha}) - \bar{P}_k^{\text{eb}}) \frac{\partial P^{\text{eb}}}{\partial \alpha_p} \right\} \end{aligned} \quad (6.27)$$

where N is either 3 or 4 in the present examples. The derivatives of the Ogden first Piola-Kirchhoff stress required above are given in the case of uniaxial tension by

$$\frac{\partial P^{\text{ua}}}{\partial \mu_p} = \frac{1}{\lambda} (\lambda^{\alpha_p} - \lambda^{-\alpha_p}) \quad (6.28)$$

$$\frac{\partial P^{\text{ua}}}{\partial \alpha_p} = \frac{\log \lambda}{\lambda} \mu_p (\lambda^{\alpha_p} + \lambda^{-\alpha_p}) , \quad (6.29)$$

and for equibiaxial deformations by

$$\frac{\partial P^{\text{eb}}}{\partial \mu_p} = \frac{1}{\lambda} (\lambda^{\alpha_p} - \lambda^{-2\alpha_p}) \quad (6.30)$$

$$\frac{\partial P^{\text{eb}}}{\partial \alpha_p} = \frac{\log \lambda}{\lambda} \mu_p (\lambda^{\alpha_p} + 2\lambda^{-2\alpha_p}) . \quad (6.31)$$

These functions are plotted in figure 6.10.

We focus on the case of $N = 4$ with optimisation of the 8 Ogden parameters to fit the uniaxial and equibiaxial data simultaneously. The partial derivatives of the appropriate objective function Q_4^c are obtained from equations (6.24) and (6.27). These have been evaluated at each of the three best parameter sets, C4-1, C4-2 and C4-3, obtained by the optimisation procedure and the absolute values are listed in table 6.7. In each of the 3 cases the objective function is markedly more sensitive to changes

Table 6.7: Sensitivity of the objective function Q_4^c evaluated at the fitted parameter sets given in table 6.6.

	C4-1		C4-2		C4-3	
	$\left \frac{\partial Q_4^c}{\partial \mu_p} \right $	$\left \frac{\partial Q_4^c}{\partial \alpha_p} \right $	$\left \frac{\partial Q_4^c}{\partial \mu_p} \right $	$\left \frac{\partial Q_4^c}{\partial \alpha_p} \right $	$\left \frac{\partial Q_4^c}{\partial \mu_p} \right $	$\left \frac{\partial Q_4^c}{\partial \alpha_p} \right $
1	1.7108	55.2881	2.3990	19.0252	1.9189	41.6546
2	0.2490	1.4520	0.2464	1.4282	0.2483	1.4487
3	0.2482	1.4463	0.2456	1.4226	0.2474	1.4429
4	0.2474	1.4406	0.2448	1.4171	0.2466	1.4372

in μ_1 and especially α_1 than to the other parameters. The relative insensitivity to μ_2 , α_2 , μ_3 and α_3 may be due to the fact that for each parameter set α_2 is close to α_3 and μ_2 is fairly close to $-\mu_4$ (refer to table 6.6). This means that the sum of the $p = 2$ and $p = 4$ terms in the Ogden stresses (equations 6.12 and 6.13) and the corresponding contributions to the objective function are small. The insensitivity to μ_4 and α_4 probably due simply to α_4 being smaller in magnitude than α_1 , α_2 and α_3 and positive. Figure 6.10 shows that all the derivatives of the stress are small in such conditions at all stretches and this will tend to make the objective function derivative small in magnitude also.

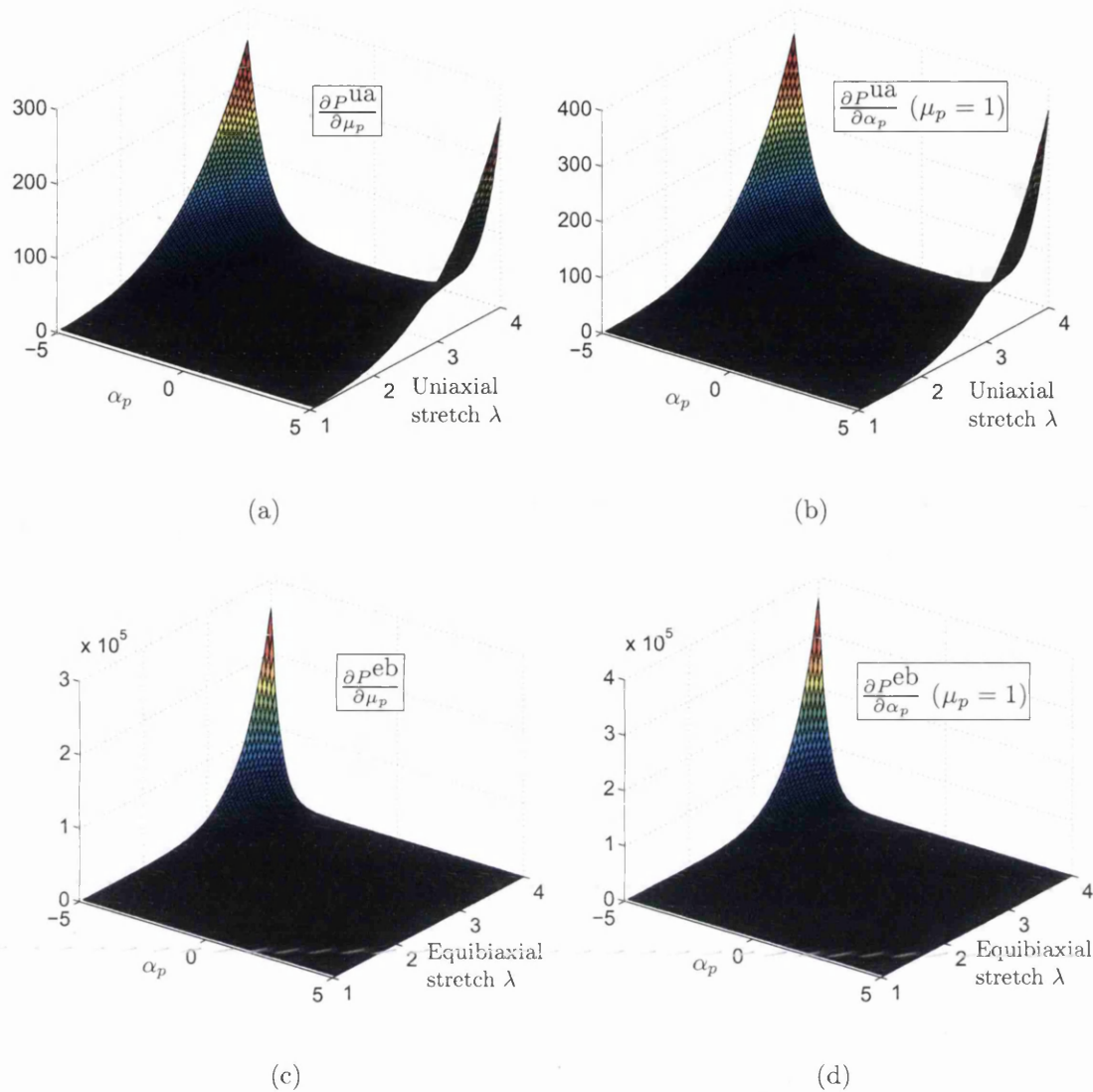


Figure 6.10: Derivatives of the Ogden first Piola-Kirchhoff stress with respect to material parameters for uniaxial and equibiaxial tension.

6.3.7 Macroscopic boundary value problem

In order to further assess fitted macroscopic models a macroscopic boundary value problem is considered. This consists of a sheet (300×200 units) with a centrally placed circular hole stretched along its long direction in plane stress. Owing to the twofold symmetry of the arrangement it suffices to model a quarter of the sheet with suitable boundary conditions on the axes of symmetry as shown in figure 6.11. The problem was solved in three ways for comparison:

1. By the finite element method using a coarse mesh uniformly assigned the Ogden constitutive model with optimised parameters. Each of the parameter sets UA3-

- 1, EB3-1, C3-3 and C4-1 was used separately. The mesh is illustrated in figure 6.12(a) and consists of 8-node plane stress quadrilateral elements each integrated with 4 Gauss points.
2. By the finite element method using a fine mesh representing directly the microstructural array of circular inclusions. Material properties of the matrix and inclusions are the same as used in the RVE model 6.3.1. The mesh is illustrated in figure 6.12(a) and consists of 8-node plane stress quadrilateral elements each integrated with 4 Gauss points.
3. By a fully coupled finite element based multiscale method. That is using the finite element method with computational homogenisation performed at each Gauss point to provide the constitutive response¹. The same RVE model was used throughout the macroscopic mesh model as used previously to generate the homogenised data for optimisation (see subsection 6.3.1). The macroscopic mesh, illustrated in figure 6.12(a), is the same coarse mesh used with the fitted macroscopic model as described above.

In each case the stretching of the sheet was accomplished by imposing an increasing series of prescribed displacements in the y direction uniformly on the nodes along the top edge of the sheet. For each prescribed displacement the sum of the y components of reactions along the bottom edge of the mesh was calculated. In this way a graph of force against displacement was plotted for each of the modelling approaches itemised above. The curves are shown together in figure 6.13.

It is apparent from the graphs that all the fitted models that have been plotted, with the notable exception of EB3-1, provide a fairly good match to both the fine scale mesh and the coupled multi-scale solution. The fine mesh solution is stiffer than all the others except the outlying curve of EB3-1. Recall that the Ogden model with the EB3-1 parameters provides a good match for the homogenised behaviour of the composite under equibiaxial deformations of the type described by equation (6.5). Clearly the macroscopic problem of stretching the perforated plate involves local deformations that do not conform to this type. It would seem that the behaviour of the EB3-1 model departs considerably from the composite behaviour under at least some of the deformations brought about in stretching the plate. In order to confirm

¹The multi-scale functionality of the finite element code `mpap2` developed by W.G. Dettmer and D.D. Somer of Swansea University was used for this purpose.

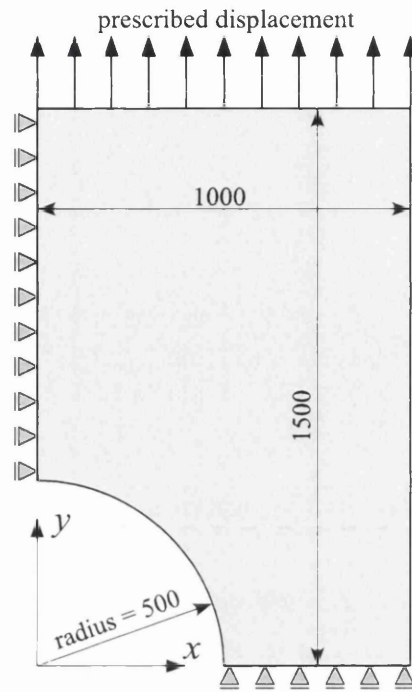


Figure 6.11: Stretching of perforated rectangular sheet – dimensions and boundary conditions on one quarter of sheet.

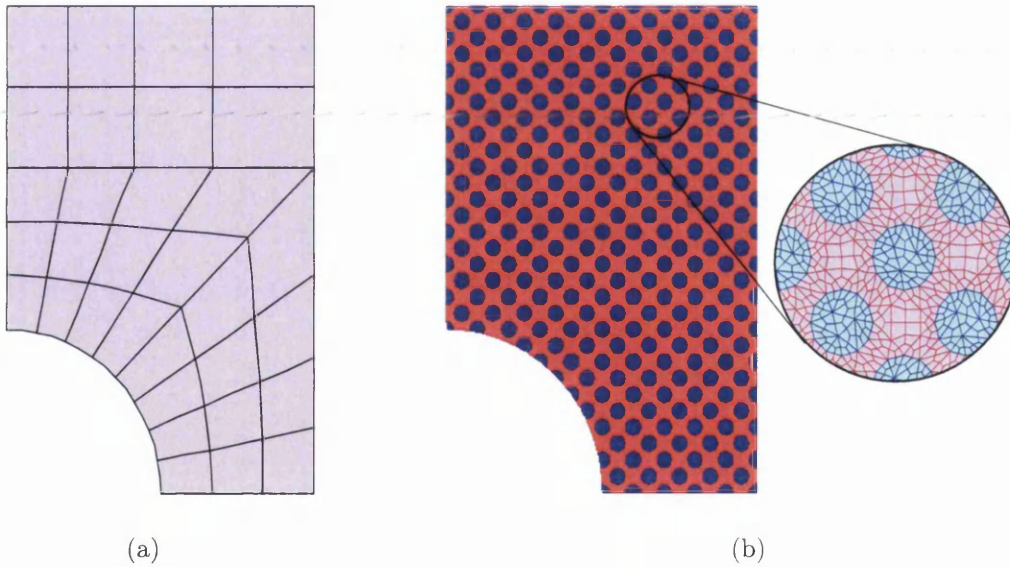


Figure 6.12: Coarse (a) and fine (b) meshes for the macroscopic problem.

that the performance of the Ogden model can be markedly different with different parameter sets even when they match well over certain deformations we consider isochoric uniaxial loading of the type characterised by a deformation gradient of the

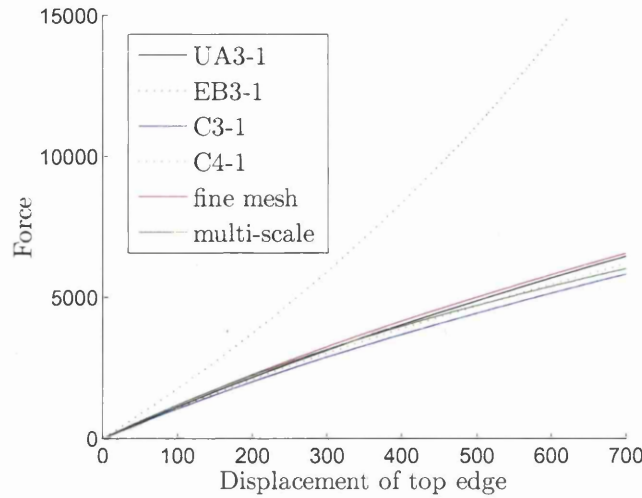


Figure 6.13: Force v displacement for the perforated sheet problem calculated variously using the fitted macro models, a fine scale mesh and the coupled multiscale method.

form

$$\mathbf{F}(\lambda) = \begin{bmatrix} \lambda & 0 & 0 \\ 0 & \lambda^{-0.5} & 0 \\ 0 & 0 & \lambda^{-0.5} \end{bmatrix}. \quad (6.32)$$

Note that this is different from the uniaxial deformations used for optimisation (equation (6.4)) where $F_{11} = 1$. Figure 6.14(a) plots the first Piola-Kirchhoff stress (11 component) against stretch for each of the Ogden models UA3-1, EB3-1, C3-3 and C4-1 under stretching of the type described above by equation (6.32). The model using parameter set EB3-1 is strikingly stiffer than the others even though under equibiaxial loading it behaves very similarly to C3-3 and C4-1 (figure 6.14(b)). Under this latter type of deformation it is UA3-1 which provides an outlying curve.

We may conclude that equibiaxial testing of the RVE is insufficient on its own to determine a macroscopic model for the particular macro boundary value problem considered here.

6.3.8 Conclusions

It has been shown that it is possible to obtain a good approximation to the homogenised behaviour in uniaxial and equibiaxial tension of a composite consisting of an array of circular Ogden type inclusions in a softer Ogden type matrix by means of an Ogden type macroscopic model with fitted parameters.

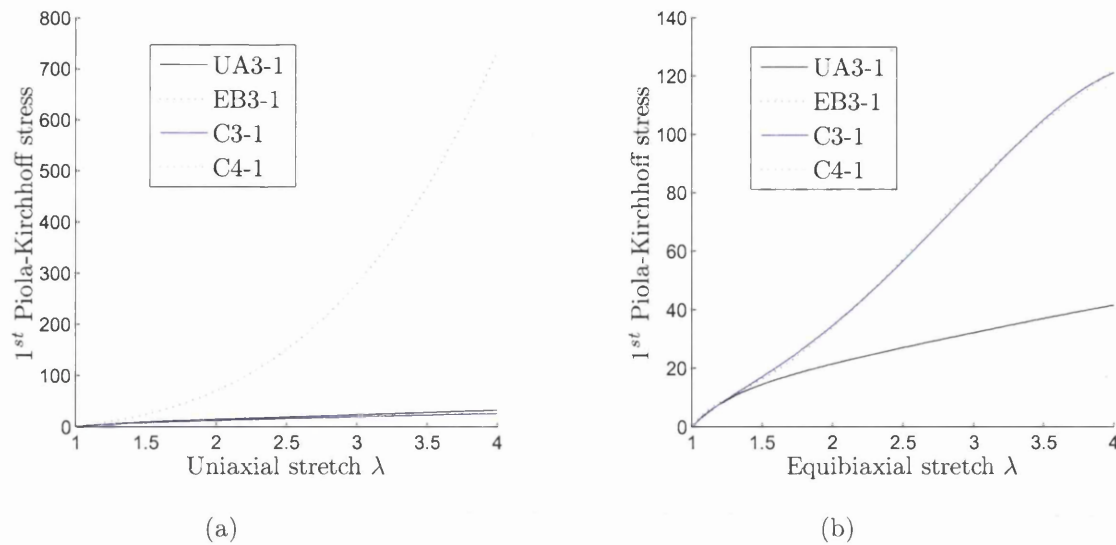


Figure 6.14: Comparison of stress response of selected optimised parameter sets in (a) uniaxial deformation of type characterised by equation (6.32) and (b) equibiaxial deformation of the type (6.5).

It is noted that in the case of uniaxial and equibiaxial stretching certain distinct sets of material parameters may give rise to the same function of stress on stretch. This appears to be reflected in the attainment of very similar fits to the homogenised data with different parameter sets.

In a macroscopic boundary value problem it is possible to obtain good agreement between fitted models and both a multi-scale solution and a solution based on a fine scale representation of the composite structure. However some of the fitted parameter sets yielded macro solutions that were markedly different. This emphasises the importance of basing the optimisation procedure on tests of the RVE under a sufficiently large sample of different deformation patterns or at least a set of deformations that adequately reflect the types of deformation likely to encountered in macro problems of interest.

Chapter 7

Computational homogenisation for modelling of arterial walls

7.1 Introduction

Recent years have seen growing research interest in the mechanical modelling of soft biological tissues in general and artery walls in particular. The importance to cardiovascular medicine is a clear motivation. Good constitutive models for vascular tissues should help toward improving mechanical clinical interventions such as balloon angioplasty as well as the design of stents and other implants. They may moreover facilitate the understanding of changes in the mechanical properties of arteries associated with aging and the onset of important cardiovascular diseases such as atherosclerosis.

Among a good number of hyperelastic constitutive models proposed for arterial tissue are those presented by Holzapfel *et al.* [53] and Zulliger *et al.* [129]. We attempt to fit some of the parameters of these two models to the homogenised response of a finite element model of the arterial microstructure. The finite element model follows closely the simplified view of the artery wall composition adopted by Zulliger *et al.* in formulating their own constitutive model. Optimisation is performed in turn on the basis of various objective functions using different microcell boundary conditions, different ranges of deformations and both strain energy and stress formulations. We compare the optimised models in the solution of a macro boundary value problem representing the inflation of an artery.

The example is offered as an illustration of the method and a first step toward

modelling arterial tissue on the basis of a multi-scale approach. However many of the assumptions used about the microstructure are speculative so the fitted macro models cannot yet be considered for practical application.

7.2 Structure and histology of the arterial wall

Clearly any microstructurally based attempt at modelling arterial tissue must begin with a description of the artery structure itself. In this section some details of the composition of artery walls are provided followed by an account of certain pertinent features of their mechanical behaviour. Much of the information is drawn from the text by Humphrey [55] and the concise descriptions in Holzapfel *et al.* [53] and Gasser *et al.* [31]. Another source is the account of the middle layer of the human aorta found in Dingemans *et al.* [20].

7.2.1 Structure and histology

Arteries are the vessels that carry oxygen-rich blood from the heart to the rest of the body (*systemic* arteries) and oxygen-poor blood from the lungs to the heart (*pulmonic* arteries). Their structure is highly complex and varies with age, site and disease. The description offered in this section focuses on healthy human arteries although there are similarities with other blood vessels in humans and with other species. For obvious reasons a good deal of experimental data is derived from non human tissue. Indeed some modelling efforts draw upon observations of different species at once.

A distinction is often made between so called *elastic* and *muscular* arteries. The categorisation is not a strict one. Rather a spectrum of vessels may be found possessing features of both archetypes in varying degrees.

Elastic arteries are generally larger than their muscular counterparts and tend to be found closer to the heart. Examples include the aorta, common carotids, common iliacs and main pulmonary artery. At systole (the contraction of the heart) the elastic arteries distend in response to the increase in blood pressure hence moderating the flow of blood. As pressure drops during diastole (dilation of the heart) they regain their shape. This contraction prolongs the surge in blood flow. In this way the elasticity of these large arteries helps to smooth the cyclic blood flow around the circulatory system. Figure 7.1 is a diagrammatic representation of a healthy elastic

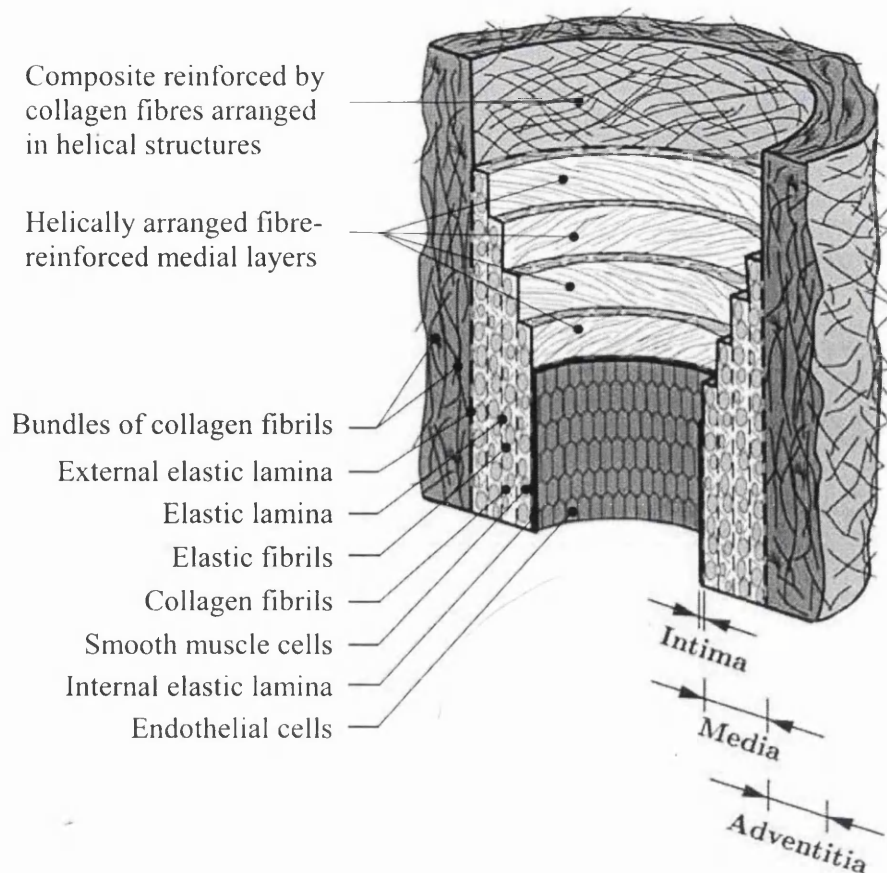


Figure 7.1: Schematic diagram of a healthy young elastic artery. (reproduced from Holzapfel *et al.* [53]) with permission

artery.

In muscular arteries the diameter of the lumen (inner channel) can be increased or decreased by relaxation or contraction of muscles in the walls. This function can help regulate blood flow to different parts of the body. Thus exercising muscles for instance can be prioritised or blood flow to injured tissue restricted to reduce bleeding. The coronary, cerebral and renal arteries are examples of the muscular type.

Common to both kinds of artery is a division of the wall into three concentric layers or *tunica*. These are, in order from innermost to outermost, the *tunica intima*, the *tunica media* and *tunica adventitia*. Two fenestrated membranes of the protein elastin, known as the internal and external laminae, separate the media from the intima and adventitia respectively. Each layer is described below.

The tunica intima

The principle feature of the innermost tunica is a single layer of flat endothelial cells (typically $\sim 0.4\mu\text{m}$ thick) lining the lumen. These adhere to a thin (typically $\sim 80\text{nm}$) collagenous membrane known as the basal lamina. The endothelial layer and basal lamina are generally thought to make a negligible contribution to the overall mechanical properties of the artery.

Immediately outside the basal lamina is the subendothelial layer. In young and healthy arteries this is very thin, especially in elastic arteries, and is insignificant from the mechanical modelling point of view. However a thickening and stiffening (arteriosclerosis) is associated with ageing. The subendothelium is typically composed mainly of the protein collagen in fibrous form with some smooth muscle cells and fibrous elastin. The collagen fibres have been observed in layers each with a distinct but loosely preferred fibre orientation.

Subendothelial thickening can also be produced by disease (atherosclerosis). This is characterised by the build up of lipids, fibrous tissue, calcium and various other deposits forming an asymmetric plaque that intrudes on the lumen and causes a potentially dangerous narrowing of the opening.

The tunica media

Next in sequence is the tunic media. This is separated from the intima by the internal elastic lamina. The media consists of smooth muscles interspersed with connective tissue – mainly collagen and elastin. The arrangement of the media differs between elastic and muscular arteries.

In elastic arteries the smooth muscle is arranged in unicellular layers ($\sim 5 - 15\mu\text{m}$ thick) separated by fenestrated elastic laminae similar to the internal and external laminae. The spindle shaped muscle cells (typically $\sim 100\mu\text{m}$ long and $\sim 5\mu\text{m}$ diameter) are aligned with their thin ends overlapping. Their orientation tends to be helical although with a small pitch – i.e. close to circumferential. Individual cells are invested in a substance similar to the basal lamina. Numerous collagen fibrils are found in the intracellular matrix especially close to the elastic laminae where they are bundled as fibres oriented in a near circumferential direction. Some elastic fibrils and other connective tissue is also present between the laminae. Taken together the sandwich of two elastic laminae and intervening tissue form a basic structural unit that repeated concentrically makes up the elastic tunica media. Termed variously

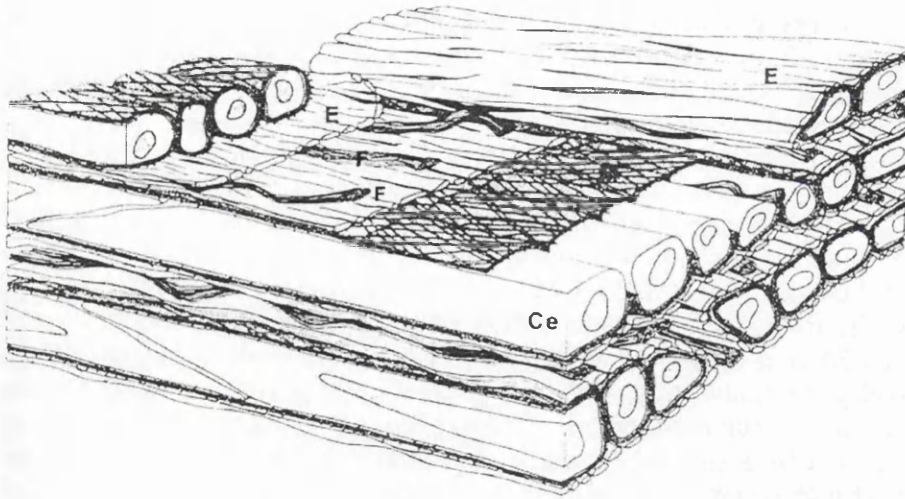


Figure 7.2: Schematic view of the musculo-elastic fascicle drawn by Clark and Glagov [13]. F – collagen fibres; E – elastin; Ce – smooth muscle cells.

the musculo-elastic fascicle [13] (see figure 7.2) or the lamellar unit [36], these layers have a thickness that hardly changes with radial position in the artery. The number of units changes with the thickness of the media so that larger arteries are formed by the addition of units rather than by thicker units. The human aorta can number between 53 and 78 lamellar units [20].

In the media of muscular arteries the smooth muscle cells are also layered and oriented. In larger muscular arteries the layers can number up to 25 or 35. However the elastic laminae are largely absent. By contrast the internal elastic membrane is more prominent.

According to Holzapfel *et al.* [53], citing [99,104] the collagen fibrils, elastic fibrils and laminae and muscle together form a “continuous fibrous helix”. This is crucial feature in motivating some of the constitutive models proposed for arterial tissue.

The tunica media’s outer boundary is marked by the external elastic lamina (cerebral vessels are an exception as they have no external lamina).

The tunica adventitia

The outermost layer is the tunica adventitia. It is composed of fibrous collagen along with fibroblasts and fibrocytes (cells which maintain connective tissue through the synthesis of collagen and elastin) and some other connective tissue. The collagen fibrils tend to be thicker than in the media and are grouped into fibre bundles. These are arranged in two families with opposing helical orientation. The alignment of

fibres in each family is far from strict with considerable individual variance from the averages.

The thickness of the adventitia varies considerable with site and its outer edge is sometimes ill defined as it blends with the perivascular tissue.

Collagen and elastin

Most sources agree that the passive mechanical behaviour (i.e. with muscles relaxed) of arteries is governed mainly by collagen and elastin.

Collagen is a protein with 15 varieties distinguished by details of there chemical composition. Types I, III and IV are commonly found in arterial tissue. Type IV is synthesised by the endothelial cells to form the basal lamina. Types I and II originate in fibroblasts and smooth muscle cells.

Typically the synthesising cells secrete triple helical molecules into the extracellular matrix. There by a process of polymerisation the molecules form into long microfibrils (4-8nm diameter) and fibrils(10-500nm diameter). The fibrils in turn can be bundled into fibre(1-500 μ m). These are usually undulating or wavy when unloaded. Thus until a fibre is stretched sufficiently to straighten it out it will provide little or no resistance.

Elastin is formed in arteries mainly by smooth muscle cells. Amorphous elastin is a relatively unstructured network of molecules with many crosslinks. Elastic fibres can form from aggregates of microfibrils(10nm diameter) embedded in the amorphous elastin. These fibres have a tendency to bifurcate forming networks or membranes.

Of the two materials collagen is by far the stiffer – *once fibres are straight*. However elastin is better able to undergo large elastic deformations. Straight elastic fibres may still recover their initial length after undergoing a stretch of 2.5. The comparable figure for collagen is less than 0.1.

7.2.2 Characteristic passive mechanical behaviour of arteries

Given the nature of the arterial microstructure a high degree anisotropy may be expected in the composite material. This is indeed the case. Most investigators accept a cylindrical orthotropic symmetry is appropriate. The experimental findings of [93]are usually cited in support.

Nonlinearity in the stress strain response is another feature of arterial tissue. Under moderate tensile loading the stiffness increases markedly with strain. This is

usually attributed to the recruitment of increasing numbers of straightened collagen fibres.

In addition a *pre-conditioning* effect is evident. Uniaxial cyclic loading tests on a patch of tissue [53] show a pronounced stress softening between cycles. This only occurs for the first few cycles after which the response settles to a repeatable elastic or viscoelastic curve. The tissue is then said to be pre-conditioned. If the stress is increased beyond the initial cyclic maximum the curve flattens. Further cyclic loading pre-conditions the tissue again to a new repeatable curve. However a residual plastic deformation is apparent. That is to say under zero load the tissue does not regain its initial configuration. Many models neglect this latter non-elastic effect and address only the elastic loading regime (which extends beyond physiological conditions) where a hyperelastic model is justifiable.

Another important feature of arterial mechanics is the evidence of pre-stress in the tissue. Arteries excised from the body contract in length evidencing an axial pre-stretch in vivo. If an excised segment of artery is subject to a further cut along its length the cylinder will spring open into a C shape. This shows the existence of residual circumferential stresses in the unloaded intact cylinder. These two phenomenon require that care is taken in formulating mechanical problems to correctly identify the true zero stress state as the reference configuration.

A final important property of arterial tissue is their near incompressibility. The investigations of Carew *et al.* [10] are the primary source of evidence. The assumption of perfect incompressibility provides convenient simplification in attempts to model arterial tissue and is adopted in most research.

7.3 Macroscopic constitutive models for arterial tissue

Many constitutive laws for the composite behaviour of artery walls have been proposed. Some of the better known models [18,30,54,107,121] are reviewed by Holzapfel *et al.* in [53]. These are purely phenomenological models. A novel hyperelastic model based on structural considerations is introduced in [53] and has proved highly influential. More recently another hyperelastic model, also structurally motivated, has been proposed by Zulliger *et al.* [129]. These last two models were selected as canonical macroscopic models to be fitted to results of the computationally homogenised

RVE outlined in section 7.4. The models by Zulliger *et al.* and Holzapfel *et al.* are described below.

7.3.1 Arterial wall constitutive model by Zulliger *et al.*

In formulating their model Zulliger *et al.* [129] represent the artery wall schematically as a cylinder of isotropic elastin containing two helically disposed families of collagen fibres oriented at angles α and $-\alpha$ respectively to the circumferential direction. Figure 7.3 shows the arrangement.

Individual collagen fibres are assumed to possess a waviness which causes them to remain unstressed until extended beyond a critical axial strain, ε_{act} . The following strain energy function is used to describe their behaviour,

$$\Psi_{fibre}(\varepsilon, \varepsilon_{act}) = \begin{cases} 0 & \text{for } \varepsilon \leq \varepsilon_{act} \\ c_{coll} [\varepsilon - \varepsilon_{act} - \log(\varepsilon - \varepsilon_{act} + 1)] & \text{for } \varepsilon > \varepsilon_{act} \end{cases} \quad (7.1)$$

where $\varepsilon = \lambda - 1$ is the axial strain in a fibre subject to axial stretch λ . The probability of any fibre have activating strain ε_{act} is assumed to follow a log-logistic probability density function given by

$$\rho_{fibre}(\varepsilon_{act}) = \begin{cases} 0 & \text{for } \varepsilon_{act} \leq 0 \\ \frac{k(\varepsilon_{act}/b)^{k-1}}{b[1+(\varepsilon_{act}/b)^k]^2} & \text{for } \varepsilon_{act} > 0 \end{cases} \quad (7.2)$$

where b and k are model parameters. The average strain energy of a large population of collagen fibres subjected to axial strain ε is then obtained from,

$$\Psi_{coll}(\varepsilon) = \int_{-\infty}^{\infty} \Psi_{fibre}(\varepsilon, \varepsilon_{act}) \rho_{fibre}(\varepsilon_{act}) d\varepsilon_{act} . \quad (7.3)$$

The elastin part of the artery is assumed to have the following strain energy function,

$$\Psi_{elast} = c_{elast}(I_1 - 3)^{\frac{3}{2}}, \quad (7.4)$$

where $I_1 = \text{tr} \mathbf{C}$ in terms of the right Cauchy-Green tensor \mathbf{C} and c_{elast} is another model parameter.

In accordance with the assumptions described above Zulliger propose an overall arterial strain energy function with two terms as follows:

$$\Psi_Z = f_{elast} \Psi_{elast} + f_{coll} \Psi_{coll}(\sqrt{I_4} - 1), \quad (7.5)$$

where f_{elast} and f_{coll} are the ratios of elastin volume and collagen volume respectively to the total volume and

$$I_4 = \mathbf{C} : (\mathbf{a} \otimes \mathbf{a}) , \quad (7.6)$$

in terms of the unit vector \mathbf{a} locally parallel to either family of collagen fibres. Owing to the assumed symmetry between the two families it does not matter which defines \mathbf{a} . Perfect incompressibility of the material is assumed. We note that underlying the construction of the strain energy function (SEF) (7.5) is the assumption that different fractions in the composite material experience the same deformation. This is akin to the use of the so called Taylor kinematic assumption [111] in self consistent homogenisation.

Given that the direction vector \mathbf{a} is a function of the fibre angle α , the constitutive model represented by equation (7.5) has a total of seven parameters – f_{elast} , c_{elast} , α , f_{coll} , c_{coll} , k and b . For the purposes of our exercise in optimisation we fixed $f_{elast} = 0.306$, $\alpha = 35.08^\circ$, $f_{coll} = 0.203$, $k = 22.54$ and $b = 0.6588$, and sought optimal values of c_{elast} and c_{coll} .

7.3.2 Arterial wall constitutive model by Holzapfel *et al.*

Holzapfel *et al.* [53] have proposed a hyperelastic strain energy function which also takes fibre orientation into account. If the fibre groups are symmetrically disposed as assumed in 7.3.1 then the SEF may be written

$$\Psi_H = \frac{c}{2}(I_1 - 3) + \frac{k_1}{k_2} \left(e^{k_2(I_4 - 1)^2} - 1 \right) , \quad (7.7)$$

where c , k_1 and k_2 are parameters of the model and the invariants I_1 and I_4 are defined as before. Once again perfect incompressibility of the material is assumed.

The constitutive model represented by (7.7) has four parameters in total c , k_1 , k_2 and the fibre angle α which appears in the definition of I_4 . For the purposes of the present study we fixed $\alpha = 39.76^\circ$ and optimised c , k_1 and k_2 .

7.4 FE model of microstructure

The basic micro-mesh – M20

A 2-D finite element mesh, which we shall refer to as M20, was constructed to represent the arterial micro-structure. This consisted of 192 linear triangular elements

under plane stress representing elastin overlaid with 96 truss elements representing collagen fibres. Figure (7.4) shows the configuration. Dimensions of the rectangular microcell were 3559.78 horizontally by 3000.00 vertically so that the truss elements were inclined at 35.08° to the mesh x direction – the same angle adopted for parameter α in the two macro models. Details of the mesh were as follows:

- Matrix of triangular elements:

Constitutive model – SEF defined by equation (7.4) with perfect incompressibility.
(Zulliger *et al.* [129] model for elastin)

Model parameter – $c_{elast} = 24.6458$ kPa.

Thickness – 500.

- Truss elements:

Constitutive model – SEF defined by equation (7.1) with perfect incompressibility.
(Zulliger *et al.* [129] model for collagen)

Model parameters – $c_{coll} = 101800$ kPa;
 ε_{act} randomly allocated for each element to one of 24 values
so that numbers of elements in each group are in proportion
to
the probability distribution (7.2) with $k = 22.54$ and $b = 0.6588$.

Cross sectional area – 135723.1

We identify the x direction of the mesh with the local circumferential direction of the artery and the y direction with its longitudinal axis.

The design of the microcell is intended to reflect the macro model by Zulliger *et al.* described in section 7.3.1. However the volume fractions of elastin and collagen in the microcell, which we shall denote f_{elast}^μ and f_{coll}^μ respectively, are not equal to the fixed values $f_{elast} = 0.306$ and $f_{coll} = 0.203$ used in that model. This is because the macro model volume fractions do not sum to one thereby indicating the presence of some structurally insignificant material. The micro mesh by contrast has no provision for such material. The elastin and collagen parts together account for the total cell volume so that

$$f_{elast}^\mu + f_{coll}^\mu = 1. \quad (7.8)$$

However the thickness of the elastin triangles and the cross sectional area of collagen truss elements have been chosen to ensure that the ratio of elastin volume to collagen volume is equal to 0.306/0.203. i.e.

$$\frac{f_{elast}^\mu}{f_{coll}^\mu} = \frac{f_{elast}}{f_{coll}}. \quad (7.9)$$

Moreover since the Zulliger *et al.* SEF depends only on the products $f_{elast}c_{elast}$ and $f_{coll}c_{coll}$ we may say that the microcell is compatible to the Zulliger model provided that

$$c_{elast}^{\mu} f_{elast}^{\mu} = c_{elast} f_{elast} \quad (7.10)$$

$$c_{coll}^{\mu} f_{coll}^{\mu} = c_{coll} f_{coll} , \quad (7.11)$$

where the superscript μ distinguishes the microcell parameters from the macro model values. This of course assumes that all the other corresponding microcell and macro model parameters match each other as indeed they do. Taking equations (7.8) to (7.11) together we find that

$$c_{elast} = \frac{c_{elast}^{\mu}}{f_{elast} + f_{coll}} \quad (7.12)$$

$$c_{coll} = \frac{c_{coll}^{\mu}}{f_{elast} + f_{coll}} . \quad (7.13)$$

These two equations define effective macro values of the elastin and collagen stiffness parameters. In view of this microcell M20 described above may be considered compatible with model (7.5) with parameter values:

$$\begin{aligned} f_{elast} &= 0.306 & ; & & c_{elast} &= 48.42 kPa; & & \alpha &= 35.08^{\circ}; & & f_{coll} &= 0.203; \\ c_{coll} &= 200000 kPa; & & k &= 22.54 & ; & & b &= 0.6588; \end{aligned} \quad (7.14)$$

In fact the homogenised response of the microcell under Taylor boundary conditions should be the same as model (7.5) with parameter set (7.14) up to discrepancies introduced by numerical errors and the discrete approximation to the probability distribution of activating strains (7.2).

Additional micro-meshes

In order to examine how changes to the collagen stiffness used for the microcell were reflected in the optimised parameters a further four micro-meshes were constructed. These were identical to the mesh M20 described above except that the effective parameter c_{coll} as defined in (7.13) was set variously to 100000, 150000, 250000 and 300000. We shall refer to these as M10, M15, M25 and M30 respectively.



Figure 7.3: Schematic view of artery with helical arrangement of collagen fibres. The artery is shown cut along its length to relieve residual stresses.

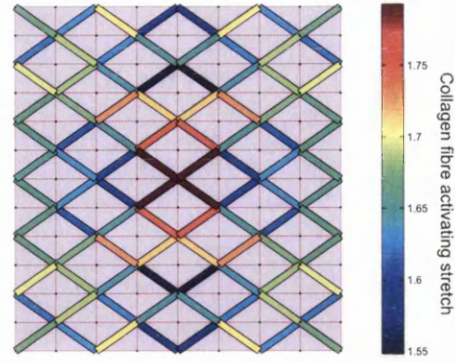


Figure 7.4: Mesh of collagen fibres overlaid on triangular elastin elements. The colour of each truss element indicates the activating stretch of the fibre.

7.5 Objective functions

Two sets of biaxial isochoric deformations were considered. The first was applied to the microcell M20 described in 7.4 and is expressed in terms of the right Cauchy-Green tensor with respect to (r, θ, z) coordinates as follows:

$$\mathbf{C}_k = \begin{bmatrix} 2.0164(0.6 + 0.05k)^{-1} & 0 & 0 \\ 0 & 0.6 + 0.05k & 0 \\ 0 & 0 & 2.0164 \end{bmatrix} \quad \text{for } k = 0 \text{ to } 52. \quad (7.15)$$

We obtained the corresponding average strain energies $\bar{\Psi}_k^{Tay}$ and $\bar{\Psi}_k^{per}$ under the Taylor and periodic boundary conditions respectively and the corresponding first Piola-Kirchhoff stress tensors $\bar{\mathbf{P}}_k^{Tay}$ and $\bar{\mathbf{P}}_k^{per}$.

The second larger set of deformations, defined by the Cauchy-Green tensors

$$\mathbf{C}_{jk} = \begin{bmatrix} (0.2 + 0.0776j)^{-1}(0.2 + 0.0776k)^{-1} & 0 & 0 \\ 0 & 0.2 + 0.0776j & 0 \\ 0 & 0 & 0.2 + 0.0776k \end{bmatrix} \quad \text{for } j = 0 \text{ to } 49, k = 0 \text{ to } 49, \quad (7.16)$$

was applied to the microcells M10, M15, M20, M25 and M30 with the periodic boundary condition enforced to obtain corresponding sets of homogenised strain energy

$\bar{\Psi}_{jk}^{per(10)}$, $\bar{\Psi}_{jk}^{per(15)}$, $\bar{\Psi}_{jk}^{per(20)}$, $\bar{\Psi}_{jk}^{per(25)}$ and $\bar{\Psi}_{jk}^{per(30)}$.

Having this homogenised data to hand a number of objective functions were formulated. Four objective functions to optimise the macro model by Zulliger *et al.* (section 7.3.1) were defined based on the homogenised response of micro mesh M20 to the deformation set (7.15):

$$Q_1^{Zul}(c_{elast}, c_{coll}) = \sum_{k=1}^{12} \left(\Psi^{Zul}(\mathbf{C}_k, c_{elast}, c_{coll}) - \bar{\Psi}_k^{Tay} \right)^2 \quad (7.17)$$

$$Q_2^{Zul}(c_{elast}, c_{coll}) = \sum_{k=1}^{12} \left(\Psi^{Zul}(\mathbf{C}_k, c_{elast}, c_{coll}) - \bar{\Psi}_k^{per} \right)^2 \quad (7.18)$$

$$Q_3^{Zul}(c_{elast}, c_{coll}) = \sum_{k=1}^{12} \left\| \mathbf{P}^{Zul}(\mathbf{C}_k, c_{elast}, c_{coll}) - \bar{\mathbf{P}}_k^{Tay} \right\|_2^2 \quad (7.19)$$

$$Q_4^{Zul}(c_{elast}, c_{coll}) = \sum_{k=1}^{12} \left\| \mathbf{P}^{Zul}(\mathbf{C}_k, c_{elast}, c_{coll}) - \bar{\mathbf{P}}_k^{per} \right\|_2^2, \quad (7.20)$$

where \mathbf{P}^{Zul} is the first Piola-Kirchoff stress derived from the SEF (7.5) with $f_{elast} = 0.306$, $\alpha = 35.08^\circ$, $f_{coll} = 0.203$, $k = 22.54$ and $b = 0.6588$.

A further four objective functions, also based on the deformation set (7.15) and the mesh M20, were defined as follows for optimising the macro model by Holzapfel *et al.* (section 7.3.2):

$$Q_1^{Hol}(c, k_1, k_2) = \sum_{k=1}^{12} \left(\Psi^{Hol}(\mathbf{C}_k, c, k_1, k_2) - \bar{\Psi}_k^{Tay} \right)^2 \quad (7.21)$$

$$Q_2^{Hol}(c, k_1, k_2) = \sum_{k=1}^{12} \left(\Psi^{Hol}(\mathbf{C}_k, c, k_1, k_2) - \bar{\Psi}_k^{per} \right)^2 \quad (7.22)$$

$$Q_3^{Hol}(c, k_1, k_2) = \sum_{k=1}^{12} \left\| \mathbf{P}^{Hol}(\mathbf{C}_k, c, k_1, k_2) - \bar{\mathbf{P}}_k^{Tay} \right\|_2^2 \quad (7.23)$$

$$Q_4^{Hol}(c, k_1, k_2) = \sum_{k=1}^{12} \left\| \mathbf{P}^{Hol}(\mathbf{C}_k, c, k_1, k_2) - \bar{\mathbf{P}}_k^{per} \right\|_2^2, \quad (7.24)$$

where \mathbf{P}^{Hol} is the first Piola-Kirchoff stress derived from the SEF (7.7) with $\alpha = 35.08^\circ$.

Finally the homogenised strain energy values for the deformations specified by

(7.16) were used to define a further five Zulliger *et al.* based objective functions:

$$Q_{10}^{Zul}(c_{elast}, c_{coll}) = \sum_{j=1}^{52} \sum_{k=1}^{52} \left(\Psi^{Zul}(C_{jk}, c_{elast}, c_{coll}) - \bar{\Psi}_{jk}^{per(10)} \right)^2 \quad (7.25)$$

$$Q_{15}^{Zul}(c_{elast}, c_{coll}) = \sum_{j=1}^{52} \sum_{k=1}^{52} \left(\Psi^{Zul}(C_{jk}, c_{elast}, c_{coll}) - \bar{\Psi}_{jk}^{per(15)} \right)^2 \quad (7.26)$$

$$Q_{20}^{Zul}(c_{elast}, c_{coll}) = \sum_{j=1}^{52} \sum_{k=1}^{52} \left(\Psi^{Zul}(C_{jk}, c_{elast}, c_{coll}) - \bar{\Psi}_{jk}^{per(20)} \right)^2 \quad (7.27)$$

$$Q_{25}^{Zul}(c_{elast}, c_{coll}) = \sum_{j=1}^{52} \sum_{k=1}^{52} \left(\Psi^{Zul}(C_{jk}, c_{elast}, c_{coll}) - \bar{\Psi}_{jk}^{per(25)} \right)^2 \quad (7.28)$$

$$Q_{30}^{Zul}(c_{elast}, c_{coll}) = \sum_{j=1}^{52} \sum_{k=1}^{52} \left(\Psi^{Zul}(C_{jk}, c_{elast}, c_{coll}) - \bar{\Psi}_{jk}^{per(30)} \right)^2, \quad (7.29)$$

As before $f_{elast} = 0.306$, $\alpha = 35.08^\circ$, $f_{coll} = 0.203$, $k = 22.54$ and $b = 0.6588$ in the evaluation of Ψ^{Zul} .

7.6 Optimisation results

Minimisation of the objective functions defined in (7.17) to (7.29) was performed using the Optimization Toolbox of the commercial software package MATLAB (version 7.3.0.267 R2006b). Those functions based on the model by Zulliger *et al.* required only a linear least squares algorithm (Matlab function *lsqnonneg*) since the nonlinear parameters in Ψ_Z had been fixed. Table 7.1 lists the optimised parameter values for Q_1^{Zul} – Q_4^{Zul} and table 7.3 lists the optimised parameter values for Q_{10}^{Zul} – Q_{30}^{Zul} .

Nonlinear optimisation was performed for the Holzapfel *et al.* based objective functions using the trust-region reflective Newton algorithm (Matlab function *lsqnonlin*). This is an iterative procedure which is judged to have converged either when the Newton step becomes less than the chosen tolerance ($\text{TolX} = 1 \times 10^{-10}$) or the gradient becomes less than tolerance ($\text{TolFun} = 1 \times 10^{-10}$). For each nonlinear objective function 30 different sets of randomly chosen starting values were used. The converged parameter values are given in table 7.2. Among the 30 results for each objective function only the parameter set yielding the minimum value of the function is listed. Mostly the different starting values converged to very similar parameter values with similar residuals (within 0.2%). However on occasions the optimisation algorithm converged to a completely different set of parameters. Ogden *et al.* [86] in

optimising hyperelastic models to fit experimental tests on rubber also report multiple points of convergence. In the present study all the alternative convergent parameter sets yield residuals more than 5 times the minimum.

The residuals listed in tables 7.1, 7.2 and 7.3 are the values of the objective functions evaluated at minimum converged parameter values. Note that it is not instructive to compare the residuals of functions Q_1^{Zul} , Q_2^{Zul} , Q_1^{Hol} and Q_2^{Hol} with those of Q_3^{Zul} , Q_4^{Zul} , Q_3^{Hol} and Q_4^{Hol} since the former group are based on strain energies which in the present example take lower values than the stresses on which the latter group are based. Similarly the residuals of the objective functions based on the deformations (7.15) are not comparable to those based on deformations (7.16) since they contain many fewer data points. The quality of fit for the models optimised using Q_1^{Zul} – Q_4^{Zul} and Q_1^{Hol} – Q_4^{Hol} can be assessed visually from figure 7.6 where the strain energy, circumferential stress and radial stress are plotted along with the homogenised data.

Figures 7.6(a), 7.6(c) and 7.6(e) show the models based on Taylor homogenisation while 7.6(b), 7.6(d) and 7.6(f) relate to the periodic condition. As one would expect the more tightly constrained Taylor condition leads to stiffer constitutive models.

Considering the Taylor based optimisation results first, we see as expected that the Zulliger *et al.* model provides a very good match to the homogenised data regardless of whether the strain energy formulation or stress formulation is used in the objective function. By contrast the Holzapfel *et al.* stress based objective function (Q_3^{Hol}) yields a noticeably stiffer optimal model than the strain energy formulation (Q_1^{Hol}) especially at higher strains.

The results for the periodic condition also show the Holzapfel *et al.* stress based optimisations produce stiffer behaviour than their strain energy based counterparts. The optimised Zulliger models differ significantly between stress and strain energy formulations but one is not consistently stiffer than the other. We can however see from this example that significant differences in outcome can result in choosing between stress and strain energy based formulations of the objective function.

It seems clear overall that the Zulliger *et al.* model, being based on the same assumptions used for the micro model, is better able than the Holzapfel *et al.* model to capture the homogenised behaviour. This is true even though the Holzapfel *et al.* optimisation contained one more ‘free’ parameter thus emphasising the importance of choosing a suitable form of macro model.

Table 7.3 shows the optimal parameter values for objective functions Q_{10}^{Zul} , Q_{15}^{Zul} ,

Table 7.1: Optimised parameters for the macro model by Zulliger *et al.* – optimisation based on deformation range (7.15)

Parameter set	Z1	Z2	Z3	Z4
Objective function	Q_1^{Zul}	Q_2^{Zul}	Q_3^{Zul}	Q_4^{Zul}
c_{elast}^{opt} (kPa)	48.1341	47.9364	47.9354	40.8101
c_{coll}^{opt} (kPa)	198959.64	30691.27	200513.84	87074.35
residual	0.5798	18.0564	74.5010	48337.1410

Table 7.2: Optimised parameters for macro model by Holzapfel *et al.* – optimisation based on deformation range (7.15)

Parameter set	H1	H2	H3	H4
Objective function	Q_1^{Hol}	Q_2^{Hol}	Q_3^{Hol}	Q_4^{Hol}
c^{opt} (kPa)	28.478	16.158	39.240	49.374
k_1^{opt}	0.385	4.609	0.121	1.250×10^{-7}
k_2^{opt}	1.623	0.225	2.319	6.846
residual	142.896	38.442	14539.4785	9944.2568

Q_{20}^{Zul} , Q_{25}^{Zul} and Q_{30}^{Zul} . These are the functions based on deformation range (7.16) with varying microcell values of c_{coll}^μ . Figure 7.5 shows the relationship between optimised Zulliger *et al.* model parameters c_{elast}^{opt} and c_{coll}^{opt} and the value of collagen stiffness used in the microcell. The ratios $c_{elast}^{opt}/c_{elast}^{eff}$ and $c_{coll}^{opt}/c_{coll}^{eff}$ have been plotted against c_{coll}^{eff} . Here c_{elast}^{eff} and c_{coll}^{eff} are the effective values of elastin and collagen parameters (as defined by equations (7.12) and (7.13)). Note that both the optimized macro parameters c_{coll}^{opt} and c_{elast}^{opt} are smaller than their RVE counterparts. This is because the periodic condition applied in homogenization yields a softer response than the rule of mixtures. The stiffening effect of increasing c_{coll}^{eff} in the RVE leads to increased c_{coll}^{opt} in the optimized model but is also accompanied by a degree of softening in c_{elast}^{opt} .

Table 7.3: Optimised parameters for the macro model by Zulliger *et al.* – optimisation based on deformation range (7.16) with varying microcell values of c_{coll}^μ

Parameter set	Z10	Z15	Z20	Z25	Z30
Objective fn.	Q_{10}^{Zul}	Q_{15}^{Zul}	Q_{20}^{Zul}	Q_{25}^{Zul}	Q_{30}^{Zul}
c_{elast}^{opt} (kPa)	46.3734	45.3121	44.2494	43.1861	42.1225
c_{coll}^{opt} (kPa)	97511.424	146236.23	194960.95	243685.67	292410.41
residual	89248.86	205809.09	370608.77	583673.61	845016.63

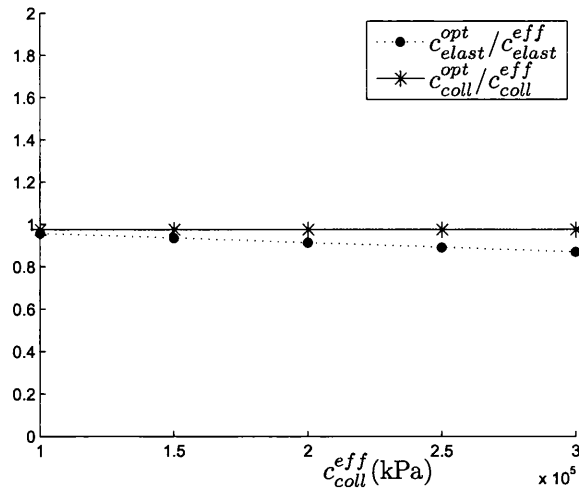


Figure 7.5: Relationship between optimised Zulliger *et al.* model parameters c_{elast} and c_{coll} and the value of collagen stiffness used in the microcell.

7.7 Macro boundary value problem – inflation and extension of artery

In an unloaded state arteries are known to retain some residual stresses. These are thought to be relieved by a radial cut through the wall [41] allowing the artery to spring open with a characteristic opening angle, Θ_0 , as shown in figure 7.7(a). We follow authors such as [55] and assume that extension and axisymmetric inflation of an artery without twisting may be represented by the following mapping from reference cylindrical coordinates (R, Θ, Z) in the zero stress state to the deformed cylindrical coordinates (r, θ, z)

$$r = r(R), \quad \theta = \frac{\pi}{\Theta_0} \Theta, \quad z = \lambda Z. \quad (7.30)$$

Here λ is a constant axial stretch. It may be seen that the principle directions of the deformation gradient coincide with the cylindrical basis vectors i.e. the radial, circumferential and axial directions, and we obtain the principle circumferential and axial stretches as

$$\lambda_\theta = \frac{r}{R} \frac{\partial \theta}{\partial \Theta} = \frac{\pi r}{\Theta_0 R}, \quad \lambda_z = \frac{\partial z}{\partial Z} = \lambda. \quad (7.31)$$

Since perfect incompressibility is assumed ($\lambda_r \lambda_\theta \lambda_z = 1$) the radial stretch is given by

$$\lambda_r = \frac{\partial r}{\partial R} = \frac{\Theta_0 R}{\pi \lambda r}. \quad (7.32)$$

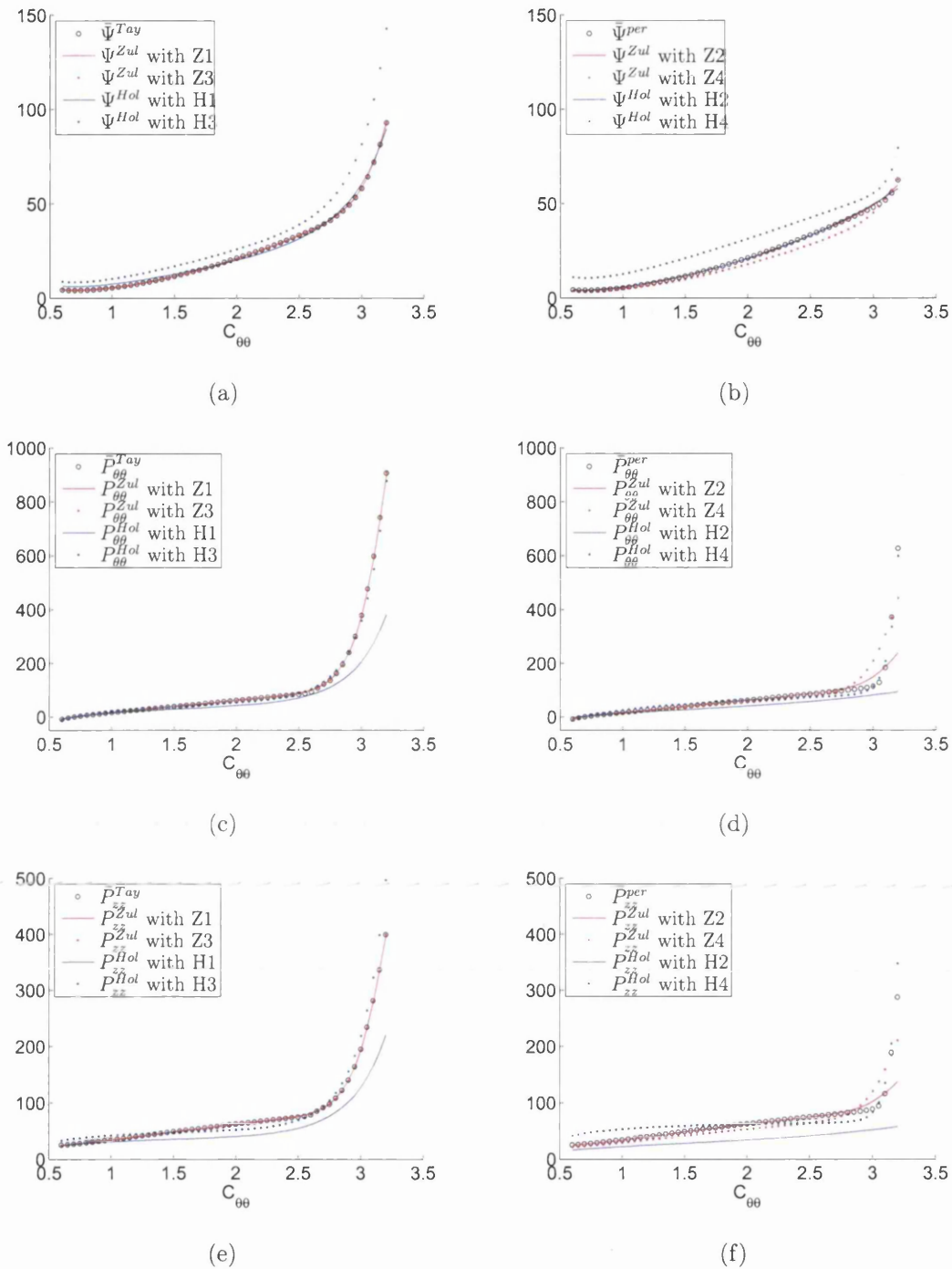


Figure 7.6: Optimised strain energy functions ((a) and (b)), circumferential stresses ((c) and (d)) and axial stresses ((e) and (f)) assuming plane stress in the θ - z plane.

This may be integrated to obtain the relationship between R and r as

$$R = \sqrt{R_o^2 - \frac{\pi\lambda}{\Theta_0}(r_o^2 - r^2)}, \quad (7.33)$$

where r_o is the current radius of the outer surface. It is now seen from equations (7.31), (7.32) and (7.33) that if the initial geometry, axial stretch and current outer

radius are known then the state of deformation is fully determined by r and the one dimensional nature of the problem becomes apparent.

Now it may be shown (see e.g [55]) that, assuming shear stresses are absent, equilibrium of the artery requires the following expression for the internal lumen pressure to hold:

$$p = \int_{r_i}^{r_o} (\sigma_{\theta\theta} - \sigma_{rr}) \frac{dr}{r}. \quad (7.34)$$

Note that (7.33) with $r = r_i$ may be inverted to obtain r_i in terms of r_o . Furthermore since the deformation is a known function of r then if the constitutive function of the artery material is determined, equation (7.34) may be integrated to obtain the lumen pressure as a function of current outer radius.

Using these relations we obtained graphs of p_o versus p for the two macro constitutive models with optimised parameter sets Z1–Z4, Z20 and H1–H4. Figure 7.8(a) shows the graphs calculated using the models fitted to the Taylor data. The graphs relating to the periodic boundary condition are shown in figure 7.8(b) with the exception of the curve based on Z20. This is shown in figure 7.7 along with the graph for Z2 for comparison. Also plotted in each figure are the curves obtained by using the homogenised response of the finite element microcell directly as a constitutive relation. Note that only the difference $(\sigma_{\theta\theta} - \sigma_{rr})$ appears in (7.34) so that hydrostatic pressure terms in $\sigma_{\theta\theta}$ and σ_{rr} cancel out. This means that the plane stress response of the microcell is adequate for calculating the pressure even though the artery wall is not typically in a state of plane stress.

In figure 7.8(a) we see predictably that the Zulliger *et al.* model produces a much better fit than the model by Holzapfel *et al.*, with little difference evident between strain energy and stress based objective functions. By contrast the results of the stress based optimisation (H3) are notably better than those of the energy based optimisation (H1) for the Holzapfel model. However in figure 7.8(b) the energy based Zulliger optimisation (Z2) models the periodic homogenised response much better than its stress based counterpart (Z4). Thus we cannot conclude that a stress based objective function shows advantages over a strain energy based formulation.

In figure 7.7 the curves for Zulliger *et al.* parameter sets Z20 and Z2 are compared. Both sets arise from optimizations based on periodic homogenisation using a strain energy formulation. Only the range of deformations evaluated in the respective objective functions differentiates them. Note that the inflation of the cylinder represented by figure 7.7 induces deformations in the material of the wall such that the

circumferential right Cauchy-Green component $C_{\theta\theta}$ is contained within the envelope $[0.089, 1.042]$ with the axial component $C_{\theta\theta}$ constant at 2.0164. Neither of the sets of deformations used to obtain Z2 (7.15) and Z20 (7.16) matches this envelope in extent. However the deformations for Z2 involve far fewer data points (in absolute and proportionally terms) that lie well outside the envelope. This probably explains why the Z2 parameters produce the curve closer to the homogenised response. The difference between the two curves emphasises the importance of choosing a range of deformations appropriate to the problems to which the macro model is intended to be applied.

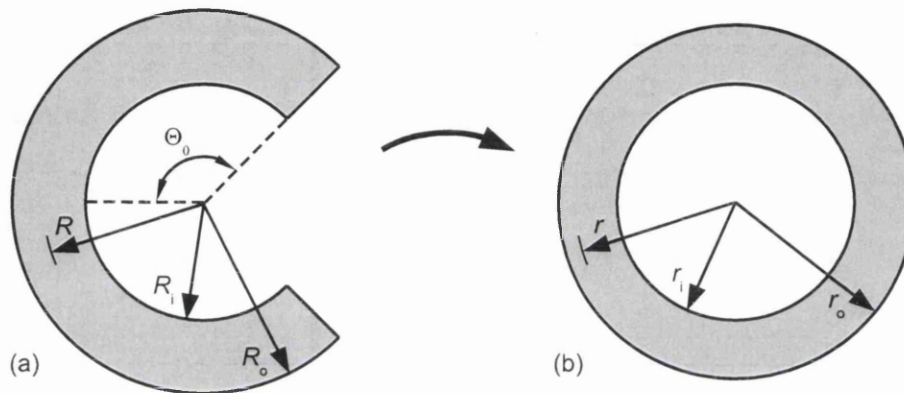


Figure 7.7: (a) Initial stress free configuration and (b) current configuration of artery cross-section. The opening angle Θ_0 is half the angle of the arc.

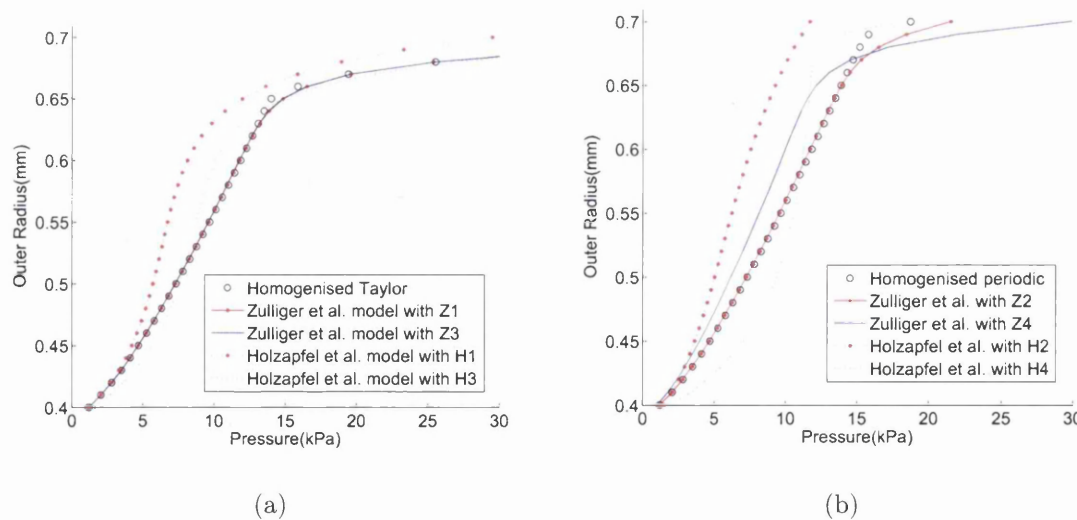


Figure 7.8: Outer radius versus pressure for each of the optimised models. ($\Theta_0 = 112^\circ$, $\lambda = 1.42$, $R_i = 0.96\text{mm}$, $R_o = 1.102\text{mm}$)

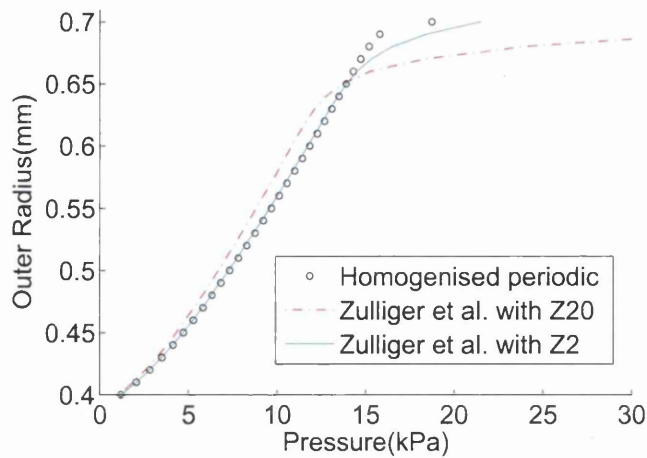


Figure 7.9: Outer radius versus pressure for each of the optimised models. ($\Theta_0 = 112^\circ$, $\lambda = 1.42$, $R_i = 0.96\text{mm}$, $R_o = 1.102\text{mm}$)

7.8 Conclusion

A procedure has been presented to determine hyperelastic model parameters for heterogeneous materials through modelling of the microstructure. The practicality of the method is demonstrated by example. Comparing the performance of different optimised models in a macro boundary value problem highlights the substantial differences in outcome between choices of canonical macro models and between objective function formulations based on stress and strain energy respectively. The computational expense of evaluating multiple micro-cell responses and the potential difficulties in finding objective function minima are recognised. Nevertheless the microstructure based optimisation procedure described here potentially offers a practical way of obtaining useful single scale macro models which account for detailed microstructure information.

Chapter 8

Conclusion

The description of the mechanical constitutive behaviour of micro-heterogeneous materials by means of effective macroscopically homogeneous models is now well established. Among approaches adopted to derive such models those based on computational homogenisation offer considerable advantages in their ability to cope with arbitrary microstructural geometry, advanced constituent materials and large deformations. In this thesis a concise finite element formulation, developed through a variational treatment of the fundamental theory, has been described. An implementation of this has been tested on a variety of hyperelastic microstructures. Basic properties of the homogenised responses such as their relative stiffness under different boundary conditions and material symmetries were confirmed and some limited studies on microstructural geometry presented.

In chapters 6 and 7 an uncoupled two scale method has been considered, whereby an explicit macroscopic constitutive model is fitted to data from computational homogenisation. The procedure was applied to a micro model representing arterial tissue.

In general terms the methodology has some advantages. It takes full account of microstructural information and interactions but still yields an explicit model which can be easily used with existing finite element codes. Once the optimisation of material parameters has been accomplished the solution of macroscopic boundary problems is therefore usually much faster than the coupled multi-scale method. Even including all the necessary optimisation calculations the procedure may be more efficient if the macroscopic model is used heavily.

Disadvantages of the optimisation approach include the loss of accuracy compared with directly coupled multiscale modelling. Here the canonical form of the macro

model is crucial and so its choice requires some judgement. Another shortcoming lies in the optimisation process. For highly nonlinear macro models and deformation modes it can be difficult to find the optimal parameter values.

The range of deformations chosen to provide data points for optimisation can have a large effect on the outcome on the eventual fitted macro model. Economy of computational effort requires that known or assumed symmetries and constraints should be exploited to minimise this range. In addition the desired range of applicability of the macro model should be taken into account.

Suggestions for further work

A number of enhancements to the general optimisation based uncoupled modelling approach suggest themselves

- *Parallelization*: The procedure requires the solution of a potentially large number of independent optimisation calculations to determine the homogenised response to a set of deformations. This stage of the overall process therefore seems well suited to parallel computing methods.
- *Improved optimisation algorithms*: The work in this thesis relied on iterative algorithms available as off-the-shelf MATLAB functions. Difficulties were experienced with large data sets and complex parameter dependency. As the field of optimisation is an important and evolving one there is scope for examining more advanced methods such as genetic algorithms.
- *Second order homogenisation*: In order to take account of size effects the use of second order homogenisation is desirable. However the additional dependency on the second gradient of displacement increases the space of deformations that need to be considered and hence increases the number of data points for adequate homogenisation. A second order formulation is thus not easy to implement but still worthy of further consideration.

As regards the specific application of the method to the modelling of arterial tissue some possible directions for further research are

- *Modelling damage in collagen fibres*: The stress strain behaviour of artery tissue is known to exhibit hysteresis similar to the Mullins effect in rubber. Introducing damage properties to the fibres in the microstructural model may have the potential to capture this phenomenon.

- *More empirical data:* There is an obvious need for more experimental information – both macroscopic test results to validate the macro model and measurements of the microstructure to construct a more accurate representative volume element.
- *Dispersion of fibre angles:* Collagen fibres are clearly not aligned with perfect regularity. There is scope to include a dispersion of fibres effects in the RVE micro model.
- *3-D formulation:* A three dimensional model will be able to take into account the full range of deformation states and the effect of fibres running in the radial direction.

As a final suggestion there seem to be good reasons to consider a database approach to modelling heterogeneous materials with hyperelastic microstructures. That is to say the compilation of a large database of computed homogenised stress responses of the RVE at a discrete set of points in the space of deformation gradients. Once the database is in place the homogenised response to an arbitrary deformation is obtained by interpolation between the known points. The interpolated response should typically be more accurate than a fitted macro model. The advantage over the coupled multi-scale method is that it is quicker once the database is in place. Moreover in solving macroscopic problems it is likely that very similar states of deformation arise numerous times. Using the coupled approach each such instance requires the computation of the RVE problem. This duplication of effort is avoided with a database approach. In the literature the methodology has been applied to problems in plasticity [94] (the present author has not seen examples in hyperelasticity). However the method seem more conveniently applied to microstructure with hyperelastic constituent phases. The advantage of hyperelastic materials is that their constituent behaviour may be fully characterised by the current deformation gradient alone without considering the deformation history. This reduces the dimension of the database space. If further constraints can be invoked such as incompressibility and material symmetry the required database may be reduced further to manageable proportions.

References

- [1] J. Aktaa, H. Kiewel, and J. Turki. Modelling of the influence of damage on the deformation behaviour by a self-consistent embedded cell model. *Computational Materials Science*, 12:64–72, 1998.
- [2] N.W. Ashcroft and N.D. Mermin. *Solid state physics*. Saunders College, Philadelphia, HRW International edition, 1987.
- [3] G. Bao, J.W. Hutchinson, and R.M. McMeeking. Particle reinforcement of ductile matrices against plastic flow and creep. *Acta Metallurgica et Materialia*, 39(8):1871–1882, 1991.
- [4] K.J. Bathe. *Finite element procedures*. Prentice-Hall, New Jersey, 1996.
- [5] A. Bensoussan, J. Lionis, and G. Papanicolaou. *Asymptotic analysis for periodic microstructures*. North-Holland, Amsterdam, 1978.
- [6] R.D. Bhargava and H.C. Radhakrishna. Elliptic Inclusion in Orthotropic Medium. *Journal of the Physical Society of Japan*, 19:396, 1964.
- [7] J. Bonet and R.D. Wood. *Nonlinear continuum mechanics for finite element analysis*. Cambridge University Press, Cambridge, 1997.
- [8] B. Boso, C. Pellegrino, U. Galvanetto, and B.A. Schrefler. Macroscopic damage in periodic composite materials. *Communications in Numerical Methods in Engineering*, 16:615–623, 2000.
- [9] B. Budiansky. On the elastic moduli of some heterogeneous materials. *Journal of the Mechanics and Physics of Solids*, 13:223–227, 1965.
- [10] T.E. Carew, R.N. Vaishnav, and D.J. Patel. Compressibility of the arterial wall. *Circulation Research*, 23:61–68, 1968.

- [11] V. Carvelli and A. Taliercio. A micromechanical model for the analysis of unidirectional elastoplastic composites subjected to 3D stresses. *Mechanics Research Communications*, 26(5):547–553, 1999.
- [12] P. Chadwick. *Continuum mechanics: concise theory and problems*. Dover, New York, 1999.
- [13] J.M. Clark and S. Glagov. Transmural organization of the arterial media. *Arteriosclerosis*, 5:19–34, 1985.
- [14] T.F. Coleman and Y. Li. On the Convergence of Reflective Newton Methods for Large-Scale Nonlinear Minimization Subject to Bounds. *Mathematical Programming*, 67(2):189–224, 1994.
- [15] T.F. Coleman and Y. Li. An Interior, Trust Region Approach for Nonlinear Minimization Subject to Bounds. *SIAM Journal on Optimization*, 6:418–445, 1996.
- [16] E. A. de Souza Neto and R. A. Feijóo. Variational foundations of multi-scale constitutive models of solid: small and large strain kinematical formulation. Internal Research Development Report 16, National Laboratory for Scientific Computing (LNCC/MCT), Brazil, 2006.
- [17] E.A. de Souza Neto, D. Perić, and D.R.J. Owen. *Computational plasticity: small and large strain finite element analysis of elastic and inelastic solids*. Awaiting publication.
- [18] A. Delfino, N. Stergiopoulos, J.E. Moore, and J.-J. Meister. Residual strain effects on the stress field in a thick wall finite element model of the human carotid bifurcation. *Journal of Biomechanics*, 30:777–786, 1997.
- [19] F. Devries, H. Dumontet, G. Duvaut, and F. Lene. Homogenization and damage for composite structures. *International Journal for Numerical Methods in Engineering*, 27:285–298, 1989.
- [20] K.P. Dingemans, P. Teeling, J.H. Lagendijk, and A.E. Becker. Extracellular matrix of the human aortic media: an ultrastructural histochemical and immunohistochemical study of the adult aortic media. *The Anatomical Record*, 258:1–14, 2000.

- [21] M. Dong and S. Schmauder. Transverse mechanical behaviour of fiber reinforced composites – FE modelling with embedded cell models. *Computational Materials Science*, 5:53–66, 1996.
- [22] J.M. Duva and J.W. Hutchinson. Constitutive potentials for dilutely voided nonlinear materials . *Mechanics of Materials*, 3:41–54, 1984.
- [23] J.D. Eshelby. The determination of the elastic field of an ellipsoidal inclusion and related problems. *Proceedings of the Royal Society of London A*, 241:376–396, 1957.
- [24] J.D. Eshelby. The Elastic Field Outside an Ellipsoidal Inclusion . *Proceedings of the Royal Society of London A*, 252:561–569, 1959.
- [25] J.D. Eshelby. Elastic inclusions and inhomogeneities. In R. Hill, editor, *Progress in Solid Mechanics Vol II*, pages 89–140, North-Holland, Amsterdam, 1961.
- [26] F. Feyel. *Parallélisme et approches multi-échelles en mécanique des matériaux*. PhD Thesis, École Normale Supérieure de Mines de Paris, 1999.
- [27] F. Feyel. A multilevel finite element method (FE^2) to describe the response of highly non-linear structures using generalized continua. *Computer Methods in Applied Mechanics and Engineering*, 192:3233–3244, 2003.
- [28] F. Feyel and J. Chaboche. FE^2 multiscale approach for modelling the elastoviscoplastic behaviour of long fiber SiC/Ti composite materials. *Computer Methods in Applied Mechanics and Engineering*, 183:309–330, 2000.
- [29] J. Fish, Q. Yu, and K. Shek. Computational damage mechanics for composite materials based on mathematical homogenization. *International Journal for Numerical Methods in Engineering*, 45:1657–1679, 1999.
- [30] Y.C. Fung, K. Fronek, and P. Patitucci. Pseudoelasticity of arteries and the choice of its mathematical expression. *American Journal of Physiology - Heart and Circulatory Physiology*, 237:H620–H631, 1979.
- [31] T.C. Gasser, R.W. Ogden, and G.A. Holzapfel. Hyperelastic modelling of arterial layers with distributed collagen fibre orientations. *Journal of the Royal Society Interface*, 3:15–35, 2006.

- [32] S. Ghosh, K. Lee, and S. Moorthy. Multiple scale analysis of heterogeneous elastic structures using homogenization theory and Voronoi cell finite element method. *International Journal of Solids and Structures*, 32(1):27–62, 1995.
- [33] S. Ghosh, K. Lee, and S. Moorthy. Two scale analysis of heterogeneous elastic-plastic materials with asymptotic homogenization and Voronoi cell finite element model. *Computer Methods in Applied Mechanics and Engineering*, 132:63–116, 1996.
- [34] S. Ghosh, K. Lee, and P. Raghavan. A multi-level computational model for multi-scale damage analysis in composite and porous materials. *International Journal of Solids and Structures*, 38:2335–2385, 2001.
- [35] S. Ghosh and S. Moorthy. Particle fracture simulation in non-uniform microstructures of metal-matrix composites. *Acta Materialia*, 46:965–982, 1998.
- [36] S. Glagov and H. Wolinsky. A lamellar unit of aortic medial structure and function in mammals. *Circulation Research*, 20:99–111, 1967.
- [37] S. Goktepe and C. Miehe. A micro-macro approach to rubber-like materials. Part III: The micro-sphere model of anisotropic Mullins-type damage. *Journal of the Mechanics and Physics of Solids*, 53:2259–2283, 2005.
- [38] H. Goldstein. *Classical mechanics*. Addison-Wesley, Reading, Massachusetts, 2nd edition, 1980.
- [39] A.E. Green and J.E. Adkins. *Large elastic deformations*. Oxford, London, 1960.
- [40] M.E. Gurtin. *An introduction to continuum mechanics*. Academic Press, San Diego, 1981.
- [41] H.C. Han and Y.C. Fung. Direct measurements of transverse residual strains in aorta. *American Journal of Physiology - Heart and Circulatory Physiology*, 270:H750–759, 1996.
- [42] Z. Hashin. The elastic moduli of heterogeneous materials. *Journal of Applied Mechanics*, 29:143–150, 1962.
- [43] Z. Hashin and S. Shtrikman. On some variational principles in anisotropic and nonhomogeneous elasticity. *Journal of the Mechanics and Physics of Solids*, 10:335–342, 1962.

- [44] Z. Hashin and S. Shtrikman. A variational approach to the theory of the elastic behaviour of multiphase materials. *Journal of the Mechanics and Physics of Solids*, 11:127–140, 1963.
- [45] H. Hencky. The elastic behaviour of vulcanized rubber. *Journal of Applied Mechanics*, 1:45–53, 1933.
- [46] A.V. Hershey. The elasticity of an isotropic aggregate of anisotropic cubic crystals. *Journal of Applied Mechanics*, 21:236,241, 1954.
- [47] R. Hill. The elastic behaviour of a crystalline aggregate. *Proceedings of the Physical Society (London)*, A65:349–354, 1952.
- [48] R. Hill. A self-consistent mechanics of composite materials. *Journal of the Mechanics and Physics of Solids*, 13:213–222, 1965.
- [49] R. Hill. Continuum micro-mechanics of elastoplastic polycrystals. *Journal of the Mechanics and Physics of Solids*, 13:89–101, 1965.
- [50] R. Hill. Theory of mechanical properties of fibre-strengthened materials – III. Self-consistent model. *Journal of the Mechanics and Physics of Solids*, 13:189–198, 1965.
- [51] S.J. Hollister and N. Kikuchi. A comparison of homogenization and standard mechanics analysis for periodic porous composites. *Computational Mechanics*, 10:73–95, 1992.
- [52] G.A. Holzapfel. *Nonlinear solid mechanics: a continuum approach for engineering*. John Wiley & Sons, Chichester, 2000.
- [53] G.A. Holzapfel, T.C. Gasser, and R.W. Ogden. A new constitutive framework for arterial wall mechanics and a comparative study of material models. *Journal of Elasticity*, 61:1–48, 2000.
- [54] J.D. Humphrey. An evaluation of the pseudoelastic descriptors used in arterial mechanics. *J. Biomech. Engr.*, 121:259–262, 1999.
- [55] J.D. Humphrey. *Cardiovascular solid mechanics: cells, tissues, and organs*. Springer-Verlag, New York, 2002.

- [56] A. Ibrahimbegović and D. Markovič. Strong coupling methods in multi-phase and multi-scale modeling of inelastic behaviour of heterogeneous structures. *Comp. Meth. Appl. Mech. Engrg*, 192:3089–3107, 2003.
- [57] B. Johannesson and O.B. Pedersen. Analytical determination of the average Eshelby tensor for transversely isotropic fiber orientation distributions. *Acta Materialia*, 9:3165–3173, 1998.
- [58] K. Terada K. Matsui and K. Yuge. Two-scale finite element analysis of heterogeneous solids with periodic microstructures. *Comp. Struct.*, 82:593–606, 2004.
- [59] Ł. Kaczmarczyk. Generalized micro-to-macro transitions of microstructures for the first and second order continuum. In K.J. Bathe, editor, *Computational Fluid and Solid Mechanics*, pages 271–274, MIT, 2005.
- [60] V. Kouznetsova, W.A.M. Brekelmans, and F.P.T. Baaijens. An approach to micro-macro modeling of heterogeneous materials. *Computational Mechanics*, 27:37–48, 2001.
- [61] V. Kouznetsova, M.G.D. Geers, and W.A.M. Brekelmans. Multi-scale constitutive modelling of heterogeneous materials with a gradient-enhanced computational homogenization scheme. *Int. J. Numer. Meth. Engng*, 54:1235–1260, 2002.
- [62] V. Kouznetsova, M.G.D. Geers, and W.A.M. Brekelmans. Multi-scale second order computational homogenization of multi-phase materials: A nested finite element solution strategy. *Comp. Meth. Appl. Mech. Engrg*, 193:5525–5550, 2004.
- [63] V. G. Kouznetsova. *Computational homogenization for the multi-scale analysis of multi-phase materials*. PhD Thesis, Technische Universiteit Eindhoven, 2002.
- [64] P. Ladeveze and D. Dureisseix. A multi-level and mixed domain decomposition approach for structural analysis. *Decomposition methods, Contemporary Mathematics*, 10:246–253, 1998.
- [65] P. Ladeveze and D. Dureisseix. A new micro-macro computational strategy for structural analysis. *Comptes-Rendus de l’Académie des Sciences, Paris*, 327:1237–1244, 1999.

- [66] P. Ladeveze, O. Loiseau, and D. Dureisseix. A micro-macro and parallel computational strategy for highly heterogeneous structures. *International Journal for Numerical Methods in Engineering*, 52:121–138, 2001.
- [67] K. Lee and S. Ghosh. A microstructure based numerical method for constitutive modeling of composite and porous materials. *Materials Science and Engineering*, A272:120–133, 1999.
- [68] K. Levenberg. A method for the solution of certain problems in least squares. *Quarterly of Applied Mathematics*, 2:164–168, 1944.
- [69] X. Li and W. E. Multiscale modeling of the dynamics of solids at finite temperature. *Journal of the Mechanics and Physics of Solids*, 53:1650–1685, 2005.
- [70] J. Mandel. Plasticité classique et viscoplasticité. In *CISM Lecture Notes*, Udine, Italy, 1971.
- [71] D. Marquardt. An algorithm for least squares estimation on nonlinear parameters. *SIAM Journal of Applied Mathematics*, 11:431–441, 1963.
- [72] J.C. Michel, H. Moulinec, and P. Suquet. Effective properties of composite materials with periodic microstructures: a computational approach. *Computer Methods in Applied Mechanics and Engineering*, 172:109–143, 1999.
- [73] C. Miehe. Strain-driven homogenization of inelastic microstructures and composites based on an incremental variational formulation. *International Journal for Numerical Methods in Engineering*, 55:1285–1322, 2002.
- [74] C. Miehe. Computational micro-to-macro transitions for discretized microstructures of heterogeneous materials at finite strains based on the minimization of averaged incremental energy. *Computer Methods in Applied Mechanics and Engineering*, 192:559–591, 2003.
- [75] C. Miehe and J. Dettmar. A framework for micro-macro transitions in periodic particle aggregates of granular materials. *Computer Methods in Applied Mechanics and Engineering*, 193:225–256, 2004.
- [76] C. Miehe and A. Koch. Computational micro-to-macro transitions of discretized microstructures undergoing small strains. *Archive of Applied Mechanics*, 72:300–317, 2002.

- [77] C. Miehe, J. Schotte, and M. Lambrecht. Computational micro-macro transitions and overall moduli in the analysis of polycrystals at large strains. *Comput. Materials Sci.*, 16:372–382, 1999.
- [78] C. Miehe, J. Schotte, and M. Lambrecht. Homogenization of inelastic solid materials at finite strains based on incremental minimization principles. Application to the texture analysis of polycrystals. *Journal of the Mechanics and Physics of Solids*, 50:2123–2167, 2002.
- [79] S. Moorthy and S. Ghosh. A model for analysis of arbitrary composite and porous microstructures with Voronoi cell finite elements. *Int. J. Numer. Methods Eng.*, 39:2363–2398, 1996.
- [80] T. Mori and K. Tanaka. Average stress in the matrix and average elastic energy of materials with misfitting inclusions. *Acta Metallurgica*, 21:571–574, 1973.
- [81] H. Moulinec and P. Suquet. A numerical method for computing the overall response of non-linear composites with complex microstructure. *Computer Methods in Applied Mechanics and Engineering*, 157:69–94, 1998.
- [82] S. Nemat-Nasser. Multi-inclusion method for finite deformations: exact results and applications. *Materials Science and Engineering*, A285:239–245, 2000.
- [83] S. Nemat-Nasser and M. Hori. *Micromechanics: overall properties of heterogeneous materials*. Elsevier, Amsterdam, 1999.
- [84] R.W. Ogden. Large deformation isotropic elasticity - on the correlation of theory and experiment for incompressible rubberlike solids. *Proceedings of the Royal Society London A*, 326:565–584, 1972.
- [85] R.W. Ogden. *Non-linear elastic deformations*. Dover, New York, 1997.
- [86] R.W. Ogden, G. Saccomandi, and I. Sgura. Fitting hyperelastic models to experimental data. *Computational Mechanics*, 34:484–502, 2004.
- [87] N. Ohno, X. Wu, and T. Matsuda. Homogenized properties of elastic-viscoplastic composites with periodic internal structures. *International Journal of Mechanical Sciences*, 42:1519–1536, 2000.
- [88] E. Kröner. Berechnung der elastischen Konstanten des Vielkristalls aus den Konstanten des Einkristalls. *Z. Physik*, 151:504–518, 1958.

- [89] E. Kröner. Zur plastischen verformung des vielkristalls. *Acta Metallurgica*, 9:155–161, 1961.
- [90] E. Sanchez Palencia. *Non-homogeneous media and vibration theory*. Springer-Verlag, Berlin, 1980.
- [91] M. Partovi. Computational implementation of multi-scale non-linear solid material models. Masters thesis, University of Wales, Swansea, 2004.
- [92] M. Partovi. *Computational Strategies for Multiscale Analysis of Material Behaviour*. PhD Thesis, University of Wales, Swansea, School of Engineering, 2007.
- [93] D.J. Patel and D.L. Fry. The elastic symmetry of arterial segments in dogs. *Circulation Research*, 24:1–8, 1969.
- [94] C. Pellegrino, U. Galvanetto, and B.A. Schrefler. Numerical homogenization of periodic composite materials with non-linear material components. *International Journal for Numerical Methods in Engineering*, 46:1609–1637, 1999.
- [95] S. Reese. Meso-macro modelling of fibre-reinforced rubber-like composites exhibiting large elastoplastic deformations. *International Journal of Solids and Structures*, 40:951–980, 2003.
- [96] S. Reese, T. Raible, and P. Wriggers. Finite element modelling of orthotropic material behaviour in pneumatic membranes. *International Journal of Solids and Structures*, 38:9525–9544, 2001.
- [97] B.J.E. Rens, W.A.M. Brekelmans, and F.P.T. Baaijens. Homogenization of the elastoplastic behaviour of perforated plates. *Computers and Structures*, 69:537–545, 1998.
- [98] G. Ryskin. Misconception which led to the “material frame-indifference controversy”. *Physical Review A*, 32:1239–1240, 1985.
- [99] B.S. Schultze-Jena. Über die schraubenförmige Struktur der Arterienwand. *Gegenbauers Morphol. Jahrbuch*, 83:230–246, 1939.

- [100] R.J.M. Smit, W.A.M. Brekelmans, and H.E.H. Meijer. Prediction of the mechanical behaviour of nonlinear heterogeneous systems by multi-level finite element modeling. *Computer Methods in Applied Mechanics and Engineering*, 155:181–192, 1998.
- [101] R.J.M. Smit, W.A.M. Brekelmans, and H.E.H. Meijer. Prediction of the large-strain mechanical response of heterogeneous polymer systems: local and global deformation behaviour of a representative volume element of a voided polycarbonate. *Journal of the Mechanics and Physics of Solids*, 47:201–221, 1999.
- [102] D.D. Somer, E.A. de Souza Neto, W.G. Dettmer, and D. Perić. Computational strategies for the multi-scale analysis of solids: small and large strain formulations. In E. Oñate, D.R.J. Owen, and B. Suárez, editors, *Computational Plasticity IX. Fundamentals and Applications*, pages 421–424, CIMNE, Barcelona, Spain, 2007.
- [103] A.J.M. Spencer. *Continuum mechanics*. Longman Scientific & Technical, Cambridge, 1980.
- [104] J. Staubesand. Anatomie der Blutgefäße. I. Funktionelle Morphologie der Arterien, Venen und arterio-venösen Anastomosen. In M. Ratschow, editor, *Angiology*, pages 23–82, Stuttgart, 1959.
- [105] P. Suquet. On bounds for the overall potential of power law materials containing voids with an arbitrary shape. *Mech. Res. Comm.*, 19:51–58, 1992.
- [106] P. Suquet. Overall potentials and extremal surfaces of power law or ideally plastic materials. *Journal of the Mechanics and Physics of Solids*, 36:29–58, 1993.
- [107] K. Takamizawa and K. Hayashi. Strain energy density function and uniform strain hypothesis for arterial mechanics. *Journal of Biomechanics*, 20:7–17, 1987.
- [108] D.R.S. Talbot and J.R. Willis. Variational principles for inhomogeneous nonlinear media. *IMA. J. Appl. Math.*, 35:39–54, 1985.
- [109] D.R.S. Talbot and J.R. Willis. The overall behaviour of a nonlinear fiber reinforced composite. In G.J. Dvorak, editor, *Inelastic Deformation of Composite Materials*, pages 527–545, Springer, New York, 1991.

- [110] D.R.S. Talbot and J.R. Willis. Some explicit bounds for the overall behaviour of nonlinear composites. *Int. J. Solids Structures*, 29:1981–1987, 1992.
- [111] G.I. Taylor. Plastic strain in metals. *Journal of Institute of Metals*, 62:307–324, 1938.
- [112] K. Terada and N. Kikuchi. Nonlinear homogenization method for practical applications. In S. Ghosh and M. Ostoj-Starzewski, editors, *Computational Methods in Micromechanics (Proceedings of 1995 ASME International Mechanical Engineering Congress and Exposition)*, pages 1–16, San Francisco, USA, 1995.
- [113] K. Terada and N. Kikuchi. A class of general algorithms for multi-scale analysis of heterogeneous media. *Comp. Meth. Appl. Mech. Engrg.*, 190:5427–5464, 2001.
- [114] K. Terada, I. Saiki, K. Matsui, and Y. Yamakawa. Two-scale kinematics and linearisation for simultaneous two scale analysis of periodic heterogeneous solids at finite strains. *Comp. Meth. Appl. Mech. Engrg.*, 192:3531–3563, 2003.
- [115] P. Ponte Castañeda. The effective properties of brittle/ductile incompressible composites isotropic composites. In G.J. Dvorak, editor, *Inelastic Deformation of Composite Materials*, pages 215–231, Springer, New York, 1991.
- [116] P. Ponte Castañeda. New variational principles in plasticity and their application to composite materials. *Journal of the Mechanics and Physics of Solids*, 40:1757–1788, 1991.
- [117] P. Ponte Castañeda. The effective mechanical properties of nonlinear isotropic composites. *Journal of the Mechanics and Physics of Solids*, 39:45–71, 1991.
- [118] A. Tolenado and H. Murakami. A high-order mixture model for periodic particle composites. *Int. J. Solids Structures*, 23:989–1002, 1987.
- [119] C. Truesdell. *Six lectures on modern natural philosophy*. Springer-Verlag, Berlin, 1966.
- [120] C. Truesdell. *A first course in rational continuum mechanics, Volume 1*. Academic Press, New York, 1977.
- [121] R.N. Vaishnav, J.T. Young, and D.J. Patel. Distribution of stresses and of strain-energy density through the wall thickness in a canine aortic segment. *Circulation Research*, 32:577–583, 1973.

- [122] O. van der Sluis, P.J.G. Schreurs, and H.E.H. Meijer. Effective properties of a viscoplastic constitutive model obtained by homogenisation. *Mechanics of Materials*, 31:743–759, 1999.
- [123] W. Voigt. Über die Beziehung zwischen den beiden Elastizitätskonstanten isotroper Körper. *Wied. Ann. Physik*, 38:573–587, 1889.
- [124] J.R. Willis. The overall response of composite materials. *ASME Journal of Applied Mechanics*, 50:1202–1209, 1983.
- [125] Q.-S. Yang and Q.-H. Qin. Modelling the effective elasto-plastic properties of unidirectional composites reinforced by fibre bundles under transverse tension and shear loading. *Materials Science and Engineering*, A344:140–145, 2003.
- [126] O.C. Zienkiewicz, J. Too, and R.L. Taylor. Reduced integration technique in general analysis of plates and shells. *International Journal for Numerical Methods in Engineering*, 3:275–90, 1971.
- [127] O. C. Zienkiewicz and R.L.Taylor. *The finite element method – Volume 2: Solid mechanics*. Butterworth Heinemann, Oxford, 5th edition, 2000.
- [128] T.I. Zohdi and P. Wriggers. Aspects of the computational testing of the mechanical properties of microheterogeneous material samples. *International Journal for Numerical Methods in Engineering*, 50:2573–2599, 2001.
- [129] M.A. Zulliger, P. Fridez, K. Hayashi, and N. Stergiopoulos. A strain energy function for arteries accounting for wall composition and structure. *Journal of Biomechanics*, 37:989–1000, 2004.